Fast Multipole Method for 3-D elastodynamic boundary integral equations. Application to seismic wave propagation

Stéphanie Chaillat

Méthode multipôle rapide pour les équations intégrales de frontière en élastodynamique 3-D. Application à la propagation d'ondes sismiques.

THÈSE

présentée et soutenue publiquement le 8 décembre 2008
pour l'obtention du diplôme de

Docteur de l'École Nationale des Ponts et Chaussées

(spécialité Mécanique)
par

Stéphanie CHAILLAT

Composition du jury

Directeurs :	M. Marc BONNET (École Polytechnique)
	M. Jean-François SEMBLAT (LCPC Paris)
Rapporteurs :	M. Dimitri KOMATITSCH (Université de Pau)
	M. Martin SCHANZ (Graz University of Technology, Autriche)
Examinateurs :	M. Pierre-Yves BARD (LGIT Grenoble/LCPC)
	M. Jacobo BIELAK (Carnegie Mellon University, USA)
	M. Antoine CHAIGNE (ENSTA)
	M. Abdellatif EL BADIA (UTC)

Laboratoire de Mécanique des Solides, École Polytechnique, 91128 Palaiseau Cedex.
Laboratoire Central des Ponts et Chaussées, 58, boulevard Lefebvre 75732 Paris Cedex 15.

Fast Multipole Method
for 3-D elastodynamic boundary integral equations.
Application to seismic wave propagation.

Stéphanie CHAILLAT

Laboratoire de Mécanique des Solides, École Polytechnique, 91128 Palaiseau Cedex.
Laboratoire Central des Ponts et Chaussées, 58, boulevard Lefebvre 75732 Paris Cedex 15.

Résumé étendu

Contexte

La propagation des ondes sismiques peut être simulée à l'aide de différentes méthodes numériques : méthode des éléments finis, méthode des différences finies, méthode des éléments spectraux, méthode des éléments de frontière (BEM, pour Boundary Element Method), ... Cette dernière présente l'avantage de ne nécessiter que la discrétisation de la frontière du domaine de calcul considéré. De plus, elle permet de simuler des milieux étendus en évitant la forte dispersion numérique associée à d'autres schémas. La BEM est donc bien adaptée pour le calcul de la propagation d'ondes sismiques. Le principal inconvénient de la formulation intégrale de frontière est qu'elle conduit à un système linéaire dont la matrice est pleine et non symétrique. Les solveurs adaptés à ce type de problèmes sont de deux types. D'une part, les solveurs directs, qui factorisent la matrice du système, ont une complexité de l'ordre de $O(N^3)$ en temps et $O(N^2)$ en mémoire (N étant le nombre de degrés de liberté). Ils sont donc inutilisables dès que N devient grand. D'autre part, les solveurs itératifs construisent une suite convergeant vers la solution. La complexité est alors de l'ordre de $O(n_{\text{iter}} \times N^2)$ en temps et en mémoire. La contrainte de stockage en mémoire les rend difficiles à appliquer aux systèmes BEM de taille supérieure à $O(10^4)$ inconnues. La résolution de problèmes réalistes en termes de géométrie, hétérogénéité, longueur d'onde ... est donc limitée par le nombre de degrés de liberté que peut traiter le solveur sur une machine donnée. De plus, comme l'analyse est menée dans le domaine fréquentiel, la taille des maillages est liée à la fréquence du problème. Le spectre des fréquences étudiées est donc aussi restreint par ces considérations.

L'idée est alors d'appliquer une méthode d'accélération de l'évaluation des opérateurs intégraux, étape essentielle du calcul d'un produit matrice-vecteur utilisé par le solveur itératif (GMRES dans notre cas) afin de diminuer le temps CPU d'une itération mais aussi les besoins en stockage. Cette réorganisation du calcul est rendue possible par la méthode multipôle rapide (*Fast Multipole Method* ou FMM en anglais). Initialement développée pour les problèmes à N corps par Rokhlin et Greengard [102] dans les années 80, la méthode a ensuite été adaptée aux équations de l'électromagnétisme par Rokhlin [175] et Chew [198] . Actuellement, la FMM est appliquée dans de nombreux domaines [159] : astrophysique, mécanique des fluides, acoustique [158], ... Dans le domaine de l'élastodynamique, très peu de travaux ont été réalisés. On peut citer les travaux de Takahashi et al. [201, 202] dans le domaine temporel. Dans le domaine fréquentiel, la première étude en 2-D est due à Chen et al. [44]. En 3-D, on peut citer les travaux de Yoshida [213] où la méthode est appliquée à l'étude de la propagation de fissures et ceux de Fujiwara [90] où quelques applications sismiques basses fréquences sont présentées. Le but de cette thèse est de développer un solveur numérique efficace pour résoudre des problèmes de propagation d'ondes sismiques de grande taille. Dans ce but, une méthode BEM accélérée par la FMM est développée. Ce mémoire

est découpé en deux parties précédées d'un chapitre introductif. La première partie est consacrée à la formulation et la mise en oeuvre de la FMM pour les équations de l'élastodynamique 3-D. Dans la deuxième partie, ces méthodes sont appliquées à des problèmes sismiques, afin de montrer leurs capacités.

PARTIE I : FORMULATION ET MISE EN OEUVRE DE LA FMM POUR LES ÉQUATIONS DE L'ÉLASTODYNAMIQUE 3-D

Méthode multipôle rapide pour les équations de l'élastodynamique 3-D. Dans le Chapitre 2, la formulation de la FMM pour les équations de l'élastodynamique 3-D, ainsi que sa mise en oeuvre et validation sont présentées. La présence du terme $\frac{\exp(ikr)}{r}$ (fonction de Green pour l'équation de Helmholtz, pour l'espace infini) dans les tenseurs de Green de l'espace infini élastique (2.2a,b) (où k est le nombre d'onde et (x, y) un couple de points sur la frontière), permet de les reformuler en termes de développements en séries multipôles (2.13a,b, 2.14a,b), analogues à ceux connus en électromagnétisme [198]. Ainsi, les variables x et y de l'intégrale sont séparées. Il n'est plus nécessaire de recalculer les solutions élémentaires pour chaque couple de points sur la frontière de l'objet et, dans l'intégrale, il est possible de réutiliser les intégrations précédentes selon x. Les contributions mutuelles entre tous les points x et y sont ainsi réduites à quelques contributions entre paquets de points x et paquets lointains de points y (Figure 2.4). De plus, afin de diminuer le coût mémoire et le temps de calcul du produit matrice-vecteur, la matrice du système n'est jamais explicitement assemblée (contrairement à la méthode BEM classique). La FMM existe sous deux formes : simplifiée et complète. La première, mono-niveau, s'appuie sur un découpage en boîtes cubiques de la région de l'espace contenant la frontière du domaine, et permet de calculer le produit matrice-vecteur en $O(N^{3/2})$ opérations. Dans la seconde, multi-niveaux, le découpage en boîtes cubiques est récursif, ce qui permet d'obtenir une complexité inférieure du calcul produit matrice-vecteur, de l'ordre de $O(N \log_2 N)$.

La méthode utilise plusieurs paramètres dont dépendent la rapidité et la précision du calcul (taille des cellules, nombre de niveaux de grilles, troncature de la série du développement multipôle, ...). Dans le cas de l'élastodynamique, les valeurs optimales pour obtenir un bon compromis entre efficacité et précision sont déterminées pour les approches mono et multi-niveaux dans la Section 2.4. Les complexités théoriques sont vérifiées numériquement dans la Section 2.5 (voir la Figure 2.18). Dans la Section 2.6, des tests sur des cas simples, dont la solution analytique est connue, valident la méthode et montrent sa précision. Ces calculs montrent encore que l'erreur introduite par la FMM par rapport à la BEM classique n'a pas d'incidence pratique sur la qualité du résultat. Pour terminer, cette approche permet, par exemple dans le cadre de la sismologie, de résoudre des problèmes plus réalistes et pour un spectre de fréquences plus large. Un des exemples proposés montre ainsi qu'il est possible d'étudier la propagation des ondes sismiques dans un canyon, sans restriction forte sur la taille du domaine discrétisé (y compris surface libre), pour des fréquences supérieures à celles habituellement utilisées pour ce type de calcul et ce avec une discrétisation fine sur tout le domaine.

FM-BEM pour les problèmes multi-domaines. La méthode présentée dans le Chapitre 2 est limitée aux milieux homogènes car les solutions fondamentales utilisées sont celles de l'espace élastique infini. Or, pour étudier des configurations réalistes, cette limitation est trop restrictive. Le

but du Chapitre 3 est d'étendre la formulation présentée au Chapitre 2 à des configurations multi-domaines, grâce au développement d'une stratégie de couplage élément de frontière-élément de frontière. Tout d'abord, la formulation BEM continue, adaptée à l'étude de la propagation d'ondes sismiques dans des structures géologiques complexes (irrégularités topographiques, bassins sédimentaires, ...) est présentée dans la Section 3.2. Ensuite, la stratégie de couplage est présentée dans la Section 3.3. Cette méthode repose sur l'utilisation, de manière indépendante dans chaque sous-domaine homogène, de la méthode FMM présentée au Chapitre 2. La stratégie de couplage ne se réduit pas à la concaténation des équations intégrales de frontière dans chaque sous-domaine en un système global d'équations: l'interpolation des inconnues en déplacement étant linéaire et celle des inconnues en tractions constante, le système global ainsi obtenu serait sur-determiné. On propose alors d'effectuer des combinaisons linéaires judicieuses des équations intégrales de frontière. Différents détails sur la mise en oeuvre efficace de cette méthode (choix des coefficients de pondération définissant les combinaisons linéaires, mise à l'échelle des équations, ordre des inconnues et orientation des normales) sont présentés dans la Section 3.4. Dans la Section 3.5, cette stratégie de couplage est validée sur un problème de propagation d'ondes planes dans un bassin sédimentaire, pour lequel une solution de référence est disponible dans la littérature. Des calculs à plus hautes fréquences ont pu être effectués grâce à ce nouveau solveur. De plus, il est montré dans la Section 3.6 que la méthode peut aussi être utilisée pour traiter des problèmes dans le domaine temporel, via l'utilisation d'une transformée de Fourier.

Préconditionnement et autres améliorations de la formulation. Le solveur FM-BEM pour les équations de l'élastodynamique 3-D présenté dans les Chapitres 2 et 3 a déjà permis d'améliorer les performances de la BEM standard. Toutefois, la méthode peut encore être ameliorée. Dans le Chapitre 4, différents points qui peuvent augmenter les performances de la FM-BEM developpée dans cette thèse, sont présentés. Tout d'abord, une méthode de préconditionnement est introduite afin de réduire le nombre d'itérations du solveur itératif et ainsi accélérer le temps de résolution. La méthode proposée (voir l'Algorithme 4.3) est basée sur l'utilisation de deux solveurs itératifs emboités. Le solveur extérieur est un GMRES flexible et le solveur intérieur, qui permet de calculer l'inverse du préconditionneur M, est un GMRES classique. La définition d'un préconditionneur efficace est une question cruciale mais délicate dans le cadre de la FMM car la matrice du système n'est jamais explicitement formée. On propose ici d'utiliser comme préconditionneur la seule matrice à notre disposition, la matrice des interactions proches $M = K^{\text{near}}$. On montre que l'utilisation de ce préconditionneur réduit de manière significative le nombre d'itérations pour des problèmes de propagation d'ondes planes dans des canyons ou bassins sédimentaires.

Ensuite, une méthode pour réduire le nombre nécessaire de moments multipôles est présentée dans la Section 4.2. Au lieu d'utiliser les coordonnées cartésiennes, l'idée est de reformuler les moments multipôles sur une base appropriée. Ainsi le nombre de moments multipôles requis est réduit de 8 à 6 et on espère que les coûts mémoire et temps CPU seront également réduits. Cette méthode n'est pas mise en oeuvre au moment de la rédaction de cette thèse mais le sera prochainement.

Pour terminer, dans la Section 4.3, une méthode pour formuler le développement multipôle de la solution fondamentale du demi-espace élastique est proposée. Le principal avantage de l'utilisation de la solution fondamentale du demi-espace élastique est que la condition de surface libre y est déjà incluse. Il n'est donc pas nécessaire de discrétiser la surface libre et on réduit ainsi le nombre de degrés de liberté. Toutefois, il n'existe pas actuellement de développement multipôle adapté à ces solutions fondamentales. Pour trouver un tel développement, on propose d'adapter une

méthode utilisée par ailleurs [61, 100] pour la définition des méthodes multipôles basses fréquences, reposant sur une transformée de Fourier par rapport aux deux variables spatiales parallèles au plan de la surface libre. La transformée de Fourier de la solution fondamentale est ainsi formulée comme l'intégrale du produit d'une fonction de $\boldsymbol{x}$ et d'une fonction de $\boldsymbol{y}$. La difficulté réside dans le calcul numérique de la transformée de Fourier inverse. On propose d'utiliser une méthode basée sur la décomposition en valeurs singulières, non encore mise en oeuvre au moment de la rédaction de ce mémoire. Cette formulation devrait permettre d'améliorer de manière significative les capacités de la BEM accélérée par FMM appliquée aux milieux semi-infinis.

PARTIE II : APPLICATION À LA PROPAGATION D'ONDES SISMIQUES

La deuxième partie de ce mémoire est consacrée à l'application de cette nouvelle méthode pour l'étude de problèmes sismiques.

Problèmes sismiques canoniques. Tout d'abord, dans le Chapitre 5, la méthode est appliquée à l'étude de la propagation et l'amplification d'ondes planes P et SV, d'incidence oblique, dans des canyons et bassins canoniques. Les exemples traités sont issus de notre contribution au projet de recherche ANR "Quantitative Seismic Hazard Assessment" (QSHA, http://qsha.unice.fr/) sous la forme d'une participation au développement d'outils numériques pour la simulation de la propagation des ondes sismiques. Plusieurs partenaires, possédant une expertise sur différentes méthodes numériques (méthode des éléments finis, méthode des différences finies, méthode des volumes finis, méthode des éléments spectrales, méthode des éléments discrets et méthode des éléments de frontière) étant impliqués dans le projet QSHA, une série de problèmes canoniques a été proposée à tous les participants afin de comparer la précision et les performances de toutes ces méthodes numériques. Au moment de la rédaction de cette thèse, les comparaisons ne sont pas encore disponibles. On a toutefois choisi de présenter nos résultats pour permettre des comparaisons. De plus, ce chapitre a permis de tester l'efficacité du préconditionneur présenté au Chapitre 4, en termes de réduction du nombre d'itérations pour les problèmes de propagation dans un canyon ou un bassin. Il est ainsi remarqué que même si le nombre d'itérations augmente toujours avec la fréquence, cette augmentation est beaucoup moins rapide si le préconditionneur proposé est utilisé (voir Figure 5.12 par exemple).

Application sismique réaliste : étude d'une vallée Alpine. Tous les résultats présentés dans les chapitres précédents concernent des problèmes pour des géométries canoniques. Le but du Chapitre 6 est d'utiliser l'efficacité de la méthode pour traiter un problème plus réaliste. La propagation d'ondes planes dans une vallée alpine (Grenoble) est ainsi étudiée. Ce problème permet de mettre en avant le gain d'efficacité apporté par cette nouvelle formulation par rapport à la méthode BEM standard utilisée dans [64] pour traiter la même géométrie. Cet exemple a aussi permis de pointer une autre nécessité d'amélioration de la méthode pour traiter des problèmes réalistes. Ainsi, si il existe un fort contraste de vitesse entre deux couches en regard, le nombre de points par longueur d'onde est adapté au matériau le plus mou. Par conséquent, comme le maillage est conforme, l'interface est maillée beaucoup trop finement pour la couche la plus dure. Or, la FMM perd de son efficacité quand le maillage présente de fortes hétérogénéités de densité. Pour pouvoir traiter de manière efficace de grands problèmes sismiques réalistes, on pourrait par exemple développer

une méthode stable à toutes fréquences [117, 164] (associant une FMM basses fréquences à la FMM hautes fréquences employée dans ce travail). Ceci permettrait d'utiliser des cellules plus petites et donc de conserver un nombre d'inconnues par cellule à peu près constant sans nuire à la précision. Une autre méthode peut consister en l'utilisation d'un maillage non-conforme, via le développement d'un couplage faible, pour les problèmes multi-régions à forts contrastes de propriétés.

Conclusion et perspectives

Conclusion. Dans ce mémoire la méthode multipôle rapide a été étendue avec succès aux équations de l'élastodynamique 3-D. Dans un premier temps, une méthode mono-domaine a été présentée. Pour pouvoir traiter des problèmes sismiques dans des milieux homogènes par couches, une méthode de couplage élément de frontière-élément de frontière a été développée. Une méthode de préconditionnement a également été mise en place pour augmenter les capacités de la méthode. La méthode présentée peut toutefois encore être améliorée. On a proposé dans ce but deux formulations à mettre en oeuvre. Dans une deuxième partie, la méthode a été appliquée pour traiter des modèles canoniques et plus réalistes. On a ainsi montré qu'il est possible de traiter des problèmes comportant jusqu'à $N = O(10^6)$ degrés de liberté pour des modèles canoniques mais qu'il reste nécessaire d'apporter quelques améliorations pour traiter des problèmes réalistes à haute fréquence.

Perspectives. Cette première étude sur la méthode multipôle rapide pour les équations de l'élastodynamique 3-D, menée au LMS et au LCPC, a ouvert de nombreuses perspectives. On propose, par exemple, pour améliorer les capacités de la méthode d'essayer de la paralléliser ou d'étudier plus en détails les méthodes de préconditionnement. De plus, dans cette étude, seules les équations de l'élasticité sont traitées. On montre qu'il est possible d'étendre la méthode à l'étude des équations de la viscoélasticité. Une autre perspective est de coupler la méthode avec d'autres méthodes numériques ou bien de l'utiliser comme solveur direct pour résoudre des problèmes inverses.

Annexes

Le mémoire se termine avec cinq annexes qui donnent des détails sur : la mise en oeuvre de la BEM standard, les champs d'ondes incidents, les fonctionnalités et l'utilisation du code développé, les fonctions spéciales. Pour terminer, la dernière annexe reprend un travail publié [42], effectué en parallèle de la thèse.

Principales publications associées à ce travail

Articles. Le travail présenté dans cette thèse a fait l'objets de plusieurs publications dans des revues avec comité de lecture:

- S. Chaillat, M. Bonnet et J. F. Semblat. A new fast multi-domain BEM to model seismic wave propagation and amplification in 3D geological structures. *Geophys. J. Int.*, accepté, 2008.
- S. Chaillat, M. Bonnet et J. F. Semblat. A fast multipole accelerated BEM for 3-D elastic wave computation. *Revue Européenne de Mécanique Numérique*, 17: 701–712, 2008.

- S. Chaillat, M. Bonnet et J. F. Semblat. A multi-level fast multipole BEM for 3-D elastodynamics in the frequency domain. *Comp. Meth. Appl. Mech. Engng.*, 197:4233–4249, 2008.
- S. Chaillat et H. D. Bui. Resolution of linear viscoelastic equations in the frequency domain using real Helmholtz boundary integral equations. *C. R. Mecanique*, 335:746–750, 2007.
- S. Chaillat, M. Bonnet et J. F. Semblat. A fast multipole method formulation for 3D elastodynamics in the frequency domain. *C. R. Mecanique*, 335:714–719, 2007.

Chapitre. Un chapitre dans un ouvrage scientifique est aussi tiré de ce travail:

- M. Bonnet, S. Chaillat and J. F. Semblat. Multi-level fast multipole BEM for 3-D elastodynamics. *Dans Recent Advances in BEM* (D. Polyzos et G. Manolis, eds.), à paraître, 2008.

Conférences. Ce travail a été présenté lors de 5 conférences internationales et 3 conférences nationales.

Contents

Chapter 1

Introduction

Contents

1.1 GENERAL OVERVIEW

The present work is concerned with the numerical modelling of 3-D elastic wave propagation. The Boundary Element Method (BEM) is known to be well suited to deal with unbounded domains, but in its traditional form leads to high CPU costs and memory requirements. The main goal of this thesis is to develop a fast BEM to increase the capabilities of the standard method in the context of 3-D elastic wave propagation. To this end, the Fast Multipole Boundary Element Method, already developed in other areas such as electromagnetism, is extended to 3-D multi-domain elastodynamics. This Fast Multipole accelerated BEM is then applied to study seismic wave propagation and amplification in sedimentary basins. The methodology presented in the following is applied to seismic waves but it is not limited to this kind of waves. It is a first step at the LCPC and LMS toward the development of fast solvers for elastic waves and in the future, other applications of the present work will be performed: soil-structure interaction, inverse problems, vibration induced waves, ...

1.2 SEISMIC WAVE PROPAGATION AND AMPLIFICATION

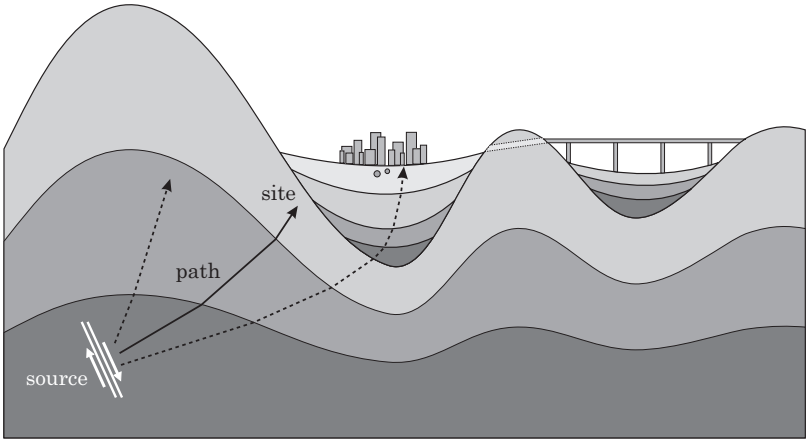

Figure 1.1: *Seismic wave propagation at various scales (from Semblat and Pecker [193]).*

Nowadays, earthquake engineering and seismology are very active research fields because of the huge human and economical issues underlying the challenging scientific topics. For example, the seismic events in Mexico (1985), Kobé (1995) or Bam (2003) caused many casualties and extensive damage. The seismic ground motion is not only influenced by the source features but also by the path from the source to the site and by local amplification in surficial alluvial deposits (site effects, Fig. 1.1). For this reason, various studies deal with seismic wave propagation in complex media. In this work, only seismic wave propagation and amplification in surficial alluvial deposits is considered. The phenomenon was first considered during the Michoacan 1985 earthquake in Mexico. It was observed that, in the center of Mexico, located 400 kilometers away from the epicenter, the maximum acceleration was very large. A likely explanation is the geological structure under Mexico city, characterized by thick clay deposits. In France, where seismicity is moderate, site effects are nevertheless studied. For example, in Alpine valleys, the deep and narrow alluvial deposits may lead to complex propagation phenomena. Due to multiple reflections and diffractions

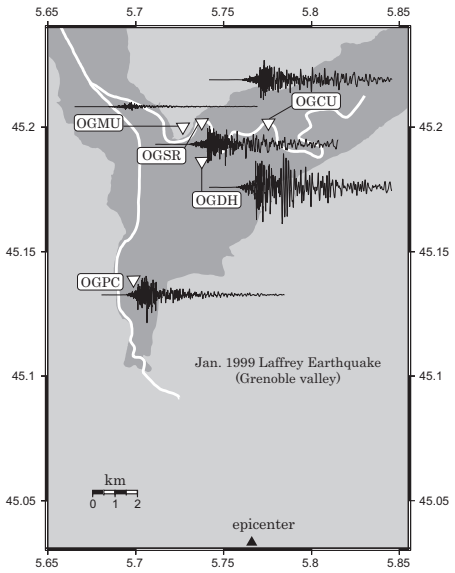

Figure 1.2: *Seismic wave amplification in deep alluvial deposits (Grenoble, France): velocities (N-S component) recorded at various locations during the 1999 Laffrey earthquake (data: French accelerometric network, www-rap.obs.ujf-grenoble.fr), from Semblat and Pecker [193].*

at the basin edges, the seismic motion may be strongly amplified (see for example the Grenoble basin in Fig. 1.2, where the reference bedrock site is called OGMU). Site effects are caused by the velocity contrast between the various soil layers, and their geometry. They can be decomposed into three phenomena that we now briefly review.

Topographical site effects. The first important cause of site effects is the site topography: crests, hills, canyons, edges, . . . The incident wave field is modified by the surface topographical irregularities and the effect of the scattering is an important factor in the amplification of the surface ground motion (Fig. 1.3). The wave type, the geometry or the presence of heterogeneities may modify this process. Experimental and numerical studies have been performed to understand this site amplification effect (Bard [11], Paolucci [166]). On one hand, it is known that convex geometries as hills

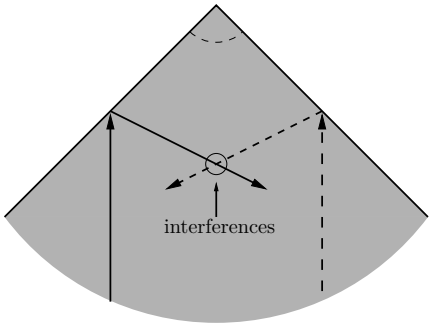

Figure 1.3: *Constructive interferences due to a simple topographic irregularity (from Semblat and Pecker [193]).*

and mountains may lead to a significant amplification of the seismic motion. On the other hand, concave geometries generally reduces the motion. For example, during the 1909 Lambesc (France) earthquake, the area of the village of Rognes, located on a hill, was severely damaged. Another example of such phenomenon took place in Bam, Iran (2003).

Stratigraphic site effects. The surface ground motion is due to the propagation of seismic waves through the various layers and consequently depends upon the layer properties (vertical heterogeneities). In other words, due to the velocity contrast between alluvial deposits and the bedrock, the transmitted wave fields are amplified and trapped in the uppermost layers as surface waves (Fig. 1.4). This leads to surface motion amplification and longer signal records. Ground motion amplification occurs when a seismic ray travels through an interface from a stiffer medium to a softer one. The governing parameters for such phenomena are:

- the thicknesses of, and the wave velocities in, the sedimentary layers;
- the frequency range, polarization and incidence angle of the waves.

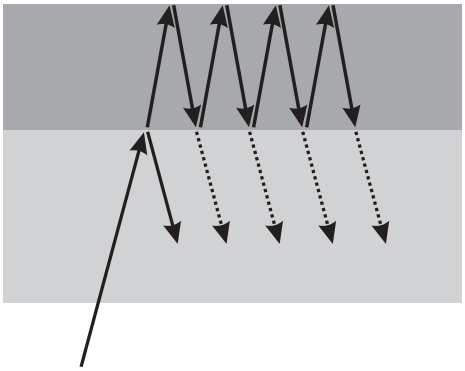

Figure 1.4: *Principle of 1-D stratigraphic site effect (from Semblat and Pecker [193]).*

Basin effects. Finally, the influence of the "horizontal heterogeneities" (e.g. alluvial basins) should also be taken into account. The basin shape may cause some focusing of the wave field in the basin (Fig. 1.5). Moreover, the basin edges effect generally leads to trapping surface waves. These effects lead to some (possibly strong) motion amplification and increase the duration of the signal as well (Bard and Bouchon [12, 13]).

1.3 MODELLING SEISMIC WAVE PROPAGATION

To analyze site effects, it is possible to consider modal approaches (Semblat et al. [192]) or directly investigate wave propagation phenomena. Modelling seismic wave propagation has become an important field of research. For simple geometries, the solution can be obtained by analytical means. For example, the *Aki-Larner method* [4], in which the scattered wave field is represented as a superposition of plane waves propagating in various directions, is used to deal with simple geometries (e.g. in Bouchon et al. [36]). We also mention the *series expansions of wave functions*,

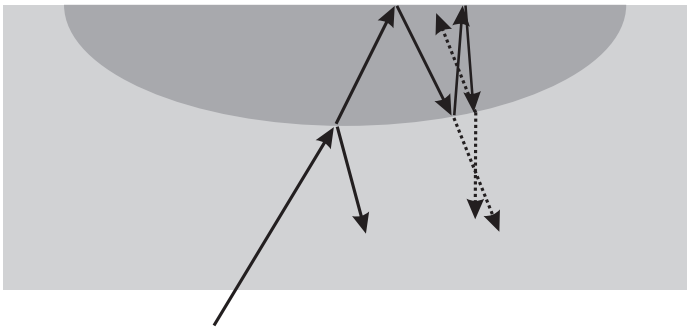

Figure 1.5: *Principle of 2-D site effect in alluvial basins (from Semblat and Pecker [193]).*

introduced by Sánchez-Sesma [183], where scattered fields are expressed as linear combinations of chosen wave functions (which are solutions of Navier's equation) whose coefficients are determined (for simple geometries) so as to satisfy the boundary conditions in a least-squares sense. For complex geological structures, numerical methods are needed. With the continuing increase of computational resources, realistic simulations of waveforms in the presence of highly heterogeneous structures and source models become feasible. Numerical methods most prominently applied to wave propagation problems are the finite difference method, the finite element method, the spectral element method, the discontinuous Galerkin method, the finite volume method, the discrete element method and the boundary element method. We now briefly review the main characteristics of these methods in the framework of seismic wave propagation.

Finite-difference method. The finite-difference (FD) method has been widely used since the 90s (e.g. Frankel and Leith [83], Frankel and Vidale [84], Frankel [82], Graves [98] and Olsen et al. [163]). One reason of the widespread use is the simplicity of the method and its implementation. Another reason is that viscoelasticity, or finite sources, can be treated in a relatively straightforward way. Finally, the local nature of finite-difference operators makes the method suitable for parallelization. In seismic applications, the velocity-stress formulation proposed by Madariaga [140] and Virieux [207] is used. Recently, some improvements have been proposed by Saenger et al. [181] with the use of a *new rotated straggered grid* to simulate media with heterogeneities (cracks, pores or free surface) without using boundary conditions. Zingg et al. [215, 216] have proposed a maximum-order scheme and an optimized scheme for modelling long-range linear wave propagation. In spite of these recent improvements, the main limitations are the extensive consumption of computational resources in terms of both core memory and CPU time, the limitation to simple geometries and the poor accuracy for the computation of surface waves. A review by Moczo et al. on the use of FD methods can be found in [153].

Finite element method. The finite element (FE) method is more efficient for dealing with complex geometries and heterogeneous media. FE is applied to seismology since 1972 (e.g. Lysmer and Drake [139]). This method is also applicable with inelastic constitutive models (e.g. Bonilla [30]). Recently, Bielak et al. [27] have developed an efficient FE-based computational platform for large-scale ground motions. Nevertheless, low approximation orders may lead to large numerical dispersion, as explained in Marfurt [147]. As a result, mesh refinement is required to reduce numerical

dispersion but may lead to a large numerical cost even if parallelization is possible. Some high order FEM computations, even if not often considered for wave propagation simulations, were also shown to be more accurate (e.g. Semblat et Brioist [190]). Recently, Hughes et al. [115] have shown that the interpolation errors of standard finite elements diverge with respect to the order of approximation. But, the behavior of non-uniform rational B-splines (NURBS) is better: they converge with respect to the order of approximation.

Spectral element method. The spectral element (SE) method combines the flexibility of the FE to handle complex geometries with the accuracy and exponential convergence rate afforded by spectral approximations (e.g. Kosloff et al. [125], Carcione et al. [39]). This time-domain method is based on high order approximations of elastodynamic variational formulations, and hence takes naturally into account interface conditions and free surfaces. The first uses of SE methods in 3-D elastodynamics were proposed by Faccioli et al. [74] and Komatitsch and Vilotte [124]. These articles show the very high accuracy and low numerical dispersion of the SE. Then, parallel implementations of SE for wave propagation have been proposed in Komatitsch and Vilotte [124], Komatitsch et al. [121] and Chaljub et al. [43]. The SEM is generally applied to linear media (see however e.g. Di Prisco et al. [66] for a use to non-linear media) and hexahedral meshes. The lack of meshing flexibility is a major limitation, as explained by Delavaud [63].

Discontinuous Galerkin method. The discontinuous galerkin (DG) method is an extension of SE or FE in which the condition of continuity between elements is relaxed, the solution being approximated using piecewise continuous polynomials basis functions. The main advantage of this method is the development of high-order accurate solutions using unstructured and non-conforming meshes. The DG method is also well suited for parallel implementation. As a particular case of the DG method, the finite volume (FV) method uses approximations of order zero. Recent interesting results on DG and FV methods can be found in Benjemaa [21], Dormy and Tarantola [68] and Dumbser and Kaser [69]. The main limitation of these methods is related to the following basic concept: the unknowns are element-based, in contrast to most other general volume methods which are vertex-based.

Discrete element method. In the discrete element (DE) method, the medium is modelled by particles which interact with their neighbours (attractive and repulsive interactions) according to local/discrete mechanical laws. This method was first developed to model granular materials, rocks and discontinuities at grain scale. This method is well suited to deal with non-linear materials and rupture of brittle materials (e.g. Ibrahimbegovic and Delaplace [116]). The main limitations of this method are the high CPU costs which make it difficult to deal with fully 3-D domains, the characterization of the mechanical characteristics of the links at the interfaces, and the use of spherical particles.

Boundary element method. The Boundary element method (BEM) is based on boundary integral equations. The main advantage of such method is that only the domain boundary and interfaces are meshed. As a result, it is well suited to deal with unbounded domains that arise in seismology. The other advantage is that it does not need the introduction of absorbing conditions and does not suffer from numerical dispersion (in terms of cumulative errors). On the other hand, the method is

largely limited to piecewise homogeneous and linear media. The former limitation can sometimes be overcome using appropriate Green tensors (e.g. for the half-space, for layered media), which are however more complicated to implement and computationally more demanding than the usual free-space Green tensor. The main computational limitation of the BEM in its standard form is that the influence matrix is fully-populated. The numerical solution is thus expensive in terms of CPU time and memory requirements. As a result, standard BEM is limited in terms of frequency-range, geometrical complexity and heterogeneities, especially for 3-D configurations.

Comprehensive presentations of integral equation methods can be found in the books by Bonnet [31], Dominguez [67] and Manolis and Beskos [144]. A general review of the use of elastodynamic BEM is found in the articles by Beskos [24, 25]. In seismology, the BEM is used to study the effect of irregular topography on earthquake ground motion, in 2-D (e.g. in Mogi and Kawakami [154], Reinoso et al. [170], Sánchez-Sesma and Campillo [184]). Some works deal with 3-D problems, for example Reinoso et al. [169] and Niu and Dravinski [161] for homogeneous anisotropic canyons. In many publications, BEM are also applied to the seismic response of sedimentary basins and alluvial valleys, see e.g. Reinoso et al. [170] or Semblat et al. [191] for 2-D cases and Dangla et al. [56], Mossessian and Dravinski [156] or Reinoso et al. [169] for 3-D cases. A comprehensive review by Bouchon and Sánchez-Sesma on the use of BEM for seismic problems is found in [37].

Wave propagation in unbounded media: methodology survey. In seismology, the domain is generally treated as unbounded. On one hand, the volume methods (FE,SE, ...) need to truncate the domain. Absorbing boundaries are usually prescribed in order to reduce reflections of outgoing waves at the boundaries of the discrete model. The first type of absorbing conditions, efficient at almost normal incident, is based on first-order expansions (paraxial approximation proposed by Clayton and Engquist [48]). The method has been then improved by Higdon [113] to deal with surface waves and higher orders, but is more complex to implement. Since surface waves are essential and frequently encountered in various applications, Bérenger [22, 23] first introduced Perfectly Matched Layers (PMLs) for electromagnetism. The major idea is to define a selective attenuation of the fields propagating in one prescribed direction (thanks to the introduction of a system with stretched coordinates). PMLs were developed for elastic wave propagation by Basu and Chopra [15, 16], Festa and Vilotte [77] and Komatitsch and Tromp [123]. The velocity-stress formulation of PMLs for elastic wave equations has been introduced by Collino and Tsogka [52]. PMLs are used in FD methods (e.g. Festa et al. [76], Marcinkovich and Olsen [146]), in FE or SE methods (e.g. Komatitsch and Tromp [123]) and are very efficient for both body and surface waves (except shallow depth and low-frequency) but the efficiency decreases for grazing incidences (the horizontal/normal wavenumber being very small). Festa and Vilotte [77] and Komatitsch and Martin [122] have reduced this problem by introducing a numerical filtering. Festa et al. [75] have developed new absorbing conditions for 2-D problems to reduce the interference between low-frequency Rayleigh waves and the absorbing layer. Bécache et al. [20] have shown that exponentially growing solutions could appear in some models for anisotropic media. Recently, Meza-Fajardo and Papageorgiou [151] have proposed multi-dimensional PMLs for grazing incidences and anisotropic media (2-D problems). On the other hand, surface methods do not need such treatment since they are naturally formulated for unbounded domains.

Ongoing comparative study. All these numerical methods are currently the subject of a comparative study in the framework of a French research project named "Quantitative Seismic Hazard Assessment" (QSHA; http://qsha.unice.fr) and funded by the French National Agency for Research. The project aims at (a) obtaining a better description of crustal structures, (b) improving the source characterization and the determination of earthquake scenarios, (c) developping more precise modelling of seismic waves, (d) improving empirical and semi-empirical techniques based on observed data and (e) obtaining a quantitative estimation of ground motion based on previous information.

Each method is more or less well adapted to seismic problems depending on the scale, the basin shape, the soil behavior (linear/non-linear, ...), among other parameters. These methods should be considered as complementary rather that competitive. For example, in seismology, FE methods are used to model some non-linear or heterogeneous subregions (nearfield), whereas BE methods are used to model the complementary, linear and homogeneous domain (farfield). Examples of such FE-BE coupling have been done by Clouteau et al. [50], Fu [86], Liu et al. [132] or Mossessian and Dravinski [155]. There also exists works on the coupling of DE with SE (e.g. Gavoille et al. [93]).

Overall goals of this thesis. The BEM is an extremely useful tool to deal with unbounded media even though it is limited to simple linear properties. The subject of this thesis is to develop an alternative to the classical BEM formulation, namely a fast-BEM approach to improve the efficiency of standard BEM. This thesis is limited to BE methods for linear elastodynamic equations, in the frequency domain. It lays, however, the ground work for many useful extensions, such as a fast-BEM treatment of wave propagation in viscoelastic media or the coupling of fast BEM with FEM, that will be adressed in a subsequent thesis (Eva Grasso, 2008-2011).

1.4 ELASTIC WAVES: PRELIMINARIES

Before introducing the elastodynamic boundary integral equations in Section 1.5, some basic background on elastic waves is recalled in this section.

Elastodynamic equation. Let Ω denote the region of space occupied by an elastic solid with isotropic constitutive properties defined by mass density ρ, shear modulus μ, Poisson's ratio ν (or, equivalently, the Lamé parameter $\lambda = 2\mu\nu/(1-2\nu)$). The displacement is noted $\boldsymbol{u}$ and the Cauchy stress tensor is denoted $\boldsymbol{\sigma}$. The equations of elasticity consist of the conservation of momentum, the linear-elastic constitutive relation, and the compatibility equation. The differential form of the conservation of momentum, i.e. the Cauchy's first law of motion, is:

$$\boldsymbol{\nabla}.\boldsymbol{\sigma} + \rho\boldsymbol{F} = \rho\ddot{\boldsymbol{u}} \tag{1.1}$$

where $\boldsymbol{F}(\boldsymbol{x}, t)$ is a given body-force distribution and $\ddot{\boldsymbol{u}}$ denotes the second-order time derivative of $\boldsymbol{u}$. The deformation of the medium is described by the strain tensor $\boldsymbol{\varepsilon}$. The relation between strain and displacement, for linear elasticity under small strains, is:

$$\varepsilon_{ij} = \frac{1}{2}(u_{i,j} + u_{j,i}) \tag{1.2}$$

where u_i denotes the i-th component of the displacement and $u_{i,j}$ is the derivative of u_i with respect to x_j. The linear constitutive relation between the stress tensor $\boldsymbol{\sigma}$ and the strain tensor $\boldsymbol{\varepsilon}$ is

$$\sigma_{ij} = C_{ijk\ell}\varepsilon_{k\ell} \tag{1.3}$$

where, in the case of isotropic elasticity:

$$C_{ijk\ell} = \mu\Big[\frac{2\nu}{1-2\nu}\delta_{ij}\delta_{k\ell} + \delta_{ik}\delta_{j\ell} + \delta_{i\ell}\delta_{jk}\Big] \tag{1.4}$$

Substituting (1.2), (1.3), (1.4) into (1.1) yields the displacement-based Navier equation of motion:

$$\frac{\mu}{1-2\nu}\boldsymbol{\nabla}(\boldsymbol{\nabla}.\boldsymbol{u}) + \mu\boldsymbol{\nabla}^2\boldsymbol{u} + \rho\boldsymbol{F} = \rho\ddot{\boldsymbol{u}}$$

which, using the identity $\boldsymbol{\nabla}^2\boldsymbol{u} = \boldsymbol{\nabla}(\boldsymbol{\nabla}.\boldsymbol{u}) - \boldsymbol{\nabla}\wedge\boldsymbol{\nabla}\wedge\boldsymbol{u}$, where $\wedge$ denotes the vector cross-product, can be recast into the equivalent form:

$$\frac{2\mu(1-\nu)}{1-2\nu}\boldsymbol{\nabla}(\boldsymbol{\nabla}.\boldsymbol{u}) - \mu\boldsymbol{\nabla}\wedge\boldsymbol{\nabla}\wedge\boldsymbol{u} + \rho\boldsymbol{F} = \rho\ddot{\boldsymbol{u}}. \tag{1.5}$$

Well-posed wave problems. To ensure the well-posedness of a wave problem, conditions at the domain boundary have to be prescribed. Neumann boundary conditions consist in prescribing the traction $\boldsymbol{t} = \boldsymbol{\sigma}.\boldsymbol{n}$ (where $\boldsymbol{n}$ denotes the outward normal to the domain). For instance, traction-free surfaces ($\boldsymbol{t} = \boldsymbol{0}$; free-surface condition) are often considered. Dirichlet boundary conditions consist in prescribing given displacement values. When $\boldsymbol{t}$ is given over a part of $\partial\Omega$ and $\boldsymbol{u}$ over a complementary part, the boundary conditions are said to be mixed.

Initial conditions at $t = 0$ are also required:

$$\boldsymbol{u}(\boldsymbol{x},0) = \boldsymbol{u}_0(\boldsymbol{x}), \qquad \dot{\boldsymbol{u}}(\boldsymbol{x},0) = \boldsymbol{v}_0(\boldsymbol{x})$$

with inital rest ($\boldsymbol{u}_0 = \boldsymbol{v}_0 = 0$) frequently assumed in practice. Finally, when dealing with an unbounded domain Ω, conditions at infinity have to be prescribed. In the context of elastodynamic boundary integral equations, decay and radiation conditions, which ensure that the energy flux at infinity is outgoing, are customarily used (Eringen and Suhubi [72]).

Body waves. In (1.5), we see that elastic waves have both dilatational $\boldsymbol{\nabla}.\boldsymbol{u}$ and rotational $\boldsymbol{\nabla}\wedge\boldsymbol{u}$ motions. The displacement $\boldsymbol{u}$ can be expressed as the sum of a scalar ϕ and a vector potential $\boldsymbol{\psi}$:

$$\boldsymbol{u} = \boldsymbol{\nabla}\phi + \boldsymbol{\nabla}\wedge\boldsymbol{\psi}, \qquad \text{with } \boldsymbol{\nabla}.\boldsymbol{\psi} = 0 \tag{1.6}$$

This is a convenient approach since the two potentials satisfy uncoupled wave equations. Substituting (1.6) into (1.5) (assuming no body forces for simplicity), it follows:

$$\boldsymbol{\nabla}^2\phi = \frac{2(1-\nu)}{1-2\nu}\frac{\mu}{\rho}\ddot{\phi}, \qquad \boldsymbol{\nabla}^2\boldsymbol{\psi} = \frac{\mu}{\rho}\ddot{\boldsymbol{\psi}}$$

As a result, two types of body waves may propagate in elastic solids: pressure, or primary (P), waves, and shear, or secondary (S), waves (Fig. 1.6). In seismic wave propagation, two shear waves are distinguished: horizontally-polarized (SH) and vertically-polarized (SV) shear waves. The velocities of P– and S–waves are given in terms of the materials parameters by:

$$c_{\mathrm{P}} = \sqrt{\frac{2(1-\nu)}{1-2\nu}}\sqrt{\frac{\mu}{\rho}}, \qquad c_{\mathrm{S}} = \sqrt{\frac{\mu}{\rho}}, \qquad \gamma = \frac{c_{\mathrm{S}}}{c_{\mathrm{P}}} = \sqrt{\frac{1-2\nu}{2(1-\nu)}} \tag{1.7}$$

and P–waves propagate thus faster than S–waves.

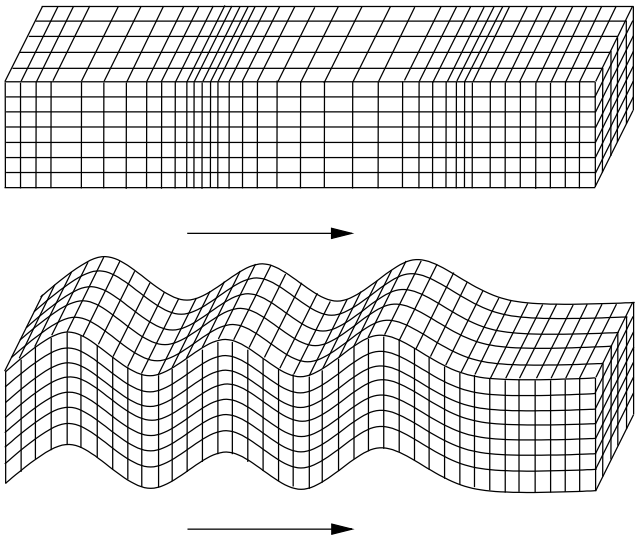

Figure 1.6: *Pressure (top) and shear (bottom) waves.*

Surface and interfacial waves. Unlike in the acoustic case, elastic waves may be generated and propagated along medium boundaries and interfaces. Surface waves consist of Rayleigh and Love waves. Surface waves travel more slowly than body waves. Because of their frequency lower than that of body waves, long duration and large amplitude, they can cause major damage. The Rayleigh waves are generated by the interaction of P– and S–waves at the free surface. The Love waves only occur in non-homogeneous media.

Frequency-domain elastodynamic equation. This work is based on solving frequency-domain elastodynamic wave propagation problems. Using the Fourier transform, a transient signal is decomposed into the continuous superposition of time-harmonic, or frequency, components. The Fourier transform is defined by:

$$\tilde{\boldsymbol{u}}(\boldsymbol{x},\omega) = \int_{-\infty}^{+\infty} \boldsymbol{u}(\boldsymbol{x},t) e^{-i\omega t} dt = \mathcal{F}\Big(\boldsymbol{u}(\boldsymbol{x},t)\Big) \tag{1.8}$$

For time-domain problems, the use of an inverse Fourier transform enables to solve, in the Fourier domain, a transient dynamic problem since:

$$\boldsymbol{u}(\boldsymbol{x},t) = \frac{1}{2\pi} \int_{-\infty}^{+\infty} \tilde{\boldsymbol{u}}(\boldsymbol{x},\omega) e^{i\omega t} d\omega = \mathcal{F}^{-1}\Big(\tilde{\boldsymbol{u}}(\boldsymbol{x},\omega)\Big) \tag{1.9}$$

In frequency-domain elastodynamics, the body forces and boundary conditions are harmonic in time with a given circular frequency ω, so that the solution is sought in the form:

$$\boldsymbol{u}(\boldsymbol{x},t) = \mathcal{R}e\{\bar{\boldsymbol{u}}(\boldsymbol{x}) e^{-i\omega t}\}$$

where $\bar{\boldsymbol{u}}$ is a complex-valued function. The implicit factor $e^{-i\omega t}$ will be systematically omitted in the following, and the notation $\boldsymbol{u}$ used instead of $\bar{\boldsymbol{u}}$. Finally, the Cauchy's first law of motion (1.1) becomes, for time-harmonic problems:

$$\boldsymbol{\nabla}.(\boldsymbol{\sigma}) + \rho\omega^2 \boldsymbol{u} + \rho \boldsymbol{F} = 0 \quad \text{in } \Omega. \tag{1.10}$$

We recall some other useful quantities in elastodynamics ($\alpha = P, S$):

$$k_\alpha = \frac{\omega}{c_\alpha} \text{ (wavenumber); } \lambda_\alpha = \frac{2\pi}{k_\alpha} \text{ (wavelength); } f = \frac{\omega}{2\pi} \text{ (frequency).} \tag{1.11}$$

The reader may find more details on wave propagation in the books by Achenbach [2], Graff [97], Harris [111] and Semblat and Pecker [193].

Another approach, not considered in this thesis and mentioned here for completeness, consists in using a Laplace transform instead of a Fourier transform. The BEM is solved in the Laplace domain [3]. The Laplace transform is defined by:

$$\hat{f}(s) = \mathcal{L}(\hat{f}(t)) = \int_0^\infty f(t)e^{-st}dt$$

and the fundamental solutions (see Section 1.5) in the Laplace domain are obtained from the fundamental solutions in the Fourier domain, using $\omega = -is$. The difficulty is the subsequent numerical inverse transform to obtain the response in time domain. Other numerical methods to avoid the difficult inverse Laplace transform have been developed. For example, Schanz and Antes [189] use the convolution quadrature method proposed by Lubich [136] to numerically evaluate the convolution integrals of time-domain elastodynamic fundamental solutions, the quadrature weights being based on the Laplace transformed fundamental solutions.

Viscoelasticity. The ideal model of a linear elastic soil is not well adapted to many seismic problems. To take into account wave attenuation into soils, viscoelastic constitutive models may be used. The constitutive relation for linear viscoelastic media has the general form (see e.g. the book by Christensen for details on the general theory of viscoelastic materials [46]):

$$\sigma_{ij}(\boldsymbol{x}, t) = \int_{-\infty}^{t} C_{ijk\ell}(t-\tau)\frac{d\varepsilon_{k\ell}(\boldsymbol{x}, t)}{d\tau}d\tau$$

where $C_{ijk\ell}$ is the relaxation tensor. It can be shown (see e..g the book by Dominguez [67]), that in the frequency domain, this equation is equivalent to the constitutive relation for linear elasticity (1.3) with the only difference that λ and ν are complex-valued constant or frequency-dependent-parameters. The complex-valued Lamé constants are thus frequently written as:

$$\mu = \mathcal{R}\text{e}(\mu)(1 + 2i\beta_\mu); \quad \lambda = \mathcal{R}\text{e}(\lambda)(1 + 2i\beta_\lambda). \tag{1.12}$$

In Schanz [188] and Schanz and Antes [189], the convolution quadrature method is proposed to solve viscoelastic problems. Various rheological models having different frequency dependent complex moduli may be considered (Aki and Richards [5], Semblat and Pecker [193]).

1.5 BOUNDARY INTEGRAL EQUATIONS AND REPRESENTATIONS

Starting from the elastodynamic equations, we recall in this section the boundary integral equations (BIE) and representations. Boundary integral equations were first introduced more than one century ago. The Somigliana identity [196] for elastostatics for example, was formulated in 1886. The integral formulation of the elastodynamic problem was first developed by Wheeler and Sternberg [209] for time-domain and by Cruse and Rizzo [55, 53] for frequency-domain. In the present

work, we only consider the frequency-domain formulation. Boundary integral equation formulations can be split into two broad categories, namely (i) direct formulations, which relate the values taken on the boundary by primary physical variables (displacement and traction), and (ii) indirect formulations (such as those used in the potential theory, e.g. Kupradze [127]), which employ secondary unknowns (real or fictitious source distributions). An example of the latter for seismic waves can be found in Sánchez-Sesma and Campillo [184]. In this work, only the direct formulation for frequency-domain elastodynamics is considered. The boundary integral equations and representations are now recalled.

Reciprocity theorem. The well-known boundary integral formulation for frequency-domain elastodynamics is now established. We first recall the well-known reciprocity theorem that relates a pair of solutions throughout an elastic body Ω. Given two distinct elastodynamic states $(\boldsymbol{u^{(1)}}, \boldsymbol{\sigma^{(1)}}, \boldsymbol{F^{(1)}})$ and $(\boldsymbol{u^{(2)}}, \boldsymbol{\sigma^{(2)}}, \boldsymbol{F^{(2)}})$ on Ω, they satisfy the time-harmonic equation of motion (1.10):

$$\sigma^{(1)}_{ji,j} + \rho\omega^2 u^{(1)}_i + \rho F^{(1)}_i = 0 \tag{1.13a}$$

$$\sigma^{(2)}_{ji,j} + \rho\omega^2 u^{(2)}_i + \rho F^{(2)}_i = 0 \tag{1.13b}$$

The combination (1.13b) $.\boldsymbol{u}^{(1)}-$ (1.13a) $.\boldsymbol{u}^{(2)}$ gives:

$$\rho(F^{(2)}_i u^{(1)}_i - F^{(1)}_i u^{(2)}_i) = -u^{(1)}_i \sigma^{(2)}_{ji,j} + u^{(2)}_i \sigma^{(1)}_{ji,j}$$

Noting that $\sigma^{(1)}_{ji} u^{(2)}_{i,j} = \sigma^{(2)}_{ji} u^{(1)}_{i,j}$ because of the symmetry properties of the elastic constitutive equation, it follows:

$$\rho(F^{(2)}_i u^{(1)}_i - F^{(1)}_i u^{(2)}_i) = (\sigma^{(1)}_{ji} u^{(2)}_i - \sigma^{(2)}_{ji} u^{(1)}_i)_{,j} \tag{1.14}$$

After integration of (1.14) over Ω, the reciprocity theorem thus reads:

$$\int_{\partial\Omega} [T^n(\boldsymbol{u}^{(1)}).\boldsymbol{u}^{(2)} - T^n(\boldsymbol{u}^{(2)}).\boldsymbol{u}^{(1)}] dS = \int_\Omega \rho \Big[\boldsymbol{F}^{(2)}.\boldsymbol{u}^{(1)} - \boldsymbol{F}^{(1)}.\boldsymbol{u}^{(2)}\Big] dV \tag{1.15}$$

where $\boldsymbol{u} \rightarrow T^n[\boldsymbol{u}] \equiv \boldsymbol{\sigma}[\boldsymbol{u}].\boldsymbol{n}$ is the traction vector associated with a given displacement field. When unbounded domains Ω are considered, (1.15) holds provided both states 1 and 2 satisfy decay and radiation conditions at infinity.

Fundamental solutions. The definition of an *elementary (or fundamental) solution* is now necessary. It is defined as the displacement solution of the elastodynamic equation (1.10) with a time-harmonic force of unit magnitude applied at a specified fixed point $\boldsymbol{x}$, for a given domain geometry and set of homogeneous boundary conditions. For some simple geometries, for example for the free (i.e. infinite) space or half-space, closed-form expressions are available (see e.g. Kupradze [127]). Noting $U^k_i(\boldsymbol{x}, \boldsymbol{y}; \omega)$ the displacement vector and $\Sigma^k_{ij}(\boldsymbol{x}, \boldsymbol{y}; \omega)$, the elastic stress tensor at a point $\boldsymbol{y}$, due to the application of a unit point force along the k direction at point $\boldsymbol{x}$. Such solution is also known as an elastodynamic Green's tensor.

We will see in the following that the fundamental solution most amenable to a Fast Multipole (FM) treatment is the free-space fundamental solution (known as the Helmholtz fundamental

solution), given by:

$$\begin{aligned} U_i^k(\boldsymbol{x},\boldsymbol{y};\omega) &= \frac{1}{4\pi\mu r}[A\delta_{ik} + Br_{,i}r_{,k}], \\ \Sigma_{ij}^k(\boldsymbol{x},\boldsymbol{y};\omega) &= \frac{1}{4\pi r^2}[2Cr_{,i}r_{,k}r_{,j} + (\delta_{ik}r_{,j} + \delta_{jk}r_{,i})D + \delta_{ij}r_{,k}E], \end{aligned} \tag{1.16}$$

where δ_{ij} stands for the Kronecker symbol, $r = |\boldsymbol{y} - \boldsymbol{x}|$ and A, B, C, D, E are defined by:

$$\begin{aligned} A &= \Big(1 + \frac{i}{x_{\mathrm{S}}} - \frac{1}{x_{\mathrm{S}}^2}\Big)e^{ix_{\mathrm{S}}} - \gamma^2\Big(\frac{i}{x_{\mathrm{P}}} - \frac{1}{x_{\mathrm{P}}^2}\Big)e^{ix_{\mathrm{P}}}, \\ B &= \Big(\frac{3}{x_{\mathrm{S}}^2} - \frac{3i}{x_{\mathrm{S}}} - 1\Big)e^{ix_{\mathrm{S}}} - \gamma^2\Big(\frac{3}{x_{\mathrm{P}}^2} - \frac{3i}{x_{\mathrm{P}}} - 1\Big)e^{ix_{\mathrm{P}}}, \\ C &= \Big(\frac{-15}{x_{\mathrm{S}}^2} + \frac{15i}{x_{\mathrm{S}}} + 6 - ix_{\mathrm{S}}\Big)e^{ix_{\mathrm{S}}} - \gamma^2\Big(\frac{-15}{x_{\mathrm{P}}^2} + \frac{15i}{x_{\mathrm{P}}} + 6 - ix_{\mathrm{P}}\Big)e^{ix_{\mathrm{P}}}, \\ D &= (ix_{\mathrm{S}} - 1)e^{ix_{\mathrm{S}}} + 2B, \qquad E = (1 - 2\gamma^2)(ix_{\mathrm{P}} - 1)e^{ix_{\mathrm{P}}} + 2B, \end{aligned}$$

with $x_{\mathrm{P}} = k_{\mathrm{P}}r$, $x_{\mathrm{S}} = k_{\mathrm{S}}r$ and $\gamma = c_{\mathrm{S}}/c_{\mathrm{P}}$ given by (1.7).

Anticipating that this thesis is concerned with the extension of the Fast Multipole Method (FMM) to elastodynamics, we note that expressions (1.16) of the fundamental solution are not convenient for this purpose. The following reformulation of (1.16), proposed by Yoshida [213], is better suited to a FMM treatment, as it is expressed in terms of the scalar kernels $G(r,k)$, for which multipole expansions are available:

$$\begin{aligned} U_i^k(\boldsymbol{x},\boldsymbol{y};\omega) &= \frac{1}{k_{\mathrm{S}}^2\mu}\Big((\delta_{qs}\delta_{ik} - \delta_{qk}\delta_{is})\frac{\partial}{\partial x_q}\frac{\partial}{\partial y_s}G(|\boldsymbol{y}-\boldsymbol{x}|;k_{\mathrm{S}}) + \frac{\partial}{\partial x_i}\frac{\partial}{\partial y_k}G(|\boldsymbol{y}-\boldsymbol{x}|;k_{\mathrm{P}})\Big), \\ T_i^k(\boldsymbol{x},\boldsymbol{y};\omega) &= C_{ijh\ell}\frac{\partial}{\partial y_\ell}U_h^k(\boldsymbol{x},\boldsymbol{y};\omega)n_j(\boldsymbol{y}), \end{aligned} \tag{1.17}$$

in which $G(|\boldsymbol{y}-\boldsymbol{x}|;k_\alpha)$ ($\alpha = S, P$), defined by

$$G(|\boldsymbol{y}-\boldsymbol{x}|;k_\alpha) = \frac{\exp(\mathrm{i}k_\alpha|\boldsymbol{y}-\boldsymbol{x}|)}{4\pi|\boldsymbol{y}-\boldsymbol{x}|}, \tag{1.18}$$

is the free-space Green's function for the Helmholtz equation with wavenumber k_α corresponding to either P or S elastic wave velocity, $\boldsymbol{n}(\boldsymbol{y})$ is a unit normal, and $C_{ijh\ell}$ are the components of the fourth-order elasticity tensor (1.4).

A review by Kausel of useful fundamental solutions in elastodynamics can be found in [119]. Fundamental solutions for more complicated geometries are adressed in e.g. articles by Guzina and Pak for the analytical formulation for a smoothly heterogeneous elastic half-space [107] and a multi-layered viscoelastic half-space [108]; see also Kennett [120] on horizontally-layered media.

Integral representation. Using the reciprocity identity (1.15) with states 1 and 2 respectively chosen as the unknown state in Ω and the fundamental solution, the boundary integral representation can be formulated (if $\boldsymbol{x} \notin \partial\Omega$):

$$\kappa u_k(\boldsymbol{x}) = \int_{\partial\Omega}[t_i(\boldsymbol{y})U_i^k(\boldsymbol{x},\boldsymbol{y};\omega) - u_i(\boldsymbol{y})T_i^k(\boldsymbol{x},\boldsymbol{y};\omega)]dS_y + \int_\Omega \rho F_i(\boldsymbol{y})U_i^k(\boldsymbol{x},\boldsymbol{y};\omega)dV_y, \tag{1.19}$$

where $\kappa = 1$ if $\boldsymbol{x} \in \Omega$ and $\kappa = 0$ if $\boldsymbol{x} \notin \Omega$ and U_i^k and T_i^k stand for any fundamental solution defined on Ω.

Boundary integral equation. When $\boldsymbol{x} \in \partial\Omega$, a singularity occurs in $\boldsymbol{y} = \boldsymbol{x}$. With the help of a well-documented limiting process (e.g. Guiggiani and Gigante [104]), the singular elastodynamic integral equation reads:

$$c_{ik}(\boldsymbol{x})u_i(\boldsymbol{x}) = \int_{\partial\Omega} t_i(\boldsymbol{y})U_i^k(\boldsymbol{x},\boldsymbol{y};\omega)dS_y - (\text{P.V.})\int_{\partial\Omega} u_i(\boldsymbol{y})T_i^k(\boldsymbol{x},\boldsymbol{y};\omega)dS_y \;\; (\boldsymbol{x} \in \partial\Omega) \quad (1.20)$$

where (P.V.) indicates a Cauchy principal value (CPV) singular integral and the *free-term* $c_{ik}(\boldsymbol{x})$ is equal to $1/2\delta_{ik}$ in the usual case where $\partial\Omega$ is smooth at $\boldsymbol{x}$. The integral operator in (1.20) may be recast into alternative, equivalent regularized forms which are free of CPV integrals (see for example Bui et al. [38], Krishnasamy et al. [126], Pak and Guzina [165], Dangla et al. [56] and Appendix A for implementation details). Equations (1.19) and (1.20) are applicable to either interior or exterior elastodynamic problems.

1.6 BOUNDARY ELEMENT METHOD: STANDARD FORM

Boundary element methods were first numerically implemented during the sixties with Shaw [195], Rizzo [171] and Cruse [54]. They exploit a transposition of field variable interpolation and geometry representation techniques initially created and developed for the finite element method (see e.g. Bathe [17], Hughes [114]).

1.6.1 Standard Boundary Element Method (BEM)

In the frequency domain, only a spatial discretization is needed. The discretization of the domain boundary and of the unknown fields leads to a linear system (Appendix A). The main advantage of the boundary element method is that only the domain boundary is meshed. As a result, this method is suitable to deal with unbounded media. To discretize the boundary integral equation, two main approaches are available. The first one is the collocation method, which consists of enforcing the boundary integral equation (1.20) at a finite number of collocation points $\boldsymbol{x}$ (see e.g. Bonnet [31]). The second one is the Galerkin method, a variational approach based on a weak form of (1.20), see e.g. Bielak and Maccamy [28], Bonnet et al. [34], Kallivokas et al. [118]. Its main advantage is that, in contrast with the collocation method, it may lead to a symmetric system of equations, albeit at the cost of evaluating *double* surface integrals. In fact, the collocation method is a particular case of the non-symmetric Galerkin BEM for which the test function is a Dirac distribution at $\boldsymbol{x}$.

In this work, the collocation method is applied. The numerical solution of boundary integral equation (1.20) is based on a boundary element (BE) discretization of the surface $\partial\Omega$ and boundary traces (u, t), leading to the system:

$$[H]\{u\} + [G]\{t\} = 0, \quad (1.21)$$

where $[H]$ and $[G]$ are fully populated, nonsymmetric, matrices and vectors $\{u\}$, $\{t\}$ gather the displacement and traction degrees of freedom (DOFs). Upon introduction of boundary conditions, the matrix equation (1.21) is recast in the form:

$$[K]\{v\} = \{f\},$$

where the N-vector $\{v\}$ collects the unknown degrees of freedom (DOFs), while the $N \times N$ matrix of influence coefficients $[K]$ contains the columns of $[H]$ and $[G]$ associated with the unknown

components. The influence matrix $[K]$ is fully-populated and non-symmetric. Storing $[K]$ is thus limited, on ordinary computers, to BEM models of size not exceeding $N = O(10^4)$. Direct solvers such as the LU factorization require $O(N^3)$ arithmetic operations (i.e. they have a $O(N^3)$ complexity), and are thus also limited to moderately-sized BEM models. BEM problems of larger size are preferably solved by means of iterative algorithms (GMRES, initially proposed by Saad and Schultz [180], being the usual choice), which build sequences of solution candidates until convergence within a predefined tolerance is reached. Each GMRES iteration requires one evaluation of $[K]\{v\}$ for a given vector $\{v\}$, a task requiring a computing time of order $O(N^2)$ if either $[K]$ is stored or $[K]\{v\}$ is evaluated by means of standard BEM numerical integration procedures. In the latter case, the $O(N^2)$ complexity stems from the fact that all element integrals must be recomputed for each collocation point. Applications of the BEM to large models (typically $N = O(10^6)$) require evaluation procedures for $[K]\{v\}$ that are fast (i.e. of complexity below $O(N^2)$) and that avoid explicit formation and storage of $[K]$. This has motivated the formulation and implementation of accelerated BEMs. Their appearance, allowing complexities lower than those of traditional BEMs, has dramatically improved the capabilities of BEMs for many areas of application, largely owing to the development of the Fast Multipole Method (FMM) over the last 10-15 years (see the review article by Nishimura [159]). Such approaches have resulted in considerable solution speed up, memory requirement reduction, and model size increase. The FMM is now known in many other fields as a very efficient, flexible and mature fast BEM approach. It is therefore chosen as the basis for the formulation and implementation of a fast elastodynamic BEM in 3-D proposed in this thesis.

1.6.2 Fast Multipole-accelerated BEM (FM-BEM)

Overview of fast BEMs. Fast BEMs, i.e. BEMs of complexity lower than that of traditional BEMs, appeared around 1985 in Rokhlin [173] with an iterative integral-equation approach for solving 2-D Laplace problems within $O(N)$ CPU time per iteration. The goal of fast BEMs is to speed up the matrix-vector product computation required for each iteration of the iterative solver applied to the BEM-discretized equations and to reduce memory requirements. They intrinsically rely upon an iterative solution approach for the linear system of discretized BEM equations, with solution times typically of order $O(N)$ per iteration for kernel of the type $O(1/r)$ and $O(N \log N)$ per iteration for frequency-domain wave propagation problems (instead of $O(N^2)$ per iteration with traditional forms of the BEM). There are two main fast-BEM approaches. The first approach is purely algebraic. Low rank approximations of the system matrix are defined to reduce the CPU time and memory requirements. The second one, the fast multipole method (FMM), exploits a reformulation of the fundamental solutions in terms of products of functions of $\boldsymbol{x}$ and of $\boldsymbol{y}$, so that (unlike in the traditional BEM) integrations with respect to $\boldsymbol{y}$ can be reused when the collocation point $\boldsymbol{x}$ is changed. The FMM concept was introduced by Greengard and Rokhlin in [99, 102], in the context of many-particle simulations. The FMM then naturally led to fast multipole boundary element methods (FM-BEMs), whose scope and capabilities have rapidly progressed in various areas. The FMM approach is used in the present work and will be presented in detail in Chapters 2 and 3. Here, we briefly review the other existing types of fast BEMs.

Kernel-independent fast BEMs are acceleration approaches which do not rely on known analytical expansions of fundamental solutions (also known as kernel functions). Ying et al. [211] have developed a new fast BEM for particle simulations, which does not require evaluation of mul-

tipole expansions. This method uses the same structure as the original adaptive FMM but, instead of using analytic expansions of the kernel to represent the potential generated by sources inside a cell, a continuous distribution of an equivalent density on a surface enclosing the cell is used. These representations are computed by solving local exterior or interior problems using integral equation formulations. The method is originally valid only for second-order non-oscillatory elliptic PDEs, but was extended by Engquist and Ying [70] to highly oscillatory kernels. Another type of kernel-independent fast BEM approach is the Adaptive Cross-Approximation technique (ACA). This method is purely algebraic and reduces time consuming and memory requirements to $O(N \log N)$ by splitting the system matrix into several block matrices of various sizes and then adaptively approximates these matrices by low rank submatrices (Bebendorf [18], Bebendorf and Rjasanow [19]). In the ACA method, the matrices are hierarchically partitioned into blocks using the $\mathcal{H}$-matrix concept proposed by Hackbusch [109]. The method was introduced by Kurz in [128] for electromagnetic and electromechanical problems. The extension to elastodynamics of this method is under progress (e.g. Messner and Schanz [150]). An ongoing investigation done by Darve and Fong [59] concerns the development of a black box FMM based on Chebyshev polynomial interpolation and singular value decomposition of kernels. But this method is, for the moment, only developed and efficient for kernels of the type $O(1/r)$ appropriate for static problems.

The wavelet-based method (e.g. Beylkin et al. [26], Tausch [204]) is another type of fast BEM approach which compresses the system matrix. The boundary integral equations are discretized using wavelet basis and so the system matrix is approximated by a sparse matrix containing only nearby wavelet interactions.

Still another fast BEM is the panel clustering developed by Hackbusch and Nowak [110]. This algorithm has a complexity of order $O(N \log^{\kappa} N)$ where $\kappa \in [4, 7]$. The main idea of such methods is to approximate by polynomials the kernel function of the integral operator using products of polynomial functions of $\boldsymbol{x}$ and $\boldsymbol{y}$. The approximation is done using the concept of DOFs clustering. Sauter [185] introduced the variable order method where the approximation is based on a block partioning of the surface and the idea is to approximate the small blocks using low-order approximation and larger blocks with increasing orders.

Various fields of application of the FMM. The method is now applied in various fields in science and engineering such as astrophysics (e.g. Warren and Salmon [208]) and molecular dynamics (e.g. Board et al. [29]). In fluid dynamics, we mention works by Fu and Rodin [87], Gómez and Power [94, 95], Mammoli and Ingber [142, 143]. The FMM is especially well developed for electromagnetic problems (e.g. Gumerov and Duraiswami [105], Lu and Chew [134, 135], Song and Chew [197], Sylvand [200]), for which unbounded domains are often considered. The method is also adopted for industrial applications like MEMS (Frangi and Di Gioia [80, 81]) involving media with simple properties (air, Stokes flows) but extremely complex geometries with moving parts. FMMs for computational mechanics have been proposed more recently. For example, in acoustics we can cite the works by Fischer and Gaul [78], Nemitz and Bonnet [158], Sakuma and Yasuda [182]. In 2-D elastostatics we can cite Peirce and Napier [167] and Greengard et al. [101]. In 3-D elastostatics, the first work is due to Hayami and Sauter [112]. In [88], Fu et al. have developed a formulation based on the observation that the Green's function for linear elasticity can be formulated as derivatives of $O(1/r)$ kernels. Nishimura et al. [160] and Yoshida et al. [214], for example, have worked on the application of the FMM in elastostatics for crack problems. Margonari and Bonnet have worked on BEM-FEM coupling in elastostatics [148]. Liu

et al. [133] have developed the method for three-dimensional analysis of fiber reinforced composites based on a rigid-inclusion model. Many of these investigations are summarized in a review article by Nishimura [159].

FMM in elastodynamics. For equations of Helmholtz type (e.g. linear acoustics, electromagnetism or elastodynamics in the frequency domain), two types of FMM are available. The first one is the low frequency FMM. As for static cases, the complexity of this algorithm is $O(N)$. But this complexity is due to the fact that the wavelength is much longer than the domain size. On the other hand, if the wavelength is shorter than the geometrical feature, the complexity of low frequency FMM increases to $O(N^2)$ and so this method is not anymore efficient. For this reason, computational efficiency of fast BEMs in the mid-frequency regime is enhanced by using the so-called diagonal form for the Helmholtz Green's function, proposed by Rokhlin [174, 175, 176] with a complexity of $O(N \log N)$. Empton and Dembart also proposed a similar technique [71]. The upper limit stems from the fact that the size N becomes intractable at high frequencies, but the diagonal form also breaks down at very low frequencies and must be replaced with other types of expansions (Cheng et al. [45], Darve and Havé [61], Jiang and Chew [117]). Greengard et al. [100, 103] have developed techniques based on the integral representation of a fundamental solution. Only a few references address the application of FMM to elastodynamics. Time-domain problems are addressed by Takahashi et al. [201, 202]. In 2-D frequency-domain elastodynamics, the first work is due to Chen et al. [44]. Then, the method for low frequencies was developed by Fujiwara [89] and Fukui and Inoue [91] (in Japanese). The first 3-D implementation was proposed by Fujiwara [90] using a multi-level and diagonal form. In this article, some low frequency seismic oriented examples are presented. Yoshida [213] proposed a low frequency FMM for crack problems in 3-D. Since 2001, to the author knowledge, no article on the improvement of the method in frequency-domain elastodynamics has been presented.

Recent developments of FMM. Recently, several techniques to enhance the efficiency of the FMM have been proposed by several authors. We have seen that the low frequency FMM is not efficient at high frequency and that the diagonal form is not accurate at low frequencies. But, the definition of high or low frequency is in fact relative to the cell level. Some works, dealing with the combination of these two techniques have been developed for Helmholtz equation (e.g. Jiang and Chew [117], Otani and Nishimura [164]). So far, the combination of low frequency and diagonal form FMM has not been applied to elastodynamics.

1.7 AIMS AND OUTLINE OF THIS THESIS

With a view toward future applications in seismology and dynamic soil-structure interaction, the principal aim of this work is to develop an efficient numerical solver to deal with large scale seismic wave propagation problems. Because the seismic problems are usually unbounded, the numerical method chosen is the BEM. We have seen that standard BEM is usually restricted to moderate numbers of DOFs, and is thus limited in terms of frequency range, heterogeneities and geometric complexity when dealing with 3-D problems. To overcome these major limitations, the FM-accelerated BEM is developed in this work to investigate seismic wave propagation in complex geological structures.

This thesis is organized as follows. Its main contents, following this introductory Chapter 1, are divided into two parts.

The first part deals with the formulation and implementation of an elastodynamic FMM aimed at the study of seismic wave propagation in homogeneous or piecewise homogeneous elastic media. In Chapter 2, the formulation and implementation of a multi-level FM-BEM for 3-D elastodynamics in the frequency domain is presented. As the free-space fundamental solution used in elastodynamic boundary integral formulations is expressed in terms of the full-space Green's function for the scalar Helmholtz equation and its derivatives, many of the existing developments towards fast integral solvers for equations of the Helmholtz type (including in particular the Maxwell equations) could be transposed into the proposed elastodynamic BEMs. A complete presentation of such elastodynamic FM-BEM formulation based on such transposition is the main purpose of this chapter. In particular, computational efficiency of fast elastodynamic BEMs in the mid-frequency regime is enhanced by using the so-called diagonal form for the Helmholtz Green's function. A first set of seismology oriented examples, dealing with diffraction of a plane wave by a canyon, are presented at the end of this chapter. Then, in Chapter 3, the formulation is extended to multi-domain situations, with emphasis on alluvial-basin configurations, by developing a FMM-based BE-BE coupling approach suitable for 3-D piecewise-homogeneous media. The coupling strategy is validated on problems with exact or previously-published solutions. Finally, Chapter 4, of a more preliminary nature, is concerned with improvements of the present FM-BEM: preconditioning strategy, reduction of the number of moments, and formulation of a multipole expansion for the half space fundamental solutions.

The second part deals with some seismological applications of the method. First, in Chapter 5, the FM-BEM is applied to various canonical problems, namely the diffraction of oblique incident P– and SV–waves by semi-ellipsoidal canyons and basins, used as benchmark problems. This set of results contributes to comparative studies under way, in the context of the project Quantitative Seismic Hazard Assessment (QSHA, 2006-2009) funded by the French National Research Agency. In Chapter 6, the capabilities of the present FM-BEM are finally applied to a more realistic seismological study, namely the diffraction of a vertically incident plane P–wave by an Alpine basin (Grenoble).

Finally, some directions for future work opened by this thesis are given in a concluding chapter: parallelization, other preconditioning strategies, viscoelasticity, coupling with other numerical methods, forward solver for inverse problems.

This dissertation ends with five appendices. In Appendix A, the standard BEM implementation details used in the present work are presented. In Appendix B, the analytical expressions of the free-field displacement vectors are given for the two types of incident plane waves used in this work (P and SV). Appendix C describes the capabilities of the code developed during this thesis and explains how to prepare data and use the code. The main properties of special functions used in this work are reviewed in Appendix D. Finally, Appendix E presents a published work with Professor H.D. Bui on boundary integral equations for viscoelasticity.

Part I

Extension of the FMM to multi-region 3-D elastodynamics

Chapter 2

Extension of the Fast Multipole Method to elastodynamic equations

Contents

2.1 INTRODUCTION

In the introductory Chapter 1, the standard BEM has been shown to be well suited to deal with unbounded-domain idealizations commonly used in e.g. acoustics, electromagnetics or seismology since only the domain boundaries and possible interfaces are discretized. However, it has also be shown that in traditional boundary element (BE) implementations, the dimensional advantage with respect to domain discretization methods is offset by the fully-populated nature of the BEM coefficient matrix, with set-up and solution times rapidly increasing with the problem size N. It is thus essential to develop alternative, faster strategies (as FMM) that allow to still exploit the known advantages of BEMs when large N prohibit the use of traditional implementations.

This chapter is concerned with the formulation and implementation of a multi-level FM-BEM for 3-D elastodynamics in the frequency-domain. As the free-space fundamental solution used in elastodynamic boundary integral formulations is expressed in terms of the full-space Green's function for the scalar Helmholtz equation and its derivatives, many of the existing developments towards fast integral solvers for equations of the Helmholtz type (including in particular the Maxwell equations) are transposable to elastodynamic BEMs. A complete presentation of an elastodynamic FM-BEM formulation based on such transposition is the main purpose of this chapter. In particular, computational efficiency of fast elastodynamic BEMs in the mid-frequency regime is enhanced by using the so-called diagonal form for the Helmholtz Green's function. Both the single-level and multi-level forms of the FM-BEM are considered, with emphasis on the latter. A substantial fraction of the chapter is then devoted to the discussion, backed with the results of numerical experiments, of crucial implementation details (many of which transposing methods previously proposed for electromagnetic FM-BEMs [58, 200] to the present 3-D elastodynamic context) and a complexity analysis for both the single-level and multi-level versions.

The chapter is organized as follows. Classical concepts pertaining to elastodynamic BEMs are recalled in Section 2.2. Then, Section 2.3 presents underlying motivations and fundamental concepts for the elastodynamic FMM. Next, several crucial computational and implementation issues are addressed in Section 2.4. Section 2.5 is devoted to the analysis and numerical verification of the algorithmic complexity of single-level and multi-level versions. Finally, the correctness and computational performances of the proposed FM-BEM are assessed in Section 2.6 on numerical examples involving up to $N = O(10^6)$ nodal unknowns.

2.2 BOUNDARY ELEMENT METHOD

Boundary integral representation. Let $\Omega \subset \mathbb{R}^3$ denote the region of space occupied by a three-dimensional elastic solid with isotropic constitutive properties defined by μ (shear modulus), ν (Poisson's ratio) and ρ (mass density). Time-harmonic motions, with circular frequency ω, induced by a prescribed traction distribution $\boldsymbol{t}^{\mathrm{D}}$ on the boundary $\partial\Omega$ and in the absence of body forces are considered for definiteness in this chapter. This type of boundary conditions corresponds to often-encountered situations where scattering of waves by cavities or free surfaces is considered. The accomodation of other boundary conditions needs only minor modifications to the treatment proposed therein (and is implemented). Moreover, transmission conditions between dissimilar perfectly-bonded media will be considered in Chapter 3. As presented in Chapter 1, the

displacement $\boldsymbol{u}$ is given at an interior point $\boldsymbol{x} \in \Omega$ by the representation formula:

$$u_k(\boldsymbol{x}) = -\int_{\partial\Omega} u_i(\boldsymbol{y}) T_i^k(\boldsymbol{x}, \boldsymbol{y}; \omega) dS_y + \int_{\partial\Omega} t_i^{\mathrm{D}}(\boldsymbol{y}) U_i^k(\boldsymbol{x}, \boldsymbol{y}; \omega) dS_y \qquad (\boldsymbol{x} \in \Omega), \tag{2.1}$$

where $U_i^k(\boldsymbol{x}, \boldsymbol{y}; \omega)$ and $T_i^k(\boldsymbol{x}, \boldsymbol{y}; \omega)$ denote the i-th components of the elastodynamic fundamental solution, given by:

$$U_i^k(\boldsymbol{x}, \boldsymbol{y}; \omega) = \frac{1}{k_{\mathrm{S}}^2 \mu}\Big((\delta_{qs}\delta_{ik} - \delta_{qk}\delta_{is}) \frac{\partial}{\partial x_q}\frac{\partial}{\partial y_s} G(|\boldsymbol{y} - \boldsymbol{x}|; k_{\mathrm{S}}) + \frac{\partial}{\partial x_i}\frac{\partial}{\partial y_k} G(|\boldsymbol{y} - \boldsymbol{x}|; k_{\mathrm{P}}) \Big), \tag{2.2a}$$

$$T_i^k(\boldsymbol{x}, \boldsymbol{y}; \omega) = C_{ijh\ell} \frac{\partial}{\partial y_\ell} U_h^k(\boldsymbol{x}, \boldsymbol{y}; \omega) n_j(\boldsymbol{y}), \tag{2.2b}$$

in which k_{S} and k_{P} are the respective wavenumbers of S and P elastic waves defined by equations (1.7) and (1.11). $G(\cdot; k)$ is the free-space Green's function for the Helmholtz equation with wavenumber k, given by

$$G(r; k) = \frac{\exp(\mathrm{i}kr)}{4\pi r}, \tag{2.3}$$

$\boldsymbol{n}(\boldsymbol{y})$ is the unit normal to $\partial\Omega$ directed outwards of Ω, and $C_{ijh\ell}$ are the components of the fourth-order elasticity tensor (1.4).

Boundary integral equation. As presented in Section 1.5, when $\boldsymbol{x} \in \partial\Omega$, a singularity occurs in $\boldsymbol{y} = \boldsymbol{x}$ and the integral representation (2.1) yields the integral equation:

$$(\mathcal{K}u)(\boldsymbol{x}) = f(\boldsymbol{x}) \qquad (\boldsymbol{x} \in \partial\Omega), \tag{2.4}$$

with the linear integral operator $\mathcal{K}$ and the right-hand side f defined by

$$(\mathcal{K}u)(\boldsymbol{x}) = c_{ik}(\boldsymbol{x}) u_i(\boldsymbol{x}) + (\text{P.V.}) \int_{\partial\Omega} u_i(\boldsymbol{y}) T_i^k(\boldsymbol{x}, \boldsymbol{y}; \omega) dS_y \tag{2.5}$$

$$f(\boldsymbol{x}) = \int_{\partial\Omega} t_i^{\mathrm{D}}(\boldsymbol{y}) U_i^k(\boldsymbol{x}, \boldsymbol{y}; \omega) dS_y, \tag{2.6}$$

Boundary Element Method. The numerical solution of boundary integral equation (2.4) is based on a discretization of the surface $\partial\Omega$ into N_E isoparametric boundary elements. Piecewise-linear interpolation of displacements, based on three-noded triangular boundary elements, is used in this chapter. The N_I displacement interpolation nodes thus defined also serve as collocation points. This discretization process transforms (2.4) into a square complex-valued matrix equation of size $N = 3N_I$ of the form

$$[K]\{u\} = \{f\}, \tag{2.7}$$

where the N-vector $\{u\}$ collects the sought degrees of freedom (DOFs), namely the nodal displacement components, while the $N \times N$ matrix of influence coefficients $[K]$ and the N-vector $\{f\}$ arise from (2.5) and (2.6), respectively. Setting up the matrix $[K]$ classically requires the computation of all element integrals for each collocation point, thus needing a computational time of order $O(N^2)$. More details on the numerical implementation of standard BEM are given in Appendix A.

Solution strategy for the BEM equations. As presented in Section 1.6.1, the influence matrix $[K]$ is fully-populated. Storing $[K]$ is thus limited, on ordinary computers, to BEM models of size not exceeding $N = O(10^4)$. BEM problems of larger size are preferably solved by means of iterative algorithms (as GMRES). With reference to (2.7), each GMRES iteration requires one evaluation of $[K]\{u\}$ for given $\{u\}$, a task requiring a computing time of order $O(N^2)$ if either $[K]$ is stored or $[K]\{u\}$ is evaluated by means of standard BEM numerical integration procedures. In the latter case, the $O(N^2)$ complexity stems from the fact that, again, all element integrals must be recomputed for each collocation point. Applications of the BEM to large models (typically $N = O(10^6)$) require evaluation procedures for $[K]\{u\}$ that are fast (i.e. of complexity below $O(N^2)$) and that avoid explicit formation and storage of $[K]$. The fast multipole method (FMM) is known in many other fields as a very efficient approach for achieving these objectives. It is therefore chosen as the basis for the present formulation and implementation of a fast elastodynamic BEM.

2.3 FAST MULTIPOLE METHOD: PRINCIPLE

2.3.1 Multipole expansions of the elastodynamic fundamental solutions

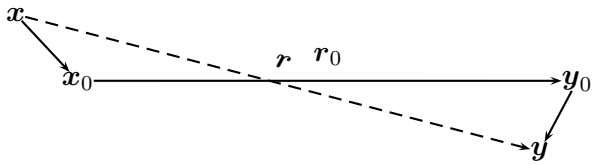

Figure 2.1: *Decomposition of the position vector: notation.*

The FMM is based on a reformulation of the fundamental solutions in terms of products of functions of $\boldsymbol{x}$ and of $\boldsymbol{y}$. This allows to re-use integrations with respect to $\boldsymbol{y}$ when the collocation point $\boldsymbol{x}$ is changed, thereby lowering the $O(N^2)$ complexity per iteration entailed by standard BEMs. The elastodynamic fundamental solutions (2.2a,b) are linear combinations of derivatives of the Green's function (2.3) for the Helmholtz equation. On recasting the position vector $\boldsymbol{r} = \boldsymbol{y} - \boldsymbol{x}$ in the form $\boldsymbol{r} = \boldsymbol{r}_0 + (\boldsymbol{y} - \boldsymbol{y}_0) - (\boldsymbol{x} - \boldsymbol{x}_0)$, where $\boldsymbol{x}_0$ and $\boldsymbol{y}_0$ are two poles and $\boldsymbol{r}_0 = \boldsymbol{y}_0 - \boldsymbol{x}_0$ (Fig. 2.1), the Helmholtz Green's function is shown [71, 57] to admit the decomposition

$$G(|\boldsymbol{r}|;k) = \lim_{L\to+\infty} \int_{\hat{\boldsymbol{s}}\in S} e^{\mathrm{i}k\hat{\boldsymbol{s}}.(\boldsymbol{y}-\boldsymbol{y}_0)} \mathcal{G}_L(\hat{\boldsymbol{s}};\boldsymbol{r}_0;k) e^{-\mathrm{i}k\hat{\boldsymbol{s}}.(\boldsymbol{x}-\boldsymbol{x}_0)}\, \mathrm{d}\hat{\boldsymbol{s}}, \tag{2.8}$$

where S is the unit sphere of $\mathbb{R}^3$, $\hat{s}$ a quadrature point and the *transfer function* $\mathcal{G}_L(\hat{\boldsymbol{s}};\boldsymbol{r}_0;k)$ is defined in terms of the Legendre polynomials P_p and the spherical Hankel functions of the first kind $h_p^{(1)}$ by:

$$\mathcal{G}_L(\hat{\boldsymbol{s}};\boldsymbol{r}_0;k) = \frac{\mathrm{i}k}{16\pi^2} \sum_{0\le p\le L} (2p+1)\mathrm{i}^p h_p^{(1)}(k|\boldsymbol{r}_0|) P_p\big(\cos(\hat{\boldsymbol{s}},\boldsymbol{r}_0)\big). \tag{2.9}$$

The decomposition (2.8)–(2.9) is seen to achieve the desired separation of variables $\boldsymbol{x}$ and $\boldsymbol{y}$. Then, to recast the elastodynamic fundamental solutions in a form similar to (2.8)-(2.9), one simply notes

that (2.8) implies:

$$\frac{\partial}{\partial x_i}\mathcal{F}(|\boldsymbol{r}|;k) = -\mathrm{i}k\hat{s}_i\mathcal{F}(|\boldsymbol{r}|;k), \qquad \frac{\partial}{\partial y_i}\mathcal{F}(|\boldsymbol{r}|;k) = \mathrm{i}k\hat{s}_i\mathcal{F}(|\boldsymbol{r}|;k), \tag{2.10}$$

where $\mathcal{F}(|\boldsymbol{r}|;k) = e^{\mathrm{i}k\hat{\boldsymbol{s}}.(\boldsymbol{y}-\boldsymbol{y}_0)}\mathcal{G}_L(\hat{\boldsymbol{s}};\boldsymbol{r}_0;k)e^{-\mathrm{i}k\hat{\boldsymbol{s}}.(\boldsymbol{x}-\boldsymbol{x}_0)}$ and $\hat{s}_i$ is the i-th component of the vector $\hat{\boldsymbol{s}}$. Then, on substituting (2.10) into (2.2a,b) and invoking decomposition (2.8)-(2.9), the following multipole decomposition of the elastodynamic fundamental solutions is obtained:

$$\begin{aligned} U_i^k(\boldsymbol{x},\boldsymbol{y};\omega) = &\lim_{L\to+\infty}\int_{\hat{\boldsymbol{s}}\in S} e^{\mathrm{i}k_\mathrm{P}\hat{\boldsymbol{s}}.(\boldsymbol{y}-\boldsymbol{y}_0)}\,\mathcal{U}_{i,L}^{k,\mathrm{P}}(\hat{\boldsymbol{s}};\boldsymbol{r}_0)\,e^{-\mathrm{i}k_\mathrm{P}\hat{\boldsymbol{s}}.(\boldsymbol{x}-\boldsymbol{x}_0)}\,\mathrm{d}\hat{\boldsymbol{s}} \\ &+\lim_{L\to+\infty}\int_{\hat{\boldsymbol{s}}\in S} e^{\mathrm{i}k_\mathrm{S}\hat{\boldsymbol{s}}.(\boldsymbol{y}-\boldsymbol{y}_0)}\,\mathcal{U}_{i,L}^{k,\mathrm{S}}(\hat{\boldsymbol{s}};\boldsymbol{r}_0)\,e^{-\mathrm{i}k_\mathrm{S}\hat{\boldsymbol{s}}.(\boldsymbol{x}-\boldsymbol{x}_0)}\,\mathrm{d}\hat{\boldsymbol{s}}, \end{aligned} \tag{2.11}$$

$$\begin{aligned} T_i^k(\boldsymbol{x},\boldsymbol{y};\omega) = &\lim_{L\to+\infty}\int_{\hat{\boldsymbol{s}}\in S} e^{\mathrm{i}k_\mathrm{P}\hat{\boldsymbol{s}}.(\boldsymbol{y}-\boldsymbol{y}_0)}\,\mathcal{T}_{i,L}^{k,\mathrm{P}}(\hat{\boldsymbol{s}};\boldsymbol{r}_0)\,e^{-\mathrm{i}k_\mathrm{P}\hat{\boldsymbol{s}}.(\boldsymbol{x}-\boldsymbol{x}_0)}\,\mathrm{d}\hat{\boldsymbol{s}} \\ &+\lim_{L\to+\infty}\int_{\hat{\boldsymbol{s}}\in S} e^{\mathrm{i}k_\mathrm{S}\hat{\boldsymbol{s}}.(\boldsymbol{y}-\boldsymbol{y}_0)}\,\mathcal{T}_{i,L}^{k,\mathrm{S}}(\hat{\boldsymbol{s}};\boldsymbol{r}_0)\,e^{-\mathrm{i}k_\mathrm{S}\hat{\boldsymbol{s}}.(\boldsymbol{x}-\boldsymbol{x}_0)}\,\mathrm{d}\hat{\boldsymbol{s}}, \end{aligned} \tag{2.12}$$

with the elastodynamic transfer functions given in terms of the acoustic transfer function $\mathcal{G}_L$ by

$$\mathcal{U}_{i,L}^{k,\mathrm{P}}(\hat{\boldsymbol{s}};\boldsymbol{r}_0) = \frac{\gamma^2}{\mu}\hat{s}_i\hat{s}_k\mathcal{G}_L(\hat{\boldsymbol{s}};\boldsymbol{r}_0;k_\mathrm{P}), \tag{2.13a}$$

$$\mathcal{T}_{i,L}^{k,\mathrm{P}}(\hat{\boldsymbol{s}};\boldsymbol{r}_0) = \frac{\mathrm{i}k_\mathrm{S}\gamma^3}{\mu}C_{ijh\ell}\hat{s}_\ell\hat{s}_h\hat{s}_k\mathcal{G}_L(\hat{\boldsymbol{s}};\boldsymbol{r}_0;k_\mathrm{P})n_j(\boldsymbol{y}), \tag{2.13b}$$

$$\mathcal{U}_{i,L}^{k,\mathrm{S}}(\hat{\boldsymbol{s}};\boldsymbol{r}_0) = \frac{1}{\mu}(\delta_{ik}-\hat{s}_k\hat{s}_i)\mathcal{G}_L(\hat{\boldsymbol{s}};\boldsymbol{r}_0;k_\mathrm{S}), \tag{2.14a}$$

$$\mathcal{T}_{i,L}^{k,\mathrm{S}}(\hat{\boldsymbol{s}};\boldsymbol{r}_0) = \frac{\mathrm{i}k_\mathrm{S}}{\mu}(\delta_{hk}-\hat{s}_k\hat{s}_h)C_{ijh\ell}\hat{s}_\ell\mathcal{G}_L(\hat{\boldsymbol{s}};\boldsymbol{r}_0;k_\mathrm{S})n_j(\boldsymbol{y}). \tag{2.14b}$$

Truncation error and clustering. In practice, the limiting process $L\to+\infty$ in (2.8) or (2.11), (2.12) cannot be performed exactly and is replaced with an evaluation for a suitably chosen finite value of L. A key error analysis result [57] states that there exist four constants C_1, C_2, C_3, C_4 such that

$$\begin{aligned} L = C_1 + C_2k|\boldsymbol{r}-\boldsymbol{r}_0| + C_3\ln(k|\boldsymbol{r}-\boldsymbol{r}_0|) + C_4\ln\epsilon^{-1} \\ \Longrightarrow \left|\frac{\exp(\mathrm{i}k|\boldsymbol{r}|)}{4\pi|\boldsymbol{r}|} - \int_{\hat{\boldsymbol{s}}\in S} e^{\mathrm{i}k\hat{\boldsymbol{s}}.(\boldsymbol{y}-\boldsymbol{y}_0)}\mathcal{G}_L(\hat{\boldsymbol{s}};\boldsymbol{r}_0;k)e^{-\mathrm{i}k\hat{\boldsymbol{s}}.(\boldsymbol{x}-\boldsymbol{x}_0)}\,\mathrm{d}\hat{\boldsymbol{s}}\right| < \epsilon \end{aligned} \tag{2.15}$$

for any chosen error level $\epsilon < 1$, whenever

$$|\boldsymbol{r}-\boldsymbol{r}_0|/|\boldsymbol{r}_0| = |(\boldsymbol{y}-\boldsymbol{y}_0)-(\boldsymbol{x}-\boldsymbol{x}_0)|/|\boldsymbol{r}_0| \le 2/\sqrt{5}. \tag{2.16}$$

The error bound (2.15), (2.16) implies that expansions (2.11), (2.12) must be used for well-separated sets of collocation and integration points clustered around poles $\boldsymbol{x}_0$ and $\boldsymbol{y}_0$. Moreover, (2.15) also indicates that the value of the truncation parameter L allowing to achieve a given level of accuracy ϵ increases with the size of these clusters. Other studies on error control in multipole expansions for Helmholtz equations can be found in e.g. [162, 105].

2.3.2 Single-level fast multipole formulation

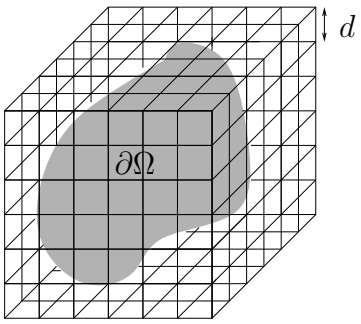

Figure 2.2: *3-D cubic grid embedding the boundary $\partial\Omega$.*

In the single-level FMM, a 3-D cubic grid of linear spacing d embedding the boundary $\partial\Omega$ is introduced (Fig. 2.2). The centers of the cubic cells thus defined are taken as poles $\boldsymbol{x}_0$ or $\boldsymbol{y}_0$ in decompositions (2.11), (2.12). Two cells are deemed *adjacent* if they have at least one common point, e.g. a vertex (Fig. 2.3). Whenever $\boldsymbol{x}$ and $\boldsymbol{y}$ belong to cells $\mathcal{C}_x$, $\mathcal{C}_y$ that are not adjacent, condition (2.16) is automatically fulfilled (as one then always has $|\boldsymbol{r}-\boldsymbol{r}_0|/|\boldsymbol{r}_0| \leq \sqrt{3}/2 < 2/\sqrt{5}$) and expansions (2.11), (2.12) can be safely used. Conversely, when $\boldsymbol{x}$ and $\boldsymbol{y}$ lie in adjacent cells, condition (2.16) is not assured and the classical expressions (2.2a,b) of the fundamental solutions are used instead.

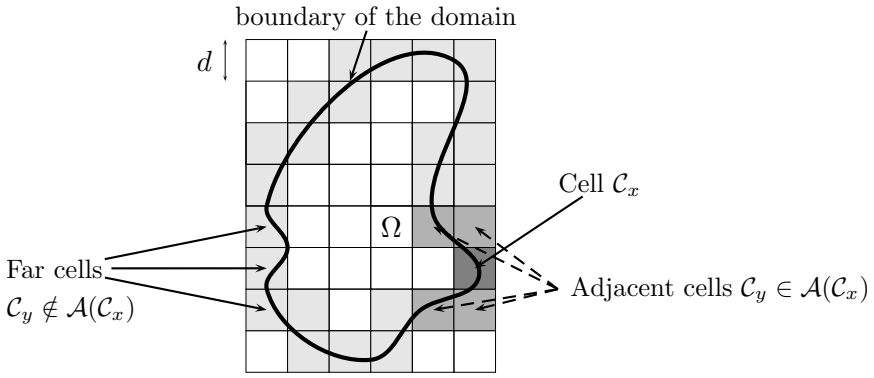

Figure 2.3: *Definition of the adjacent cells.*

These considerations lead to reformulate expressions (2.5) and (2.6), for any collocation point $\boldsymbol{x}$ lying in a given cell $\mathcal{C}_x$, as

$$\begin{aligned} (\mathcal{K}u)(\boldsymbol{x}) &= (\mathcal{K}u)^{\text{near}}(\boldsymbol{x}) + (\mathcal{K}u)^{\text{FM}}(\boldsymbol{x}), \\ f(\boldsymbol{x}) &= f^{\text{near}}(\boldsymbol{x}) + f^{\text{FM}}(\boldsymbol{x}) \end{aligned} \qquad (\boldsymbol{x} \in \partial\Omega \cap \mathcal{C}_x), \tag{2.17}$$

where, letting $\mathcal{A}(\mathcal{C})$ denote the set of cells which are adjacent to a given cubic cell $\mathcal{C}$ (Fig. 2.3), the "near" parts are defined for each collocation point $\boldsymbol{x}$ as the net contributions from the portion of

boundary situated in cells adjacent to that containing $\boldsymbol{x}$, i.e. by

$$(\mathcal{K}u)^{\text{near}}(\boldsymbol{x}) = c_{ik}(\boldsymbol{x})u_i(\boldsymbol{x}) + \sum_{\mathcal{C}_y \in \mathcal{A}(\mathcal{C}_x)} (\text{P.V.}) \int_{\partial\Omega\cap\mathcal{C}_y} u_i(\boldsymbol{y}) T_i^k(\boldsymbol{x},\boldsymbol{y};\omega) dS_y, \tag{2.18a}$$

$$f^{\text{near}}(\boldsymbol{x}) = \sum_{\mathcal{C}_y \in \mathcal{A}(\mathcal{C}_x)} \int_{\partial\Omega\cap\mathcal{C}_y} t_i^{\text{D}}(\boldsymbol{y}) U_i^k(\boldsymbol{x},\boldsymbol{y};\omega) dS_y. \tag{2.18b}$$

The "FM" parts then collect all contributions from cells that are not adjacent to $\mathcal{C}_x$:

$$(\mathcal{K}u)^{\text{FM}}(\boldsymbol{x}) = \sum_{\mathcal{C}_y \notin \mathcal{A}(\mathcal{C}_x)} \int_{\partial\Omega\cap\mathcal{C}_y} u_i(\boldsymbol{y}) T_i^k(\boldsymbol{x},\boldsymbol{y};\omega) dS_y, \tag{2.19a}$$

$$f^{\text{FM}}(\boldsymbol{x}) = \sum_{\mathcal{C}_y \notin \mathcal{A}(\mathcal{C}_x)} \int_{\partial\Omega\cap\mathcal{C}_y} t_i^{\text{D}}(\boldsymbol{y}) U_i^k(\boldsymbol{x},\boldsymbol{y};\omega) dS_y. \tag{2.19b}$$

The "near" contributions (2.18a,b) are evaluated by means of standard BE techniques. The treatment of the "FM" contributions (2.19a,b) exploits expansions (2.11), (2.12) truncated at a finite L and in a manner suggested by their multiplicative form, i.e. (i) evaluate integrals over each cell $\mathcal{C}_y$ and associate obtained values to the cell center $\boldsymbol{y}_0$, (ii) apply transfer functions to obtain quantities associated to the center $\boldsymbol{x}_0$ of cell $\mathcal{C}_x$, and (iii) evaluate contribution at each collocation point $\boldsymbol{x} \in \mathcal{C}_x$. Accordingly, *multipole moments*, defined by

$$\mathcal{R}_k^{\text{S},u}(\hat{\boldsymbol{s}};\mathcal{C}_y) = -\text{i}k_{\text{S}}\big[\delta_{ik}\hat{s}_j + \delta_{jk}\hat{s}_i - 2\hat{s}_i\hat{s}_j\hat{s}_k\big] \int_{\partial\Omega\cap\mathcal{C}_y} u_i(\boldsymbol{y}) n_j(\boldsymbol{y}) e^{\text{i}k_{\text{S}}\hat{\boldsymbol{s}}.(\boldsymbol{y}-\boldsymbol{y}_0)} dS_y \tag{2.20a}$$

$$\mathcal{R}^{\text{P},u}(\hat{\boldsymbol{s}};\mathcal{C}_y) = -\text{i}k_{\text{S}}\gamma^3\Big[\frac{2\nu}{1-2\nu}\delta_{ij} + 2\hat{s}_i\hat{s}_j\Big] \int_{\partial\Omega\cap\mathcal{C}_y} u_i(\boldsymbol{y}) n_j(\boldsymbol{y}) e^{\text{i}k_{\text{P}}\hat{\boldsymbol{s}}.(\boldsymbol{y}-\boldsymbol{y}_0)} dS_y \tag{2.20b}$$

$$\mathcal{R}_k^{\text{S},t}(\hat{\boldsymbol{s}};\mathcal{C}_y) = \frac{1}{\mu}\big[\delta_{ka} - \hat{s}_k\hat{s}_a\big] \int_{\partial\Omega\cap\mathcal{C}_y} t_a(\boldsymbol{y}) e^{\text{i}k_{\text{S}}\hat{\boldsymbol{s}}.(\boldsymbol{y}-\boldsymbol{y}_0)} dS_y \tag{2.21a}$$

$$\mathcal{R}^{\text{P},t}(\hat{\boldsymbol{s}};\mathcal{C}_y) = \frac{\gamma^2}{\mu} \int_{\partial\Omega\cap\mathcal{C}_y} \hat{s}_a t_a(\boldsymbol{y}) e^{\text{i}k_{\text{P}}\hat{\boldsymbol{s}}.(\boldsymbol{y}-\boldsymbol{y}_0)} dS_y \tag{2.21b}$$

are computed for each cell $\mathcal{C}_y$ (step (i)). The notations $\mathcal{R}_k^{\text{S},u}(\hat{\boldsymbol{s}};\mathcal{C}_y), \ldots$ are also meant to reflect the fact that step (iii) will feature an integration over the unit sphere. Then, *local expansions* for the cell $\mathcal{C}_x$ are evaluated by applying the transfer functions to the multipole moments according to

$$\mathcal{L}_k^{\text{S},u}(\hat{\boldsymbol{s}};\mathcal{C}_x) = \sum_{\mathcal{C}_y \notin \mathcal{A}(\mathcal{C}_x)} \mathcal{G}_L(\hat{\boldsymbol{s}};\boldsymbol{r}_0;k_{\text{S}}) \mathcal{R}_k^{\text{S},u}(\hat{\boldsymbol{s}};\mathcal{C}_y), \tag{2.22a}$$

$$\mathcal{L}^{\text{P},u}(\hat{\boldsymbol{s}};\mathcal{C}_x) = \sum_{\mathcal{C}_y \notin \mathcal{A}(\mathcal{C}_x)} \mathcal{G}_L(\hat{\boldsymbol{s}};\boldsymbol{r}_0;k_{\text{P}}) \mathcal{R}^{\text{P},u}(\hat{\boldsymbol{s}};\mathcal{C}_y) \tag{2.22b}$$

$$\mathcal{L}_k^{\text{S},t}(\hat{\boldsymbol{s}};\mathcal{C}_x) = \sum_{\mathcal{C}_y \notin \mathcal{A}(\mathcal{C}_x)} \mathcal{G}_L(\hat{\boldsymbol{s}};\boldsymbol{r}_0;k_{\text{S}}) \mathcal{R}_k^{\text{S},t}(\hat{\boldsymbol{s}};\mathcal{C}_y), \tag{2.23a}$$

$$\mathcal{L}^{\text{P},t}(\hat{\boldsymbol{s}};\mathcal{C}_x) = \sum_{\mathcal{C}_y \notin \mathcal{A}(\mathcal{C}_x)} \mathcal{G}_L(\hat{\boldsymbol{s}};\boldsymbol{r}_0;k_{\text{P}}) \mathcal{R}^{\text{P},t}(\hat{\boldsymbol{s}};\mathcal{C}_y), \tag{2.23b}$$

where $\boldsymbol{r}_0 = \boldsymbol{y}_0 - \boldsymbol{x}_0$ joins the centers of cells $\mathcal{C}_x$ and $\mathcal{C}_y$ (step (ii)). Upon multiplying (2.22a,b), (2.23a,b) by the local factors $\exp\left[\mathrm{i}k_\alpha \hat{\boldsymbol{s}}.(\boldsymbol{x}-\boldsymbol{x}_0)\right]$ (step (iii)) and replacing the integration over the unit sphere in (2.11), (2.12) by a numerical quadrature rule based on a set of Q quadrature points $\hat{\boldsymbol{s}}_q \in S$ and weights w_q (see Section 2.4.3), the "FM" contributions finally take the form

$$(\mathcal{K}u)_k^{\mathrm{FM}}(\boldsymbol{x}) \approx \sum_{q=1}^{Q} w_q \Big[e^{-\mathrm{i}k_{\mathrm{S}}\hat{\boldsymbol{s}}_q.(\boldsymbol{x}-\boldsymbol{x}_0)} \mathcal{L}_k^{\mathrm{S},u}(\hat{\boldsymbol{s}}_q;\mathcal{C}_x) + e^{-\mathrm{i}k_{\mathrm{P}}\hat{\boldsymbol{s}}_q.(\boldsymbol{x}-\boldsymbol{x}_0)} (\hat{\boldsymbol{s}}_q)_k \mathcal{L}^{\mathrm{P},u}(\hat{\boldsymbol{s}}_q;\mathcal{C}_x) \Big] \tag{2.24}$$

$$f_k^{\mathrm{FM}}(\boldsymbol{x}) \approx \sum_{q=1}^{Q} w_q \Big[e^{-\mathrm{i}k_{\mathrm{S}}\hat{\boldsymbol{s}}_q.(\boldsymbol{x}-\boldsymbol{x}_0)} \mathcal{L}_k^{\mathrm{S},t}(\hat{\boldsymbol{s}}_q;\mathcal{C}_x) + e^{-\mathrm{i}k_{\mathrm{P}}\hat{\boldsymbol{s}}_q.(\boldsymbol{x}-\boldsymbol{x}_0)} (\hat{\boldsymbol{s}}_q)_k \mathcal{L}^{\mathrm{P},t}(\hat{\boldsymbol{s}}_q;\mathcal{C}_x) \Big] \tag{2.25}$$

Expression (2.24) defines the "FM" contribution to the matrix-vector product $[K]\{u\}$, and hence is evaluated once per GMRES iteration, while (2.25) provides the "FM" contribution to the right-hand side $\{f\}$ and is computed once, prior to calling the GMRES solver. Figure 2.4 schematically depicts the acceleration mechanism achieved by the previously described steps.

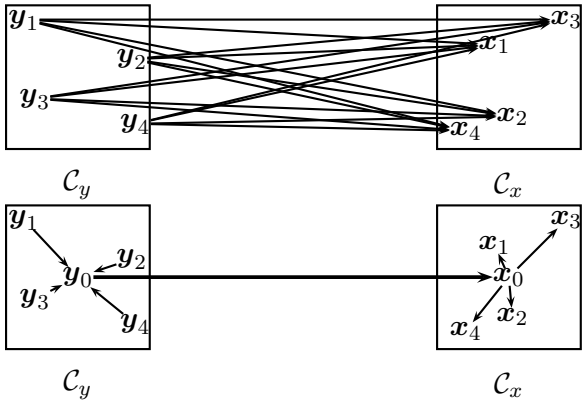

Figure 2.4: *Matrix-vector product without FMM (top) and with FMM (bottom).*

As remarked in Section 2.3.1, the truncation parameter L, and hence the maximum degree of Legendre polynomials featured in the transfer functions $\mathcal{G}_L(\hat{\boldsymbol{s}};\boldsymbol{r}_0;k_\alpha)$, increases with the cell size d. Consequently, the number Q of quadrature points necessary for achieving a given accuracy in (2.24), (2.25) is also an increasing function of L, i.e. of d (see Section 2.4.1 for further elaboration).

The single-level elastodynamic FMM is more efficient than the classical BEM, with a complexity of $O(N^{3/2})$ per GMRES iteration (as shown in Section 2.5.1). Further acceleration is achievable by adopting a multi-level approach, as described next for the present context of 3-D elastodynamics.

2.3.3 Multi-level fast multipole formulation

To have maximal efficiency, FM-BEM algorithms must confine non-FM calculations to the smallest possible portion of the boundary while clustering whenever possible the computation of influence terms into the largest possible non-adjacent groups. This is achieved by the multi-level FMM [58, 198, 133, 159, 200], which is based on using large cells and hierarchically subdividing each cell

into $2\times2\times2=8$ children cubic cells. This cell-subdivision approach is systematized by means of an oct-tree structure of cells. The level $\ell=0$, composed of only one cubic cell containing the whole surface $\partial\Omega$, is the tree root. The level-0 cell is divided into $2\times2\times2=8$ children cubic cells, which constitute the level $\ell=1$. All level-1 cells being adjacent, the FMM cannot be applied to them. The level $\ell=2$ is then defined by dividing each level-1 cell into 8 children cells, and so contains 64 cells. The subdivision process is further repeated until the finest level $\ell=\bar{\ell}$, implicitly defined by a preset subdivision-stopping criterion, is reached. Level-$\bar{\ell}$ cells are usually termed *leaf cells*. The FMM is applied from level $\ell=2$ to level $\ell=\bar{\ell}$, i.e. features $\bar{\ell}-1$ "active" levels.

The multi-level approach basically consists in first applying the FMM to all influence computations between disjoint level-2 cells (so as to use the largest clusters whenever possible), and then recursively tracing the tree downwards, applying the FMM to all interaction between disjoint level-ℓ cells that are children of adjacent level-$(\ell-1)$ cells (Fig. 2.5). Finally, interactions between adjacent leaf cells are treated using traditional (i.e. non FM-based) BE techniques. This approach thus minimizes the overall proportion of influence computations requiring the traditional treatment.

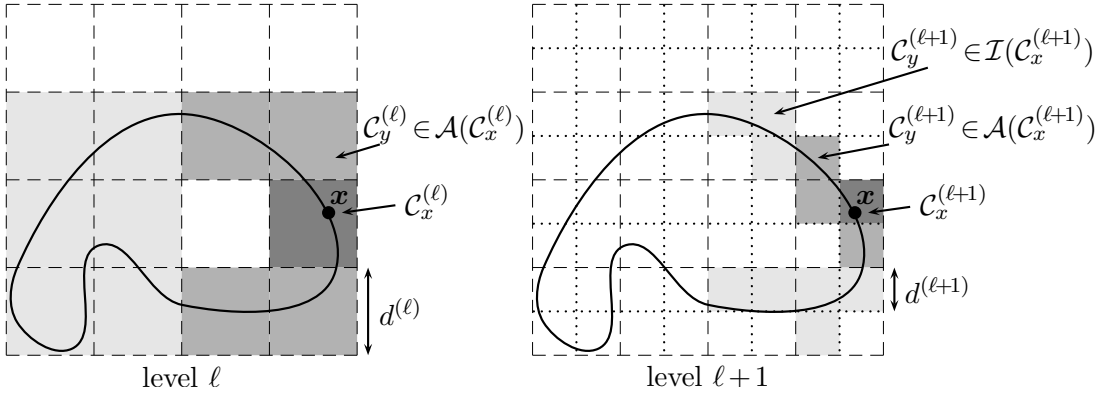

Figure 2.5: *Multi-level fast multipole algorithm. Only multipole moments from non-adjacent (light-grey) cells $\mathcal{C}_y^{(\ell)}\notin\mathcal{A}(\mathcal{C}_x^{(\ell)})$ may provide (through transfer) FM-computed contributions to $(\mathcal{K}u)^{FM}(\boldsymbol{x})$ at collocation points $\boldsymbol{x}$ lying in cell $\mathcal{C}_x^{(\ell)}$. Upon cell subdivision (right), new FM-computed contributions to collocation points in cell $\mathcal{C}_x^{(\ell+1)}$ originate from cells $\mathcal{C}_y^{(\ell+1)}$ in the* interaction list $\mathcal{I}(\mathcal{C}_x^{(\ell+1)})$ *of $\mathcal{C}_x^{(\ell+1)}$, while the adjacent region $\mathcal{A}(\mathcal{C}_x^{(\ell+1)})$ reduces in size.*

The computation of the discretized linear operator (2.5), i.e. of the matrix-vector product $[K]\{u\}$, by the multi-level elastodynamic FMM hence consists of the following main steps:

1. *Initialization*: compute multipole moments (2.20a,b) for all lowest-level cells $\mathcal{C}_y=\mathcal{C}_y^{\bar{\ell}}$.
2. *Upward pass*: recursively aggregate multipole moments by moving upward in the tree until level 2 is reached. Denoting by $\mathcal{S}(\mathcal{C})$ the set of children of a given cell $\mathcal{C}$, the transition from a level-$(\ell+1)$ cell to its parent level-ℓ cell is based on identities

$$\mathcal{R}_k^{\mathrm{S},u}(\hat{\boldsymbol{s}};\mathcal{C}_y^{(\ell)})=\sum_{\mathcal{C}_y^{(\ell+1)}\in\mathcal{S}(\mathcal{C}_y^{(\ell)})}\exp\big[-\mathrm{i}k_{\mathrm{S}}\hat{\boldsymbol{s}}.(\boldsymbol{y}_0^{(\ell+1)}-\boldsymbol{y}_0^{(\ell)})\big]\mathcal{R}_k^{\mathrm{S},u}(\hat{\boldsymbol{s}};\mathcal{C}_y^{(\ell+1)}) \tag{2.26a}$$

$$\mathcal{R}^{\mathrm{P},u}(\hat{\boldsymbol{s}};\mathcal{C}_y^{(\ell)})=\sum_{\mathcal{C}_y^{(\ell+1)}\in\mathcal{S}(\mathcal{C}_y^{(\ell)})}\exp\big[-\mathrm{i}k_{\mathrm{P}}\hat{\boldsymbol{s}}.(\boldsymbol{y}_0^{(\ell+1)}-\boldsymbol{y}_0^{(\ell)})\big]\mathcal{R}^{\mathrm{P},u}(\hat{\boldsymbol{s}};\mathcal{C}_y^{(\ell+1)}). \tag{2.26b}$$

It is essential at this point to emphasize a crucial feature of the elastodynamic multi-level FMM, namely that the number and location of the quadrature points on S are level-dependent ($\hat{\boldsymbol{s}}^{(\ell)}$ denoting a generic level-ℓ quadrature point, see Section 2.4.3 for details), a consequence of the previously-mentioned dependence of L, the truncation parameter in expansions (2.11), (2.12), on the cell size. Hence, application of identities (2.26a,b) requires an extrapolation procedure furnishing the values of $\mathcal{R}_k^{\mathrm{S},u}$, $\mathcal{R}^{\mathrm{P},u}$ at the level-ℓ quadrature points from those at the level-$(\ell+1)$ quadrature points (Section 2.4.4).

3. *Transfer*: initialize local expansions for each level-ℓ cell $\mathcal{C}_x^{(\ell)}$ and at each level $2 \leq \ell \leq \bar{\ell}$ using

$$\mathcal{L}_k^{\mathrm{S},u}(\hat{\boldsymbol{s}}^{(\ell)};\mathcal{C}_x^{(\ell)}) = \sum_{\mathcal{C}_y^{(\ell)} \in \mathcal{I}(\mathcal{C}_x^{(\ell)})} \mathcal{G}_L(\hat{\boldsymbol{s}}^{(\ell)};\boldsymbol{r}_0;k_{\mathrm{S}})\mathcal{R}_k^{\mathrm{S},u}(\hat{\boldsymbol{s}}^{(\ell)};\mathcal{C}_y^{(\ell)}) \tag{2.27a}$$

$$\mathcal{L}^{\mathrm{P},u}(\hat{\boldsymbol{s}}^{(\ell)};\mathcal{C}_x^{(\ell)}) = \sum_{\mathcal{C}_y^{(\ell)} \in \mathcal{I}(\mathcal{C}_x^{(\ell)})} \mathcal{G}_L(\hat{\boldsymbol{s}}^{(\ell)};\boldsymbol{r}_0;k_{\mathrm{P}})\mathcal{R}^{\mathrm{P},u}(\hat{\boldsymbol{s}}^{(\ell)};\mathcal{C}_y^{(\ell)}) \tag{2.27b}$$

where $\mathcal{I}(\mathcal{C})$, the *interaction list* of a given cell $\mathcal{C}$ (Fig. 2.5), is the set of *same-level* cells which are not adjacent to $\mathcal{C}$ while having a parent cell adjacent to that of $\mathcal{C}$. For a level-2 cell, (2.27a,b) coincides with (2.22a,b), as $\mathcal{I}(\mathcal{C}^2)$ collects all level-2 cells not adjacent to $\mathcal{C}^2$.

4. *Downward pass*: for all levels $3 \leq \ell \leq \bar{\ell}$, the local expansion for each level-ℓ cell $\mathcal{C}_x^{(\ell)}$ is updated with the contribution from the parent level-$(\ell-1)$ cell, by means of the identity

$$\mathcal{L}_k^{\mathrm{S},u}(\hat{\boldsymbol{s}};\mathcal{C}_x^{(\ell)}) = \mathcal{L}_k^{\mathrm{S},u}(\hat{\boldsymbol{s}};\mathcal{C}_x^{(\ell)}) + \exp\big[-\mathrm{i}k_{\mathrm{S}}(\hat{\boldsymbol{s}}.(\boldsymbol{x}_0^{(\ell-1)} - \boldsymbol{x}_0^{(\ell)}))\big]\mathcal{L}_k^{\mathrm{S},u}(\hat{\boldsymbol{s}};\mathcal{C}_x^{(\ell-1)}) \tag{2.28a}$$

$$\mathcal{L}^{\mathrm{P},u}(\hat{\boldsymbol{s}};\mathcal{C}_x^{(\ell)}) = \mathcal{L}^{\mathrm{P},u}(\hat{\boldsymbol{s}};\mathcal{C}_x^{(\ell)}) + \exp\big[-\mathrm{i}k_{\mathrm{P}}(\hat{\boldsymbol{s}}.(\boldsymbol{x}_0^{(\ell-1)} - \boldsymbol{x}_0^{(\ell)}))\big]\mathcal{L}^{\mathrm{P},u}(\hat{\boldsymbol{s}};\mathcal{C}_x^{(\ell-1)}) \tag{2.28b}$$

Similarly to step 2, application of identity (2.28a,b) requires an inverse extrapolation procedure furnishing the values of $\mathcal{L}_k^{\mathrm{S},u}$, $\mathcal{L}^{\mathrm{P},u}$ at the level-ℓ quadrature points from those at the level-$(\ell-1)$ quadrature points (Section 2.4.4).

5. When the leaf level $\ell = \bar{\ell}$ is reached, all local expansions have been computed. The contribution $(\mathcal{K}u)^{\mathrm{FM}}(\boldsymbol{x})$ is evaluated using (2.24) with the level-$\bar{\ell}$ quadrature points, and the near-field contribution is evaluated according to (2.18a,b) for all level-$\bar{\ell}$ (leaf) cells $\mathcal{C}_x$.

The computation of the right-hand side (2.6) follows the same steps, with the multipole moments $\mathcal{R}_k^{\mathrm{S},u}$, $\mathcal{R}^{\mathrm{P},u}$ and local expansions $\mathcal{L}_k^{\mathrm{S},u}$, $\mathcal{L}^{\mathrm{P},u}$ replaced with their counterparts $\mathcal{R}_k^{\mathrm{S},t}$, $\mathcal{R}^{\mathrm{P},t}$ and $\mathcal{L}_k^{\mathrm{S},t}$, $\mathcal{L}^{\mathrm{P},t}$. The above steps are shown in Section 2.5.2 to have a complexity of at most $O(N \log N)$, with the exception of the direct and inverse extrapolations in steps 2 and 4, whose complexity is $O(N^{3/2})$.

2.3.4 Computation of near-field contributions

The near-field contributions (2.18a,b) involve (i) CPV-singular, (ii) weakly-singular and (iii) non-singular element integrals. CPV-singular integrals are split according to

$$\begin{aligned}(\text{P.V.}) \int_{\partial\Omega} u_i(\boldsymbol{y}) T_i^k(\boldsymbol{x},\boldsymbol{y};\omega) dS_y \\ = \int_{\partial\Omega} u_i(\boldsymbol{y})\big[T_i^k(\boldsymbol{x},\boldsymbol{y};\omega) - T_i^k(\boldsymbol{x},\boldsymbol{y})\big] dS_y + (\text{P.V.}) \int_{\partial\Omega} u_i(\boldsymbol{y}) T_i^k(\boldsymbol{x},\boldsymbol{y}) dS_y\end{aligned}$$

where $T_i^k(\boldsymbol{x},\boldsymbol{y})$ are the traction components of the (singular) static fundamental solution and the difference $T_i^k(\boldsymbol{x},\boldsymbol{y};\omega) - T_i^k(\boldsymbol{x},\boldsymbol{y})$ is non-singular [31]. The remaining CPV integral is then evaluated analytically, taking advantage of the fact that three-noded triangular elements, which have constant unit normal and Jacobian, are used. Weakly-singular integrals (which feature the kernel $U_i^k(\boldsymbol{x},\boldsymbol{y};\omega)$) and non-singular integrals are computed using numerical Gaussian quadrature (the weak singularity being first cancelled by means of a suitable change of coordinates). Finally, when $\partial\Omega$ presents an edge or corner at $\boldsymbol{x}$, the free-term $c_{ij}(\boldsymbol{x})$ is evaluated using the method of [145]. Details on the numerical evaluation of integrals are given in Appendix A.

2.4 FAST MULTIPOLE METHOD: COMPUTATIONAL ASPECTS

Both the single-level and multi-level elastodynamic FMM have been implemented, for three-noded triangular boundary elements, using a public domain version of the GMRES solver [221] with a convergence criterion set to $\|\{\mathcal{K}u - f\}\| \,/\, \|\{f\}\| \leq 10^{-3}$. All examples, presented in this chapter, have been run on the same single-processor PC (RAM: 3GB, CPU frequency: 3.40 GHz). Except where indicated otherwise, the multi-level FMM is used.

The numerical efficiency and accuracy of the FMM is strongly affected by several factors, such as the truncation of the transfer function, the quadrature over the unit sphere and the number of levels, and great care must be taken in the implementation. This section is devoted to a discussion of these issues, and of various algorithmic choices and improvements. The latter are largely based on a transposition to the present elastodynamic context of ideas and methods proposed in [58, 200] for the FMM applied to the 3-D frequency-domain Maxwell equations. At several places, illustrative numerical results for the test problem of a spherical cavity of radius a embedded in an elastic isotropic infinite medium (with $\nu = 0.25$), subjected to an internal time-harmonic uniform pressure P (Fig. 2.6) are given. This problem has a simple, spherically-symmetric, exact solution [72], with the radial displacement and stress given in terms of the normalized radial coordinate $\hat{r} = r/a$ by:

$$\begin{aligned} u_r(\hat{r}) &= \frac{aP}{\mu}\,\frac{1}{\hat{r}^2}\,\frac{\gamma^2(1-\mathrm{i}k_{\mathrm{P}}a\hat{r})}{4\gamma^2(1-\mathrm{i}k_{\mathrm{P}}a)-(k_{\mathrm{P}}a)^2}\,\exp(\mathrm{i}k_{\mathrm{P}}a(\hat{r}-1)) \\ \sigma_{rr}(\hat{r}) &= P\,\frac{1}{\hat{r}^3}\,\frac{(k_{\mathrm{P}}a)^2\hat{r}^2-4\gamma^2(1-\mathrm{i}k_{\mathrm{P}}a\hat{r})}{4\gamma^2(1-\mathrm{i}k_{\mathrm{P}}a)-(k_{\mathrm{P}}a)^2}\,\exp(\mathrm{i}k_{\mathrm{P}}a(\hat{r}-1)) \end{aligned} \tag{2.29}$$

with the wave velocity ratio γ and the wavenumber k_{P} defined in (1.7,1.11).

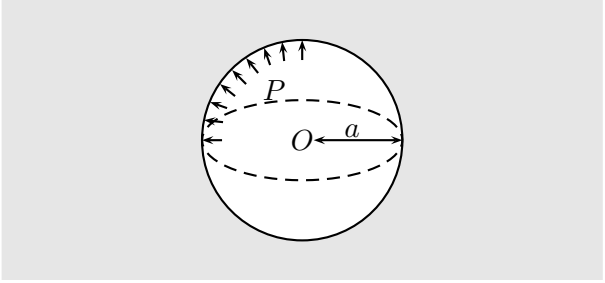

Figure 2.6: *Pressurized spherical cavity: notation.*

2.4.1 Truncation of the transfer function

As already mentioned in Section 2.3.1, the decomposition (2.8) is shown in [57] to be convergent in the limit $L \to +\infty$, which immediately implies convergence for the corresponding expressions (2.11), (2.12) of the elastodynamic kernels. However, the spherical Hankel functions $h_p^{(1)}(z)$ behave like $(p/z)^p$ for large p [1] and their evaluation must therefore be avoided for orders p significantly larger than $k|\boldsymbol{r}_0|$. Hence, the truncation level L used in (2.9) has to be large enough to guarantee sufficient accuracy in (2.8) while avoiding divergence of the Hankel functions appearing in (2.9). Appropriate values for L achieving the "numerical convergence" of the transfer function $\mathcal{G}_L(\tilde{\boldsymbol{s}}; \boldsymbol{r}_0; k)$ are selected using formulae empirically established from numerical experiments. One such formula, known from previous studies on FMMs for Maxwell equations [58], reads:

$$L(d) = \sqrt{3}kd + C_\epsilon \log_{10}(\sqrt{3}kd + \pi). \tag{2.30}$$

In this work, distinct truncation levels L_P and L_S are defined according to (2.30) with $k = k_\mathrm{P}$ and $k = k_\mathrm{S}$, respectively. The transfer functions (2.13a,b) and (2.14a,b) are then evaluated using $L = L_\mathrm{S}$ and $L = L_\mathrm{P}$, respectively. The truncation parameter value defined by (2.30) is level-dependent through the cell size d, and L is (roughly) doubled for each upwards transition to a new level.

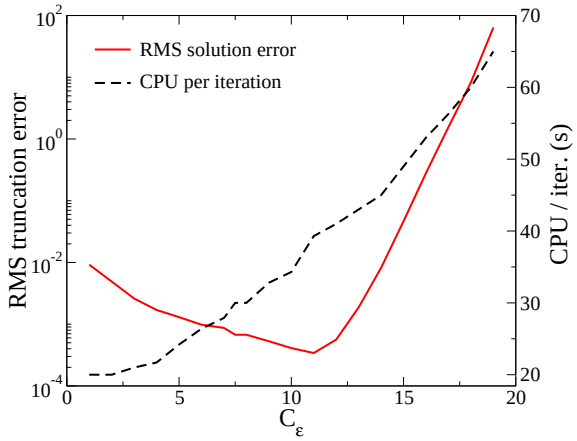

Figure 2.7: *Truncation error and CPU time per iteration as a function of adjustable parameter C_ϵ.*

Formula (2.30) features a constant C_ϵ which has to be adjusted from numerical experiments. For that purpose, the test problem is now considered for $N = 30,726$ DOFs, with a leaf level $\bar{\ell} = 5$ and a leaf-cell size $d^{(\bar{\ell})} = 0.6\lambda_\mathrm{S}$ (where $\lambda_\mathrm{S} = 2\pi/k_\mathrm{S}$ denotes the S–wavelength). A subset of 10 columns of the influence matrix $[K]$ are computed using both the present FM-BEM (by performing matrix-vector products $[K]\{u\}$ with all entries of $\{u\}$ set to zero except that corresponding to the selected column of $[K]$, set to unity) and standard BEM techniques. The relative root mean square (RMS) difference between these two sets of matrix columns measures the truncation error introduced by the FMM with finite truncation level L. This truncation error (solid line), and the CPU time (dashed line) for one FMM iteration, are plotted against C_ϵ in Fig. 2.7. Error levels below 10^{-3} are achieved for $5 \leq C_\epsilon \leq 12.5$, which corroborates the previously-discussed notion of a numerically optimal truncation level L. Values of C_ϵ outside the above range lead to values

of L that are either too small (insufficient convergence in (2.8)) or too large (divergence of Hankel functions in (2.9)). Figure 2.7 also shows that the CPU time for one FMM iteration increases with C_ϵ, which was to be expected since L given by (2.30) also increases with C_ϵ. The value $C_\epsilon = 7.5$ is found to achieve to keep a good compromise between accuracy and computational cost, and is retained in the present implementation. This observation is consistent with that made in [200] for 3-D electromagnetics.

2.4.2 Number of levels

The choice of the leaf level $\bar{\ell}$ is crucial, as it affects both the overall computational time and the accuracy of the elastodynamic FM-BEM algorithm. A too-small number of levels increases the proportion of near interactions, thus pushing the complexity of the computation closer to $O(N^2)$, while a too-large number of levels increases the number of transfers between levels (see Table 2.1 where several values of $\bar{\ell}$ are considered, with $k_p a = 6\pi$ and $N = 122,886$ DOFs).

Table 2.1: *Error and CPU time against the number of levels.*

$\bar{\ell}$ (leaf level)	$k_{\mathrm{S}} d^{(\bar{\ell})}/2\pi$	error / BEM	CPU time / iter (s)
3	1.32	$1.1\,10^{-5}$	367
4	0.66	$4.7\,10^{-4}$	134
5	0.33	$3.7\,10^{-3}$	104
6	0.17	$5.1\,10^{-2}$	200
7	0.083	$1.7\,10^{-1}$	380

The truncation parameter L at any level depends on the leaf-cell size $d^{(\bar{\ell})}$. This is now illustrated with the help of the comparison method and test problem of Section 2.4.1: relative RMS differences between matrices generated by FM-BEM (with L determined at all levels by (2.30)) and standard BEM produced by this comparison are plotted in Fig. 2.8 against C_ϵ for several choices of $d^{(\bar{\ell})}$. For small values of $k_{\mathrm{S}} d^{(\bar{\ell})}$, the FM-BEM algorithm is seen to be insufficiently accurate. This stems from the fact that the distances $|\boldsymbol{r}_0|$ between leaf cells scale with d, and the spherical Hankel functions in (2.9) are known to diverge in the small-argument limit. Estimate (2.15) accordingly predicts that L has a $O(\ln kd)$ divergence in the small cell size limit, and formula (2.30) does not provide adequate values of L in this case, even upon increasing the constant C_ϵ, as evidenced by the results of Fig. 2.8. This suggests that the leaf cell size $d^{(\bar{\ell})}$ must be chosen larger to a minimum value $d^{\min}$ to avoid divergence; for instance, results obtained using $d^{(\bar{\ell})} = 0.075\lambda_{\mathrm{S}}$ have very poor accuracy. A minimum leaf cell size $d^{\min} = \lambda/10$ is adopted in [58]. Accuracy and computational efficiency considerations make higher values of $d^{\min}$ preferable. In this work, the subdivision-stopping criterion defining the leaf level $\bar{\ell}$ is set to: $d^{(\bar{\ell}+1)} \leq d^{\min} \leq d^{(\bar{\ell})}$, with $d^{\min} = 0.3\lambda_{\mathrm{S}}$.

Configurations for which cells of size significantly smaller than $d^{\min} \approx 0.3\lambda_{\mathrm{S}}$ are desirable (e.g. geometries with complex details at sub-wavelength scales) require an adaptation to elastodynamics of approaches combining the diagonal form (2.8) with other types of expansions valid for low wavenumbers, see [61, 45, 117].

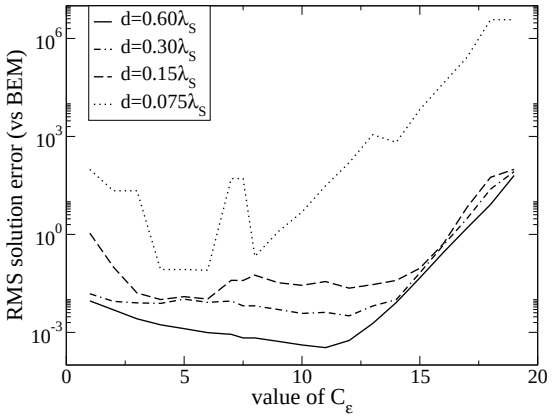

Figure 2.8: *Truncation error as a function of adjustable parameter C_ϵ for several values of leaf-cell size $d^{(\bar{\ell})}$.*

2.4.3 Quadrature over the unit sphere

Another practical issue is the numerical computation of integrals over the unit sphere S in (2.11), (2.12). The quadrature method of [58], based on a product rule in the angular spherical coordinates θ, ϕ, employs quadrature points and weights of the form $\hat{\boldsymbol{s}}_q = (\theta_i, \phi_j)$ and $w_q = w_i^\theta w_j^\phi$, where (θ_i, w_i^θ) $(1 \leq i \leq L)$ correspond to a $L+1$-point Gaussian rule on $[0, \pi]$ while (ϕ_j, w_j^ϕ), given by

$$\phi_j = \frac{2\pi}{2L+1} j, \quad w_j^\phi = \frac{2\pi}{2L+1} \qquad (0 \leq j \leq 2L), \tag{2.31}$$

correspond to a uniform rule on $[0, 2\pi]$. This approach, which employs $Q = (L+1)(2L+1)$ quadrature points overall, is designed so as to integrate exactly the $L^2(S)$-orthonormal set of spherical harmonics $\big(Y_{p,m}(\theta,\phi)\big)_{0\leq p\leq L, -p\leq m\leq p}$ of order $\leq L$, a requirement which, together with (2.30), implies that the number of quadrature points must be level-dependent. It is adopted here, in a form slightly modified as explained next.

Reduction of the number of quadrature points. The transfer function $\mathcal{G}_L$ given by (2.9) has the form $\mathcal{G}_L(\boldsymbol{r}_0, \hat{\boldsymbol{s}}, k) = \sum_{p=0}^{L} \mathcal{H}_p(\boldsymbol{r}_0) P_p\big(\cos(\hat{\boldsymbol{s}}, \boldsymbol{r}_0)\big)$. The factor $\mathcal{H}_p(\boldsymbol{r}_0)$ does not depend on $\hat{\boldsymbol{s}}$, and is computed once for each $\boldsymbol{r}_0$. Then, for each pair $(\boldsymbol{r}_0, \hat{\boldsymbol{s}})$, the Legendre polynomials are computed by induction:

$$\begin{cases} P_p(x) = (2 - 1/p)xP_{p-1}(x) + (1/p - 1)P_{p-2}(x), \\ P_0(x) = 1, \quad P_1(x) = x \end{cases} \qquad \Big(x = \frac{\boldsymbol{r}_0.\hat{\boldsymbol{s}}}{|\boldsymbol{r}_0|\,|\hat{\boldsymbol{s}}|}\Big). \tag{2.32}$$

The Legendre polynomials are known to satisfy the identity $P_p(-x) = (-1)^p P_p(x)$. This can be exploited to reduce the number of quadrature points $\hat{\boldsymbol{s}}$: a grid that is invariant under the transformation $\hat{\boldsymbol{s}} \to -\hat{\boldsymbol{s}}$ allows to perform the numerical integration on S with half the original quadrature points. The rule defined by (2.31) fulfils this invariance provided the uniform rule on $[0, 2\pi]$ is defined in terms of $2L + 2$, rather than $2L + 1$, points. This modified version of (2.31) features $2(L + 1)^2$ points, but only $(L + 1)^2$ points are actually computed, stored and used. As a result, the computing time and memory required by the quadrature are roughly divided by 2.

2.4.4 Extrapolation (direct/inverse)

The upward translations (2.26a,b) require evaluating multipole moments at level-ℓ quadrature points from their values at level-$(\ell+1)$ quadrature points. This important step of the algorithm has a significant impact on the overall CPU time required by the FM-BEM, and hence has to be formulated carefully. A fast method, which takes advantage of the uniform distribution (2.31) of quadrature points along ϕ and exploits $L^2(S)$-orthogonality and finite-bandwidth properties of the spherical harmonics, has been proposed in [58, 200] and is used here.

With the quadrature points at levels ℓ and $\ell+1$ of the form

$$\begin{aligned} \hat{\boldsymbol{s}}_q^{(\ell+1)} &= (\theta_i^{(\ell+1)}, \phi_j^{(\ell+1)}) \qquad 0 \le i \le L^{(\ell+1)} \quad 0 \le j \le 2L^{(\ell+1)}, \\ \hat{\boldsymbol{s}}_q^{(\ell)} &= (\theta_{i'}^{(\ell)}, \phi_{j'}^{(\ell)}) \qquad 0 \le i' \le L^{(\ell)} \quad 0 \le j' \le 2L^{(\ell)}, \end{aligned}$$

the values $\mathcal{F}_{i'j'} = \mathcal{F}(\theta_{i'}^{(\ell)}, \phi_{j'}^{(\ell)})$ at the level-ℓ quadrature points of a generic function $\mathcal{F}(\hat{s}) = \mathcal{F}(\theta, \phi)$ are extrapolated from those $\mathcal{F}_{ij} = \mathcal{F}(\theta_i^{(\ell+1)}, \phi_j^{(\ell+1)})$ at the level-$(\ell+1)$ quadrature points by means of the following three steps:

$$\begin{aligned} \tilde{\mathcal{F}}_{im}^{(\ell+1)} &= \sum_{j=0}^{2L^{(\ell+1)}} e^{-\mathrm{i}m\phi_j^{(\ell+1)}} \mathcal{F}_{ij}^{(\ell+1)} \qquad \big(|m| \le L^{(\ell+1)}\big) && \text{forward Fast Fourier Transform,} \\ \tilde{\mathcal{F}}_{i'm}^{(\ell)} &= \sum_{i=0}^{L^{(\ell+1)}} B_{i'i}^{m,\ell} \tilde{\mathcal{F}}_{im}^{(\ell+1)} && \text{dense matrix-vector product,} \\ \mathcal{F}_{i'j'}^{(\ell)} &= \sum_{m=-L^{(\ell+1)}}^{L^{(\ell+1)}} e^{\mathrm{i}m\phi_{j'}^{(\ell)}} \tilde{\mathcal{F}}_{i'm}^{(\ell)} && \text{backward Fast Fourier Transform,} \end{aligned} \tag{2.33}$$

with

$$B_{i'i}^{m,\ell} = \sum_{p=|m|}^{L^{(\ell+1)}} Q_p^m(\cos\theta_i^{(\ell+1)}) Q_p^m(\cos\theta_{i'}^{(\ell)}), \qquad Q_p^m(u) = \sqrt{\frac{2p+1}{4\pi}\frac{(p-m)!}{(p+m)!}} P_p^m(u)$$

(see Appendix D.2 for more details on the numerical computation of this matrix). Likewise, the downward translations (2.28a,b) require inverse extrapolations from level-ℓ quadrature points to level-$(\ell+1)$ points, which are based on a transposed version of the extrapolation:

$$\begin{aligned} \tilde{\mathcal{F}}_{i'm}^{(\ell)} &= \sum_{j'=0}^{2L^{(\ell)}} e^{-\mathrm{i}m\phi_{j'}^{(\ell)}} \mathcal{F}_{i'j'}^{(\ell)} \qquad \big(|m| \le L^{(\ell+1)}\big) && \text{forward Fast Fourier Transform,} \\ \tilde{\mathcal{F}}_{im}^{(\ell+1)} &= \sum_{i'=0}^{L^{(\ell+1)}} B_{i'i}^{m,\ell} \tilde{\mathcal{F}}_{i'm}^{(\ell)} && \text{dense matrix-vector product,} \\ \mathcal{F}_{i'j'}^{(\ell+1)} &= \sum_{m=-L^{(\ell+1)}}^{L^{(\ell+1)}} e^{\mathrm{i}m\phi_j^{(\ell+1)}} \tilde{\mathcal{F}}_{im}^{(\ell+1)} && \text{backward Fast Fourier Transform.} \end{aligned} \tag{2.34}$$

Other extrapolation methods have been proposed [58], some of which being of lower computational complexity but at the cost of further approximation. The above extrapolation method is exact, and will be shown in numerical experiments (Section 2.5) to account for only a modest fraction of the overall CPU time of an elastodynamic FM-BEM analysis, and hence to be satisfactory.

2.4.5 Ordering of the transfer operations

In operations (2.27a,b), the transfer functions $\mathcal{G}_L$ need to be evaluated only for vectors $\boldsymbol{r}_0$ linking the centers of two same-level cells $\mathcal{C}_y$ and $\mathcal{C}_x$. Such vectors are integer multiples of the cell size d: $\boldsymbol{r}_0 = (n_x\, n_y\, n_z)d$. Moreover, at any given level, the transfers are only computed for cells $\mathcal{C}_y$ in the interaction list of a given cell $\mathcal{C}_x$, i.e. the integers n_x, n_y, n_z necessarily belong to the set $\{-3 \leq n_x, n_y, n_z \leq 3\} \backslash \{-1 \leq n_x, n_y, n_z \leq 1\}$. The maximum number of distinct vectors $\boldsymbol{r}_0$ required for performing all operations (2.27a,b) for a given level is therefore $7^3 - 3^3 = 316$. Each transfer matrix can thus be reused many times, especially at the lowest levels. In order to take advantage of this remark, the transfer operations are first sorted according to the vector $\boldsymbol{r}_0$. Then, for each $\boldsymbol{r}_0$, the transfer matrix is computed using the method of Section 2.4.3. Moreover, the same transfer matrices are used for each GMRES iteration. It is therefore possible to precompute and store on hard drive each transfer matrix, prior to performing any GMRES iteration.

2.4.6 Matrix of near interactions

The only BEM matrix in the FMM for which storage may be considered is the near-interaction influence matrix $[K^{\text{near}}]$, such that $[K^{\text{near}}]\{u\} = \{\mathcal{K}u\}^{\text{near}}$ with reference to (2.18a), because $[K^{\text{near}}]$ is sparse. The most common storage strategy for sparse matrices is the Compressed Sparse Row (CSR) approach [179], based on three linear arrays: the nonzero matrix entries (stored row-wise), the column indices, and integer pointers to the beginning of each matrix row in the first two arrays. Products of CSR-stored sparse matrices with vectors are then computed row by row, which prevents one to take advantage of optimized matrix-vector product routines, e.g. those of the BLAS library.

A modification of this storage strategy takes advantage of the structure of the computation of the near interactions, where a cell can interact only with its neighbour cells. The idea is to store blocks representing the interaction of a cell on its neighbour cells (Fig. 2.9) and then to evaluate matrix-vector products blockwise (instead of termwise). Each block is stored in full-matrix format. For example, the largest model used in the numerical study of complexity of Section 2.5.3, for which $N = 1,215,291$, features $18,351$ non-empty leaf cells. The corresponding blockwise-sparse matrix of near interactions is made of $260,203$ blocks (i.e. a given leaf cell has on average about 14 non-empty adjacent cells, including itself, for this example).

This storage strategy has two advantages. First, it uses local lists of unknown DOFs for a given cell and its neighbours, instead of the global list. Second, optimized BLAS routines can be used to compute the product of each block of $[K^{\text{near}}]$ with the corresponding part of the solution vector. Moreover, to reduce the number of blockwise matrix-vector products, only one block is created for each leaf cell $\mathcal{C}_x$, with lines and columns corresponding to collocation nodes in $\mathcal{C}_x$ and interpolation nodes in all cells $\mathcal{C}_y \in \mathcal{A}(\mathcal{C}_x)$, respectively. The matrix entries for each such block are computed by treating the set of elements belonging to all $\mathcal{C}_y \in \mathcal{A}(\mathcal{C}_x)$ as a single (small) BEM mesh and using traditional BEM matrix set-up methods.

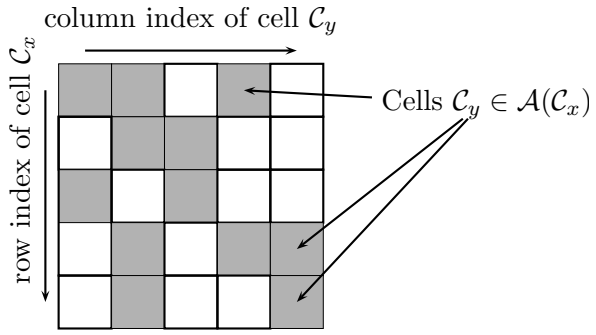

Figure 2.9: *Near interactions matrix (blockwise-sparse storage).*

2.4.7 Memory management

In the multi-level elastodynamic FM-BEM, multipole moments (2.20a,b) and (2.21a,b) and local expansions (2.22a,b) and (2.23a,b) are computed for each cell, each level and each quadrature point, and thus arise in large numbers. It is esssential to keep the storage of such quantities to a minimum. The memory needed for a given FM-BEM analysis is affected by the order in which certain tasks are performed. To compute the local expansions $\mathcal{L}_k^{\mathrm{S}}$, $\mathcal{L}^{\mathrm{P}}$ at level ℓ, $\mathcal{R}_k^{\mathrm{S}}$, $\mathcal{R}^{\mathrm{P}}$ are needed at level ℓ and $\mathcal{L}_k^{\mathrm{S}}$, $\mathcal{L}^{\mathrm{P}}$ at level $(\ell-1)$. One may therefore discard the values of $\mathcal{R}_k^{\mathrm{S}}$, $\mathcal{R}^{\mathrm{P}}$ at level $(\ell+1)$ (and reallocate the corresponding memory) once $\mathcal{R}_k^{\mathrm{S}}$, $\mathcal{R}^{\mathrm{P}}$ are computed at level ℓ. As schematized in Fig. 2.10, performing the transfer at level ℓ immediately after the upward pass from level $(\ell+1)$ to level ℓ allows to restrict the storage to the multipole moments at levels ℓ and $(\ell+1)$, and the local expansions at all levels. This ordering hence reduces by about half the memory required for storing multipole moments and local expansions.

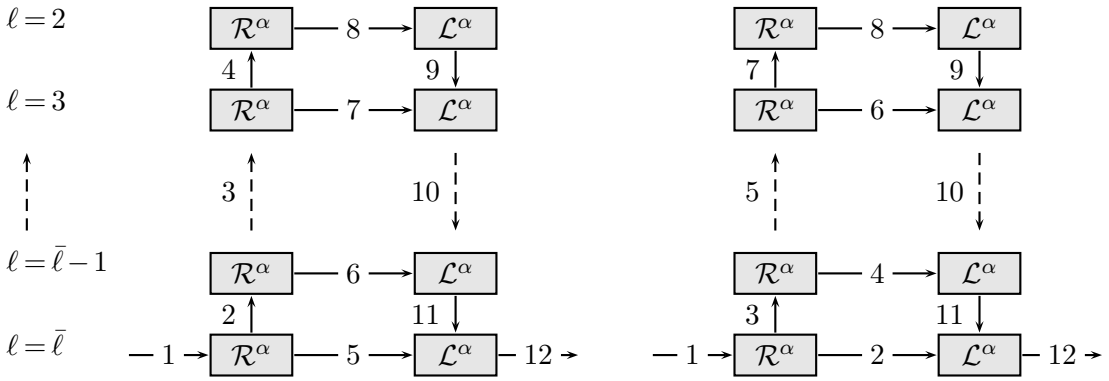

Figure 2.10: *Non-optimal (left) and optimal (right) orderings of the various steps of the multi-level FMM (the numbered arrows indicate the sequential ordering of passes for each case).*

Moreover, virtual memory is optimized for large problem sizes, as follows. Multipole moments and local expansions are written on hard drive (out-of-core). Then, for each step of the multi-level FMM, the needed information is read in the appropriate file and stored back in that file after updating. The maximum virtual memory cost is therefore incurred by the transfer pass at level $\bar{\ell}$, for which all level-$\bar{\ell}$ multipole moments and local expansions must be saved in virtual memory.

For even larger problem sizes, an improved version of this strategy, where the ℓ-level cells are

split into $\mathcal{N}_{gr}$ groups, has been implemented. The transfer pass is then effected as two nested loops over the $\mathcal{N}_{gr}$ groups, with operations (including the reordering according to vectors $\boldsymbol{r}_0$ linking the centers of two same-level cells, see Section 2.4.5) done only for cells belonging to the two currently active groups. As a result, the virtual memory required by a transfer pass is divided by $\mathcal{N}_{gr}$. This multi-group out-of-core process is applied separately to each pass of the multi-level FMM. In order to define groups of similar size at each level, the number of groups is level- and problem-dependent.

2.4.8 Post-processing: evaluation of the integral representation

Once the values of $\boldsymbol{u}(\boldsymbol{x})$ on the boundary ($\boldsymbol{x} \in \partial\Omega$) computed by solving system (2.4), the boundary integral representation (2.1) is used to obtain $\boldsymbol{u}(\boldsymbol{x})$ at interior (or exterior points) ($\boldsymbol{x} \in \Omega$). This operation only requires a single matrix-vector product which can be performed using standard BEM. However, if the number of interior points is large the use of the FMM for this step is recommended. System (2.4) is square since the DOFs are identical for lines and columns. But for the integral representation (2.1), the interpolation points (points on the boundary, $\boldsymbol{y} \in \partial\Omega$) differ from the evaluation ones (interior points, $\boldsymbol{x} \in \Omega$) (see Fig. 2.11).

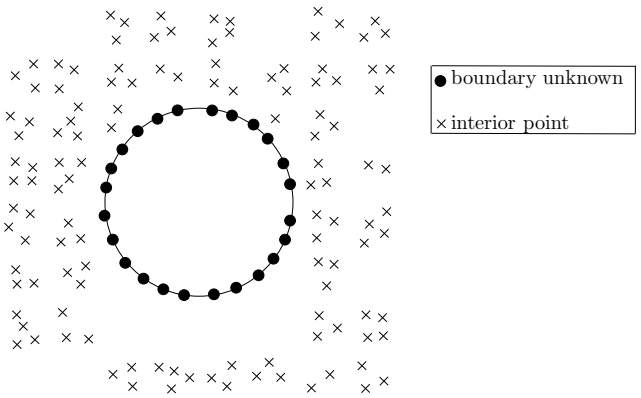

Figure 2.11: *Definition of the evaluation and interpolation points for the computation of the boundary integral representation.*

To handle such configurations, two octrees are defined. One is based on the boundary mesh of $\partial\Omega$, the second on the chosen set of interior points in Ω. Note that the latter set is just a collection of evaluation points, for which no mesh is necessary.

Concerning the FMM algorithm presented in Section 2.3, the computation of the multipole moments (2.20a,b; 2.21a,b) is performed for the interpolation points ($\boldsymbol{y} \in \partial\Omega$) and the computation of the local expansions (2.22a,b; 2.23a,b) is performed for the evaluation points ($\boldsymbol{x} \in \Omega$). As a result, the initialization pass (2.20a,b; 2.21a,b) and upward pass (2.26a,b) are performed in the column octree which corresponds to the DOFs on the domain boundary ($\boldsymbol{y} \in \partial\Omega$). On the other hand, the downward pass (2.28a,b) and computation of the local expansions (2.22a,b; 2.23a,b) are performed in the line octree which corresponds to the desired DOFs in the domain ($\boldsymbol{x} \in \Omega$).

As a result, the correspondence from the column octree to the line octree is done during the transfer pass (2.27a,b). So, the two octrees cannot be independent to enable the transfer pass. The new notions of adjacent cell and interaction list need to be defined. The simple solution imple-

mented in the present work is to build the two octrees starting from the same level-0 cell, enclosing the complete domain (see Fig. 2.12). As a result, at each level, the cells in the two octrees have the same linear size and it is easy to know if a cell in the line octree is adjacent to a cell in the column octree.

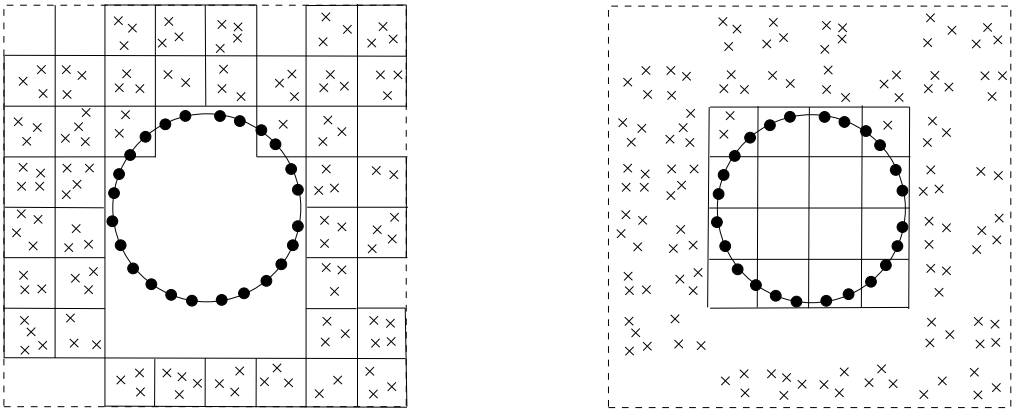

Figure 2.12: *Definition of the two octrees for the computation of the boundary integral representation.*

2.4.9 Implementation of the elastodynamic FM-BEM: summary

The elastodynamic multi-level FM-BEM solver implemented in the course of this work, whose features are discussed in Sections 2.3 and 2.4, is summarized for convenience in Figs. 2.13, 2.14 and 2.15.

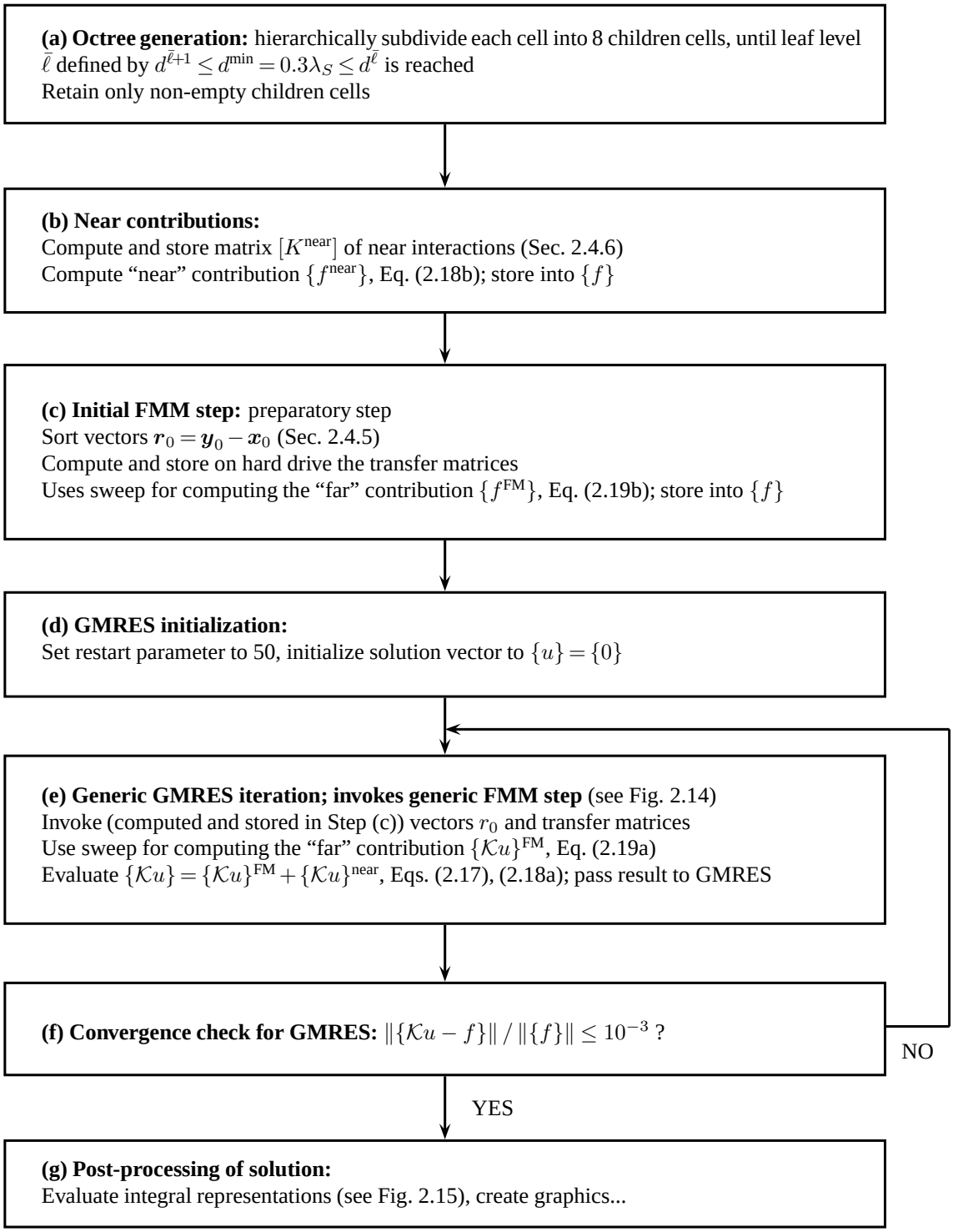

Figure 2.13: *Elastodynamic multi-level FM-BEM: schematic description of overall algorithm.*

(a) for all leaf cells $\mathcal{C}_y^{(\bar{\ell})}$
initialization : computation of multipole moments, Eqs. (2.20a,b)
transfer using $L(d^{\bar{\ell}}) = \sqrt{3}kd^{\bar{\ell}} + 7.5\log_{10}(\sqrt{3}kd^{\bar{\ell}} + \pi)$ terms in expansion, Eqs. (2.27a,b)
end for

(b) for all levels $\ell = \bar{\ell} - 1, 2$ (in this order)
for all cells $\mathcal{C}_y^{(\ell)}$
for all cells $\mathcal{C}_y^{(\ell+1)} \in \mathcal{S}(\mathcal{C}_y^{(\ell)})$
upward pass, Eqs. (2.26a,b)
end for
extrapolation, Eq. (2.33)
end for
for all cells $\mathcal{C}_x^{(\ell)}$
for all cells $\mathcal{C}_y^{(\ell)} \in \mathcal{I}(\mathcal{C}_x^{(\ell)})$
transfer using $L(d^{\ell}) = \sqrt{3}kd^{\ell} + 7.5\log_{10}(\sqrt{3}kd^{\ell} + \pi)$ terms in expansion, Eqs. (2.27a,b)
end for
end for
end for

(c) for all levels $\ell = 3, \bar{\ell}$ (in this order)
for all cells $\mathcal{C}_x^{(\ell)}$
downward pass, Eq. (2.28a,b)
inverse extrapolation, Eq. (2.34)
end for
end for

(d) for all leaf cells $\mathcal{C}_x^{(\bar{\ell})}$
for all collocation points $x \in \mathcal{C}_x^{(\bar{\ell})}$
local expansions Eq. (2.24)
add "near" part Eq. (2.18a)
end for
end for

Figure 2.14: *Elastodynamic multi-level FM-BEM: schematic description of generic FMM step.*

(a) for all leaf cells $\mathcal{C}_y^{(\bar{\ell})}$ in the column octree
initialization : computation of multipole moments, Eqs. (2.20a,b)
transfer Eqs. (2.27a,b)
end for

(b) for all levels $\ell = \bar{\ell} - 1, 2$ (in this order)
for all cells $\mathcal{C}_y^{(\ell)}$ in the column octree
for all cells $\mathcal{C}_y^{(\ell+1)} \in \mathcal{S}(\mathcal{C}_y^{(\ell)})$ in the column octree
upward pass, Eqs. (2.26a,b)
end for
extrapolation, Eq. (2.33)
end for
for all cells $\mathcal{C}_x^{(\ell)}$ in the line octree
for all cells $\mathcal{C}_y^{(\ell)} \in \mathcal{I}(\mathcal{C}_x^{(\ell)})$ in the column octree
transfer Eqs. (2.27a,b)
end for
end for
end for

(c) for all levels $\ell = 3, \bar{\ell}$ (in this order)
for all cells $\mathcal{C}_x^{(\ell)}$ in the line octree
downward pass, Eq. (2.28a,b)
inverse extrapolation, Eq. (2.34)
end for
end for

(d) for all leaf cells $\mathcal{C}_x^{(\bar{\ell})}$ in the line octree
for all collocation points $x \in \mathcal{C}_x^{(\bar{\ell})}$
local expansions Eq. (2.24)
add "near" part Eq. (2.18a)
end for
end for

Figure 2.15: *Elastodynamic multi-level FM-BEM: schematic description of the computation of the integral representation using the FMM.*

2.5 COMPLEXITY OF THE ELASTODYNAMIC FMM

In this section, the theoretical complexity of the elastodynamic FMM, i.e. the CPU time spent for each GMRES iteration as a function of N, is studied for both the single- and multi-level versions (Sections 2.5.1 and 2.5.2) and then compared to results from numerical experiments (Section 2.5.3).

2.5.1 Theoretical evaluation, single-level FMM

Noting $d \geq d^{\min}$ the linear cell size, the number of non-empty cells and the number of average DOFs per non-empty cell are $O(N/d^2)$ and $O(d^2)$ respectively; these estimates stem from the fact that the geometrical support of the unknown BE DOFs is two-dimensional. The truncation parameter $L(d)$ given by (2.30) is such that there is a positive constant H (which depends on $d^{\min}$) for which

$L(d) \leq Hd$ for any $d \geq d^{\min}$. Therefore, one may conservatively consider that $L(d) = O(d)$ and, by virtue of (2.31), that the number Q of quadrature points over S is $Q = O(d^2)$. The main steps of the single-level FMM entail the following computational complexities:

(a) Evaluation of multipole moments (2.20a,b) and local expansions (2.24), for each quadrature point and each cell: $O(Nd^2)$;

(b) Transfers (2.22a,b), for each quadrature point and each pair of non-adjacent cells: $O(d^2 \times N/d^2 \times N/d^2) = O(N^2/d^2)$;

(c) Near interactions (2.18a), for each cell, by means of the product of a $O(d^2) \times O(d^2)$ matrix with a $O(d^2)$ vector: $O(N/d^2 \times d^4) = O(Nd^2)$.

Setting $d = O(N^\alpha)$ the optimal complexity is obtained by minimizing the largest exponent in $Nd^2 = N^{1+2\alpha}$ and $N^2/d^2 = N^{2-2\alpha}$. Hence the optimal cell size in the single-level FMM is $d = O(N^{1/4})$. As a result, the optimal complexity in the single-level FMM in elastodynamics is of order $O(N^{3/2})$, and is achieved by using $O(N^{3/4})$ cells.

2.5.2 Theoretical evaluation, multi-level FMM

The leaf cell size $d^{(\bar{\ell})}$ is as small as possible, under the constraint $d^{(\bar{\ell}+1)} \leq d^{\min} \leq d^{(\bar{\ell})}$ ($d^{\min}$ being a fixed fraction of S–wavelength), as discussed in Section 2.4.2. Assuming a constant number of DOFs per wavelength, $d^{(\bar{\ell})}$ may be considered as independent of N in the complexity analysis. The size $d^{(0)}$ of the largest cells is related to $d^{(\bar{\ell})}$ by $2^{\bar{\ell}} d^{(\bar{\ell})} = d^{(0)}$. Moreover, the fact that the BEM nodes are located on a surface of characteristic diameter $O(d^{(0)})$ implies that $d^{(0)} = 2^{\bar{\ell}} d^{(\bar{\ell})} = O(N^{1/2})$. Hence, the total number of levels is:

$$\bar{\ell} = O(\log N) \tag{2.35}$$

and the number of leaf cells is $O(N)$. Moreover, since the DOFs are supported on a surface, each non-empty level-ℓ cell has on average 4 non-empty children cells, and therefore holds an average of $N^{(\ell)} = O(4^{-\ell} N)$ DOFs. The numbers of non-empty cells and of children at each level for the example of a spherical cavity with $N = 1,215,291$ DOFs, shown in Table 2.2, corroborate this estimate. Lastly, one notes that the level-ℓ truncation parameter and the number of level-ℓ quadrature points are $L^{(\ell)} = O(d^{(\ell)}) = O(d^{(0)} \times 2^{-\ell}) = O(N^{1/2} \times 2^{-\ell})$ and $Q^{(\ell)} = O\big((d^{(\ell)})^2\big) = O(N \times 4^{-\ell})$.

Based on the foregoing remarks, the computational complexities associated with the main steps of the multi-level FMM are obtained as:

(i) Multipole moments (2.20a,b) and local expansions (2.24), evaluated only at level $\bar{\ell}$: $O(N)$.

(ii) Transfers (2.27a,b), performed for each level, each cell $\mathcal{C}_x^{(\ell)}$ and each cell $\mathcal{C}_y^{(\ell)} \in \mathcal{I}(\mathcal{C}_x^{(\ell)})$: $O(4^\ell \times Q^{(\ell)}) = O(N)$ per level, i.e. $O(N \log N)$ overall.

(iii) Upward and downward passes (2.26a,b), (2.28a,b), for each level ℓ, each cell and each quadrature point $\hat{\boldsymbol{s}}^{(\ell)}$: $O(N)$ per level, i.e. $O(N \log N)$ overall.

(iv) Direct and inverse extrapolations, for each level ℓ and each cell: $O(N^{3/2})$.

Table 2.2: *Average number of non-empty cells and children at each level.*

level	number of non-empty cells	number of children
2	56	4.86
3	272	4.26
4	1,160	4.07
5	4,720	3.89
6	18,351	—

Estimate (ii) relies on the fact that the interaction list of a given cell contains at most $6^3 - 3^3 = 189$ cells, irrespective of the level and the total number of cells. Estimate (iv) stems from the observation that each extrapolation (2.33) from level $(\ell+1)$ to level ℓ (whose total number is $O(4^\ell)$) requires $L^{(\ell)}+1$ dense matrix-vector products, each of size $(L^{(\ell)}+1)\times(L^{(\ell+1)}+1)$, i.e. $O\big(4^\ell \times 2^{-\ell}N^{1/2} \times (2^{-\ell}N^{1/2} \times 2^{-(\ell+1)}N^{1/2})\big) = O\big(N^{3/2}2^{-(\ell+1)}\big)$ operations. Summing these extrapolations from level $\ell = \bar{\ell}$ to $\ell = 3$, the obtained cumulative complexity of all extrapolations is $O(N^{3/2})$ as stated. A similar analysis holds for the cumulative effect of the inverse extrapolation steps (2.34).

This analysis therefore predicts a theoretical complexity of $O(\alpha N \log N + \beta N^{3/2})$ per iteration for the multi-level FMM.

2.5.3 Numerical study of complexity

The theoretical complexities just formulated are now compared against recorded CPU times, on the pressurized spherical cavity problem (Section 2.4). This comparison aims in particular at evaluating the respective importances of the $O(\alpha N \log N)$ and $O(\beta N^{3/2})$ contributions to the overall complexity of the multi-level FMM. Several frequencies are considered, with the size of the BEM models adjusted so as to maintain a mesh density of about 10 nodes per S-wavelength (Table 2.3). This complexity study involves problem sizes of up to $N \approx 1.2\,10^6$, while the examples of [90] used $N \leq 2.5\,10^4$.

Table 2.3: *Numerical study of complexity: BEM model sizes N and non-dimensional frequencies used.*

N	30,726	122,769	217,983	389,232	449,835	530,709	635,349	771,912	955,608	1,215,291
$k_{\mathrm{P}}a/\pi$	3.05	6.14	8.31	10.9	11.66	12.68	13.91	15.2	17.4	19.24

Multi-level FMM: complexity of the main steps. With reference to items (i) to (iv) of Section 2.5.2, the cumulative CPU times recorded for the main steps of the multi-level FMM are compared to the corresponding theoretical complexities for the evaluation of (i) the multipole moments (Fig. 2.16a) and local expansions (Fig. 2.16b), (ii) the transfers (Fig. 2.16c), and (iii-iv) the upward

and downward passes including the (direct/inverse) extrapolations (Fig. 2.16d). For the latter case, coefficients (α, β) allowing a best fit of theoretical complexities of the form $O(\alpha N \log N + \beta N^{3/2})$ to the CPU data are obtained via regression as $(\alpha, \beta) = (1.3\,10^{-7}, 9.8\,10^{-9})$ for the upward pass and $(\alpha, \beta) = (1.8\,10^{-6}, 8.2\,10^{-8})$ for the downward pass. These values, which are of course code- and computer-dependent, suggest that the importance of the $O(N^{3/2})$ contribution to the upward and downward passes becomes significant for N above $O(10^5)$.

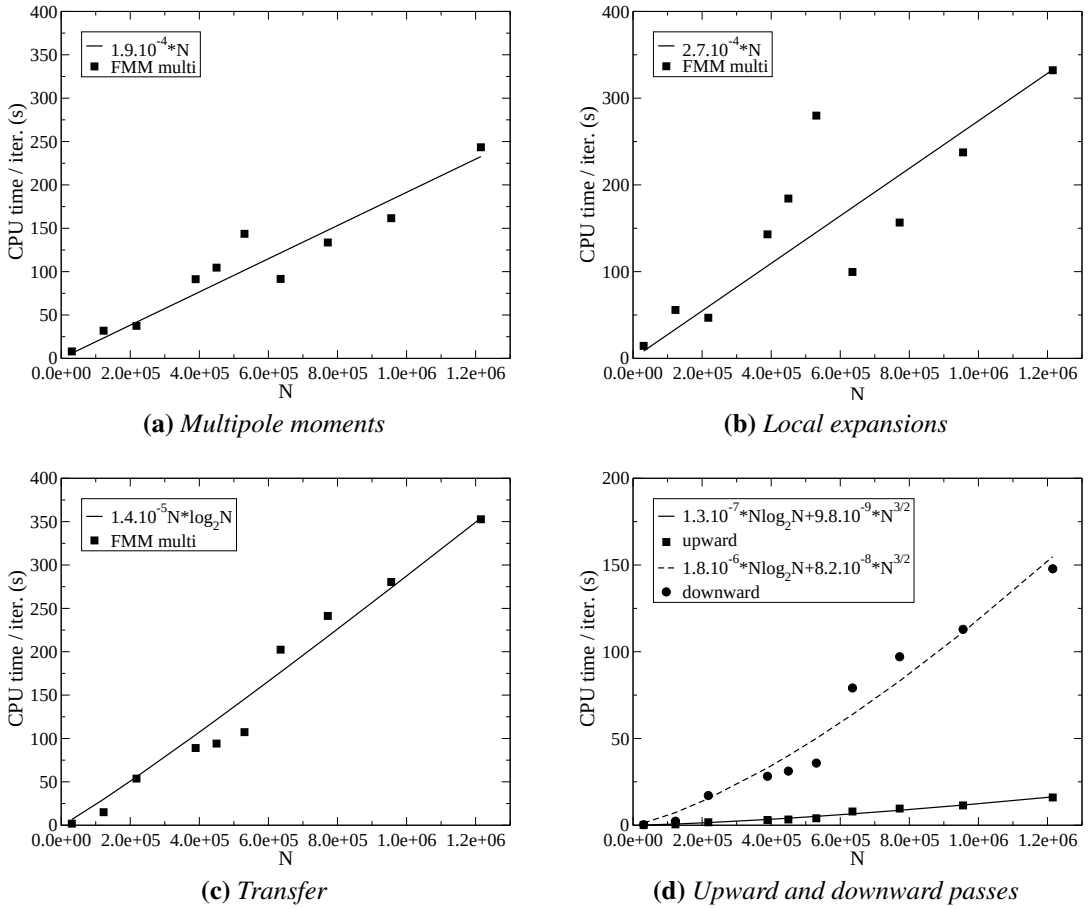

(a) *Multipole moments* **(b)** *Local expansions*

(c) *Transfer* **(d)** *Upward and downward passes*

Figure 2.16: *Theoretical complexity and recorded CPU times for the main steps of the multi-level elastodynamic FMM.*

In Fig. 2.17 the computation time required by the upward and downward passes and its estimation $\beta N^{3/2}$ are compared to the other steps of the algorithm. The results indicate that the $O(N^{3/2})$ contributions arising from the extrapolations are small compared to the $O(N \log N)$ contributions for BEM model sizes $N = O(10^6)$ or less, for which the extrapolation method of Section 2.4.4 is therefore satisfactory. Using improved algorithms for extrapolation such as those proposed in [58], of computational complexity lower than $O(N^{3/2})$, would reduce the elastodynamic FMM complexity to $O(N \log N)$. They may prove essential for BEM models involving several millions DOFs and more.

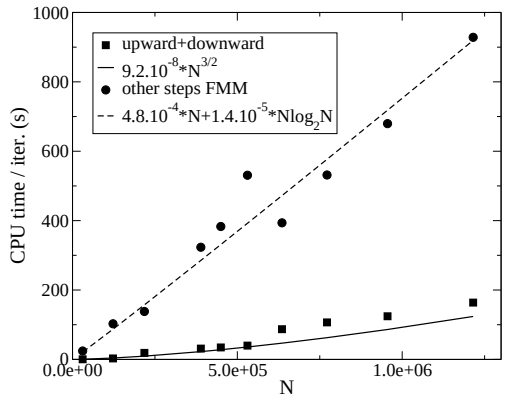

Figure 2.17: *Comparison of the cost of the upward and downward passes to the other steps of the algorithm.*

Overall complexity of the single-level and multi-level FMM. Numerical experiments, in the form of full BEM solutions obtained using the standard BEM, single-level FM-BEM and multi-level FM-BEM on BEM models of respective sizes up to $O(10^4)$, $O(10^5)$ and $O(10^6)$, corroborate the previously discussed theoretical complexities estimates for each approach, as seen in Fig. 2.18, where the $O(N^{3/2})$ contribution to the multi-level FMM has been disregarded in accordance with the previous discussion on its effect.

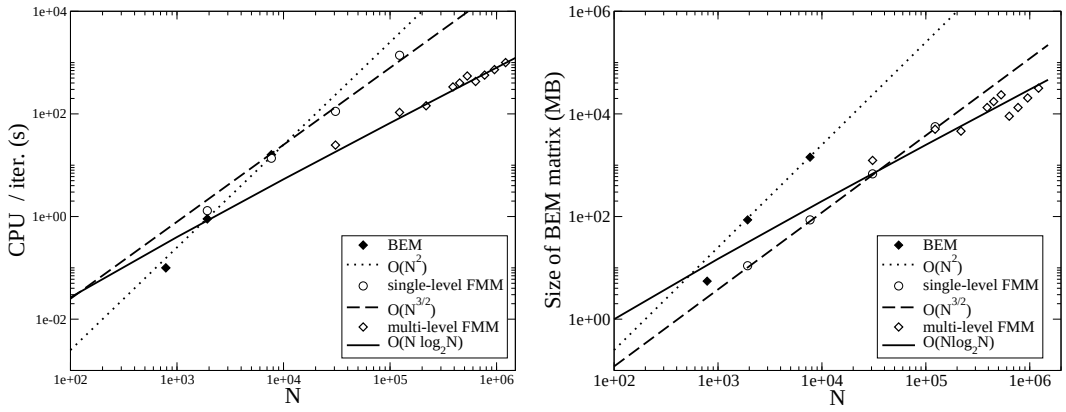

Figure 2.18: *Complexity of the standard BEM, single-level FMM and multi-level FMM (left: CPU time, right: memory).*

2.5.4 Discussion

The results of Sections 2.5.2 and 2.5.3 are consistent with corresponding studies in [200, 58] for electromagnetics, where particular the $O(N^{3/2})$ complexity of the direct and inverse extrapolations is also pointed out. The $O(N \log N)$ overall complexity is also obtained for the method stable at all frequencies proposed in [61]. In contrast, the elastodynamic FM-BEM of [90] uses a level-independent value for the truncation parameter L. This variant avoids the need for direct and inverse

extrapolation but requires $L = O(k_S d^{(0)}) = O(N^{1/2})$ by virtue of (2.30). Revisiting steps (i), (ii) and (iii) of Section 2.5.2 with fixed values for $L = O(N^{1/2})$ and $Q = O(L^2) = O(N)$, one finds a $O(N^2)$ complexity for that approach, as remarked also in [159]. In comparison, static FM-BEMs for static problems are known to have $O(N)$ complexity [159, 133] since the truncation parameter in the multipole expansion in that case depends neither on the level nor on the problem size.

2.6 NUMERICAL EXAMPLES

First, additional numerical results for the example of a pressurized spherical cavity, introduced in Section 2.4, are presented. Then, the more complex example of the diffraction of an incident plane P–wave by a spherical cavity, for which an exact solution is also available, further demonstrates the good accuracy of the present FMM. The usefulness of the proposed FMM formulation is also illustrated on the scattering of seismic plane P– or SV–waves by an irregular half-space model. Finally, the efficiency of the method for time-domain responses is presented on the example of the scattering of a seismic plane P–wave by a semi-spherical canyon.

For all results presented therein, the following computational parameters were used: $C_\epsilon = 7.5$, $d^{\min} = 0.3\lambda_S$ (unless indicated otherwise), and a convergence threshold defined by $\|\{f - \mathcal{K}u\}\|/\|\{f\}\| \leq 10^{-3}$ (using the notations of equation (2.7)) for GMRES. All the examples presented in this section are obtained without the use of a preconditioning strategy.

2.6.1 Pressurized spherical cavity

The example configuration defined in Section 2.4 is again used. First, numerically-computed solutions are compared for four non-dimensional frequencies to the corresponding exact solution (2.29).

The stopping criterion relative to cell subdivision proposed in Section 2.4.2 led to four levels for the highest frequency considered ($k_P a/\pi = 2$). Four levels were also used for the other three results in order to ensure that a sufficient proportion of the computations utilize multipole expansions (the subdivision-stopping criterion being hence disregarded for these cases). For each frequency, relative RMS errors for the radial displacement on the cavity wall and over the radial interval $a < r \leq 3a$ are presented in Table 2.4. The present FM-BEM is seen to be quite accurate, even in the low-frequency case ($k_P a/\pi = 0.1$) for which the accuracy of FMM expansions of the form (2.8) is known to deteriorate [58], whereas the standard BEM does not [56].

Table 2.4: *Pressurized spherical cavity: RMS solution error on the cavity and in the domain.*

$k_P a/\pi$	0.1	0.50	1.00	2.00
# nodes $/\lambda_S$	80	16	8	4
RMS error, $r = a$ (cavity wall)	0.025	0.006	0.006	0.021
RMS error, $a < r \leq 3a$ (domain)	0.011	0.006	0.008	0.031

Next, the effect of the number of nodes per S–wavelength on solution accuracy is examined. For that purpose, the cavity radius a and angular frequency ω are kept constant (with $k_p a = 3\pi$) while four BEM meshes with increasing mesh densities are used. The corresponding numbers

Table 2.5: *Pressurized spherical cavity: influence of the number of nodes per S–wavelength on the RMS solution error and the CPU time per iteration.*

# nodes per S–wavelength	N	RMS solution error on cavity	CPU time per iter. (s)
2.5	$1,926$	$2.0\,10^{-2}$	1.5
5	$7,686$	$4.6\,10^{-3}$	3.7
10	$30,726$	$1.3\,10^{-3}$	14.2
20	$122,886$	$4.0\,10^{-4}$	85.1

of nodes per S–wavelength are given in Table 2.5 (first column). The relative solution errors observed for these meshes (Table 2.5, second column) indicate that a good solution accuracy requires a minimum of 5 nodes per S–wavelength. The corresponding observed CPU times per iteration (Table 2.5, third column) increase due to the combined effect of mesh refinement and truncation parameter (2.30). The numerical results presented in the remainder of this chapter have been obtained using meshes featuring a minimum of 10 nodes per S–wavelength.

2.6.2 Diffraction of an incident plane P–wave by a spherical cavity

The geometrical configuration and material parameters are as in the previous example, but the cavity surface is now traction-free. An incident plane P–wave propagates along the positive z-direction (Fig. 2.19). Two frequencies are considered, defined by $k_{\mathrm{P}}a/\pi = 1$ and $k_{\mathrm{P}}a/\pi = 4$, with respective problem sizes $N = 7,686$ and $N = 122,886$. The numerical results are compared to the analytical solution given in [72] (which, incidentally, features a typographical error corrected in [56]).

The numerical results are computed along radial straight lines emanating from the cavity center in directions ($\theta = 0,\ \pi/4,\ \pi/2,\ 3\pi/4$) in the x-z plane. Figure 2.20 shows the real part of the radial displacement against the normalized radial coordinate r/a. The subdivision-stopping criterion employed for cases $k_{\mathrm{P}}a/\pi = 1$ and $k_{\mathrm{P}}a/\pi = 4$ corresponds to $d^{\min} = 0.2\lambda_{\mathrm{S}}$ and $d^{\min} = 0.3\lambda_{\mathrm{S}}$ respectively. The numerical results obtained using the present FM-BEM are seen to agree very well with the exact solution for the two frequencies considered, even along the $\theta = \pi/2$ direction corresponding to grazing incidence. For the case $k_{\mathrm{P}}a/\pi = 4$, a solution CPU time of 44 s per iteration (144 GMRES iterations, no preconditioning) is recorded. In Table 2.6, the influence of the choice of the leaf cell size (see Section 2.4.2) is further examined. Results obtained by choosing

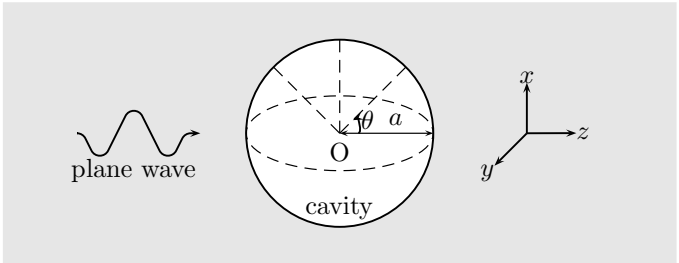

Figure 2.19: *Diffraction of an incident plane P–wave by a spherical cavity: notation.*

$d^{\min} \geq 0.1\lambda_S$ are satisfactorily accurate. On the other hand, solution errors are seen to deteriorate markedly whenever values $d^{\min} < 0.1\lambda_S$ are used. These results corroborate the validity of the recommended value $d^{\min} \geq 0.3\lambda_S$ proposed in Section 2.4.2 on the basis of an essentially one-dimensional test problem. Some of the values of $d^{\min}$ smaller than $0.3\lambda_S$ also lead to acceptable solution errors for this example. This however cannot be expected to be always true, as the test of Section 2.4.2 indicates.

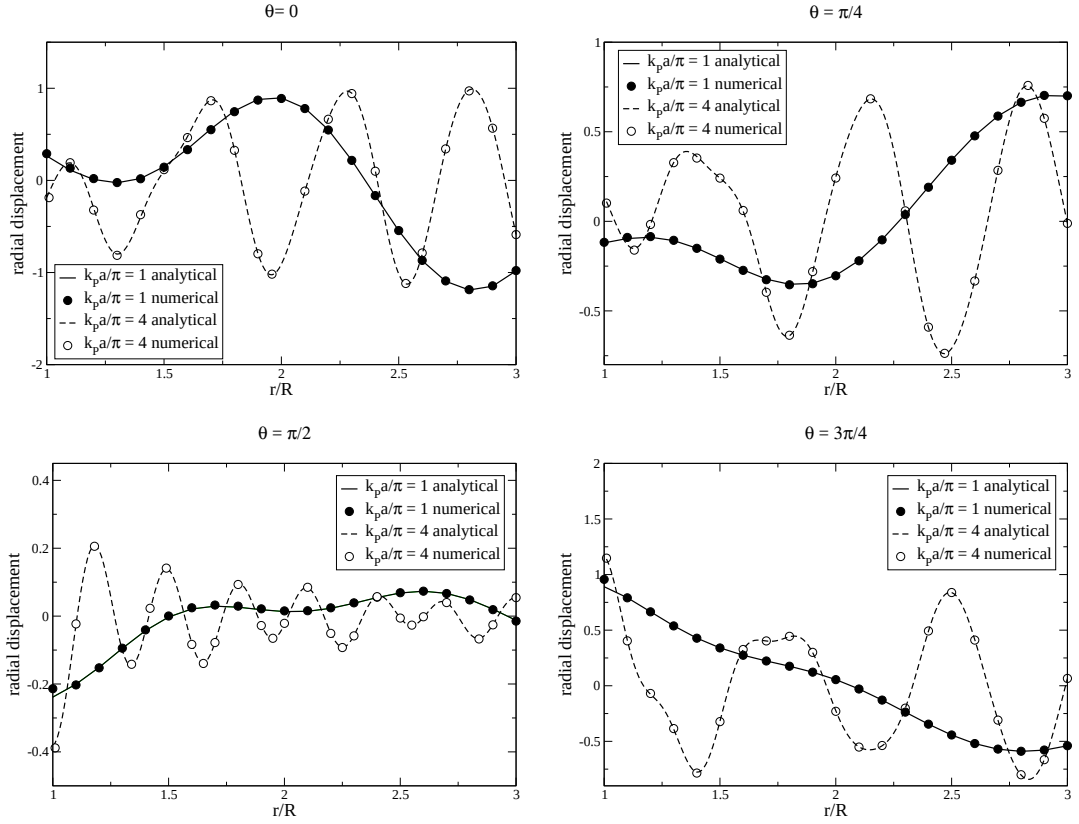

Figure 2.20: *Diffraction of an incident plane P–wave by a spherical cavity: comparison of the numerical FMM and analytical solutions for normalized frequencies* $k_{\mathrm{P}}a/\pi = 1, 4$ *and azimuths* $\theta = 0, \pi/4, \pi/2, 3\pi/4$.

2.6.3 Diffraction of an incident plane wave by a semi-ellipsoidal canyon

This example considers the diffraction by a semi-ellipsoidal canyon of a plane P– or SV–wave of unit amplitude travelling in an elastic homogeneous irregular half-space. The canyon surface is ellipsoidal, with semiaxes b, a, a respectively aligned along the coordinate directions x, y, z. The semi-ellipsoidal surface of the canyon and the surrounding portion of free surface lying inside a disk of radius $D > a, b$ are discretized using boundary elements. Such a configuration is representative of a "topographic site effect" in seismology and has been the subject of numerous studies, see [130, 131, 212, 73] and [56, 124, 152, 183, 169] where diffraction of waves by surface irregularities is considered. Three situations are considered: the diffraction of a vertical incident plane P–wave by

Table 2.6: *Diffraction of an incident plane P–wave by a spherical cavity: influence of leaf cell size on solution error.*

	$d^{\min}$	$\theta = 0$	$\theta = \pi/4$	$\theta = \pi/2$	$\theta = 3\pi/4$
$k_{\mathrm{P}}a/\pi = 1 \quad (N = 7,686)$	$0.2\lambda_{\mathrm{S}}$	$9.2\,10^{-3}$	$2.6\,10^{-3}$	$2.2\,10^{-2}$	$8.6\,10^{-4}$
	$0.1\lambda_{\mathrm{S}}$	$9.6\,10^{-3}$	$8.6\,10^{-3}$	$9.2\,10^{-3}$	$4.9\,10^{-3}$
	$0.05\lambda_{\mathrm{S}}$	$1.1\,10^{-2}$	$2.3\,10^{-2}$	$4.8\,10^{-2}$	$2.1\,10^{-2}$
	$0.02\lambda_{\mathrm{S}}$	$4.2\,10^{-2}$	$3.1\,10^{-2}$	$3.1\,10^{-1}$	$8.5\,10^{-2}$
$k_{\mathrm{P}}a/\pi = 4 \quad (N = 122,886)$	$0.3\lambda_{\mathrm{S}}$	$1.4\,10^{-2}$	$4.4\,10^{-3}$	$2.3\,10^{-2}$	$5.6\,10^{-3}$
	$0.2\lambda_{\mathrm{S}}$	$1.4\,10^{-2}$	$4.2\,10^{-3}$	$2.0\,10^{-2}$	$5.2\,10^{-3}$
	$0.1\lambda_{\mathrm{S}}$	$1.7\,10^{-2}$	$1.5\,10^{-2}$	$4.6\,10^{-2}$	$6.8\,10^{-3}$
	$0.05\lambda_{\mathrm{S}}$	$1.4\,10^{-1}$	$6.8\,10^{-2}$	$2.6\,10^{-1}$	$4.6\,10^{-2}$
	$0.02\lambda_{\mathrm{S}}$	$5.8\,10^{-1}$	$3.5\,10^{-1}$	$6.0\,10^{-1}$	$2.1\,10^{-1}$

a semi-spherical canyon, the scattering of an oblique incident plane P–wave by a semi-ellipsoidal canyon and the diffraction of an oblique incident plane SV–wave by a semi-spherical canyon. The first case is essentially 2-D (axisymmetry), whereas the last two are fully 3-D.

Semi-spherical canyon and vertically incident P–wave. First, the diffraction of a vertically incident plane P–wave by a semi-spherical canyon is considered (i.e. $b = a$, see Fig. 2.21), with

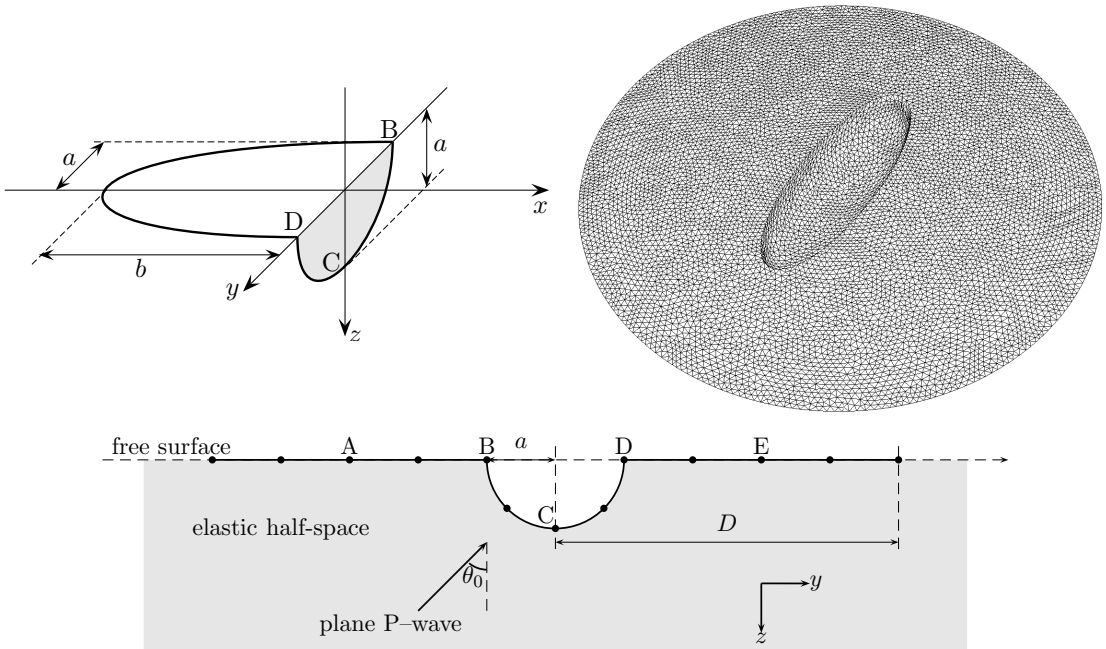

Figure 2.21: *Diffraction of an oblique incident plane P–wave by a semi-ellipsoidal canyon: notation (top left and bottom); sample BEM mesh, with $N = 25,788$ (top right).*

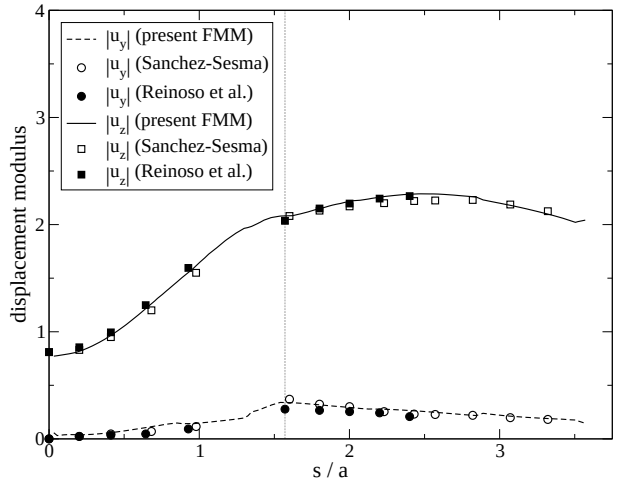

Figure 2.22: *Diffraction of an incident plane P–wave by a semi-spherical canyon: horizontal and vertical computed displacement on line CDE (with points C, D, E defined on Fig. 2.21) plotted against normalized arc-length coordinate s/a along CDE (normalized frequency $k_{\mathrm{P}}a/\pi = 0.25$). Comparison of present FMM solution to results from Sánchez-Sesma [183] and Reinoso et al. [169].*

$\nu = 0.25$. A right-handed Cartesian frame (x, y, z) is defined so that the elastic half-space occupies the region $\{(x, y, z) \,|\, z \geq 0\}$. The plane wave travels along direction $\sin\theta_0 \boldsymbol{e}_y - \cos\theta_0 \boldsymbol{e}_z$. Results obtained by the present FM-BEM for the (low) normalized frequency $k_{\mathrm{P}}a/\pi = 0.25$, by means of a BE mesh featuring $N = 23,382$ DOFs, are compared to corresponding results from [183] (based on a semi-analytical approach) and [169] (obtained using a standard elastodynamic BEM). In this case, the subdivision-stopping threshold used is $d^{\min} = 0.15\lambda_{\mathrm{S}}$, resulting in a leaf level $\bar{\ell} = 3$. Figure 2.22 shows that the horizontal and vertical displacements along line CDE (with points C, D, E defined in Fig. 2.21) produced by the three approaches are in good agreement. Note that the corresponding results in [183, 169] are plotted against the horizontal coordinate y, whereas the arc-length coordinate s along ABC is used in Fig. 2.22. The same value $D = 3a$ of the truncation radius has been used for all three sets of results. The present computation required 7 GMRES iterations and 24 s of CPU time per iteration.

Moreover, the FM-BEM allows to deal with non-dimensional frequencies significantly higher than those considered in previous studies. Figure 2.23 shows the displacements along line ABC computed for a nondimensional frequency $k_{\mathrm{P}}a/\pi = 5$ using the present method. This time, the problem size $N = 287,946$ is well beyond the capabilities of standard BEM. This computation, performed with a leaf level $\bar{\ell} = 6$, required 86 GMRES iterations (without preconditioning) and 162 s CPU time per iteration. The displacement near the canyon edge (i.e. $y = a$ and $s = \pi a/2$, see Fig. 2.21) has strong variations, as expected.

The size of the problems that can be solved is now limited by the number of iterations of the iterative solver. The number of iterations required for convergence of the GMRES solver, reported in Table 2.7 for various problem sizes N and (non-dimensional) frequencies $k_{\mathrm{P}}a/\pi$, clearly depend on both N and $k_{\mathrm{P}}a/\pi$. Reducing the iteration count requires a preconditioning strategy. This critical component of the development of efficient FM-BEM algorithms is addressed in Section 4.1.

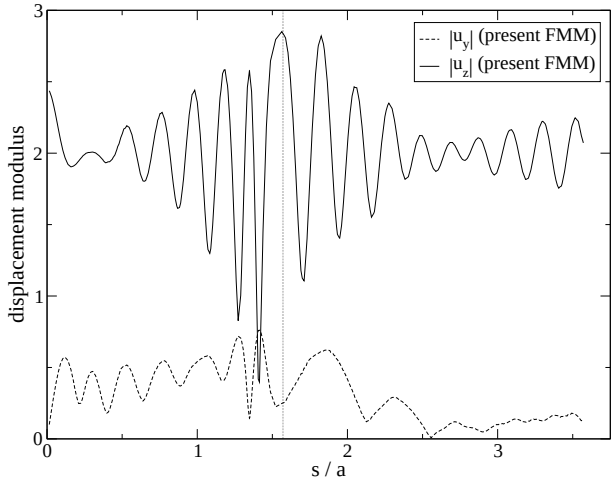

Figure 2.23: *Diffraction of an incident plane P–wave by a semi-spherical canyon: horizontal and vertical computed displacement on line CDE (with points C, D, E defined on Fig. 2.21) plotted against normalized arc-length coordinate s/a along CDE (normalized frequency $k_{\mathrm{P}}a/\pi = 5$).*

Table 2.7: *Diffraction of a plane P–wave by a semi-spherical canyon: number of GMRES iterations for various truncation radii D and nondimensional frequencies $k_{\mathrm{P}}a/\pi$ with, in parentheses, the corresponding problem sizes N.*

	$k_{\mathrm{P}}a/\pi = 0.25$	$k_{\mathrm{P}}a/\pi = 0.5$	$k_{\mathrm{P}}a/\pi = 0.75$	$k_{\mathrm{P}}a/\pi = 1.5$	$k_{\mathrm{P}}a/\pi = 5$	$k_{\mathrm{P}}a/\pi = 10$
$D = 3a$	7 (23,382)	10 (23, 382)	12 (23, 382)	19 (23, 382)	86 (287, 946)	> 280 (1, 145, 700)
$D = 5a$	7 (61, 875)	10 (61, 875)	15 (61, 875)	28 (61, 875)	159 (774, 180)	
$D = 7a$	8 (77, 565)	13 (77, 565)	17 (77, 565)	43 (77, 565)		
$D = 20a$	14 (98, 844)	39 (98, 844)	43 (98, 844)			

Semi-ellipsoidal canyon and oblique incident P–wave. A fully three-dimensional configuration is considered, namely the scattering of an oblique incident P–wave by a semi-ellipsoidal canyon (with $b = 3a$ and $\theta_0 = \pi/6$, see Fig. 2.21), with $\nu = 1/3$. A right-handed Cartesian frame (x, y, z) is defined so that the elastic half-space occupies the region $\{(x, y, z) \mid z \geq 0\}$. The plane wave travels along direction $\sin\theta_0 \boldsymbol{e}_y - \cos\theta_0 \boldsymbol{e}_z$. This problem has been previously studied in [73] by means of a wave function expansion and, for low frequencies, in [169] using a standard BEM. Results obtained by the present FM-BEM for the (low) normalized frequency $k_{\mathrm{S}}a/\pi = 0.5$, by means of a BE mesh featuring $N = 25,788$ DOFs shown in Fig. 2.21, are compared to corresponding numerical results from [169]. Figure 2.24 shows that the horizontal and vertical displacements produced by both approaches, plotted against the normalized arc-length coordinate s/a along line ABCDE (with points A, B, C, D, E defined on Fig. 2.21), are in good agreement. The present computation (featuring a truncation radius $D = 6a$ and a leaf level $\bar{\ell} = 3$) required 11 GMRES iterations (without preconditioning) and 9 s of CPU time per iteration.

Finally, results obtained using the present FM-BEM for a higher frequency defined by $k_{\mathrm{S}}a/\pi = 2$ are presented in terms of the y and z components of the displacement field (Fig. 2.25).

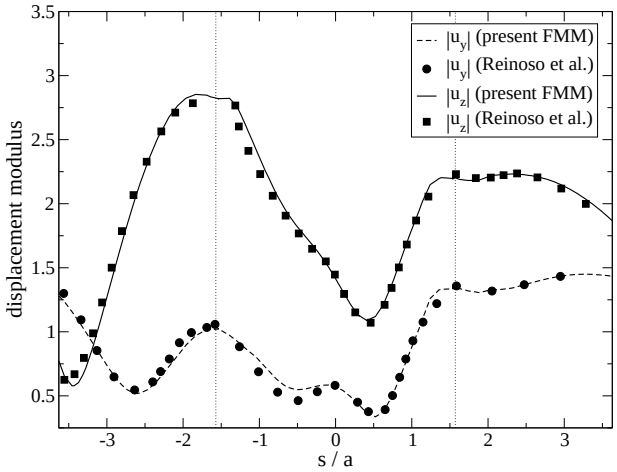

Figure 2.24: *Diffraction of an oblique incident plane P–wave by a semi-ellipsoidal canyon: horizontal and vertical computed displacement on line ABCDE (with points A, B, C D, E defined on Fig. 2.21) plotted against normalized arc-length coordinate s/a along ABCDE (normalized frequency $k_S a/\pi = 0.5$). Comparison of present FMM solution to results from Reinoso et al. [169].*

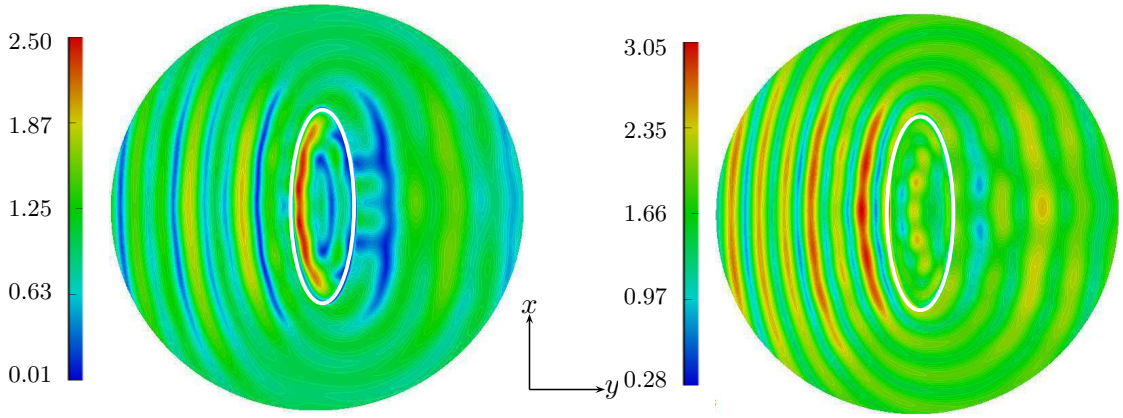

Figure 2.25: *Diffraction of an oblique incident plane P–wave by a semi-ellipsoidal canyon: horizontal (left) and vertical (right) computed displacement on the canyon surface and meshed part of free surface (normalized frequency $k_S a/\pi = 2$). The white ellipse depicts the canyon edge.*

The problem size is $N = 353,232$. The computation, performed with a leaf level $\bar{\ell} = 5$, required 32 GMRES iterations (without preconditioning) and 143 s of CPU time per iteration.

Semi-spherical canyon and oblique incident SV–wave Finally, the diffraction of an oblique incident plane SV–wave by a semi-spherical canyon (Fig. 2.26) is now considered. A right-handed Cartesian frame (x, y, z) is defined so that the elastic half-space occupies the region $\{(x, y, z) \mid z \leq 0\}$. The plane wave travels along direction $\sin\theta_0 \boldsymbol{e}_y + \cos\theta_0 \boldsymbol{e}_z$. This example has been treated, for a

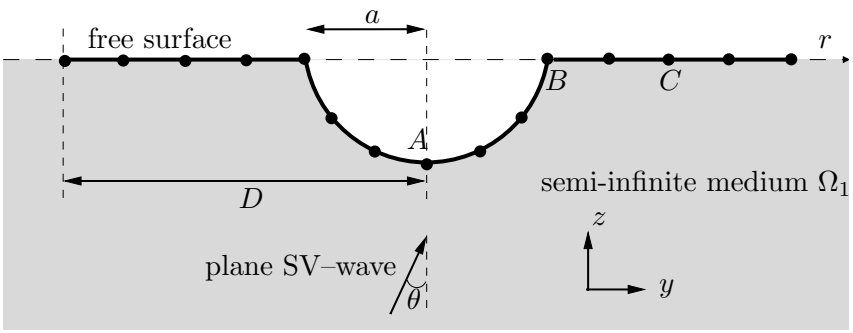

Figure 2.26: *Diffraction of an oblique incident plane SV–wave by a semi-spherical canyon: notations.*

normalized frequency of $k_S a/\pi = 0.75$ and with $\nu = 1/3$, by Eshraghi and Dravinski [73] ($\theta = 0°$) and Reinoso et al. [169] ($\theta = 0°, 30°$). The semi-spherical surface of the canyon (of radius a) and the surrounding portion of free surface lying inside a disk of radius $D > a$ are discretized using boundary elements. Table 2.8 reports the number of DOFs, the size of the leaf cells and the leaf level $\bar{\ell}$ used for this problem, along with the CPU time per iteration and iteration counts recorded.

Table 2.8: *Diffraction of an incident plane SV–wave by a semi-spherical canyon: data and computational results.*

D	N	$d^{\min}/\lambda_S$	$\bar{l}$	CPU time (s)	nb iter 0°	nb iter 30°
$2.5a$	$7,602$	0.23	3	1.5	8	11

For the case $\theta = 0°$, the horizontal and vertical computed displacements along line ABC (with points A, B, C defined in Fig. 2.26), plotted against normalized arc-length coordinate s/a, are seen in Fig. 2.27 to agree well with the results of Eshraghi et al. [73]. In this case, the truncation radius D is set to $2.5a$. For the case $\theta = 30°$, the results obtained using FMM are compared to those of Eshraghi et al. [73] and of Reinoso et al. [169] (Fig.2.28). The three sets of results are seen to be in good agreement. A possible explanation for the slight discrepancy between our results and those of Reinoso et al. [169] is the relatively poor graphical quality of the latter source.

2.6.4 Diffraction of an incident plane P–wave by a semi-ellipsoidal canyon: time-domain results

The present elastodynamic FM-BEM can also be used to deal with time-domain (i.e. transient) problems, via Fourier synthesis, taking advantage of the accelerated BEM at each sampling frequency. The time-domain response of the diffraction of a plane P–wave by a semi-ellipsoidal canyon is now considered to illustrate this procedure.

Problem definition

This example is concerned with the diffraction by a semi-ellipsoidal canyon ($b = 2a$) of a vertically incident plane P–wave of unit amplitude travelling in an elastic half space (see Fig. 2.21). The

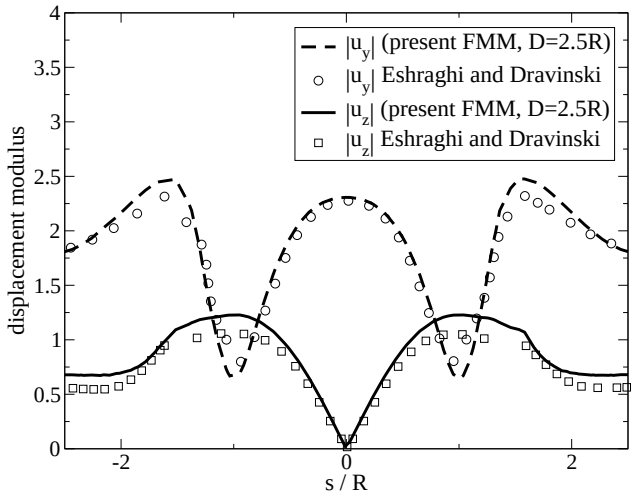

Figure 2.27: *Diffraction of an incident ($\theta = 0°$) plane SV–wave by a semi-spherical canyon: Comparison of horizontal and vertical computed displacements for $D = 2.5a$, against normalized arc-length coordinate s/a along ABC (normalized frequency $k_S a/\pi = 0.75$) with results of Eshraghi and Dravinski [73].*

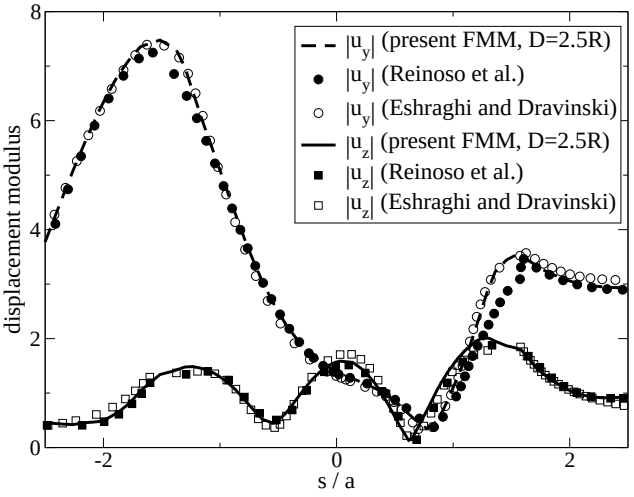

Figure 2.28: *Diffraction of an oblique ($\theta = 30°$) incident plane SV–wave by a semi-spherical canyon: Comparison of horizontal and vertical computed displacements for $D = 2.5a$, against normalized arc-length coordinate s/a along ABC (normalized frequency $k_S a/\pi = 0.75$) with results of Eshraghi and Dravinski [73] and Reinoso et al. [169].*

truncation radius is $D = 8a$. This configuration, has been studied in the time domain in [49] using a standard BEM. The mechanical parameters are defined as follows: $c_s = 1$ m.s^{-1}, $c_p = 2$ m.s^{-1}, $\mu = 1$ Pa and $\nu = 1/3$.

Synthesis of the time-domain solution

The time-domain response is computed using an inverse Fourier transform:

$$\boldsymbol{u}(\boldsymbol{x},t) = \mathcal{F}^{-1}\Big(\tilde{\boldsymbol{u}}(\boldsymbol{x},\omega)s(\omega)\Big)$$

where $\tilde{\boldsymbol{u}}(\boldsymbol{x},\omega)$ is the frequency-domain solution and $s(\omega)$ is the source spectrum. In practice, a Fast Fourier Transform is used to synthetize the time-domain results. In the following, the source spectrum is a first order Ricker wavelet:

$$\begin{aligned} \boldsymbol{s}(t) &= \Big(-2\pi^2\frac{(t-t_s)}{t_p^2}\Big)\exp\Big[-\pi^2\frac{(t-t_s)^2}{t_p^2}\Big], \\ \Rightarrow \quad \boldsymbol{s}(\omega) &= \frac{-i\omega t_p^3\sqrt{\pi}}{2\pi^3}\exp\Big[-i\omega t_s\Big]\exp\Big[\frac{-\omega^2 t_p^2}{4\pi^2}\Big]. \end{aligned} \tag{2.36}$$

where t_s is the time related to the maximum amplitude of the wavelet and t_p is the predominant period of the signal. The predominant frequency of such signal is $f_0 = 1/\sqrt{2}t_p$.

Scattering of a vertically incident plane P–wave by a semi-ellipsoidal canyon

To allow comparisons, the predominant frequency of the source is set to a relatively low value: $f_0 = 0.2$ Hz ($t_p = t_s = 5$ s). In this example, the mesh features $N = 73,320$ DOFs.

Frequency parametrization. Results are computed for frequencies ranging between 0 and 2 Hz (81 sample frequencies). Figure 2.29 (resp. Figure 2.30) displays the z-component of the FMM- (resp. standard BEM-, from [49]) computed spectral displacement along the Ox (left) and Oy (right) axes for the sample frequencies. The maximum amplification along the Ox axis for the z-component is seen to be about 1.59 (free-surface effect being removed) and located at $f = 0.425$ Hz at the canyon center. The maximum amplification (about 1.75) for the z-component against the Oy axis is obtained at the canyon edges ($x/a = \pm 1$) for a lower frequency ($f = 0.35$ Hz).

Displacements against time. The time-domain results obtained from spectral responses are now presented. The z-component of the FMM and standard BEM [49] computed displacements along the Ox (resp. Oy) direction for $t \in [0, 16]$ are plotted in Fig. 2.31 (resp. Fig. 2.32). These results, visually compared with those previously published by [49], validate our implementation. We note on these figures that the time-domain amplification is lower than the spectral amplification. This is due to the fact that in the time domain, the propagation process also influences the signal duration. To investigate this parameter, we use the definition proposed in [205]. Because the integral $\int u^2 dt$ increases rapidly and then tends asymptotically to its final amplitude A, the interval of time between $5\%A$ and $95\%A$ results from "strong motion" and is used to define the signal duration. In Fig. 2.33, the integral $\int u_z^2 dt$ is displayed against time. The duration of displacement at the canyon center is estimated on that basis as about 4.45 s.

2.7 CONCLUSIONS

In this chapter, the Fast Multipole Method has been succesfully extended to 3-D elastodynamics in the frequency-domain. Combined with the BEM formulation, it permits to reduce the computational

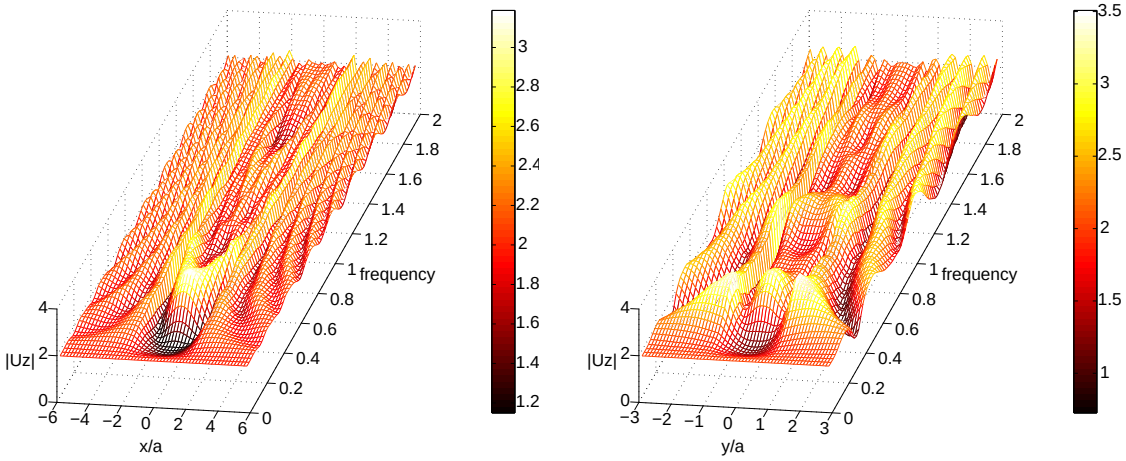

Figure 2.29: *Diffraction of a vertically incident plane P–wave by a semi-ellipsoidal canyon: z-component of the FMM computed displacement against the Ox (left) and Oy (right) axes for the sample frequencies.*

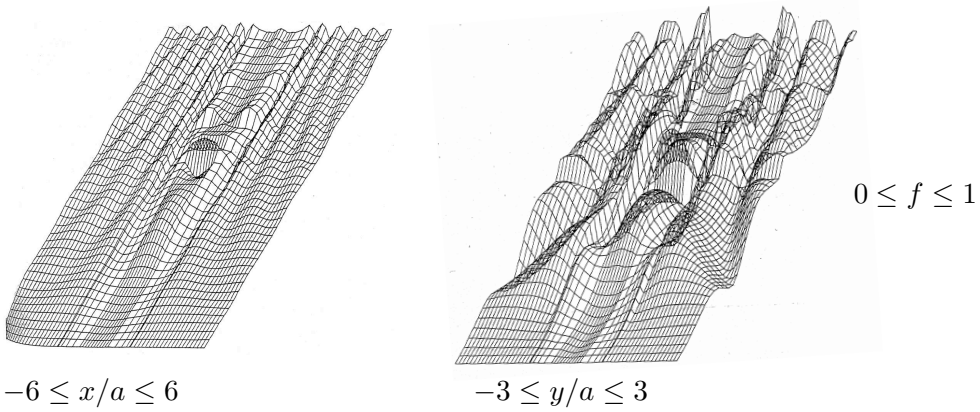

Figure 2.30: *Diffraction of a vertically incident plane P–wave by a semi-ellipsoidal canyon: z-component of the BEM computed displacement against the Ox (left) and Oy (right) axes for* 0 *Hz* $\leq f \leq 1$ *Hz (results from [49]).*

burden, in both CPU time and memory requirements, for the analysis of wave propagation (e. g. seismic), and allows to run BEM models of size $N = O(10^6)$ on an ordinary PC. Comparisons with analytical or previously published numerical results show the efficiency and accuracy of the present elastodynamic FM-BEM. Theoretical complexity estimates for both the single-level and multi-level formulations were derived and corroborated by numerical experiments. The formulation presented in this chapter is limited to the propagation in homogeneous semi-infinite elastic domains. Its extension to multi-region problems, based on a strong coupling of FM-BEM formulations for each region, is adressed next in Chapter 3.

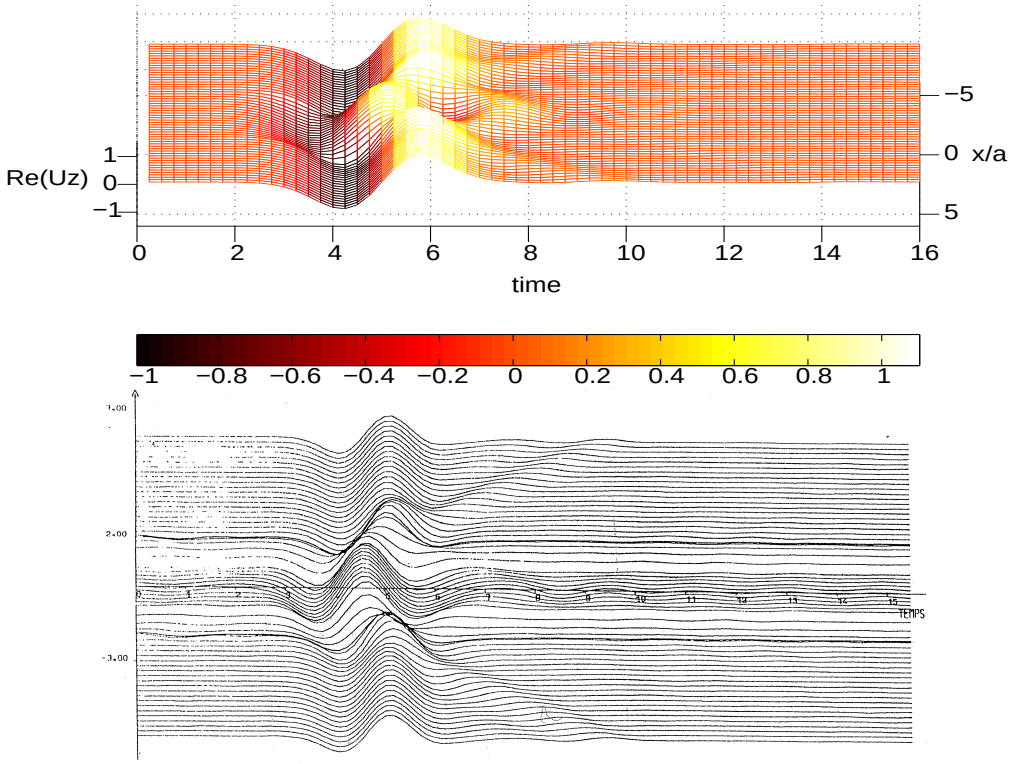

Figure 2.31: *Diffraction of a vertically incident plane P–wave by a semi-ellipsoidal canyon: z-component of FMM (top) and BEM (bottom, results from [49]) computed displacements on the Ox axis against time.*

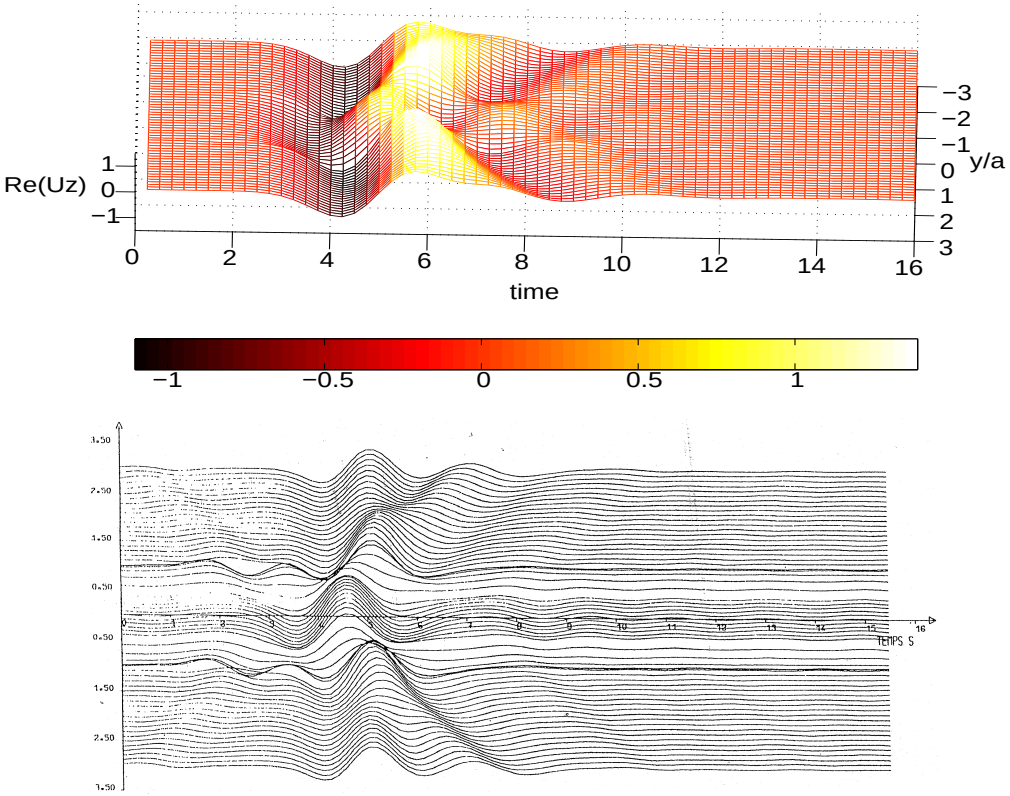

Figure 2.32: *Diffraction of a vertically incident plane P–wave by a semi-ellipsoidal canyon: z-component of FMM (top) and BEM (bottom, results from [49]) computed displacements on the Oy axis against time.*

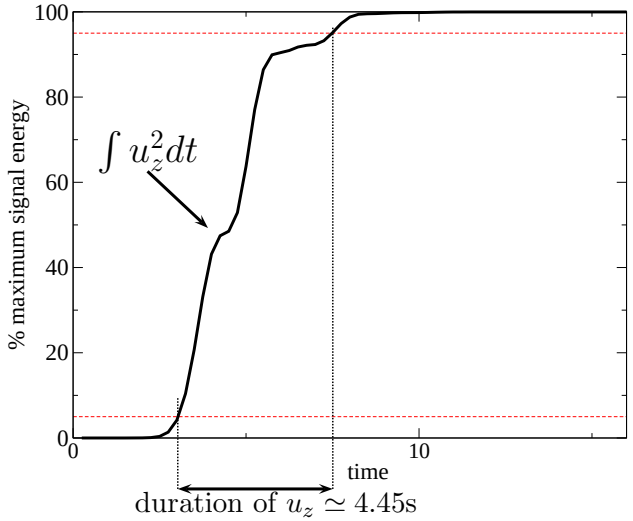

Figure 2.33: *Estimation of the signal duration for the z-component of displacement at the canyon center.*

Chapter 3

Multi-domain FM-BEM to model seismic wave propagation and amplification in 3-D geological structures

Contents

3.1 INTRODUCTION

In Chapter 2, the FM-BEM has been extended to elastodynamics in homogeneous semi-infinite domains and recent advances of FMM implementations for Maxwell equations [58] have been incorporated, allowing to run BEM models of size up to $N = O(10^6)$ on a single-processor PC. This chapter aims at extending the formulation of Chapter 2 to multi-domain situations, with emphasis on alluvial-basin configurations, by developing a FMM-based BE-BE coupling approach suitable for 3-D piecewise-homogeneous media.

This chapter is organized as follows. Section 3.2 presents the BEM formulation for seismic wave propagation in semi-infinite, piecewise-homogeneous media. Next, the FM-based BE-BE coupling strategy is presented in Section 3.3. In Section 3.4, a detailed discussion of several crucial implementation issues is given. Several examples representative of seismic wave propagation in 3-D alluvial basins are then presented in Section 3.5, including comparisons with available (low-frequency) results for various types of incident wavefields. In Section 3.6, time-domain results obtained by means of Fourier synthesis are also presented.

Single-region boundary element method. We begin by briefly summarizing existing concepts required for the multi-region FM-BEM. Let Ω denote a region of space occupied by an isotropic elastic solid characterized by μ (shear modulus), ν (Poisson's ratio) and ρ (mass density). A time-harmonic motion with circular frequency ω is assumed, and the implicit factor $e^{-i\omega t}$ will be systematically omitted. Typically, Ω is here one of the homogeneous subregions involved in the coupled BE-BE analysis to be developed. Assuming the absence of body forces, the displacement and traction over $\partial\Omega$ are related by the integral representation (2.1) yields the integral equation:

$$c_{ik}(\boldsymbol{x})u_i(\boldsymbol{x}) + (\text{P.V.})\int_{\partial\Omega} u_i(\boldsymbol{y})T_i^k(\boldsymbol{x},\boldsymbol{y};\omega)\mathrm{d}S_y - \int_{\partial\Omega} t_i(\boldsymbol{y})U_i^k(\boldsymbol{x},\boldsymbol{y};\omega)\mathrm{d}S_y = 0, \quad (\boldsymbol{x}\in\partial\Omega) \quad (3.1)$$

A subsequent boundary element discretization of the surface $\partial\Omega$ and boundary traces $(\boldsymbol{u},\boldsymbol{t})$ leads to the system:

$$[H]\{u\} + [G]\{t\} = 0, \quad (3.2)$$

where $[H]$ and $[G]$ are fully populated, nonsymmetric, matrices and vectors $\{u\}$, $\{t\}$ gather the displacement and traction degrees of freedom (DOFs). In this work, linear three-noded triangular boundary elements are used, together with a piecewise-linear continuous (i.e. isoparametric) interpolation for the displacements and a piecewise-constant interpolation of tractions. The coupling BE-BE formulation will essentially be based on a suitable combination of equations of type (3.2). Before going into the details of this formulation, it is necessary to investigate further equation (3.1) when applied to the semi-infinite configurations considered for basin problems.

3.2 CONTINUOUS BEM FORMULATIONS FOR SEISMIC WAVE PROPAGATION

In this section, the continuous BIE formulations for the propagation of seismic waves in complex geological structures (topographic irregularities, alluvial basins, ...) are presented. Such formulations, and their present implementation based on the multi-domain FM-accelerated BEM (Section 3.3), are geared towards geometrical configurations involving a semi-infinite homogeneous

reference medium with topographic irregularities and alluvial deposits (henceforth generically referred to as irregularities, Figs. 3.1 and 3.2). Although integral equation formulations for elastic-wave scattering in such configurations are not novel in their principle, they are rarely expounded in detail, hence our choice to devote this section to their comprehensive presentation for general geological configurations.

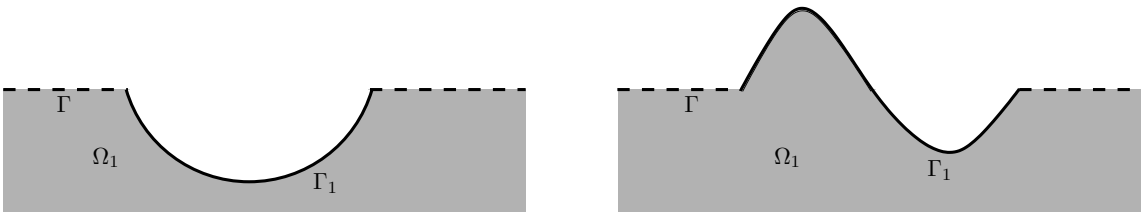

Figure 3.1: *Propagation of seismic waves through topographic irregularities (canyons, hills, ...): various geometries and related notations.*

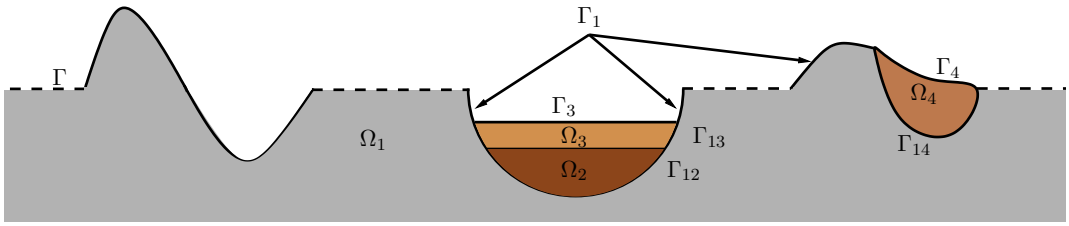

Figure 3.2: *Propagation of seismic waves in complex geological structures (alluvial deposits, basins): various geometries and related notations.*

In the following, Ω_F denotes the free half-space $\{\boldsymbol{x} = (x_1, x_2, x_3) \mid x_3 < 0\}$ bounded by the infinite traction-free surface $\Gamma_F = \{\boldsymbol{x} \mid x_3 = 0\}$ (Fig. 3.3). Configurations treated in this chapter are perturbations of the free half-space Ω_F, where irregularities occur only in a region of finite size. For such configurations, the displacement vector $\boldsymbol{u}$ is split into:

$$\boldsymbol{u} = \boldsymbol{u}^F + \boldsymbol{u}^S \tag{3.3}$$

where $\boldsymbol{u}^F$ characterizes the free-field, a known seismic wave in the reference free half-space Ω_F composed of the incident waves and those reflected from the planar free surface Γ_F, so that $\boldsymbol{t}^F = 0$ on Γ_F. The scattered displacement $\boldsymbol{u}^S$ then arises due to the presence of irregularities (Fig. 3.3). On any non-planar part of the free surface, one has $t^S + t^F = 0$.

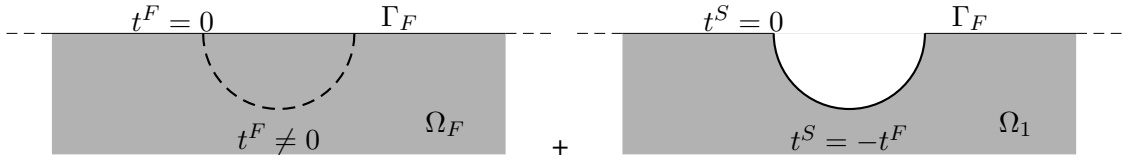

Figure 3.3: *Decomposition of the displacement and traction fields in the case of seismic waves.*

In the following, shorthand notations U_i^k and T_i^k are used instead of $U_i^k(\boldsymbol{x},\boldsymbol{y};\omega)$ and $T_i^k(\boldsymbol{x},\boldsymbol{y};\omega)$ for expository convenience.

3.2.1 Diffraction of incident waves by a topographic irregularity

The diffraction of an incident wave by topographic irregularities (e.g. a canyon), defined as deviations of the free surface from the infinite plane Γ_F, is first considered. Such configurations consist of a homogeneous semi-infinite medium occupying the domain Ω_1 situated below the infinite traction-free surface $\partial\Omega_1 = \Gamma \cup \Gamma_1$, where the bounded (and possibly non-connected) surface Γ_1 defines the topographic irregularities and $\Gamma = \partial\Omega_1 \cap \Gamma_F$ is the (unbounded) planar component of the free surface (Fig. 3.1). Because $\boldsymbol{u^S}$ and $\boldsymbol{t^S}$ satisfy the radiation condition at infinity [72, 141], it follows from (3.1) that the scattered field satisfies:

$$c_{ik}(\boldsymbol{x})u_i^S(\boldsymbol{x}) + \int_{\partial\Omega_1} \Big(u_i^S(\boldsymbol{y})T_i^k - t_i^S(\boldsymbol{y})U_i^k\Big)dS_y = 0,\ \forall \boldsymbol{x} \in \partial\Omega_1. \tag{3.4}$$

Incorporating the free-surface conditions $\boldsymbol{t}^S = \boldsymbol{0}$ (on Γ) and $\boldsymbol{t}^S + \boldsymbol{t}^F = \boldsymbol{0}$ (on Γ_1), equation (3.4) becomes:

$$c_{ik}(\boldsymbol{x})u_i^S(\boldsymbol{x}) + \int_{\partial\Omega_1} u_i^S(\boldsymbol{y})T_i^k dS_y = -\int_{\Gamma_1} t_i^F(\boldsymbol{y})U_i^k dS_y,\ \forall \boldsymbol{x} \in \partial\Omega_1. \tag{3.5}$$

The problem may thus be solved in terms of scattered wavefield only. To recover the total displacement, one may simply invoke the decomposition (3.3) in a post-processing step. However, for dealing next with the multi-domain problems arising when irregularities include deposits, the transmission conditions at the subdomain interfaces are best formulated in terms of total fields $\boldsymbol{u}, \boldsymbol{t}$. Anticipating this need, it is therefore useful to establish the counterpart of integral equation (3.5) formulated in terms of total fields.

To obtain the equation satisfied in Ω_1 by the total field, we consider the (bounded) complementary domain $\Omega_c = \Omega_c^+ \cup \Omega_c^-$ of Ω_1 relative to the half-space Ω_F, where $\Omega_c^- = \Omega_F \backslash (\Omega \cup \partial\Omega)$ and $\Omega_c^+ = \Omega \backslash (\Omega_F \cup \Gamma_F)$ are the parts of Ω_c situated below and above Γ_F, respectively (Fig. 3.4). In Ω_c^+, the displacements $\boldsymbol{u}^F(\boldsymbol{x})$ and tractions $\boldsymbol{t}^F(\boldsymbol{x})$ associated with the free-field satisfy the following equation:

$$c_{ik}^{c+}(\boldsymbol{x})u_i^F(\boldsymbol{x}) + \int_{\Gamma_{c1}^+ \cup \Gamma_c^+} u_i^F(\boldsymbol{y})T_i^k dS_y - \int_{\Gamma_{c1}^+} t_i^F(\boldsymbol{y})U_i^k dS_y = 0,\ \forall \boldsymbol{x} \in \partial\Omega_1 \tag{3.6}$$

where c_{ik}^{c+} denotes the free-term relative to Ω_c^+, having set $\Gamma_c^+ = \partial\Omega_c^+ \cap \Gamma_F$ and $\Gamma_{c1}^+ = \partial\Omega_c^+ \cap \Gamma_1$, and in which the free-surface condition is incorporated. Using similar notation, the corresponding integral equation associated with the free field in Ω_c^- reads:

$$c_{ik}^{c-}(\boldsymbol{x})u_i^F(\boldsymbol{x}) + \int_{\Gamma_{c1}^- \cup \Gamma_c^-} u_i^F(\boldsymbol{y})T_i^k dS_y - \int_{\Gamma_{c1}^-} t_i^F(\boldsymbol{y})U_i^k dS_y = 0,\ \forall \boldsymbol{x} \in \partial\Omega_1 \tag{3.7}$$

where c_{ik}^{c-} denotes the free-term relative to Ω_c^-.

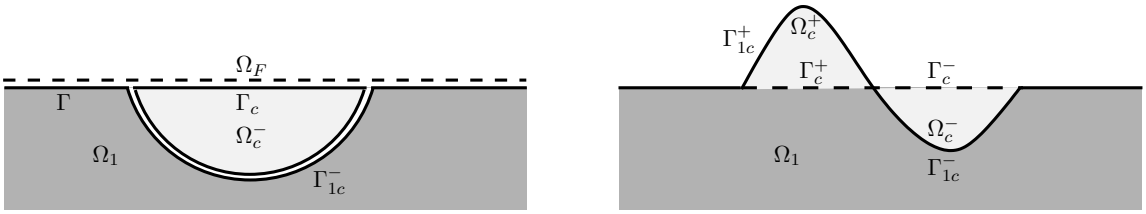

Figure 3.4: *Definition of the complementary domain $\Omega_c = \Omega_c^+ \cup \Omega_c^-$ for the determination of the total field in Ω_1.*

On setting $\Gamma_1 = \Gamma_{1c}^+ \cup \Gamma_{c1}^-$ in (3.4), performing the combination (3.4) + (3.6) - (3.7) and noting that pairs Γ_{c1}^-, Γ_{1c}^- and Γ_c^+, Γ_c define identical surfaces with opposite normals, one obtains:

$$c_{ik}(\boldsymbol{x})u_i^S(\boldsymbol{x}) - c_{ik}^{c-}(\boldsymbol{x})u_i^F(\boldsymbol{x}) + c_{ik}^{c+}(\boldsymbol{x})u_i^F(\boldsymbol{x}) + \int_{\Gamma_{1c}^+\cup\Gamma_{1c}^-} \Big(u_i^S(\boldsymbol{y}) + u_i^F(\boldsymbol{y})\Big) T_i^k dS_y$$
$$+ \int_{\Gamma} u_i^S(\boldsymbol{y}) T_i^k dS_y - \int_{\Gamma_c^+\cup\Gamma_c^-} u_i^F(\boldsymbol{y}) T_i^k dS_y - \int_{\Gamma_{1c}^+\cup\Gamma_{1c}^-} \Big(t_i^S(\boldsymbol{y}) + t_i^F(\boldsymbol{y})\Big) U_i^k dS_y = 0,$$
$$\forall \boldsymbol{x} \in \partial\Omega_1 \quad (3.8)$$

which is reformulated in terms of the total field by invoking decomposition (3.3):

$$\begin{aligned} c_{ik}(\boldsymbol{x})u_i(\boldsymbol{x}) \quad & + \int_{\Gamma_{1c}^+\cup\Gamma_{1c}^-} u_i(\boldsymbol{y}) T_i^k dS_y + \int_{\Gamma} u_i^S(\boldsymbol{y}) T_i^k dS_y - \int_{\Gamma_{1c}^+\cup\Gamma_{1c}^-} t_i(\boldsymbol{y}) U_i^k dS_y \\ & = c_{ik}^F(\boldsymbol{x})u_i^F(\boldsymbol{x}) + \int_{\Gamma_c^+\cup\Gamma_c^-} u_i^F(\boldsymbol{y}) T_i^k dS_y, \ \forall \boldsymbol{x} \in \partial\Omega_1 \end{aligned} \quad (3.9)$$

having set $c_{ik}^F(\boldsymbol{x}) = c_{ik}^{c-}(\boldsymbol{x}) - c_{ik}^{c+}(\boldsymbol{x}) + c_{ik}(\boldsymbol{x})$. To evaluate $c_{ik}^F(\boldsymbol{x})$, six cases need to be considered for the location of $\boldsymbol{x}$ on $\partial\Omega_1$, as indicated on Fig. 3.5:

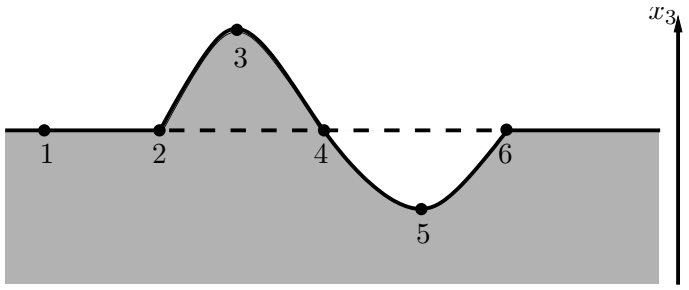

Figure 3.5: *Diffraction of a seismic wave by a canyon: various cases for the location of $\boldsymbol{x} \in \partial\Omega_1$ considered for the computation of the free term.*

$$
\begin{aligned}
&\text{case 1:} \quad c_{ik}(\boldsymbol{x}) = \tfrac{1}{2}\delta_{ik}, && c_{ik}^{c-}(\boldsymbol{x}) = c_{ik}^{c+}(\boldsymbol{x}) = 0,\\
&\text{case 2:} \quad -c_{ik}^{c+}(\boldsymbol{x}) + c_{ik}(\boldsymbol{x}) = \tfrac{1}{2}\delta_{ik}, && c_{ik}^{c-}(\boldsymbol{x}) = 0,\\
&\text{case 3:} \quad -c_{ik}^{c+}(\boldsymbol{x}) + c_{ik}(\boldsymbol{x}) = 0, && c_{ik}^{c-}(\boldsymbol{x}) = 0,\\
&\text{case 4:} \quad c_{ik}^{c-}(\boldsymbol{x}) - c_{ik}^{c+}(\boldsymbol{x}) + c_{ik}(\boldsymbol{x}) = \tfrac{1}{2}\delta_{ik}, &&\\
&\text{case 5:} \quad c_{ik}^{c-}(\boldsymbol{x}) + c_{ik}(\boldsymbol{x}) = \delta_{ik}, && c_{ik}^{c+}(\boldsymbol{x}) = 0,\\
&\text{case 6:} \quad c_{ik}^{c-}(\boldsymbol{x}) + c_{ik}(\boldsymbol{x}) = \tfrac{1}{2}\delta_{ik}, && c_{ik}^{c+}(\boldsymbol{x}) = 0.
\end{aligned}
$$

It follows that the combination $c_{ik}^{F}(\boldsymbol{x})$ has just three possible values, depending on the position of $\boldsymbol{x}$ relative to Γ_F:

$$
c_{ik}^{F}(\boldsymbol{x}) = 0 \ (x_3 > 0), \quad c_{ik}^{F}(\boldsymbol{x}) = \frac{1}{2}\delta_{ik} \ (x_3 = 0), \quad c_{ik}^{F}(\boldsymbol{x}) = \delta_{ik} \ (x_3 < 0), \tag{3.10}
$$

i.e. $c_{ik}^{F}(\boldsymbol{x})$ is identical to the usual free-term relative to the half-space Ω_F without irregularity. Finally, it is necessary for practical implementation purposes to introduce a truncated version $\Gamma(D)$ of the free surface Γ, here bounded by a circle of radius D, which will support the BE discretization. The integral in the left-hand side of eq. (3.11) below is known to be convergent in the limit $\Gamma(D) \to \Gamma$, hence so is the right-hand side:

$$
\int_{\Gamma(D)} u_i^S(\boldsymbol{y}) T_i^k dS_y = \int_{\Gamma(D)} u_i(\boldsymbol{y}) T_i^k dS_y - \int_{\Gamma(D)} u_i^F(\boldsymbol{y}) T_i^k dS_y. \tag{3.11}
$$

Incorporing (3.11) into (3.9), it follows:

$$
\begin{aligned}
c_{ik}(\boldsymbol{x}) u_i(\boldsymbol{x}) + \int_{\Gamma_1 \cup \Gamma(D)} u_i(\boldsymbol{y}) T_i^k dS_y - \int_{\Gamma_1} t_i(\boldsymbol{y}) U_i^k dS_y = c_{ik}^{F}(\boldsymbol{x}) u_i^F(\boldsymbol{x}) \\
+ \int_{\Gamma_F(D)} u_i^F(\boldsymbol{y}) T_i^k dS_y, \forall \boldsymbol{x} \in \partial\Omega_1
\end{aligned} \tag{3.12}
$$

where $c_{ik}^{F}(\boldsymbol{x})$ is defined by eq. (3.10), $\Gamma_F(D)$ is the truncated version of Γ_F, and strict equality occurs only in the limiting case $D \to +\infty$.

We emphasize that reformulation (3.12) of integral equation (3.5) is not necessary for adressing configurations featuring only topographical irregularities (e.g. the canyon problem of Chapter 2). It will, however, be very useful for the present BE-BE coupling approach, as transmission condition are written in terms of total fields.

3.2.2 Propagation of incident waves in alluvial basins

Of primary interest in this chapter is the propagation of an incident wave in an alluvial basin, leading to a multi-domain BEM formulation. Accordingly, let Ω_1 denote a semi-infinite homogeneous medium possibly featuring a topographic irregularity of finite spatial extension. Other materials (e.g. sediments) occupy $(n-1)$ bounded regions Ω_i $(2 \leq i \leq n)$ such that $\Omega_1 \cap \Omega_i = \emptyset$ (Fig. 3.2).

In the following, $\Gamma = \partial\Omega_1 \cap \Gamma_F$ denotes the (unbounded) portion of planar free surface intercepted by Ω_1, Γ_i $(i = 1, \ldots, n)$ denotes the (bounded) portion of $\partial\Omega_i$ situated on the free surface but not included in Γ (so that the disjoint union $\Gamma \cup \Gamma_1 \cup \ldots \cup \Gamma_n$ constitutes the free surface) and Γ_{ij} denotes the interface between Ω_i and Ω_j so that one has $\partial\Omega_1 = \Gamma \cup \Gamma_1 \cup \Gamma_{12} \cup \ldots \cup \Gamma_{1n}$ and $\partial\Omega_i = \Gamma_i \cup \Gamma_{i1} \cup \ldots \cup \Gamma_{in}$ $(i \geq 2)$. For subregions Ω_i, Ω_j that do not share interfaces, one

has of course $\Gamma_{ij} = \emptyset$. $\boldsymbol{t}^{ij}$ denotes the traction vector on Γ_{ij}, conventionally defined in terms of the normal $\boldsymbol{n}_{ij}$ oriented from Ω_i to Ω_j (Fig. 3.6); hence $\boldsymbol{t}^{ij} = -\boldsymbol{t}^{ji}$ with this convention. The governing equation for the total field in Ω_1 is (3.12) where Γ_1 is replaced with $\Gamma_1 \cup \Gamma_{12} \cup \ldots \cup \Gamma_{1n}$, i.e.:

$$c_{ik}(\boldsymbol{x})u_i(\boldsymbol{x}) + \int_{\Gamma_1 \cup \Gamma(D)} u_i^1(\boldsymbol{y})T_i^{k(1)}dS_y + \sum_{m=2}^{n}\Big(\int_{\Gamma_{1m}} u_i^{1m}(\boldsymbol{y})T_i^{k(1)}dS_y\Big) - \int_{\Gamma_1} t_i^1(\boldsymbol{y})U_i^{k(1)}dS_y$$
$$- \sum_{m=2}^{n}\Big(\int_{\Gamma_{1m}} t_i^{1m}(\boldsymbol{y})U_i^{k(1)}dS_y\Big) = c_{ik}^F(\boldsymbol{x})u_i^F(\boldsymbol{x}) + \int_{\Gamma_F(D)} u_i^F(\boldsymbol{y})T_i^{k(1)}dS_y,\ \forall \boldsymbol{x} \in \partial\Omega_1 \tag{3.13}$$

where $U_i^{k(1)}$ and $T_i^{k(1)}$ are the fundamental solutions defined in terms of the material parameters of Ω_1. In the free-term of (3.13), $u_i(\boldsymbol{x})$ stands for either $u_i^1(\boldsymbol{x})$ or $u_i^{1m}(\boldsymbol{x})$, according to whether the collocation point $\boldsymbol{x}$ lies on Γ_1 or Γ_{1m}.

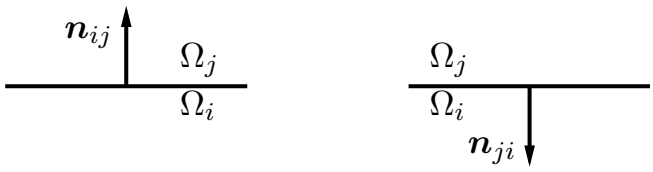

Figure 3.6: *Normals for the definition of the traction unknowns.*

The total field in subdomain Ω_ℓ ($\ell > 1$) is governed by the integral equation:

$$c_{ik}(\boldsymbol{x})u_i(\boldsymbol{x}) + \int_{\Gamma_\ell} u_i^\ell(\boldsymbol{y})T_i^{k(\ell)}dS_y + \sum_{\substack{m\geq 1\\ m\neq \ell}}\int_{\Gamma_{\ell m}}\Big(u_i^{\ell m}(\boldsymbol{y})T_i^{k(\ell)} - t_i^{\ell m}(\boldsymbol{y})U_i^{k(\ell)}\Big)dS_y = 0,$$
$$\forall \boldsymbol{x} \in \partial\Omega_\ell\ (2 \leq \ell \leq n) \tag{3.14}$$

where $U_i^{k(\ell)}$ and $T_i^{k(\ell)}$ denote the fundamental solutions defined in terms of the constitutive parameters of Ω_ℓ, the free surface condition on Γ_ℓ has been taken into account, and $u_i(\boldsymbol{x})$ stands for either $u_i^\ell(\boldsymbol{x})$ or $u_i^{\ell m}(\boldsymbol{x})$ according to whether $\boldsymbol{x} \in \Gamma_\ell$ or $\boldsymbol{x} \in \Gamma_{\ell m}$. In addition, invoking transmission conditions

$$\boldsymbol{u}^{\ell m} = \boldsymbol{u}^{m\ell};\ \boldsymbol{t}^{\ell m} = -\boldsymbol{t}^{m\ell}, \tag{3.15}$$

which express perfect bonding at interfaces, allows to eliminate $\boldsymbol{u}^{m\ell}$, $\boldsymbol{t}^{m\ell}$ and retain $\boldsymbol{u}^{\ell m}$, $\boldsymbol{t}^{\ell m}$ ($\ell < m$) as the interfacial unknowns. Equations (3.14) thus become:

$$c_{ik}(\boldsymbol{x})u_i(\boldsymbol{x}) + \int_{\Gamma_\ell} u_i^\ell(\boldsymbol{y})T_i^{k(\ell)}dS_y + \sum_{m=2}^{\ell-1}\int_{\Gamma_{\ell m}}\Big(u_i^{m\ell}(\boldsymbol{y})T_i^{k(\ell)} + t_i^{m\ell}(\boldsymbol{y})U_i^{k(\ell)}\Big)dS_y$$
$$+ \sum_{m=\ell+1}^{n}\int_{\Gamma_{\ell m}}\Big(u_i^{\ell m}(\boldsymbol{y})T_i^{k(\ell)} - t_i^{\ell m}(\boldsymbol{y})U_i^{k(\ell)}\Big)dS_y = 0,\ \forall \boldsymbol{x} \in \partial\Omega_\ell,\ (2 \leq \ell \leq n). \tag{3.16}$$

The coupled BE-BE formulation to be presented next will then be based on combining discrete versions of equation (3.13) and equations (3.16) written for each subregion Ω_ℓ ($\ell \geq 2$). It is similar to the one used for two subdomains in [90], but more general as (i) it is applicable to an arbitrary number of subdomains and (ii) it accomodates irregularities going *above* or *through* the free surface (Fig. 3.5).

3.3 FM-ACCELERATED BE-BE COUPLING STRATEGY

The present discrete coupled BE-BE formulation is based on three-noded triangular boundary elements, piecewise-linear interpolation of displacements, and piecewise-constant interpolation of tractions. Since only Neumann or transmission boundary conditions are considered here, the displacement is unknown at all mesh nodes, while the traction is unknown on each interfacial element. The proposed BE-BE coupling formulation is designed so as to invoke single-region FM-BEM computations in "black-box" fashion (here using the elastodynamic FM-BEM formulation presented in Chapter 2). To this end, a boundary integral equation is formulated for each subregion Ω_i (with material properties assumed homogeneous in each Ω_i) following Sec. 3.2.2, and discrete BE equations are generated by using (i) all displacement nodes and (ii) all interfacial element centers as collocation points ((i) and (ii) will subsequently be referred to as "nodal collocation" and "element collocation", respectively). Each subregion is treated separately, using a separate octree for FMM computations. The matrix-vector products arising in each of these integral equations can thus be evaluated using the FM-BEM procedure for homogeneous media presented in Chapter 2. The resulting algorithm is schematically described in Fig. 3.8.

The BE-BE coupling does not, however, just consist of concatenating all single-region BE equations into one global system of equations, as the latter would be overdetermined as a result. One way to ensure that the present BE-BE coupling defines a square global system of equations consists in judiciously defining linear combinations of BE equations generated at the subregion level, a treatment that can be done externally to the FM-BEM computations. Specifically, linear combinations of BE equations arising from collocation at (a) interfacial element centers relative to either subregion adjacent to that element, and (b) displacement nodes shared by more than one subregion, are defined. This approach ensures that the number of final global BE equations matches the number of unknown BE DOFs, i.e. is square. In particular, using this method, multiple displacement nodes are easily handled (see Fig. 3.7 for an example of triple points in the case of a two-layered basin).

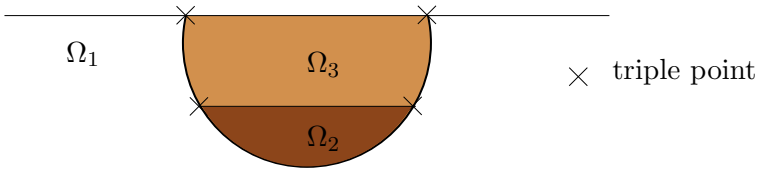

Figure 3.7: *Two-layered basin: definition of triple points.*

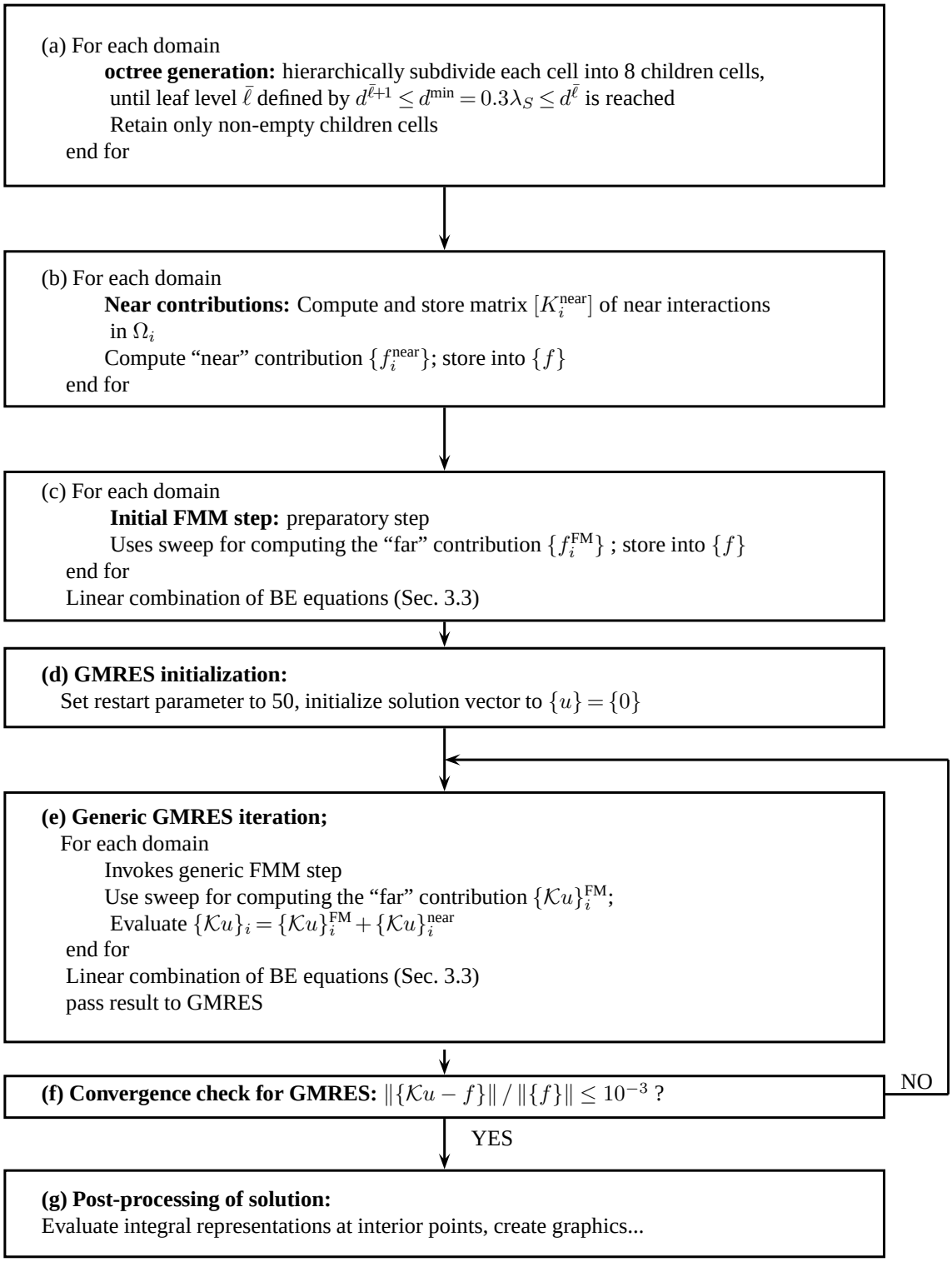

Figure 3.8: *Elastodynamic multi-domain multi-level FM-BEM: schematic description of overall algorithm.*

For the sake of definiteness, the above-outlined procedure is now going to be detailed for a representative configuration, namely the case of a two-layered basin (Fig. 3.7). First, integral equation (3.13) for the subdomain Ω_1 gives rise to the following set of equations:

$$H_1^1\boldsymbol{u}^1 + H_{12}^1\boldsymbol{u}^{12} + H_{13}^1\boldsymbol{u}^{13} + H_{123}^1\boldsymbol{u}^{123} - G_{12}^1\boldsymbol{t}^{12} - G_{13}^1\boldsymbol{t}^{13} - f^1 = 0, \tag{3.17a}$$

$$H_1^{12}\boldsymbol{u}^1 + H_{12}^{12}\boldsymbol{u}^{12} + H_{13}^{12}\boldsymbol{u}^{13} + H_{123}^{12}\boldsymbol{u}^{123} - G_{12}^{12}\boldsymbol{t}^{12} - G_{13}^{12}\boldsymbol{t}^{13} - f^{12} = 0, \tag{3.17b}$$

$$H_1^{13}\boldsymbol{u}^1 + H_{12}^{13}\boldsymbol{u}^{12} + H_{13}^{13}\boldsymbol{u}^{13} + H_{123}^{13}\boldsymbol{u}^{123} - G_{12}^{13}\boldsymbol{t}^{12} - G_{13}^{13}\boldsymbol{t}^{13} - f^{13} = 0, \tag{3.17c}$$

$$H_1^{123}\boldsymbol{u}^1 + H_{12}^{123}\boldsymbol{u}^{12} + H_{13}^{123}\boldsymbol{u}^{13} + H_{123}^{123}\boldsymbol{u}^{123} - G_{12}^{123}\boldsymbol{t}^{12} - G_{13}^{123}\boldsymbol{t}^{13} - f^{123} = 0, \tag{3.17d}$$

$$\bar{H}_1^{12}\boldsymbol{u}^1 + \bar{H}_{12}^{12}\boldsymbol{u}^{12} + \bar{H}_{13}^{12}\boldsymbol{u}^{13} + \bar{H}_{123}^{12}\boldsymbol{u}^{123} - \bar{G}_{12}^{12}\boldsymbol{t}^{12} - \bar{G}_{13}^{12}\boldsymbol{t}^{13} - \bar{f}^{12} = 0, \tag{3.17e}$$

$$\bar{H}_1^{13}\boldsymbol{u}^1 + \bar{H}_{12}^{13}\boldsymbol{u}^{12} + \bar{H}_{13}^{13}\boldsymbol{u}^{13} + \bar{H}_{123}^{13}\boldsymbol{u}^{123} - \bar{G}_{12}^{13}\boldsymbol{t}^{12} - \bar{G}_{13}^{13}\boldsymbol{t}^{13} - \bar{f}^{13} = 0. \tag{3.17f}$$

In equations (3.17a-d), notations H_β^γ (for generic single or multiple indices $\gamma,\ \beta$, e.g. $\gamma = 12$, $\beta = 123$) refer to the submatrices arising from BE discretization of the integral operator

$$\boldsymbol{c}(\boldsymbol{x}).\boldsymbol{u}(\boldsymbol{x}) + \int_{\partial\Omega_m} \boldsymbol{T}^{(m)}(\boldsymbol{x},\boldsymbol{y},\omega).\boldsymbol{u}(\boldsymbol{y})dS_y,$$

upon performing nodal collocation on Γ_γ and retaining only the columns corresponding to u^β. Following the same idea, submatrices $\bar{H}_\beta^\gamma$ are defined in terms of element collocation on Γ_γ instead of nodal collocation, and submatrices G_β^γ, $\bar{G}_\beta^\gamma$ similarly arise from the integral operator

$$\int_{\partial\Omega_m} \boldsymbol{U}^{(m)}(\boldsymbol{x},\boldsymbol{y},\omega).\boldsymbol{t}(\boldsymbol{y})dS_y.$$

Note that the subregion number m is encoded as the first index in γ. For instance, $\gamma = 123$ refers to collocation at triple points and relative to subregion Ω_1, and $\beta = 23$ refers to DOFs shared by $\partial\Omega_2$ and $\partial\Omega_3$. Finally, the right-hand sides $f^\gamma,\ \bar{f}^\gamma$ are obtained via (nodal or element) collocation of

$$\boldsymbol{c}(\boldsymbol{x}).\boldsymbol{u}^F(\boldsymbol{x}) + \int_{\Gamma_F(D)} \boldsymbol{T}^{(m)}(\boldsymbol{x},\boldsymbol{y},\omega).\boldsymbol{u}^F(\boldsymbol{y})dS_y.$$

Equations (3.17a,b,c,d) stem from nodal collocation on Γ_1, Γ_{12}, Γ_{12} and Γ_{123}, respectively, while equations (3.17e,f) stem from element collocation on Γ_{12} and Γ_{13}. Then, integral equation (3.16) for the subdomain Ω_2 gives rise to the block matrix equations:

$$H_{12}^{21}\boldsymbol{u}^{12} + H_{123}^{21}\boldsymbol{u}^{123} + G_{12}^{21}\boldsymbol{t}^{12} + H_{23}^{21}\boldsymbol{u}^{23} - G_{23}^{21}\boldsymbol{t}^{23} = 0, \tag{3.18a}$$

$$H_{12}^{213}\boldsymbol{u}^{12} + H_{123}^{213}\boldsymbol{u}^{123} + G_{12}^{213}\boldsymbol{t}^{12} + H_{23}^{213}\boldsymbol{u}^{23} - G_{23}^{213}\boldsymbol{t}^{23} = 0, \tag{3.18b}$$

$$H_{12}^{23}\boldsymbol{u}^{12} + H_{123}^{23}\boldsymbol{u}^{123} + G_{12}^{23}\boldsymbol{t}^{12} + H_{23}^{23}\boldsymbol{u}^{23} - G_{23}^{23}\boldsymbol{t}^{23} = 0, \tag{3.18c}$$

$$\bar{H}_{12}^{21}\boldsymbol{u}^{12} + \bar{H}_{123}^{21}\boldsymbol{u}^{123} + \bar{G}_{12}^{21}\boldsymbol{t}^{12} + \bar{H}_{23}^{21}\boldsymbol{u}^{23} - \bar{G}_{23}^{21}\boldsymbol{t}^{23} = 0, \tag{3.18d}$$

$$\bar{H}_{12}^{23}\boldsymbol{u}^{12} + \bar{H}_{123}^{23}\boldsymbol{u}^{123} + \bar{G}_{12}^{23}\boldsymbol{t}^{12} + \bar{H}_{23}^{23}\boldsymbol{u}^{23} - \bar{G}_{23}^{23}\boldsymbol{t}^{23} = 0, \tag{3.18e}$$

with (3.18a,b,c) produced by nodal collocation on Γ_{21}, Γ_{213} and Γ_{23}, respectively, and (3.18d,e) by element collocation on Γ_{21} and Γ_{23}. In the subdomain Ω_3, sets of linear matrix equations may be

defined as:

$$H_{13}^{31}\boldsymbol{u}^{13} + H_{123}^{31}\boldsymbol{u}^{123} + G_{13}^{31}\boldsymbol{t}^{13} + H_{23}^{31}\boldsymbol{u}^{23} + G_{23}^{31}\boldsymbol{t}^{23} + H_{3}^{31}\boldsymbol{u}^{3} = 0, \tag{3.19a}$$

$$H_{13}^{321}\boldsymbol{u}^{13} + H_{123}^{321}\boldsymbol{u}^{123} + G_{13}^{321}\boldsymbol{t}^{13} + H_{23}^{321}\boldsymbol{u}^{23} + G_{23}^{321}\boldsymbol{t}^{23} + H_{3}^{321}\boldsymbol{u}^{3} = 0, \tag{3.19b}$$

$$H_{13}^{32}\boldsymbol{u}^{13} + H_{123}^{32}\boldsymbol{u}^{123} + G_{13}^{32}\boldsymbol{t}^{13} + H_{23}^{32}\boldsymbol{u}^{23} + G_{23}^{32}\boldsymbol{t}^{23} + H_{3}^{32}\boldsymbol{u}^{3} = 0, \tag{3.19c}$$

$$H_{13}^{3}\boldsymbol{u}^{13} + H_{123}^{3}\boldsymbol{u}^{123} + G_{13}^{3}\boldsymbol{t}^{13} + H_{23}^{3}\boldsymbol{u}^{23} + G_{23}^{3}\boldsymbol{t}^{23} + H_{3}^{3}\boldsymbol{u}^{3} = 0, \tag{3.19d}$$

$$\bar{H}_{13}^{31}\boldsymbol{u}^{13} + \bar{H}_{123}^{31}\boldsymbol{u}^{123} + \bar{G}_{13}^{31}\boldsymbol{t}^{13} + \bar{H}_{23}^{31}\boldsymbol{u}^{23} + \bar{G}_{23}^{31}\boldsymbol{t}^{23} + \bar{H}_{3}^{31}\boldsymbol{u}^{3} = 0, \tag{3.19e}$$

$$\bar{H}_{13}^{32}\boldsymbol{u}^{13} + \bar{H}_{123}^{32}\boldsymbol{u}^{123} + \bar{G}_{13}^{32}\boldsymbol{t}^{13} + \bar{H}_{23}^{32}\boldsymbol{u}^{23} + \bar{G}_{23}^{32}\boldsymbol{t}^{23} + \bar{H}_{3}^{32}\boldsymbol{u}^{3} = 0, \tag{3.19f}$$

where equations (3.19a,b,c,d) stem from nodal collocation on Γ_{31}, Γ_{321}, Γ_{32} and Γ_3, respectively, while equations (3.19e,f) stem from element collocation on Γ_{31} and Γ_{32}. As previously pointed out, the set of equations (3.17a-f), (3.18a-e), (3.19a-f) is overdetermined. A square linear system of equations is obtained by setting up linear combinations of equations associated with the same collocation points and arising from different subdomains. For the present example, the square coupled BE-BE system consists of the following (combinations of) equations: (3.17a), (3.19d), α_u^{12}(3.17b)+α_u^{21}(3.18a), α_u^{13}(3.17c) +α_u^{31}(3.19a), α_u^{23}(3.18c)+α_u^{32}(3.19c), α_u^{123}(3.17d) +α_u^{213}(3.18b) +α_u^{321}(3.19b), α_t^{12}(3.17e)+α_t^{21}(3.18d), α_t^{13}(3.17f)+α_t^{31}(3.19e) and α_t^{23}(3.18e) +α_t^{32}(3.19f), where α_u^{ij} and α_t^{ij} are the weighting coefficients of the equations related to nodal collocations and element collocations respectively. This example thus involves weighted combinations of two equations and also, due to the presence of triple points, of three equations.

3.4 IMPLEMENTATION ISSUES

This section aims at studying the choice of weighting coefficients, and other implementation issues such as scaling and unknowns ordering which also strongly affect the numerical efficiency and accuracy of the multi-domain FMM, with the help of a test problem having a known exact solution. All examples have been run on the same single-processor PC (RAM: 3GB, CPU frequency: 3.40 GHz).

3.4.1 Definition of the test problem

The test problem configuration is a spherical cavity subjected to an internal time-harmonic uniform pressure P, surrounded by two spherical shells embedded in an unbounded elastic medium (Fig. 3.9). The cavity surface and the two surrounding interfaces are concentric spheres with respective radii a_1, $a_2 = 2a_1$ and $a_3 = 3a_1$. Four sets (labelled a, b, c, d) of material properties, defined in Table 3.1, are used. Variations on this testing setup T will then be referred to using the following convention. Notation $T(a, b, c)$ refers to the "standard" two-shell, three-region configuration with materials a, b, c arranged in order of increasing radii. Testing configuration $T(a, b, b)$ then consists of three regions with the outermost two made of the same material, while $T(a, b)$ refers to just two regions defined by spheres of radii a_1, a_2 (i.e. $T(a, b, b)$ and $T(a, b)$ are physically identical but numerically treated as three-region and two-region configurations, respectively). This test problem has a closed-form analytical solution which can be easily computed. The potentials ϕ_i, defined such that $u_i = \partial\phi_i/\partial r$, can be written:

$$\phi_1 = \frac{A_1}{r}e^{ik_P^{(1)}r} + \frac{B_1}{r}e^{-ik_P^{(1)}r}, \quad \phi_2 = \frac{A_2}{r}e^{ik_P^{(2)}r}$$

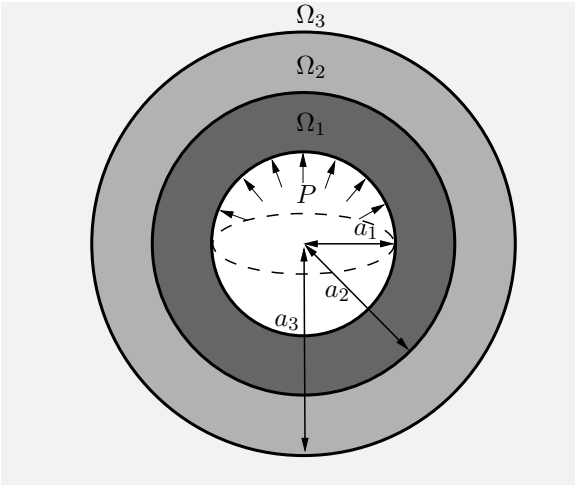

Figure 3.9: *Definition of the test problem: spherical cavity under uniform pressure.*

where $k_P^{(i)}$ denote the P–wavenumber in the subdomain i and the coefficients A_1, B_1 and A_2 are the solutions of the linear system:

$$\begin{bmatrix} e^{\alpha_1}(-1+\alpha_1) & -e^{-\alpha_1}(1+\alpha_1) & -e^{\alpha_2} \\ e^{\alpha_1}\mu_1\theta_1 & e^{-\alpha_1}\mu_1(\alpha_1^2/\gamma_1^2+4(1+\alpha_1)) & e^{\alpha_2}\mu_2\theta_2 \\ e^{\alpha_3}\mu_1\theta_3 & e^{-\alpha_3}\mu_1(\alpha_3^2/\gamma_1^2+4(1+\alpha_3)) & 0 \end{bmatrix} \times \begin{bmatrix} A_1 \\ B_1 \\ A_2 \end{bmatrix} = \begin{bmatrix} 0 \\ 0 \\ -pa_1^3 \end{bmatrix}$$

with $\alpha_1 = ik_P^{(1)}a_2$, $\alpha_2 = ik_P^{(2)}a_2$, $\alpha_3 = ik_P^{(1)}a_1$ and $\theta_i = \alpha_i^2/\gamma_i^2 + 4(1-\alpha_i)$.

Table 3.1: *Definition of the mechanical properties for the test problem.*

	a	b	c	d
ρ	3	6	2	2
μ	4	5	1	1
ν	0.25	0.25	1/3	0.25

3.4.2 Determination of optimal weightings

To determine suitable values for weighting coefficients α_u^{ij} and α_t^{ij}, some numerical experiments on two-region test configurations $T(d,d)$ (homogeneous) with $k_S^{(1)}a_1 = 7.64$ and $T(a,b)$ with $k_S^{(1)}a_1 = 4.68$ have been performed. In this case, the following set of equations are obtained using the linear combination procedure of Section 3.3:

$$\begin{aligned} H_1^1\boldsymbol{u}^1 + H_{12}^1\boldsymbol{u}^{12} - G_{12}^1\boldsymbol{t}^{12} - G_1^1\boldsymbol{t}_D^1 = 0, \\ \alpha_u^{12}\left[H_1^{12}\boldsymbol{u}^1 + H_{12}^{12}\boldsymbol{u}^{12} - G_{12}^{12}\boldsymbol{t}^{12} - G_1^{12}\boldsymbol{t}_D^1\right] + \alpha_u^{21}\left[H_{12}^{21}\boldsymbol{u}^{12} + G_{12}^{21}\boldsymbol{t}^{12}\right] = 0, \\ \alpha_t^{12}\left[\bar{H}_1^{12}\boldsymbol{u}^1 + \bar{H}_{12}^{12}\boldsymbol{u}^{12} - \bar{G}_{12}^{12}\boldsymbol{t}^{12} - \bar{G}_1^{12}\boldsymbol{t}_D^1\right] + \alpha_t^{21}\left[\bar{H}_{12}^{21}\boldsymbol{u}^{12} + \bar{G}_{12}^{21}\boldsymbol{t}^{12}\right] = 0, \end{aligned}$$

where $\boldsymbol{t}_D^1 = P\boldsymbol{e_r}$ is the traction applied on the inner sphere $r = a_1$. The mesh size is $N = 122,892$ ($\bar{\ell_1} = 4$, $\bar{\ell_2} = 4$, $d^{\min} = 0.30\lambda_S$). After having tried all 16 possible combinations where each weighting coefficient has value $\pm 1/2$, six of these combinations (defined in Table 3.2) were chosen to illustrate the effect of this choice on accuracy and convergence rate, the other ten being discarded as they all produced unsatisfactory results in terms of accuracy or convergence.

Table 3.2: *Definition of the various set of coefficients used to determine the optimal one.*

	1	2	3	4	5	6
α_u^{12}	0.5	0.5	0.5	-0.5	-0.5	-0.5
α_t^{12}	0.5	-0.5	-0.5	0.5	-0.5	-0.5
α_u^{21}	0.5	0.5	0.5	-0.5	0.5	-0.5
α_t^{21}	-0.5	0.5	-0.5	-0.5	0.5	0.5

Table 3.3 shows the relative root mean square (RMS) errors $E(\boldsymbol{u}^1)$, $E(\boldsymbol{u}^{12})$ and $E(\boldsymbol{t}^{12})$ between the respective solutions $\boldsymbol{u}^1, \boldsymbol{u}^{12}, \boldsymbol{t}^{12}$ computed with the FMM and the corresponding analytical solution. On noting that $H_{12}^{12} = -H_{12}^{21}$, $G_{12}^{12} = G_{12}^{21}$, $\bar{H}_{12}^{12} = -\bar{H}_{12}^{21}$ and $\bar{G}_{12}^{12} = \bar{G}_{12}^{21}$ when subdomains 1 and 2 have the same material properties, sets 3 and 5 are seen to yield for $T(d,d)$ a singular and almost-singular matrix system, respectively. The poor results (in terms of either accuracy or convergence) achieved by sets 3 and 5 are not surprising in this light. Sets 1, 2, 4, 6 yield matrix systems that are made of rows of blocks that are identical except for their signs. The latter feature clearly has an effect on convergence properties, with set 2 exhibiting the best convergence rate. Hence, in the remainder of this chapter, integral equations collocated on all interfaces Γ_{ij} will be weighted according to $\alpha_u^{ij} = \alpha_u^{ji} = +0.5$ and $\alpha_t^{ij} = -\alpha_t^{ji} = -0.5$ ($i < j$), as suggested by this

Table 3.3: *Solution error for the test problems $T(d,d)$ and $T(a,b)$, for the sets of coefficients listed in Table 3.2.*

test problem	coefficient set	$E(\boldsymbol{u}^1)$	$E(\boldsymbol{u}^{12})$	$E(\boldsymbol{t}^{12})$	nb iter.
$T(d,d)$	1	/	/	/	>300
	2	$3.2\,10^{-3}$	$2.5\,10^{-3}$	$1.6\,10^{-2}$	64
	3	$8.8\,10^{-1}$	$8.8\,10^{-1}$	$1.6\,10^{0}$	90
	4	/	/	/	>300
	5	/	/	/	>300
	6	/	/	/	>300
$T(a,b)$	1	$2.4\,10^{-2}$	$1.7\,10^{-2}$	$3.5\,10^{-2}$	94
	2	$2.4\,10^{-2}$	$1.8\,10^{-2}$	$3.5\,10^{-2}$	22
	3	$6.3\,10^{-1}$	$4.7\,10^{-1}$	$8.9\,10^{-1}$	2
	4	$2.4\,10^{-2}$	$1.7\,10^{-2}$	$3.5\,10^{-2}$	122
	5	/	/	/	>300
	6	$2.4\,10^{-2}$	$1.7\,10^{-2}$	$3.5\,10^{-2}$	182

test. Linear combinations of $p > 2$ block equations, which arise from collocation at nodes shared by p subregions (e.g. the triple points of the two-layered basin example of Section 3.3), are handled by assigning equal weight $1/p$ to each contributing block equation, an approach which has been successfully subjected to the test problem in its three-region form $T(a, b, c)$.

This approach, insofar as it exploits (combinations of) an initially overdetermined set of BEM matrix equations, may appear as computationally expensive. But, in fact, within a FMM framework, the additional number of collocation points only occurs on the interfacial surfaces Γ_{ij}. Moreover, only the CPU time of the last step of the FMM, namely the local expansion step which has been shown in Chapter 2 to be of $O(N)$ complexity, is increased.

3.4.3 Equation scaling

Another simple but important detail of the present BE-BE coupling formulation is that convergence rates are improved by scaling equations. For multi-domain problems, the system matrix is populated with various blocks whose magnitude depends on the material properties. Disparities in these magnitudes may lead to bad convergence rates. The introduction of scaling factors alleviates such problems. The following scaling factors are defined:

$$\tilde{g} = \frac{1}{n} \sum_{i=1}^{n} \frac{4\mu_i(1+\nu_i)}{(1-2\nu_i)}, \qquad \tilde{h} = \frac{1}{n} \sum_{i=2}^{n} d_i^{(0)}$$

where (μ_i, ν_i) are the elastic properties of Ω_i and $d_i^{(0)}$ is the level-0 cell size in the octree introduced for Ω_i. We note that, due to the fact that Ω_1 is always the infinite medium, the domain size of Ω_1 is not taken into account in $\tilde{h}$. This scaling, a modified version of that used in [10] which includes the effect of the domain size, is equivalent to introducing new, non-dimensional, unknowns $\tilde{\boldsymbol{u}}^{ij}$ and $\tilde{\boldsymbol{t}}^{ij}$:

$$\boldsymbol{u}^{ij} = \tilde{h}\, \tilde{\boldsymbol{u}}^{ij}, \qquad \boldsymbol{t}^{ij} = \tilde{g}\, \tilde{\boldsymbol{t}}^{ij}$$

and replacing the block matrices H and G with $\tilde{H} = \tilde{h}\, H$ and $\tilde{G} = \tilde{g}\, G$. Using this scaling, all coefficients of the resulting coupled system have similar magnitudes. Some results on the efficiency of the introduction of this scaling are presented in Section 3.5.1 on seismological problems involving an infinite medium Ω_1.

3.4.4 Other implementation issues

In keeping with the modular approach previously outlined, where FMM is applied separately for each subregion, separate BE meshes are defined for each subdomain, with meshes for two adjacent subdomains being compatible over the shared interface. Each adjacent mesh is oriented relative to its subdomain (Fig. 3.10). This method ensures that normals to all elements of a given subdomain have a consistent (outward) orientation.

Another important issue is the iterative solver convergence rate. For multi-domain problems, both displacements and tractions are unknown at the interfaces. Optimal ordering of the matrix blocks for a multi-zone boundary element analysis is very important when using an iterative solver (GMRES for example). Here, one may order the unknown DOF subvectors (i.e. block columns) arbitrarily, but should then use the same order for the sets of collocation points (i.e. block rows),

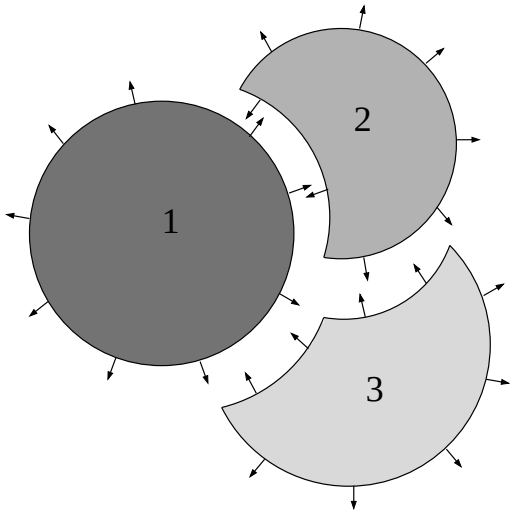

Figure 3.10: *Convention for the normal orientations.*

so as to define the global matrix closest to a symmetric matrix. For example, for the test problem $T(a,b)$ ($N = 122,892$; $k_S^{(1)} a_1 = 4.68$), a suitably ordered governing matrix is

$$\begin{bmatrix} H_1^1 & H_{12}^1 & -G_{12}^1 \\ 0.5H_1^{12} & 0.5H_{12}^{12} + 0.5H_{12}^{21} & -0.5G_{12}^{12} + 0.5G_{12}^{21} \\ -0.5\bar{H}_1^{12} & -0.5\bar{H}_{12}^{12} + 0.5\bar{H}_{12}^{21} & 0.5\bar{G}_{12}^{12} + 0.5\bar{G}_{12}^{21} \end{bmatrix} \tag{3.20}$$

so that collocation points (lines) and unknowns (columns) are ordered similarly (displacements on external surfaces, then displacements on interfaces, then tractions on interfaces). With this ordering, GMRES converges (with relative tolerance 10^{-3}) after only 22 iterations. Swapping the second and first lines in (3.20) results in a failure of GMRES to converge within $1,000$ iterations, whereas swapping also the second and third columns in (3.20) restores convergence within 22 iterations.

3.4.5 FMM computation of the integral over the free surface

In the special case of the propagation of an elastic wave in an alluvial basin, the continuous formulation presented in Section 3.2, expressed in terms of total fields, is used. A numerical difficulty arises from this formulation. The integral at the right hand side of eq. (3.12) (repeated for convenience in (3.21)) is not of the general type (3.22).

$$\int_{\Gamma_F} u_i^F(\boldsymbol{y}) T_i^k(\boldsymbol{x}, \boldsymbol{y}; \omega) dS_y, \ \boldsymbol{x} \in \partial\Omega_1. \tag{3.21}$$

$$\int_{\partial\Omega_1} u_i(\boldsymbol{y}) T_i^k(\boldsymbol{x}, \boldsymbol{y}; \omega) dS_y, \ \boldsymbol{x} \in \partial\Omega_1. \tag{3.22}$$

In integral (3.21), the collocation points $\boldsymbol{x} \in \partial\Omega_1$ differ from the interpolation points $\boldsymbol{y} \in \Gamma_F$. It has however been shown in Section 2.4.8 how to handle such type of integrals with the FMM. The same method as for the post-processing pass is implemented, i.e. the definition of two octrees.

3.4.6 Accuracy and computational efficiency of multi-domain FM-BEM

Our implementation of elastodynamic FMM was validated for single-region problems in Chapter 2, in terms of accuracy and computational efficiency on the simple test case of a pressurized spherical cavity, with observed computing times consistent with the theoretical complexity $O(N \log N)$ and accuracy similar to that of the standard (i.e. non-FMM) BEM.

To validate the present BE-BE coupling, the test problem of Section 3.4.1 is again considered. The frequency is adjusted so that the mesh features at least 10 points per S–wavelength in all cases.

Considering first homogeneous cases $T(d,d)$ and $T(d,d,d)$, Table 3.4 shows the number of degrees of freedom, the leaf-cell size parameter $d^{\min}$, the normalized frequency of the problem, the leaf level $\bar{\ell}$ and iteration counts (without preconditioning). Table 3.5 shows the relative root mean square (RMS) error $E(\boldsymbol{u}^1)$, $E(\boldsymbol{u}^{12})$, $E(\boldsymbol{t}^{12})$, $E(\boldsymbol{u}^{23})$ and $E(\boldsymbol{t}^{23})$. In this example, we observe that the precision of the FM-accelerated BEM is acceptable for $d^{\min} \geq 0.30\lambda_S$, consistently with earlier findings in Chapter 2. The bad conditioning of the matrix, and the fact that the number of iterations rapidly increases with the problem size, are also manifest, which emphasizes the desirability of a good preconditioning strategy. The same data is next given in Tables 3.6 and 3.7 for heterogeneous test problems $T(a,b)$ and $T(a,b,c)$, which exhibit much better convergence properties.

Table 3.4: *Homogeneous test problems: computational data.*

Test pb.	N	$\frac{d^{\min}}{\lambda_S^{(1)}}$	$k_S^{(1)} a_1$	$\bar{\ell}_i$	nb iter.
$T(d,d)$	30,732	0.30	3.54	3; 3	6
$T(d,d)$	122,892	0.30	7.64	4; 4	64
$T(d,d,d)$	57,778	0.21	3.54	3; 3; 3	31
$T(d,d,d)$	215,058	0.30	7.64	3; 4; 4	864

Table 3.5: *Homogeneous test problems: relative RMS error.*

Test pb.	$E(\boldsymbol{u}^1)$	$E(\boldsymbol{u}^{12})$	$E(\boldsymbol{t}^{12})$	$E(\boldsymbol{u}^{23})$	$E(\boldsymbol{t}^{23})$
$T(d,d)$	$1.3\,10^{-2}$	$4.7\,10^{-3}$	$1.7\,10^{-2}$	/	/
$T(d,d)$	$3.0\,10^{-3}$	$2.5\,10^{-3}$	$1.6\,10^{-2}$	/	/
$T(d,d,d)$	$8.3\,10^{-3}$	$9.4\,10^{-3}$	$4.5\,10^{-2}$	$1.2\,10^{-2}$	$3.4\,10^{-2}$
$T(d,d,d)$	$6.1\,10^{-3}$	$7.7\,10^{-3}$	$2.2\,10^{-2}$	$6.6\,10^{-3}$	$2.0\,10^{-2}$

3.5 PROPAGATION AND AMPLIFICATION OF SEISMIC WAVES IN ALLUVIAL BASINS

In Chapter 2, the single-domain elastodynamic FMM has been compared to the results of [183] for the scattering by an irregular homogeneous half-space of a plane vertical P–wave at normalized frequency $k_P a/\pi = 0.25$ (with $\nu = 0.25$), and then applied to the same configuration at a higher frequency ($k_P a/\pi = 5$). In this section, the present multi-domain implementation is applied to the propagation of seismic waves in alluvial basins. Unless indicated otherwise, all examples

Table 3.6: *Heterogeneous test problems: computational data.*

Test pb.	N	$\frac{d^{\min}}{\lambda_S^{(1)}}$	$k_S^{(1)} a_1$	$\bar{\ell}_i$	nb iter.
$T(a,b)$	30,732	0.17	2.17	$3;3$	21
$T(a,b)$	122,892	0.30	4.93	$3;4$	22
$T(a,b,c)$	57,778	0.13	2.17	$3;3;3$	59
$T(a,b,c)$	215,058	0.30	4.93	$3;3;4$	43

Table 3.7: *Heterogeneous test problems: relative RMS error.*

Test pb.	$E(\boldsymbol{u}^1)$	$E(\boldsymbol{u}^{12})$	$E(\boldsymbol{t}^{12})$	$E(\boldsymbol{u}^{23})$	$E(\boldsymbol{t}^{23})$
$T(a,b)$	$5.0\,10^{-3}$	$5.1\,10^{-3}$	$1.6\,10^{-2}$	/	/
$T(a,b)$	$2.4\,10^{-2}$	$1.8\,10^{-2}$	$3.5\,10^{-2}$	/	/
$T(a,b,c)$	$3.0\,10^{-2}$	$1.4\,10^{-2}$	$2.2\,10^{-2}$	$1.3\,10^{-2}$	$2.8\,10^{-2}$
$T(a,b,c)$	$1.0\,10^{-2}$	$1.3\,10^{-2}$	$1.0\,10^{-2}$	$1.4\,10^{-2}$	$1.4\,10^{-2}$

have been run on the same single-processor PC (RAM: 3GB, CPU frequency: 3.40 GHz) and no preconditioning strategy is applied.

3.5.1 Seismic wave propagation in a canonical basin

This first example is concerned with the propagation in a semi-spherical alluvial basin (i.e. soft elastic inclusion) of a plane P–wave of unit amplitude traveling vertically in an elastic homogeneous irregular half-space (Fig. 3.11). Such a configuration may lead to a strong amplification of the seismic motion in soft alluvial deposits.

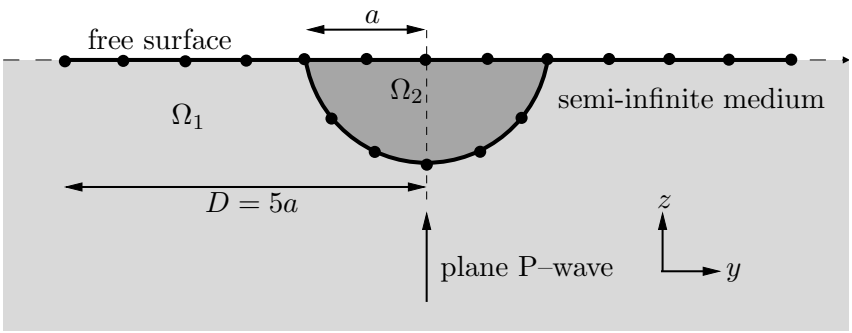

Figure 3.11: *Propagation of an incident plane P–wave in a semi-spherical alluvial basin (3-D configuration): notations.*

As in [183], we investigate the motion at the surface of the alluvial basin Ω_2, for the following values of the material parameters: $\mu^{(2)} = 0.3\mu^{(1)}$, $\rho^{(2)} = 0.6\rho^{(1)}$, $\nu^{(1)} = 0.25$ and $\nu^{(2)} = 0.3$. The normalized frequency is defined by $k_P^{(1)} a/\pi$ in terms of the properties of the elastic semi-infinite medium Ω_1. The radius of the discretized free surface is set to $D = 5a$.

Validation with existing low-frequency results. The surface displacements computed with the present multi-domain FMM are presented, along with corresponding results from [183] (using series expansion method) and [63] (using spectral element method), for $k_P^{(1)}a/\pi = 0.5$ (Fig. 3.12a) and $k_P^{(1)}a/\pi = 0.7$ (Fig. 3.12b). All results are seen to be in good agreement. For these examples, a leaf-cell size $d^{\min}$ lower than the threshold $d^{\min} = 0.30\lambda_S$ recommended in Chapter 2 has to be used as a consequence of the chosen truncation radius $D = 5a$, allowing to compare our results to the previously-published ones.

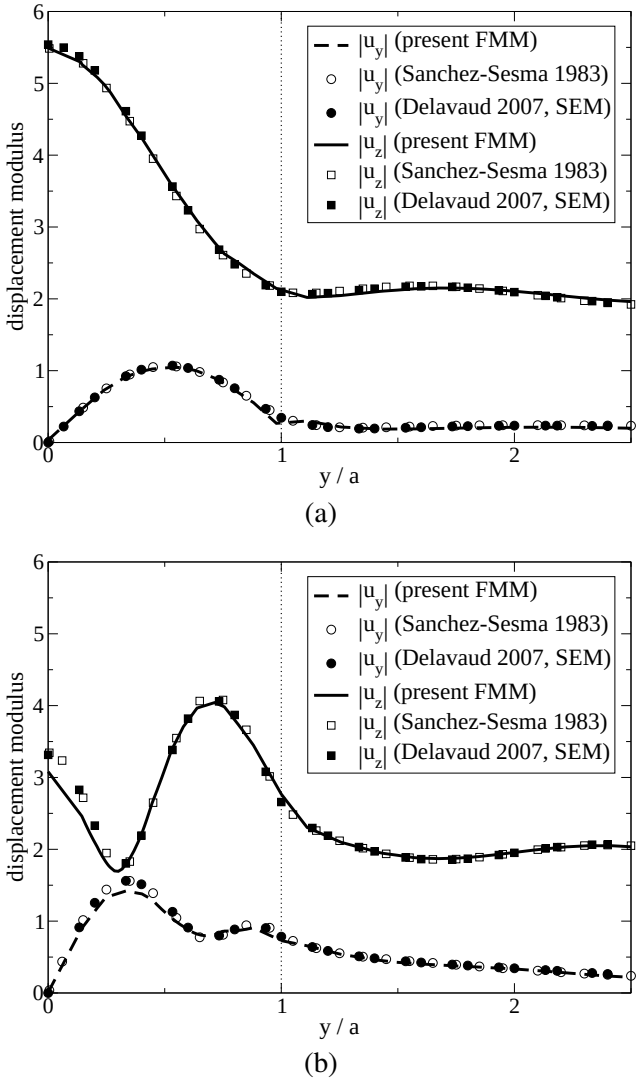

Figure 3.12: *Propagation of an incident plane P–wave in a semi-spherical alluvial basin: surface displacement at (a) $k_P^{(1)}a/\pi = 0.5$, (b) $k_P^{(1)}a/\pi = 0.7$ and comparisons with [183] and [63].*

Results for higher frequencies. Additionally, the FMM allowed to perform computations at higher frequencies $k_P^{(1)}a/\pi = 1$ (Fig. 3.13a) and $k_P^{(1)}a/\pi = 2$ (Fig. 3.13b), for which no pub-

lished results are available for comparison purposes. For such higher frequencies, the maximum amplification level is seen to range from 2 to 3 (free surface effects being removed).

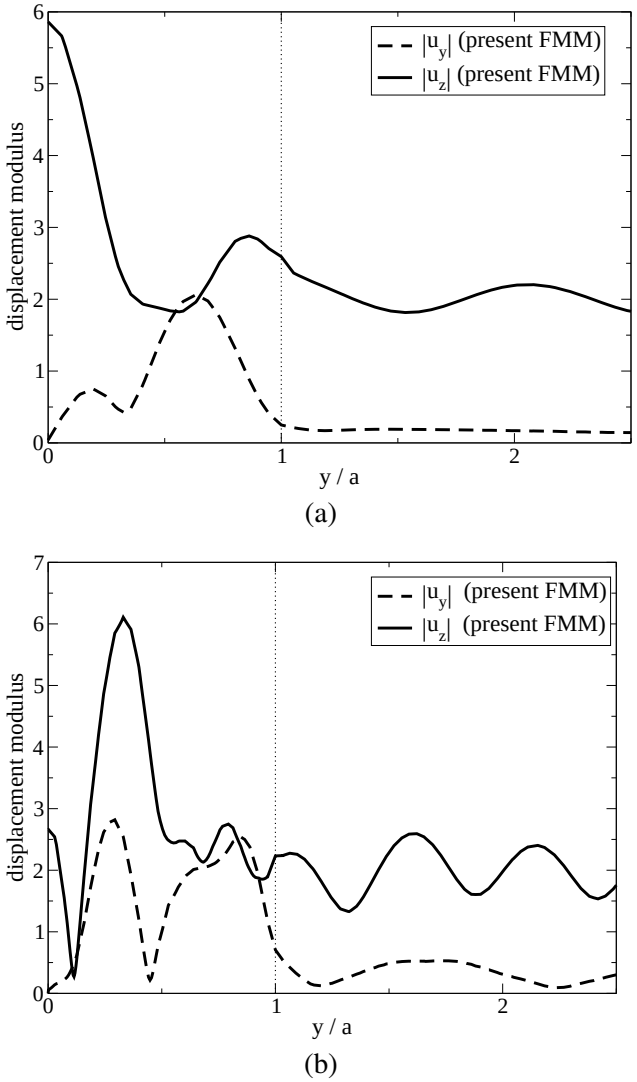

Figure 3.13: *Propagation of an incident plane P–wave in a semi-spherical alluvial basin: surface displacement at (a)* $k_P^{(1)}a/\pi = 1$ *and (b)* $k_P^{(1)}a/\pi = 2$.

Computational considerations. In Table 3.8, the number of DOFs, the size of the leaf cells and the leaf level $\bar{\ell}_i$ in each subdomain Ω_i are given for the meshes used, together with the CPU time per iteration recorded. These examples are also used to illustrate the efficiency of the scaling factors introduced in Section 3.4.3. Iteration counts using three different scalings are given in Table 3.8:

(a) using the scaling factor introduced in Section 3.4.3; (b) using a modified version of (a):

$$\tilde{h} = \frac{1}{n}\sum_{i=1}^{n} d_i^{(0)}$$

and (c) without any scaling. Scaling (a) is seen to perform best. It can be easily understood that scaling (b) is less efficient since it incorporates a characteristic size for the (truncated) infinite medium Ω_1. The equation scaling (a) is very efficient and drastically reduces (by up to 90%) the iteration counts. However, the last example also indicates that the iteration count significantly impacts the computational efficiency for problem sizes for which the CPU time per iteration and the memory requirements are still moderate. An efficient preconditioning strategy is clearly needed. A simple such approach is proposed in Chapter 4, and is shown therein to bring significant improvement. It was however not implemented at the time when the present set of results was generated.

Table 3.8: *Propagation of an incident plane P–wave in a semi-spherical alluvial basin: data and computational results.*

					various scalings		
$k_P^{(1)}a/\pi$	N	$d^{\min}/\lambda_S$	$\bar{l}_1;\bar{l}_2$	CPU (s) per iter.	nb iter. (a)	nb iter. (b)	nb iter. (c)
0.5	17,502	0.15	3; 3	8	28	44	86
0.7	17,502	0.21	4; 3	10	34	60	111
1	90,057	0.30	4; 3	49	52	192	519
2	190,299	0.30	5; 4	79	325	$3,006$	$> 5,000$

Influence of the truncation radius D. In [183], the size of the discretized free surface is set to $D = 5a$. A natural issue concerns the selection of the best value of the truncation radius D for the model, i.e. the smallest value of D for which the solution is practically insensitive to the free-surface truncation. Taking advantage of the larger problem sizes allowed by the present FMM, this issue is now investigated by means of a parametric study. The choice of D obviously depends on the size of the region for which a truncation-insensitive numerical solution is sought. Here, the latter is chosen such that $r/a \leq 3$. A similar study, restricted to $D \leq 5a$, has been done in [161] in the case of the diffraction of a plane P–wave by a semi-spherical canyon.

Figure 3.14 shows the relative difference between the solution computed at the center of the basin for several truncation radii D and a reference solution obtained for $D = 20a$, at normalized frequency $k_P^{(1)}a/\pi = 0.5$. These results suggest that the convergence is achieved for $D \geq 13a$ ($= 13\lambda_P^{(1)}/4 > 3\lambda_P^{(1)}$) and that, for $D < 13a$, the error with respect to the reference solution oscillates within a range $\pm 4\%$. Here, it can be seen that the value $D = 5a$ used in [183] yields reasonably, but not optimally, accurate results at the basin center. This parametric study is conducted for the displacement at the center of the basin because errors caused by truncation are observed to be largest there. In fact, for $r/a \geq 0.5$, the sensitivity of the results to the choice of D was found to be low (see Table 3.9).

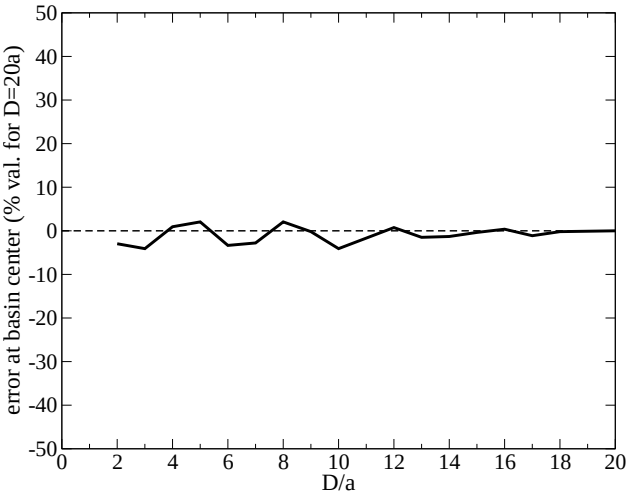

Figure 3.14: *Propagation of an incident plane P–wave in a semi-spherical basin: discrepancy between the reference solution ($D = 20a$) and solutions obtained for various truncation radii D at the basin center.*

Table 3.9: *Propagation of an incident plane P–wave in a semi-spherical basin: discrepancy between the reference solution ($D = 20a$) and solutions obtained for various truncation radii D, at three surface points (in $\%$ of the reference solution).*

D/a	2	4	6	8	10	12	14	16	18
$r = 0$	-2.97	0.93	-3.35	2.05	-4.09	0.74	-1.30	0.37	-0.19
$r = a/2$	-1.85	-0.31	-2.33	-0.02	-2.46	0.38	-1.30	-0.20	-0.35
$r = 3a/2$	0.68	0.19	0.23	-0.22	0.59	-0.27	0.24	-0.01	0.41

3.5.2 Scattering of an incident plane P–wave by a two-layered semi-spherical basin

The results of Section 3.5.1 are limited to a single-layered basin, whereas the present implementation is applicable to more general configurations featuring piecewise-homogeneous basins. To demonstrate this capability, the propagation of an incident plane P–wave in a heterogeneous semi-spherical basin is now considered for an alluvial deposit composed of two layers (Fig. 3.15).

Two layers involving identical materials. First, to check our implementation in the multi-domain case, identical mechanical properties are assumed for Ω_2 and Ω_3:

$$\mu^{(2)} = \mu^{(3)} = 0.3\mu^{(1)},\ \rho^{(2)} = \rho^{(3)} = 0.6\rho^{(1)},\ \nu^{(1)} = 0.25,\ \nu^{(2)} = \nu^{(3)} = 0.3.$$

The study is performed at normalized frequency $k_P^{(1)}a/\pi = 1$, using a truncation radius $D = 5a$. The mesh features $N = 91,893$ DOFs. The results of this computation, which took 81 iterations and 48 s per iteration ($\bar{\ell}_1 = 4$; $\bar{\ell}_2 = 3$; $\bar{\ell}_3 = 3$), are seen in Figure 3.16 to coincide (as they should) with those computed with a single-layered basin (Fig. 3.13).

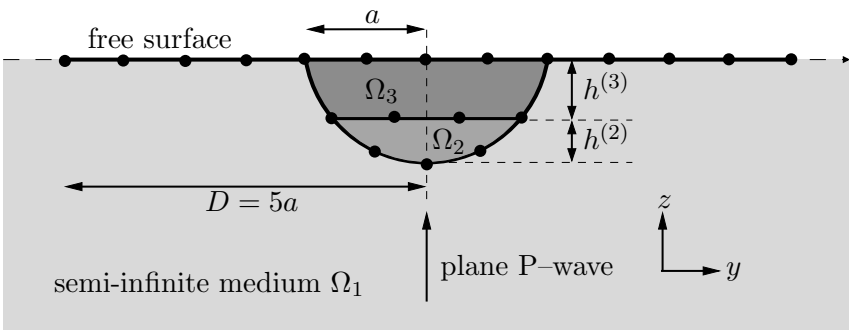

Figure 3.15: *Propagation of an incident plane P–wave in a two-layered semi-spherical basin (3-D configuration): notation.*

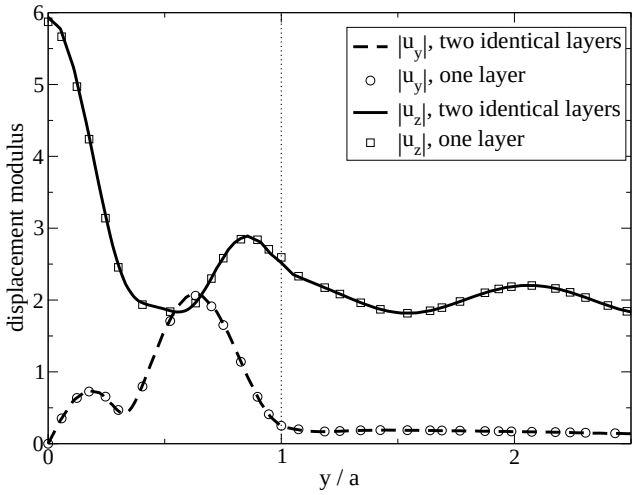

Figure 3.16: *Propagation of an incident plane P–wave in a two-layered semi-spherical basin (with the same material in Ω_2 and Ω_3 and $k_P^{(1)}a/\pi = 1$): comparison with the result for a one-layered semi-spherical basin (Fig. 3.13).*

Two-layered heterogeneous basin. Now, the two layers Ω_2 and Ω_3 are made of different materials. Symbols $\chi_P^{(ij)}$ and $\chi_S^{(ij)}$ will be used to denote the P–wave and S–wave velocity contrasts between Ω_i and Ω_j:

$$\chi_P^{(ij)} = c_P^{(j)}/c_P^{(i)}; \qquad \chi_S^{(ij)} = c_S^{(j)}/c_S^{(i)}$$

Two examples are considered. In example (a), mechanical properties are defined so that $\chi_S^{(12)}$ is the same as in Section 3.5.1 and as in [183], and that $\chi_S^{(12)} = \chi_S^{(23)}$:

$$\frac{\rho^{(2)}}{\rho^{(1)}} = \frac{\rho^{(3)}}{\rho^{(2)}} = 0.6; \quad \frac{\mu^{(2)}}{\mu^{(1)}} = \frac{\mu^{(3)}}{\mu^{(2)}} = 0.3; \quad \nu^{(1)} = 0.25; \quad \nu^{(2)} = \nu^{(3)} = 0.30 \qquad (3.23)$$

In example (b), the velocity contrasts between Ω_1, Ω_2 and Ω_2, Ω_3 are the same for P– and S–waves, $\chi_S^{(12)} = \chi_S^{(23)}$ and $\chi_P^{(12)} = \chi_P^{(23)}$:

$$\frac{\rho^{(2)}}{\rho^{(1)}} = \frac{\rho^{(3)}}{\rho^{(2)}} = 0.6; \qquad \frac{\mu^{(2)}}{\mu^{(1)}} = \frac{\mu^{(3)}}{\mu^{(2)}} = 0.3; \qquad \nu^{(1)} = 0.25; \qquad \nu^{(2)} = 0.30; \qquad \nu^{(3)} = 0.34 \tag{3.24}$$

The thickness, $h^{(2)}$ and $h^{(3)}$ of the layers Ω_2 and Ω_3 are adjusted to the wavelengths:

$$h^{(2)}/\lambda_S^{(2)} = h^{(3)}/\lambda_S^{(3)} \qquad \Rightarrow \qquad h^{(2)} = \sqrt{2}h^{(3)} = (2-\sqrt{2})a.$$

The mesh and normalized frequency ($k_P^{(1)}a/\pi = 1$) are the same as in the previous homogeneous case. The computations required 255 and 272 iterations for example (a) and (b), respectively, and 48 s per iteration ($\bar{\ell_1} = 4$; $\bar{\ell_2} = 3$; $\bar{\ell_3} = 3$).

In Figures 3.17 and 3.18, the results of the computations (a) and (b) for the two-layered semi-spherical basin are compared to those for a single-layered basin (Fig. 3.13). The introduction of the layer Ω_3 leads to stronger amplification (up to 7 for (a) or 6.5 for (b) instead of 3 for the single-layered basin, the free-surface effects being removed), with shorter wavelengths in the basin. We also see on this example the effect of the value of $\nu^{(3)}$: a higher value of $\nu^{(3)}$ leads to a smaller increase of the maximum amplification.

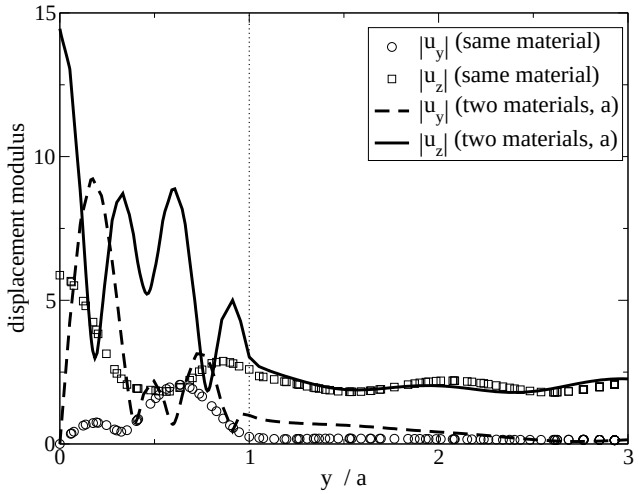

Figure 3.17: *Propagation of an incident plane P–wave in a two-layered (example (a)) semi-spherical basin (with mechanical properties (3.23), $k_P^{(1)}a/\pi = 1$).*

3.5.3 SV–wave amplification in a semi-spherical basin

All examples presented so far in this section involve incident P–waves. However, a fully 3-D validation requires considering other types of incident fields such as plane SV–waves with oblique incidence. Such configurations have been studied by [156] using standard indirect BEM (with the half-space Green's functions).

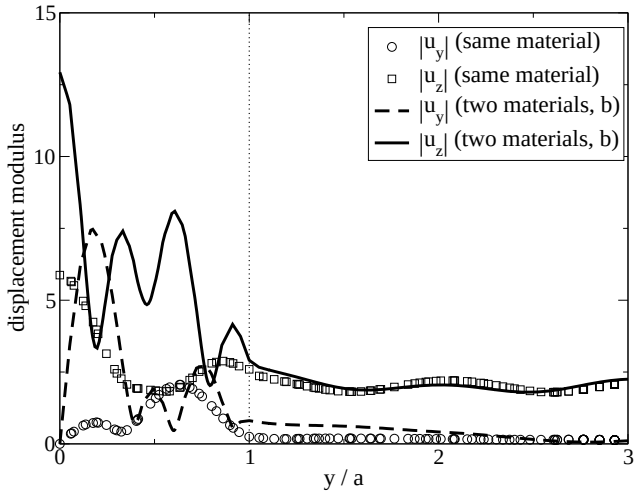

Figure 3.18: *Propagation of an incident plane P–wave in a two-layered (example (b)) semi-spherical basin (with mechanical properties (3.24), $k_P^{(1)} a/\pi = 1$).*

Problem definition. This example is concerned with the propagation in a semi-spherical basin of an oblique incident plane SV–wave of unit amplitude traveling in an elastic half space (see Fig. 3.19). A right-handed Cartesian frame (x, y, z) is defined so that the elastic half-space occupies the region $\{(x, y, z) \,|\, z \geq 0\}$. The truncation radius is $D = 5a$. The mechanical parameters are defined as follows: $c_S^{(1)} = 1$ m.s^{-1}, $c_P^{(1)} = 2$ m.s^{-1}, $\mu^{(2)}/\mu^{(1)} = 1/6$, $\rho^{(2)}/\rho^{(1)} = 2/3$ and $\nu^{(1)} = \nu^{(2)} = 1/3$. In [156], a weakly inelastic formulation (with P–wave and S–wave quality factors equal to 100) is used whereas our FMM implementation is purely elastic.

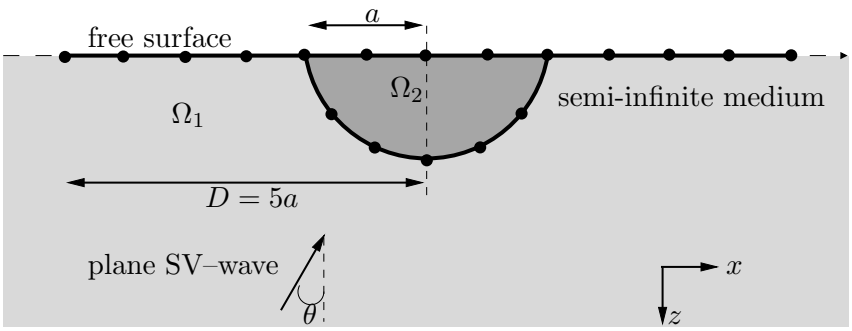

Figure 3.19: *Propagation of an oblique incident plane SV–wave in a semi-spherical basin (3D-configuration): notation.*

Validation. The example depicted in Fig. 3.19 has been treated, for a normalized frequency $k_S^{(1)} a/\pi = 0.5$ and for $\theta = 0°, 30°$. The mesh features $N = 17,502$ DOFs. The computations take 5 s per iteration, 32 iterations for the case $\theta = 0°$ and 34 iterations for the case $\theta = 30°$ ($\bar{\ell}_1 = 3$, $\bar{\ell}_2 = 3$, $d^{\min} = 0.25\lambda_S$).

For the case $\theta = 0°$ (resp. $\theta = 30°$), the x-components (resp. x-, y- and z-components) of

the computed displacements on the surface are displayed in Fig. 3.20 (resp. Fig. 3.21). They are in good agreement with the results of [156] even though, in our implementation, no attenuation is considered.

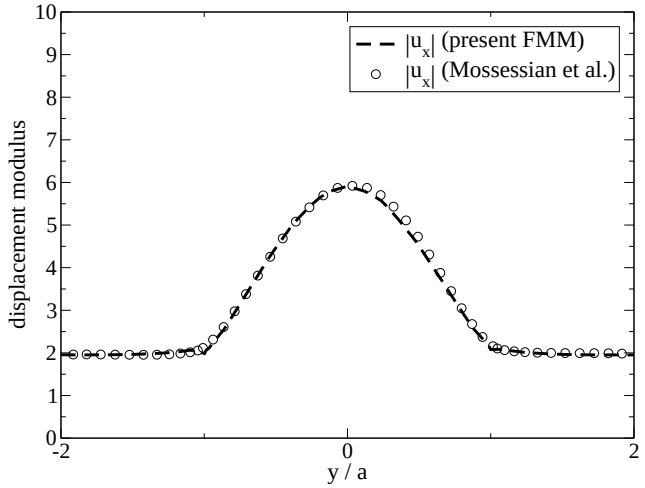

Figure 3.20: *Propagation of a vertical ($\theta = 0°$) incident plane SV–wave in a semi-spherical basin: Comparison of the FMM computed displacements (x-component) with the results of [156].*

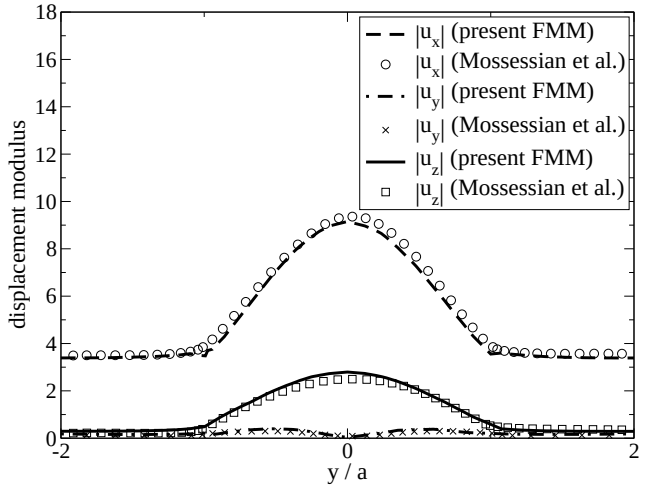

Figure 3.21: *Propagation of an oblique ($\theta = 30°$) incident plane SV–wave in a semi-spherical basin: Comparison of the FMM computed displacements (x-, y- and z-components) with the results of [156].*

3.6 SV–WAVE AMPLIFICATION IN A SEMI-SPHERICAL BASIN: TIME-DOMAIN RESULTS

All examples presented so far in this Section 3.5 are in the frequency domain. However, frequency-domain computations also allow to obtain time-domain responses via Fourier synthesis. In [157], the configuration presented in Section 3.5.3 is studied in the time domain using standard indirect BEM.

Synthesis of the time-domain solution

The time-domain response $\boldsymbol{u}(\boldsymbol{x},t)$ can be computed using an inverse Fourier transform:

$$\boldsymbol{u}(\boldsymbol{x},t) = \mathcal{F}^{-1}\Big(\tilde{\boldsymbol{u}}(\boldsymbol{x},\omega)\boldsymbol{s}(\omega)\Big),$$

where $\tilde{\boldsymbol{u}}(\boldsymbol{x},\omega)$ is the frequency-domain solution and $s(\omega)$ is the source spectrum. In practice, a Fast Fourier Transform is used to synthetize the time domain results. In the following, the source spectrum is a second-order Ricker wavelet:

$$\begin{aligned} \boldsymbol{s}(t) &= \Big(2\pi^2\frac{(t-t_s)^2}{t_p^2}-1\Big)\exp\Big[-\pi^2\frac{(t-t_s)^2}{t_p^2}\Big], \\ \Rightarrow \quad \boldsymbol{s}(\omega) &= -\frac{\sqrt{\pi}\omega^2 t_p^3}{2\pi^3}\exp\Big[-\frac{\omega^2}{4\pi^2}t_p^2\Big]\exp\Big[-i\omega t_s\Big]. \end{aligned} \tag{3.25}$$

where t_s is the time related to the maximum amplitude of the wavelet and t_p is the predominant period of the signal. The predominant frequency of such a wavelet is $f_0 = 1/t_p$.

An important numerical issue in the present approach lies with the meshes used. Usually, the mesh size is adjusted so that, for the frequency $f = 2f_0$, the mesh contains about ten points per S–wavelength. However, when using the FMM, this approach is not the most efficient as if the same mesh is used for all computations, the mesh density for low frequency computations is high relative to wavelength, increasing the computational burden for the near contributions, multipole moments and local expansions. Moreover, memory requirements are also increased. On the other hand, to perform the synthesis, the solutions for each frequency need to be eventually defined on the same mesh. A simple improvement, used here, exploits a hierarchical sequence of meshes $\mathcal{M}_0, \mathcal{M}_1, \ldots$ where the coarser mesh $\mathcal{M}_0$ is adjusted (using the 10-points-per-S-wavelength criterion) to the lowest frequency and $\mathcal{M}_{k+1}$ is obtained by splitting each triangle of $\mathcal{M}_k$ into four subtriangles. Then, the solutions obtained on coarser meshes $\mathcal{M}_0, \ldots, \mathcal{M}_{n-1}$ are linearly interpolated on the finest mesh $\mathcal{M}_n$.

Time-domain response

The configuration presented in the previous Section 3.5.3 is again considered. As the Fourier synthesis of the time-domain solution requires many FMM analyses at various frequencies, the results presented in this section have been obtained on a 8-processor PC (RAM: 32GB, CPU frequency: 2.33 GHz), each FMM analysis being performed independently on a single processor. Once the implementation validated in the frequency domain, the time-domain response is considered for $\theta = 30^\circ$. To allow comparisons with [157], the predominant frequency of the source is set to a relatively low value: $f_0 = 0.25$ Hz ($t_p = 4$ s and $t_s = 5$ s). In this example, only one mesh is used, featuring $N = 36,033$ DOFs.

Frequency parametrization. Results are computed for frequencies ranging between 0 and 0.85 Hz (32 sample frequencies). Figure 3.22 displays the x- and z-components of spectral displacement along the Ox and Oy axes for the sample frequencies. The fundamental frequency is found about 0.30 Hz ($k_p^{(2)} a/\pi = 0.60$) in all four shown cases. The maximum amplification against the Ox axis and for the x-component is seen to be about 13.15 (free-surface effect being removed) and located at a higher frequency (f=0.735 Hz) at the left of the basin center ($x/a = -0.4$) while for the z-component, this maximum is also located at the left of the basin center ($x/a = -0.2$) but with about half amplification (about 6.15). A unique maximum is obtained for the x-component while for the z-component, several local maxima of amplification are obtained. The maximum amplification (about 13.3) for the x-component of the displacement against the Oy axis is obtained at the basin center for a high frequency (f=0.74 Hz) while for the z-component this maximum (about 5.2) is obtained for a frequency of about 0.685 Hz. Once again, the maximum amplification for the x-component is about twice the maximum amplification for the z-component. If we consider a 1-D layer (having the same properties) on a half-space, the fundamental frequency is reduced to $f_0 = c_S^{(2)}/4a = 0.125$ Hz (i.e. $k_p^{(2)} a/\pi = 0.25$) and the maximum amplification is also reduced to $\rho^{(1)} c_S^{(1)} \;/\; \rho^{(2)} c_S^{(2)} = 3$. This simple example illustrates the usefulness of 3-D models to study seismic wave amplification in alluvial basins.

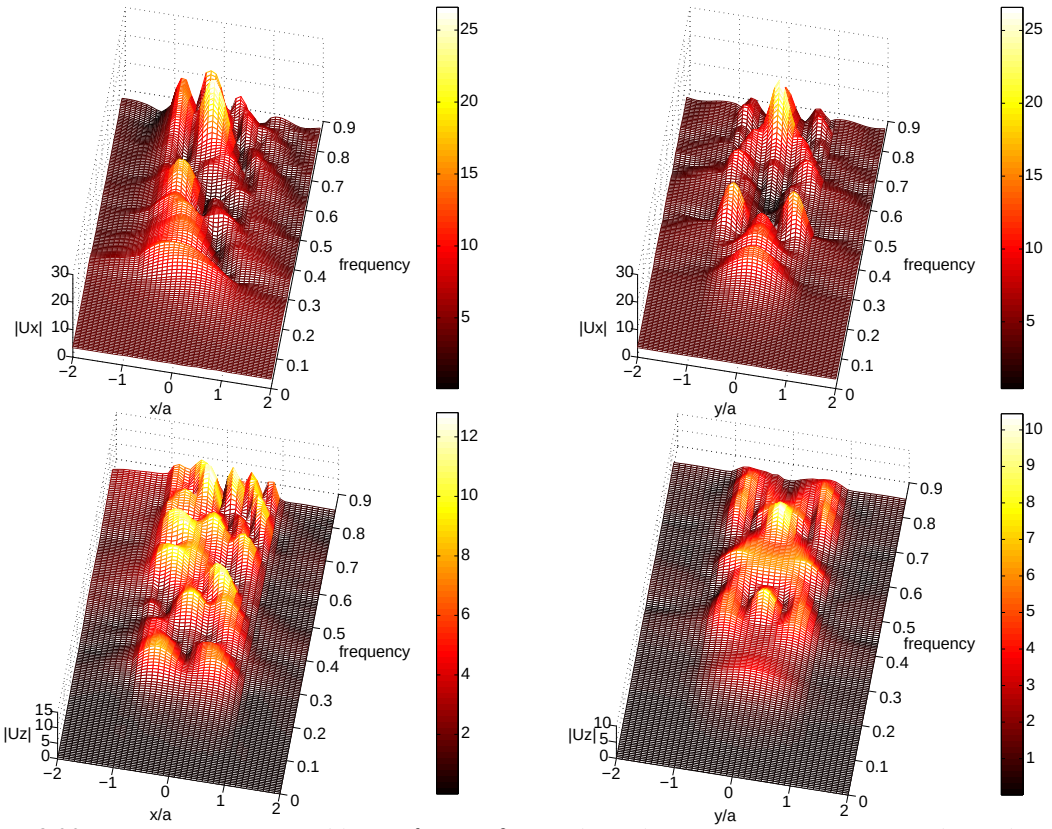

Figure 3.22: *Propagation of an oblique ($\theta = 30°$) incident plane SV–wave in a semi-spherical alluvial basin: x- (top) and z-component (bottom) of the FMM computed displacement against the x (left) and y (right) coordinate for the sample frequencies.*

Displacements against time. The time-domain results obtained from spectral responses are now presented. The x- (resp. z-) component of the FMM- and standard BEM- (results from [157]) computed displacements for $t \in [0, 30]$ are plotted against the Ox axis in Fig. 3.23 (resp. 3.24). The x- and z-components of the FMM-computed displacement for $t \in [0, 30]$ are plotted against the Oy axis in Fig. 3.25.

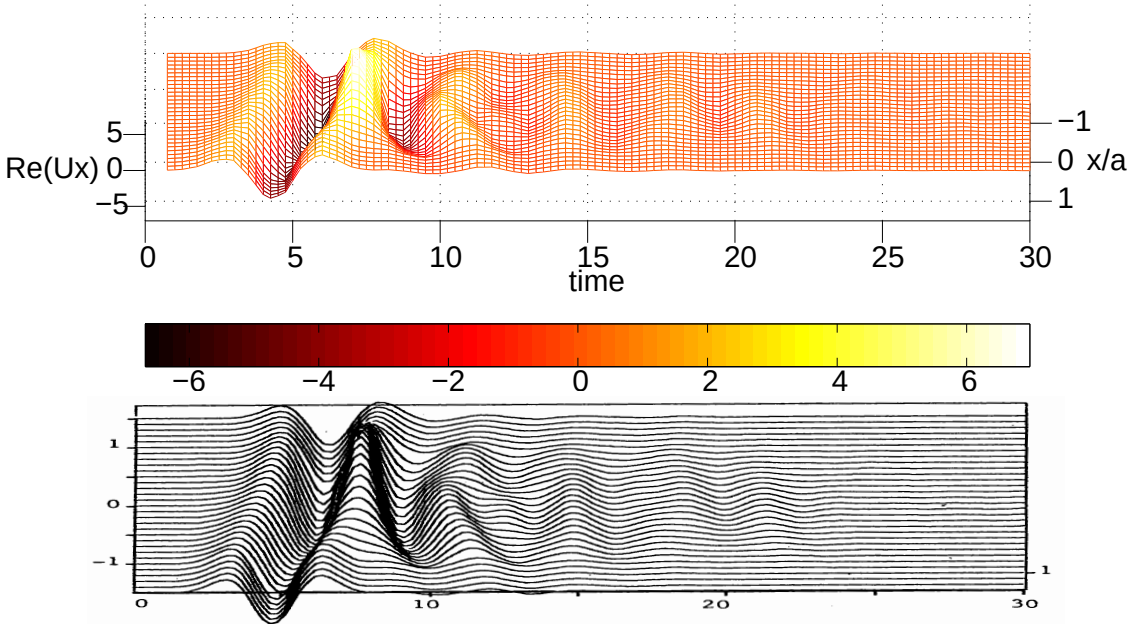

Figure 3.23: *Propagation of an oblique ($\theta = 30°$) incident plane SV–wave in a semi-spherical alluvial basin, $f_0 = 0.25$Hz: x-component of FMM (top) and standard BEM [157] (bottom) computed displacement along the Ox axis against time.*

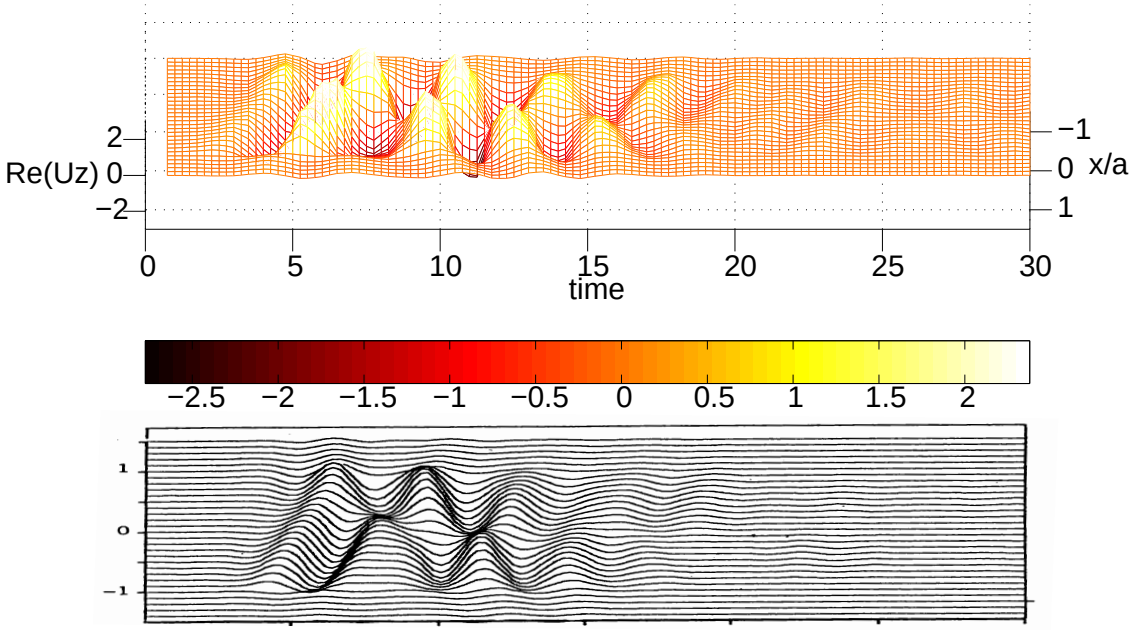

Figure 3.24: *Propagation of an oblique ($\theta = 30°$) incident plane SV–wave in a semi-spherical alluvial basin, $f_0 = 0.25$ Hz: z-component of FMM (top) and standard BEM [157] (bottom) computed displacement along the Ox axis against time.*

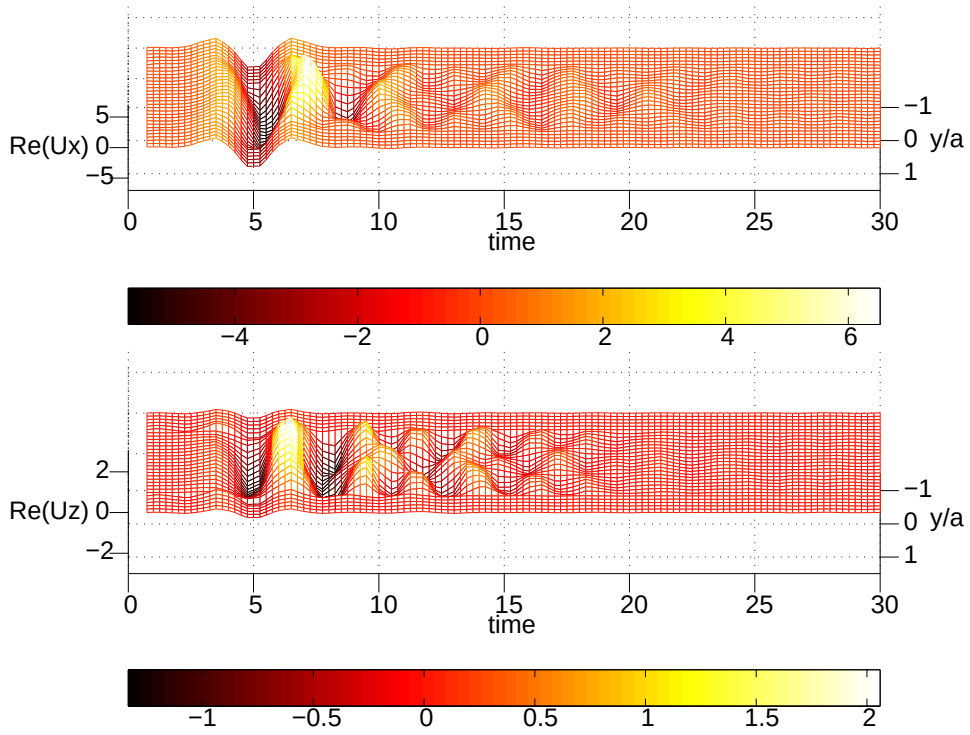

Figure 3.25: *Propagation of an oblique ($\theta = 30°$) incident plane SV–wave in a semi-spherical alluvial basin, $f_0 = 0.25$ Hz: x- (top) and z-components (bottom) of FMM computed displacement along the Oy axis against time.*

These results, visually compared with those previously published by [156], validate our implementation. We note in these figures that the time domain amplification is lower than the spectral amplification. It is due to the fact that in time domain, the propagation process also influences the signal duration. To investigate this parameter, we use the definition proposed in [205]. In Fig. 3.26, the integrals $\int u_x^2 dt$ and $\int u_z^2 dt$ are displayed against time. The duration of displacement at the basin center is estimated on that basis as about 5.9 s (for the x-component) and 8.4 s (for the z-component) while the duration of the input signal is estimated as about 3.7 s.

Higher fundamental frequency

The use of the FM-BEM allows us to consider higher fundamental frequency, for which no published results are available for comparison purposes. The following results are concerned with the same problem of an oblique incident plane SV–wave propagating in a semi-spherical basin but for a fundamental frequency twice higher: $f_0 = 0.50$Hz ($t_p = 2$ s and $t_s = 5$ s). In this example, two meshes are used: $\mathcal{M}_0$, featuring $N = 36,033$ DOFs and $\mathcal{M}_1$ (created using a subdivision procedure), featuring $N = 143,451$ DOFs. For this computation, 64 sample frequencies have been used, for frequencies ranging between 0 and 1.70 Hz. The x- and z-components of the displacement for $t \in [0, 30]$ are plotted against the Ox and Oy axes in Figs. 3.27 and 3.28, respectively.

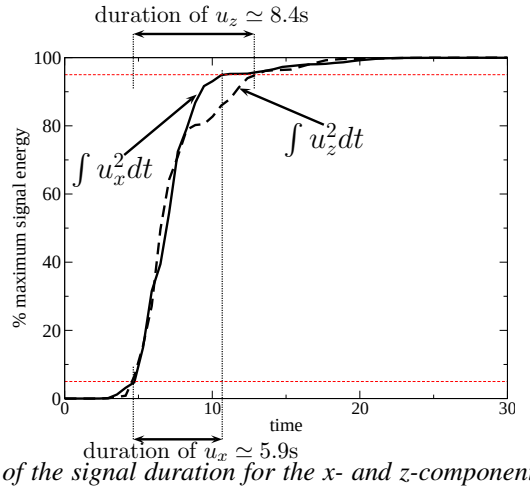

Figure 3.26: *Estimation of the signal duration for the x- and z-components of displacement at the basin center, $f_0 = 0.25$ Hz.*

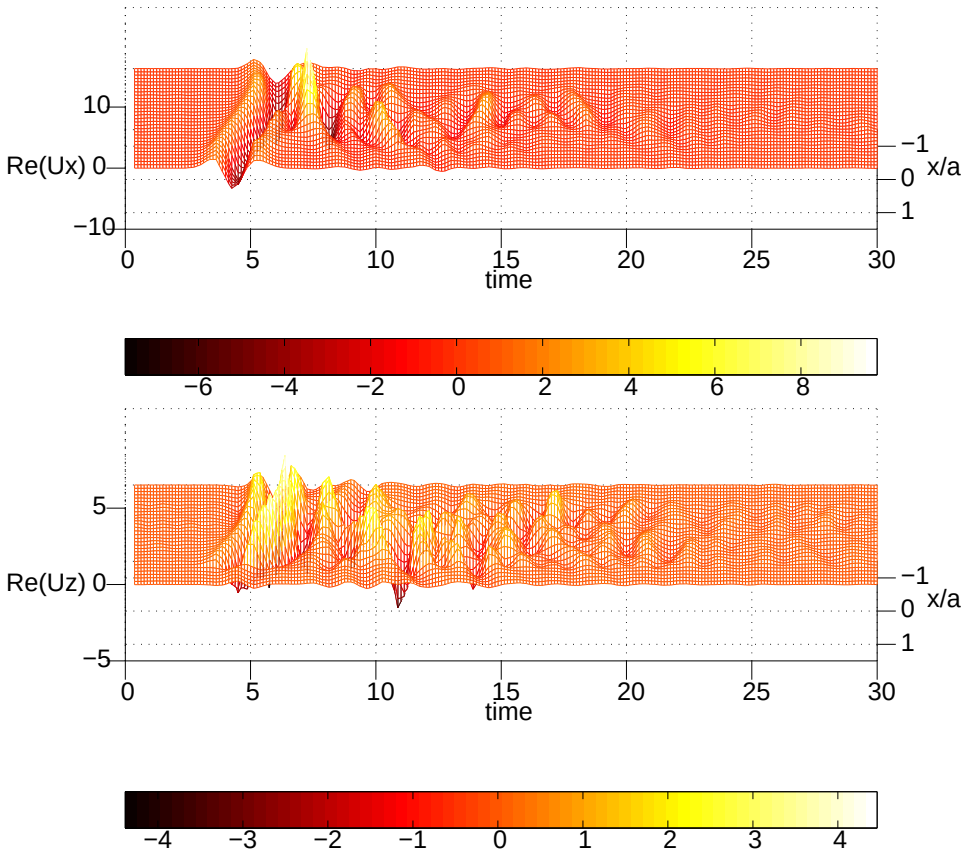

Figure 3.27: *Propagation of an oblique ($\theta = 30°$) incident plane SV–wave in a semi-spherical alluvial basin, $f_0 = 0.5$ Hz: x- (top) and z-components (bottom) of the FMM computed displacement on the Ox axis against time.*

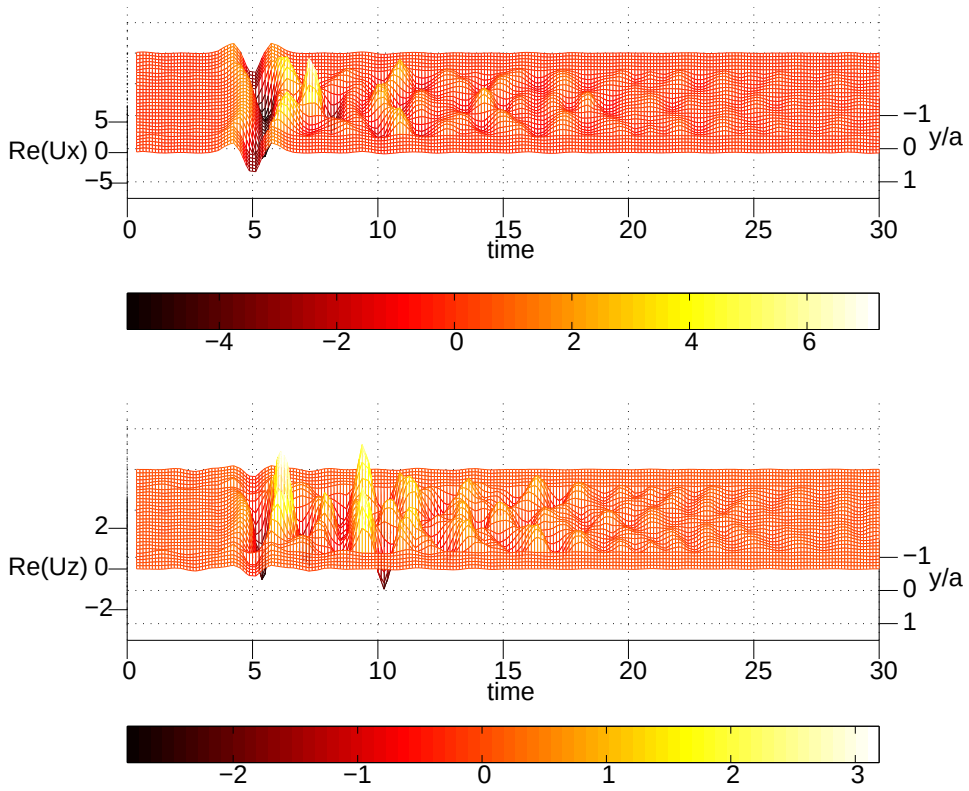

Figure 3.28: *Propagation of an oblique ($\theta = 30°$) incident plane SV–wave in a semi-spherical alluvial basin, $f_0 = 0.5$ Hz: x- (top) and z-components (bottom) of the FMM computed displacement on the Oy axis against time.*

We note in these figures that doubling the fundamental frequency led to an increase of the maximum amplification for all the components (see scales in Figs. 3.27 and 3.28). Once again, the duration of the displacement is estimated. In Figure 3.29, the integrals $\int u_x^2 dt$ and $\int u_z^2 dt$ are respectively displayed against time, leading to estimated values of bout 11.5 s (x-component) and 10 s (z-component) for the duration of displacement. Doubling the fundamental frequency thus induces a double duration of the x-component but only a small increase of the duration of the z-component.

Conclusions on the use of the present FMM for time-domain problems

Using standard BEM, the estimation of time-domain responses was limited in terms of sampling frequency range. Introducing the FMM enlarges the capabilities of the BEM in this respect, and time-domain responses with higher fundamental frequencies are now possible. In Section 3.6, a computation for a fundamental frequency twice higher that in [157] was run, even though our FM-BEM formulation is based on the full-space fundamental solutions whereas [157] use the half-space fundamental solutions. The mesh sizes used in Section 3.6 remain relatively modest for the FMM, the main computational limitation being currently caused by large GMRES iteration counts at the

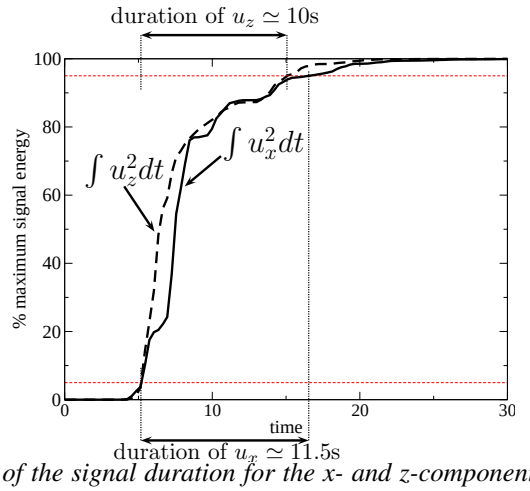

Figure 3.29: *Estimation of the signal duration for the x- and z-components of displacement at the basin center,* $f_0 = 0.50$ *Hz.*

higher sampling frequencies (up to $O(10^4)$ for this example). The current lack of a preconditioning strategy in the present formulation is addressed in Chapter 4.

3.7 CONCLUSIONS

In this chapter, a multi-level multi-domain fast multipole formulation has been proposed, based on works on single-region FMM presented in Chapter 2. A BE-BE coupling strategy has been presented. Comparisons with the analytical or previously published numerical results show the efficiency and accuracy of the present implementation.

The analysis of seismic wave propagation in canonical basins, for higher frequencies than in previously published results, show the numerical efficiency of the method and suggest that it is suitable to deal with realistic seismological applications. The transient response of 3-D basins has also been investigated to illustrate the large domain of application of the method.

We have seen that the method is now limited by the iteration counts and so that a preconditioning strategy needs to be introduced. This issue is discussed in Section 4.1 and in Chapter 5. Moreover, for time-domain response, the code is already competitive with time-domain methods but could be more efficient if the half-space fundamental solutions is used. This issue is discussed in Section 4.3.

Chapter 4

Preconditioning and other refinements of the elastodynamic FM-BEM

Contents

The efficiency of the elastodynamic FM-BEM presented in Chapters 2 (single-region) and 3 (multi-region) can still be improved in several ways. This chapter discusses in some details three avenues for enhancing the computational performances. The first one is preconditioning. A simple strategy is presented, and its efficiency demonstrated on some seismological examples (diffraction of plane waves by canyons and basins). The second one consists in reducing the number of necessary multipole moments. The third one is based on seeking a multipole expansion for the elastodynamic half-space fundamental solutions. The last two sections are of a preliminary nature, as these ideas are not implemented at the time of this writing.

4.1 PRECONDITIONING STRATEGY

In Chapters 2 and 3, it has been shown that the major limitation of the present FM-BEM iterative solver is the large number of iterations required to achieve convergence. The main limiting factor for the size of the studied examples was the very high iteration counts reached, rather than the CPU time per iteration or the memory requirement. The iteration count has been observed to increase whenever N is increased (with fixed ω) or ω is increased (with fixed N). Moreover, it seems that basin problems are more badly conditioned that canyon problems. For example for the case of the diffraction of a vertically incident plane P–wave by a semi-spherical canyon of Section 2.6.3, a problem with $N = 774,180$ DOFs requires 159 iterations. For the basin problems presented in Section 3.5, in the case of the diffraction of a vertically incident plane P–wave by a semi-spherical alluvial basin, 325 iterations are required for a problem featuring only $N = 190,299$ DOFs. A preconditioning strategy is clearly needed to improve convergence properties for the larger models.

4.1.1 General considerations on preconditioning

Preconditioning strategies for Krylov methods. The convergence of Krylov methods (as GMRES) depends on the eigenvalue distribution of the system matrix [179]. Consider the linear system:

$$Ax = b, \tag{4.1}$$

where A is the coefficient matrix, b is the right-hand side vector and x is the vector of unknowns. A *left* preconditioning strategy consists of solving the system

$$M^{-1}Ax = M^{-1}b,$$

instead of (4.1), where M is the preconditioning matrix or preconditioner. A *right* preconditioning strategy consists of considering the system

$$AM^{-1}y = b, \text{ with } Mx = y.$$

Split preconditioners can also be defined:

$$M_{\mathrm{L}}^{-1}AM_{\mathrm{R}}^{-1}y = M_{\mathrm{L}}^{-1}b, \text{ with } M_{\mathrm{R}}x = y.$$

The goal of a preconditioning strategy is to lower the condition number of the original matrix, i.e.:

$$\kappa(M^{-1}A) \leq \kappa(A) \text{ or } \kappa(AM^{-1}) \leq \kappa(A) \text{ or } \kappa(M_{\mathrm{L}}^{-1}AM_{\mathrm{R}}^{-1}) \leq \kappa(A)$$

where the condition number of a matrix X is defined as $\kappa(X) = ||X^{-1}||\ ||X||$ in terms of a matrix norm $||.||$. Moreover, a key requirement is that the computation of the preconditioning matrix M^{-1} has to be low CPU-consuming and that the application of the operator M^{-1} has to be efficient because it is applied at each iteration. The theoretical best left- or right- preconditioner is $M = A$ but it requires to invert the original matrix A, and hence does not bring any computational advantage.

Preconditioning strategies in the context of the FMM. When using the FMM, the design of robust preconditioners is an issue because the complete system matrix is not explicitly assemblied. The only explicitly available matrix is the matrix K^{near} into which the near contributions are assembled (see eq. (2.17) and Section 2.4.6). The determination of an optimal preconditioner in elastodynamics is, to the author's view, a largely open issue. In [90], a block-diagonal preconditioner is used, but problem sizes of at most $N = O(10^4)$ is considered. In electromagnetism where the FMM is more developed, this is a very active research issue. The simplest preconditioner is the one where M collects only the diagonal entries of A. The introduction of this simple preconditioner essentially amounts to scaling the equations. As scaling factors are already defined in Section 3.4.3, no significant improvement was expected, and none materialized upon testing this approach. A second possibility consists in using an incomplete LU factorization with threshold. In [194], this method has been successfully applied to various electromagnetic scattering problems, in conjunction with the FMM. A third preconditioner previously implemented for electromagnetic FMM is based on a Sparse Approximate Inverse (SPAI) of A, defined as the matrix M minimizing $||I - MA||_{\text{F}}$ subject to sparsity constrains [7]. Fourth, an embedded iterative scheme that combines nested GMRES solvers with different fast multipole computations is presented in [40]. In that work, the flexible GMRES (FGMRES [178]) and an inner-outer scheme are used: the matrix-vector product in the outer solver is done with an accurate FMM whereas in the inner solver it is done with a low-accuracy FMM preconditioned with SPAI. This method is shown to be efficient for problems featuring up to $N = O(10^6)$ DOFs.

4.1.2 Preconditioning strategy: use of the near contributions matrix

Since the definition of an efficient preconditioning is a big task, and due to time constrains, we have tried to develop a simple but efficient preconditioner. It is just a first step towards the development of an efficient preconditioning strategy and for the author, an exhaustive study needs to be done on this subject. The idea used in the present work is based on nested GMRES solvers in an inner-outer scheme where the inner GMRES solves preconditioning linear systems based on $M = K^{\text{near}}$ used as right preconditioner.

Flexible GMRES. For the definition of our inner-outer scheme, the flexible variant of GMRES is used [178]. Before presenting the Flexible GMRES (FGMRES), we recall the GMRES algorithm with right preconditioning, in Algorithm 4.1 (with ε the stopping criteria of GMRES, m the dimension of the Krylov subspaces used for the restarted GMRES, and V_m the orthonormal basis of the Krylov subspace). In this algorithm, the same preconditioner is used at each step and so the vectors $z_j = M^{-1}v_j$ are not stored.

$r_0 = b - Ax_0$, $\beta = ||r_0||_2$, $v_1 = r_0/\beta$
while $||r_0|| \geq \varepsilon(||A||||x_0|| + ||b||)$ **do**
  for $j = 1 \dots m$ **do**
    $z = M^{-1}v_j$
    $w = Az$
    for $i = 1 \dots j$ **do**
      $h_{i,j} = (w, v_i)$
      $w = w - h_{i,j}v_i$
    end for
    $h_{j+1,j} = ||w||_2$, $v_{j+1} = w/h_{j+1,j}$
    $V_m = [v_1, \dots, v_m]$, $\bar{H}_m = \{h_{i,j}\}_{1 \leq i \leq j+1, 1 \leq j \leq m}$
  end for
  $y_m = \text{argmin}_y ||\beta e_1 - \bar{H}_m y||_2$, $x_m = x_0 + M^{-1}V_m y_m$
  $x_0 = x_m$
  $r_0 = b - Ax_0$, $\beta = ||r_0||_2$, $v_1 = r_0/\beta$
end while

Algorithm 4.1: *GMRES(m) with right preconditioning.*

The flexible GMRES is based on the same principle than the right preconditioned GMRES but additionally allows to vary the preconditioner at each step. The only difference is that the vectors $z_j = M^{-1}v_j$ are now stored (see Algorithm 4.2).

$r_0 = b - Ax_0$, $\beta = ||r_0||_2$, $v_1 = r_0/\beta$
while $||r_0|| \geq \varepsilon(||A||||x_0|| + ||b||)$ **do**
  for $j = 1 \dots m$ **do**
    $z_j = M_j^{-1}v_j$
    $w = Az_j$
    for $i = 1 \dots j$ **do**
      $h_{i,j} = (w, v_i)$
      $w = w - h_{i,j}v_i$
    end for
    $h_{j+1,j} = ||w||_2$, $v_{j+1} = w/h_{j+1,j}$
    $Z_m = [z_1, \dots, z_m]$, $\bar{H}_m = \{h_{i,j}\}_{1 \leq i \leq j+1, 1 \leq j \leq m}$
  end for
  $y_m = \text{argmin}_y ||\beta e_1 - \bar{H}_m y||_2$, $x_m = x_0 + Z_m y_m$
  $x_0 = x_m$
  $r_0 = b - Ax_0$, $\beta = ||r_0||_2$, $v_1 = r_0/\beta$
end while

Algorithm 4.2: *FGMRES(m) with right preconditioning.*

Neither GMRES with right preconditioning nor FGMRES require explicit formation of the preconditioned matrix $M^{-1}A$. As a result, preconditioning systems $M_j z_j = v_j$ may themselves be solved using an iterative solver such as GMRES. But, for GMRES with right preconditioning the matrix M^{-1} needs to be explicitly formed to compute $M^{-1}V_m y_m$.

Preconditioning strategy. The preconditioning strategy implemented to speed up the convergence of the present FM-BEM is based on using two nested GMRES solvers, with the inner solver applied for the choice of preconditioning matrix $M = K^{\text{near}}$ (see Algorithm 4.3). In practice, the FGMRES routine `zPackfgmres.f` (see Appendix C and [220]) implementing Algorithm 4.2 is used, with $M_j = K^{\text{near}}$ and all systems $M_j z_j = v_j$ solved using GMRES with relative tolerance $\varepsilon_{\text{inner}} = 10^{-1}$. The advantage of this preconditioning strategy is that the computation of the preconditioner is not CPU-consuming since the sparse matrix K^{near} is already computed and stored. The matrix-vector product needed for the inner GMRES solver takes advantage of the structure of the computation of the near contributions and is accelerated using the BLAS library [218] (see Section 2.4.6).

Outer solver (FGMRES)
for $k = 1, \ldots$ **do**
  Matrix-vector product: FMM
  Preconditioning: **Inner solver** (GMRES)
  for $i = 1, \ldots$ **do**
    Matrix-vector product: multiply by the sparse matrix A^{near}
    No preconditioning
  end for
end for

Algorithm 4.3: *Inner-outer scheme used as preconditioning strategy.*

4.1.3 Efficiency of this preconditioning strategy on seismology-oriented examples

The efficiency of this preconditioning strategy is checked on various seismology-oriented problems: diffraction of plane waves in canyons or alluvial basins. In particular, all results of Chapter 5 have been obtained after having implemented the FGMRES-based preconditioner, and are thus presented with and without preconditioning. This illustrates the improvement brought by preconditioning on a large set of examples with various geometries, problem sizes and incident plane waves. In this section, a selection of these results is presented and discussed to demonstrate the efficiency of our preconditioning strategy.

Problem definition. Two examples are considered. The first one concerns the scattering of an oblique ($\theta = 30°$) incident plane P–wave by a semi-spherical canyon of radius a (Fig. 4.1) with $\nu^{(1)} = 0.25$. The free surface lies inside a disk of radius $D = 5a$ and the mesh features $N = 111,237$ DOFs.

The second one concerns the scattering of an oblique ($\theta = 30°$) incident plane P–wave by a semi-spherical basin of radius a (Fig. 4.2). The mechanical parameters are:

$$\nu^{(1)} = 0.25, \quad \mu^{(2)} = 0.3\mu^{(1)}, \quad \rho^{(2)} = 0.6\rho^{(1)}, \quad \nu^{(2)} = 0.3.$$

The free surface lies inside a disk of radius $D = 5a$ and the mesh features $N = 190,299$ DOFs. The non-dimensional frequency is set to $k_{\text{P}}^{(1)} a/\pi = 2$ for both examples.

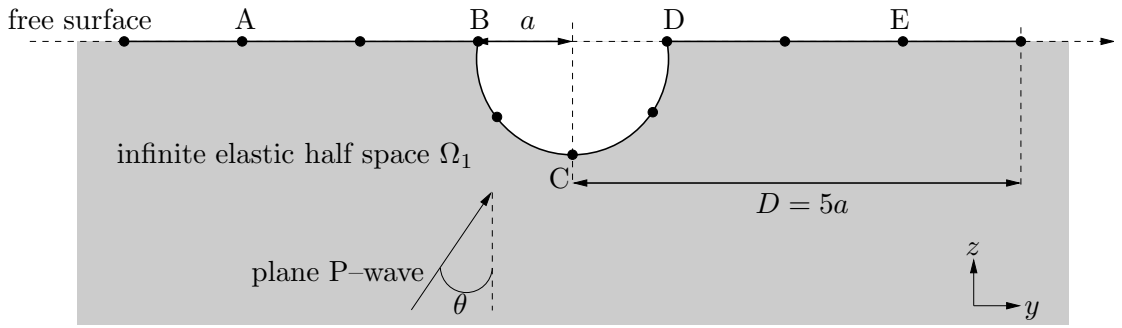

Figure 4.1: *Diffraction of an oblique incident plane P–wave by a semi-spherical canyon: notation.*

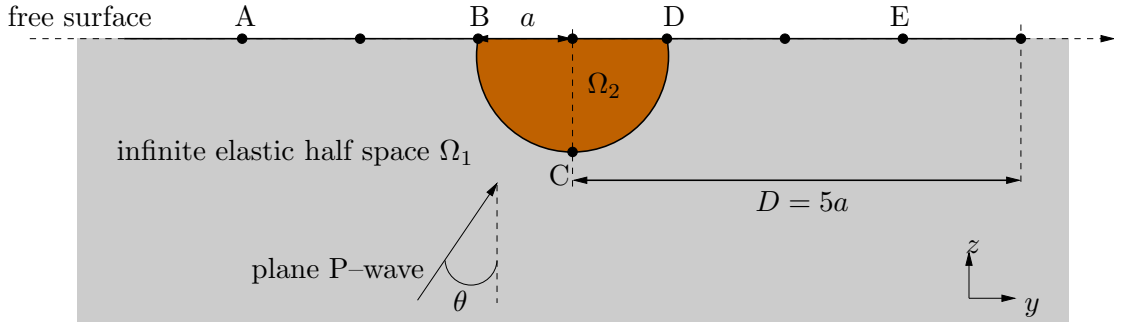

Figure 4.2: *Diffraction of an oblique incident plane P–wave by a semi-spherical basin: notation.*

Efficiency of the preconditioning strategy. In Table 4.1, the number of iterations and total CPU time without preconditioning are given for the two examples. The cumulative number of inner iterations, the number of outer iterations and the CPU time required for the complete solution procedure are also given, for the two preconditioned problems. The tolerance is set at $\varepsilon_{\text{inner}} = 10^{-1}$ for the inner solver and is still $\varepsilon_{\text{outer}} = 10^{-3}$ for the outer solver. No restart is used for the inner solver, while the outer solver is restarted every $m = 50$ iterations. The first remark is that for the two cases, the number of outer iterations is greatly reduced. Because of the use of an inner-outer scheme, the efficiency of the preconditioner should however not be evaluated solely by comparing the number of iterations without preconditioning to the number of outer iterations with preconditioning. Our preconditioning strategy involves inner iterations, which need to be taken into account for evaluating its overall efficiency. For the canyon problem, the total number of inner iterations is larger than the iteration count without preconditioning but, because the matrix-vector product in the inner solver is faster than that in the outer solver, the cumulative CPU time is reduced. For the basin problem, the total number of inner iterations is smaller than the number of iterations without preconditioning, resulting in a more substantial reduction of the total CPU time.

Influence of the tolerance used for the convergence of the inner solver. An important parameter in our inner-outer scheme is the tolerance $\varepsilon_{\text{inner}}$ used for the convergence of the inner GMRES. To study the influence of this parameter, $\varepsilon_{\text{inner}}$ is varied from $5\,10^{-2}$ to $5\,10^{-1}$. The (inner and outer) iteration counts and total CPU time are given in Table 4.2. If the precision $\varepsilon_{\text{inner}}$ is decreased, the total number of inner iterations is reduced while the number of outer iterations is increased.

Table 4.1: *Diffraction of an incident plane wave by a semi-spherical canyon and basin: iteration counts and CPU time (with and without preconditioning).*

	without prec.		with prec.		
	nb iter.	CPU time	nb iter. (inner)	nb iter. (outer)	CPU time
canyon problem	43	$33'19''$	70	17	$25'36''$
basin problem	388	$7\text{h}59'27''$	231	26	$2\text{h}30'54''$

Since outer iterations are more CPU-consuming than inner iterations, a good compromise between the number of outer iterations and the number of inner iterations need to be achieved to have an efficient preconditioning strategy. The optimal value for this problem is $\varepsilon_{\text{inner}} = 10^{-1}$. But, this value depends on the problem size (and so the ratio between the CPU time per inner iteration and the CPU time per outer iteration), the recommended value, which will be used in the following, is $\varepsilon = 10^{-1}$.

Table 4.2: *Diffraction of an incident plane wave by a semi-spherical basin: influence of the tolerance ε_{inner} used for the convergence of the inner solver.*

$\varepsilon_{\text{inner}}$	nb iter. (inner)	nb iter. (outer)	CPU time
$5\,10^{-2}$	338	25	$3\text{h}12'34''$
$8\,10^{-2}$	248	25	$2\text{h}35'43''$
$1\,10^{-1}$	231	26	$2\text{h}30'54''$
$3\,10^{-1}$	164	41	$2\text{h}50'44''$
$5\,10^{-1}$	171	58	$3\text{h}31'43''$

4.1.4 Conclusions on the preconditioning strategy

A simple and efficient preconditioning strategy has proposed and implemented in this section. This strategy is shown to be efficient on canyon problems and more on basin problems (which are more ill-conditioned). A more exhaustive study on the efficiency of this preconditioning strategy according to the geometry, non-dimensional frequency, incident plane waves is given in Chapter 5. The examples presented in Chapter 5 show that for canyon and basin problems featuring more than $N = O(10^5)$ DOFs, this preconditioning strategy is efficient. Moreover, if the non-dimensional frequency increases, the iteration count increases (and also the total CPU time) but lower if the preconditioning strategy is used. The definition of an optimal preconditioning strategy is a key point to increase the efficiency of the elastodynamic FM-BEM. We think that further study is still needed on this subject. Due to time constrains, some features of the present preconditioning strategy could not be investigated. For example, the restart parameter for both inner and outer solvers is expected to have an influence on the efficiency of our preconditioning strategy. Another promising avenue consists in introducing a threshold on the entries of K^{near}, so as to retain only the largest ones and make M sparser than the current choice $M = K^{\text{near}}$. Moreover, a comparative study with the other usual preconditioning approaches used in electromagnetic FMM (incomplete LU, SPAI, inner-outer

GMRES with two embedded FMM using various level of accuracy) is expected to bring worthwhile insight on this issue.

4.2 IMPROVED MULTIPOLE FORMULATION

After having defined a preconditioning strategy to reduce the total CPU time, the aim of this section is to give some directions to improve the elastodynamic multipole formulation presented in Chapters 2 and 3. The idea is to reduce the number of components stored for eqs. (2.20a, 2.21a) from three (using the Cartesian coordinates) to two (using an appropriate system of coordinates).

4.2.1 Formulation with two components for $\mathcal{R}^{S,t}$

The multipole moment $\mathcal{R}^{S,t}$ is defined by

$$\mathcal{R}_k^{\mathrm{S},t}(\hat{\boldsymbol{s}};\mathcal{C}_y) = \frac{1}{\mu}\big[\delta_{ka} - \hat{s}_k\hat{s}_a\big]\int_{\partial\Omega\cap\mathcal{C}_y} t_a(\boldsymbol{y})e^{\mathrm{i}k_\mathrm{S}\hat{\boldsymbol{s}}.(\boldsymbol{y}-\boldsymbol{y}_0)}dS_{\tilde{y}} \tag{4.2}$$

The only part which is dependent of the three Cartesian coordinates in eq. (4.2) is the factor $\alpha_{ka} = \delta_{ka} - \hat{s}_k\hat{s}_a$. The idea to reduce the number of multipole moments is to use the spherical orthonormal frame $(\hat{\boldsymbol{s}}(\theta,\phi), \boldsymbol{e}_\theta, \boldsymbol{e}_\phi)$ (Fig. 4.3) instead of the Cartesian system. With this notation, one has

$$I - \hat{\boldsymbol{s}}\otimes\hat{\boldsymbol{s}} = \boldsymbol{e}_\theta\otimes\boldsymbol{e}_\theta + \boldsymbol{e}_\phi\otimes\boldsymbol{e}_\phi$$

Because $\hat{\boldsymbol{s}}$ is a vector on the unit sphere, it is written:

$$\hat{\boldsymbol{s}} = \sin\theta\cos\phi\,\boldsymbol{e}_1 + \sin\theta\sin\phi\,\boldsymbol{e}_2 + \cos\theta\,\boldsymbol{e}_3$$

where θ and ϕ are the angular spherical coordinates defined in Section 2.4.3. As a result, eq. (4.2) can be reformulated with only two components:

$$\mathcal{R}_\theta^{S,t}(\hat{\boldsymbol{s}};\mathcal{C}_y) = \frac{1}{\mu}\int_{\partial\Omega\cap\mathcal{C}_y}[\boldsymbol{t}(\boldsymbol{y}).\boldsymbol{e}_\theta]e^{ik_\mathrm{S}\hat{\boldsymbol{s}}.(\boldsymbol{y}-\boldsymbol{y}_0)}dS_y, \tag{4.3a}$$

$$\mathcal{R}_\phi^{S,t}(\hat{\boldsymbol{s}};\mathcal{C}_y) = \frac{1}{\mu}\int_{\partial\Omega\cap\mathcal{C}_y}[\boldsymbol{t}(\boldsymbol{y}).\boldsymbol{e}_\phi]e^{ik_\mathrm{S}\hat{\boldsymbol{s}}.(\boldsymbol{y}-\boldsymbol{y}_0)}dS_y. \tag{4.3b}$$

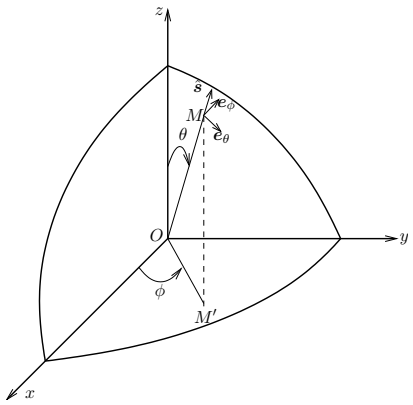

Figure 4.3: *Spherical coordinates on the unit sphere.*

The Cartesian components of $\boldsymbol{e}_\theta$, $\boldsymbol{e}_\phi$ being given by

$$\begin{aligned} \boldsymbol{e}_\theta &= \cos\theta\cos\phi\,\boldsymbol{e}_1 + \cos\theta\sin\phi\,\boldsymbol{e}_2 - \sin\theta\,\boldsymbol{e}_3, \\ \boldsymbol{e}_\phi &= -\sin\phi\,\boldsymbol{e}_1 + \cos\phi\,\boldsymbol{e}_2 \end{aligned} \tag{4.4}$$

one has:

$$\begin{aligned} \boldsymbol{t}(\boldsymbol{y}).\boldsymbol{e}_\theta = &\quad t_x(\boldsymbol{y})\cos\theta\cos\phi + t_y(\boldsymbol{y})\cos\theta\sin\phi - t_z(\boldsymbol{y})\sin\theta, \\ \boldsymbol{t}(\boldsymbol{y}).\boldsymbol{e}_\phi = &\quad -t_x(\boldsymbol{y})\sin\phi + t_y(\boldsymbol{y})\cos\phi. \end{aligned}$$

This formulation with two moments is similar to the one proposed in electromagnetism by Collino and Millot [51] and used by Sylvand [200].

4.2.2 Formulation with two components for $\mathcal{R}^{S,u}$

The same type of reformulation can be written for the multipole moment

$$\mathcal{R}_k^{\mathrm{S},u}(\hat{\boldsymbol{s}};\mathcal{C}_y) = -\mathrm{i}k_\mathrm{S}\left[\delta_{ik}\hat{s}_j + \delta_{jk}\hat{s}_i - 2\hat{s}_i\hat{s}_j\hat{s}_k\right]\int_{\partial\Omega\cap\mathcal{C}_y} u_i(\boldsymbol{y})n_j(\boldsymbol{y})e^{\mathrm{i}k_\mathrm{S}\hat{\boldsymbol{s}}.(\boldsymbol{y}-\boldsymbol{y}_0)}dS_{\tilde{y}} \tag{4.5}$$

Writting the terms under the integral using the spherical coordinates $(\hat{\boldsymbol{s}}(\theta,\phi),\boldsymbol{e}_\theta,\boldsymbol{e}_\phi)$, it appears that:

$$\begin{aligned} (\hat{s}_jn_j)\boldsymbol{u} + (\hat{s}_iu_i)\boldsymbol{n} - 2\hat{s}_iu_i\hat{s}_jn_j\hat{\boldsymbol{s}} = &\left[(\hat{s}_jn_j)(\boldsymbol{u}.\boldsymbol{e}_\theta) + (\hat{s}_iu_i)(\boldsymbol{n}.\boldsymbol{e}_\theta)\right]\boldsymbol{e}_\theta \\ &+ \left[(\hat{s}_jn_j)(\boldsymbol{u}.\boldsymbol{e}_\phi) + (\hat{s}_iu_i)(\boldsymbol{n}.\boldsymbol{e}_\phi)\right]\boldsymbol{e}_\phi \end{aligned}$$

So, the multipole moment eq. (4.5) can be reformulated:

$$\mathcal{R}_\theta^{S,u}(\hat{\boldsymbol{s}};\mathcal{C}_y) = -ik_\mathrm{S}\int_{\partial\Omega\cap\mathcal{C}_y}\left[\big(\hat{s}_jn_j(\boldsymbol{y})\big)\boldsymbol{u}(\boldsymbol{y}) + \big(\hat{s}_iu_i(\boldsymbol{y})\big)\boldsymbol{n}(\boldsymbol{y})\right].\boldsymbol{e}_\theta\; e^{ik_\mathrm{S}\hat{\boldsymbol{s}}.(\boldsymbol{y}-\boldsymbol{y}_0)}dS_y \tag{4.6a}$$

$$\mathcal{R}_\phi^{S,u}(\hat{\boldsymbol{s}};\mathcal{C}_y) = -ik_\mathrm{S}\int_{\partial\Omega\cap\mathcal{C}_y}\left[\big(\hat{s}_jn_j(\boldsymbol{y})\big)\boldsymbol{u}(\boldsymbol{y}) + \big(\hat{s}_iu_i(\boldsymbol{y})\big)\boldsymbol{n}(\boldsymbol{y})\right].\boldsymbol{e}_\phi\; e^{ik_\mathrm{S}\hat{\boldsymbol{s}}.(\boldsymbol{y}-\boldsymbol{y}_0)}dS_y \tag{4.6b}$$

4.2.3 Modified FMM algorithm with minimal number of moments

Using this new formulation, the computation of the multipole moments is done using eq. (4.3a,b) (resp. eq. (4.6a,b)) instead of eq. (2.21a) (resp. eq. (2.20a)). The transfer pass is unchanged except that the operation is performed separately on the two components (4.3a,b) (resp. (4.6a,b)) and so two local expansions are computed instead of three. For the final computation of the "FM" contributions, eq. (2.25), the local expansions are written in Cartesian coordinates:

$$\mathcal{L}^{S,\alpha}(\hat{\boldsymbol{s}};\mathcal{C}_x) = \mathcal{L}_\theta^{S,\alpha}(\hat{\boldsymbol{s}};\mathcal{C}_x).\boldsymbol{e}_\theta + \mathcal{L}_\phi^{S,\alpha}(\hat{\boldsymbol{s}};\mathcal{C}_x).\boldsymbol{e}_\phi \;\text{ with } \alpha = u,t.$$

The difficulty when using this formulation is the definition of the direct (resp. inverse) extrapolations. In [200], in the case of electromagnetism, some simple ideas are given to easily adapt the extrapolation procedure of Section 2.4.4 to such configurations. Numerical experiments have to be performed to define an adequate extrapolation procedure. The difficulty is due to the fact that, with the formulation with two multipole moments, $\boldsymbol{t}(\boldsymbol{y}).\boldsymbol{e}_\theta$ and $\boldsymbol{t}(\boldsymbol{y}).\boldsymbol{e}_\phi$ depend on $\hat{\boldsymbol{s}}$. So, to be able to reuse the extrapolation procedure defined in Section 2.4.4, the terms depending on θ and ϕ need to be of finite bandwidth.

4.2.4 Conclusions on the improved multipole formulation

With these simple changes of coordinates, the total number of multipole moments (and hence of local expansions) is reduced from 8 to 6. As a result, the memory requirements and CPU time per iteration are expected to be reduced in the same proportion. Due to time constraints, this improvement is not currently implemented, but it will be in the future.

4.3 FORMULATION OF MULTIPOLE EXPANSIONS OF THE HALF-SPACE FUNDAMENTAL SOLUTIONS

The last topic discussed in this chapter is concerned with improving the efficiency of the elastodynamic FM-BEM applied to semi-infinite media. Instead of using the elastic full-space fundamental solutions, the idea is to use the elastic half-space fundamental solutions that satisfy a traction-free boundary condition, thus avoiding any BEM discretization on the free surface. But, unlike the full-space fundamental solutions, the elastic half-space fundamental solutions are neither derivatives of the Helmholtz fundamental solution nor of $1/r$. As a result, multipole expansions of the elastic half-space fundamental solutions cannot be obtained in a simple way, and are not currently known. In this section, the formulation of multipole expansions of the elastic half-space fundamental solutions are presented and some ideas for the numerical implementation are given.

4.3.1 Computation of single-layer potential

Considering the evaluation of single-layer elastodynamic potentials of the form

$$\boldsymbol{v}(\boldsymbol{x}) = \int_B \boldsymbol{U}^{\mathrm{T}}(\boldsymbol{x},\boldsymbol{y})\boldsymbol{p}(\boldsymbol{y})\ \mathrm{d}B_y, \tag{4.7}$$

where B is a surface or a volume embedded in the lower half-space $y_3 \leq 0$ (Fig. 4.4), the density $\boldsymbol{p}$ denotes a traction distribution (over a surface) or a body force distribution and $\boldsymbol{U}(\boldsymbol{x},\boldsymbol{y})$ denotes the half-space elastodynamic fundamental solution, which satisfies a traction-free condition on the free surface, i.e.:

$$\boldsymbol{T}(\boldsymbol{x},\boldsymbol{y}) = \boldsymbol{e}_3.\boldsymbol{C} : \nabla_y \boldsymbol{U}(\boldsymbol{x},\boldsymbol{y}) = \boldsymbol{0} \quad (y_3 = 0).$$

The starting point is to decompose $\boldsymbol{U}(\boldsymbol{x},\boldsymbol{y})$ as

$$\boldsymbol{U}(\boldsymbol{x},\boldsymbol{y}) = \boldsymbol{U}_\infty(\boldsymbol{x},\boldsymbol{y}) + \bar{\boldsymbol{U}}_\infty(\boldsymbol{x},\boldsymbol{y}) + \boldsymbol{U}_{\mathrm{C}}(\boldsymbol{x},\boldsymbol{y}),$$

where $\boldsymbol{U}_\infty$ is the elastic full-space fundamental solution, $\bar{\boldsymbol{U}}_\infty$ is the image full-space fundamental solution, corresponding to a point source applied at the mirror image source point, and $\boldsymbol{U}_{\mathrm{C}}$ is the complementary fundamental solution. The single-layer potential (4.7) can accordingly be set, using obvious notation, in the form

$$\boldsymbol{v}(\boldsymbol{x}) = \boldsymbol{v}_\infty(\boldsymbol{x}) + \bar{\boldsymbol{v}}_\infty(\boldsymbol{x}) + \boldsymbol{v}_{\mathrm{C}}(\boldsymbol{x}).$$

The contributions $\boldsymbol{v}_\infty(\boldsymbol{x})$ and $\bar{\boldsymbol{v}}_\infty(\boldsymbol{x})$ can be evaluated using the "standard" FMM associated with the diagonal form-based decomposition of the full-space fundamental solution. Attention is therefore directed towards the contribution $\boldsymbol{v}_{\mathrm{C}}(\boldsymbol{x})$ involving the complementary fundamental solution. The first step is to formulate $\boldsymbol{U}_{\mathrm{C}}$ in a form which enables a "fast" computation.

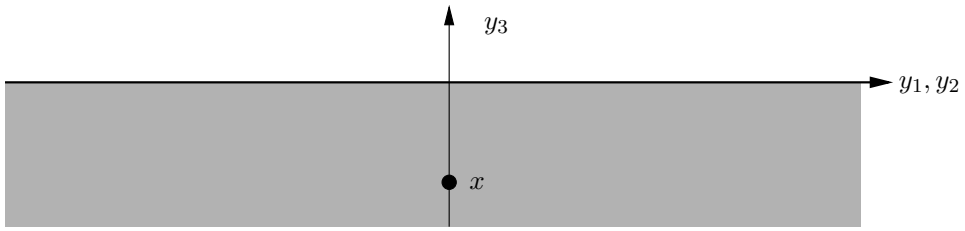

Figure 4.4: *Multipole expansions of the half-space fundamental solutions: notations.*

4.3.2 Derivation in the Fourier space

The method to formulate the complementary fundamental solution, similar to the method to define low frequency FMMs [61, 100], is based on a Fourier transform with respect to the two spatial coordinates parallel to the free-space, i.e. y_1, y_2 here. The spatial coordinates (y_1, y_2) are associated to transformed coordinates (k_1, k_2) in the Fourier space. The Fourier transform is defined by

$$\hat{\boldsymbol{u}}(k_1, k_2, y_3) = \frac{1}{4\pi^2} \int_{\mathbb{R}^2} e^{-i(y_1 k_1 + y_2 k_2)} \boldsymbol{u}(y_1, y_2, y_3) dy_1 dy_2.$$

Full-space fundamental solution. Even though this formulation is not necessary in the FMM computation of $\boldsymbol{v}_\infty$, the full-space fundamental solutions $\hat{\boldsymbol{u}}_\infty$ in the Fourier space is needed for finding the complementary fundamental solution $\hat{\boldsymbol{u}}_{\mathrm{C}}$. The free-space fundamental solution $\hat{\boldsymbol{u}}_\infty$ associated with a point force $\boldsymbol{F}$ applied at $\boldsymbol{x}$ satisfies the elastodynamic equation (1.10), which becomes in the Fourier space

$$\boldsymbol{A}\hat{\boldsymbol{u}}_\infty + \boldsymbol{B}\hat{\boldsymbol{u}}_\infty^{'} + \boldsymbol{C}\hat{\boldsymbol{u}}_\infty^{''} + \delta(y_3 - x_3)\boldsymbol{F} = 0, \tag{4.8}$$

where the prime symbol denotes differentiation with respect to y_3 and having set

$$\boldsymbol{A} = \frac{\mu}{\zeta} \begin{bmatrix} \zeta(-k^2 + k_{\mathrm{S}}^2) - k_1^2 & -k_1 k_2 & 0 \\ -k_1^2 & \zeta(-k^2 + k_{\mathrm{S}}^2) - k_2^2 & 0 \\ 0 & 0 & \zeta(-k^2 + k_{\mathrm{S}}^2) \end{bmatrix},$$

$$\boldsymbol{B} = \frac{\mu}{\zeta} \begin{bmatrix} 0 & 0 & -\mathrm{i}k_1 \\ 0 & 0 & -\mathrm{i}k_2 \\ -\mathrm{i}k_1 & -\mathrm{i}k_2 & 0 \end{bmatrix}, \quad \boldsymbol{C} = \frac{\mu}{\zeta} \begin{bmatrix} \zeta & 0 & 0 \\ 0 & \zeta & 0 \\ 0 & 0 & \zeta + 1 \end{bmatrix},$$

with $k^2 = k_1^2 + k_2^2$ and $\zeta = 1 - 2\nu$. The characteristic polynomial $P(s) = \det\Big(\boldsymbol{A} + s\boldsymbol{B} + s^2\boldsymbol{C}\Big)$ of the differential equation (4.8) has two roots: $s_{\mathrm{S}}^2 = k^2 - k_{\mathrm{S}}^2$ (double) and $s_{\mathrm{P}}^2 = k^2 - k_{\mathrm{P}}^2$ (simple). As a result, $\hat{\boldsymbol{u}}_\infty$ has a priori the form

$$\hat{\boldsymbol{u}}_\infty = \boldsymbol{U}_{\mathrm{P}}^+ e^{-s_{\mathrm{P}}(y_3 - x_3)} + \boldsymbol{U}_{\mathrm{P}}^- e^{s_{\mathrm{P}}(y_3 - x_3)} + (\boldsymbol{U}_{\mathrm{S}}^+ + y_3 \boldsymbol{V}_{\mathrm{S}}^+) e^{-s_{\mathrm{S}}(y_3 - x_3)} + (\boldsymbol{U}_{\mathrm{S}}^- + y_3 \boldsymbol{V}_{\mathrm{S}}^-) e^{s_{\mathrm{S}}(y_3 - x_3)} \tag{4.9}$$

in both regions $y_3 > x_3$ and $y_3 < x_3$. The next step consists in setting $\hat{\boldsymbol{u}}_\infty$ in the form

$$\hat{\boldsymbol{u}}_\infty = \hat{\boldsymbol{u}}_\infty^+ H(y_3 - x_3) + \hat{\boldsymbol{u}}_\infty^- H(-y_3 + x_3), \tag{4.10}$$

valid for all y_3, where H is the Heaviside step function and $\hat{\boldsymbol{u}}^+_\infty$, $\hat{\boldsymbol{u}}^-_\infty$ each have the form (4.9). Since $\hat{\boldsymbol{u}}_\infty$ must in addition decay as $y_3 \to \pm\infty$, it follows that $\boldsymbol{U}^-_{\mathrm{P}}$ and $(\boldsymbol{U}^-_{\mathrm{S}} + y_3\boldsymbol{V}^-_{\mathrm{S}})$ must be set to zero in $\hat{\boldsymbol{u}}^+_\infty$, and likewise $\boldsymbol{U}^+_{\mathrm{P}}$ and $(\boldsymbol{U}^+_{\mathrm{S}} + y_3\boldsymbol{V}^+_{\mathrm{S}})$ are zero in $\hat{\boldsymbol{u}}^-_\infty$, i.e. one seeks $\hat{\boldsymbol{u}}_\infty$ of the form (4.10) with

$$\hat{\boldsymbol{u}}^+_\infty = \boldsymbol{U}^+_{\mathrm{P}} e^{-s_{\mathrm{P}}(y_3-x_3)} + (\boldsymbol{U}^+_{\mathrm{S}} + y_3\boldsymbol{V}^+_{\mathrm{S}})e^{-s_{\mathrm{S}}(y_3-x_3)}, \tag{4.11a}$$

$$\hat{\boldsymbol{u}}^-_\infty = \boldsymbol{U}^-_{\mathrm{P}} e^{s_{\mathrm{P}}(y_3-x_3)} + (\boldsymbol{U}^-_{\mathrm{S}} + y_3\boldsymbol{V}^-_{\mathrm{S}})e^{s_{\mathrm{S}}(y_3-x_3)}. \tag{4.11b}$$

Next, enforcing that $\hat{\boldsymbol{u}}^+_\infty$ and $\hat{\boldsymbol{u}}^-_\infty$ thus defined satisfy the homogeneous equation $\boldsymbol{A}\hat{\boldsymbol{u}}_\infty + \boldsymbol{B}\hat{\boldsymbol{u}}'_\infty + \boldsymbol{C}\hat{\boldsymbol{u}}''_\infty = 0$, one finds that they must be of the form

$$\begin{aligned} \hat{\boldsymbol{u}}^+_\infty &= \boldsymbol{Q}^+\boldsymbol{E}(y_3)\boldsymbol{E}(-x_3)\boldsymbol{U}^+_\infty, \\ \hat{\boldsymbol{u}}^-_\infty &= \boldsymbol{Q}^-\boldsymbol{E}(y_3)\boldsymbol{E}(-x_3)\boldsymbol{U}^-_\infty, \end{aligned} \tag{4.12}$$

where $\boldsymbol{U}^+_\infty$ and $\boldsymbol{U}^-_\infty$ are 3-vectors of constants, and having set $\boldsymbol{E}(t) = \mathrm{Diag}\big(e^{s_{\mathrm{P}}t},\, e^{s_{\mathrm{S}}t},\, e^{s_{\mathrm{P}}t}\big)$ and

$$\boldsymbol{Q}^+ = \begin{bmatrix} \mathrm{i} & 0 & \mathrm{i}k_1/s_{\mathrm{P}} \\ 0 & \mathrm{i} & \mathrm{i}k_2/s_{\mathrm{P}} \\ k_1/s_{\mathrm{S}} & k_2/s_{\mathrm{S}} & 1 \end{bmatrix}, \quad \boldsymbol{Q}^- = \begin{bmatrix} \mathrm{i} & 0 & -\mathrm{i}k_1/s_{\mathrm{P}} \\ 0 & \mathrm{i} & -\mathrm{i}k_2/s_{\mathrm{P}} \\ -k_1/s_{\mathrm{S}} & -k_2/s_{\mathrm{S}} & 1 \end{bmatrix}.$$

The six constants involved in expressions (4.12) of $\hat{\boldsymbol{u}}^+_\infty$, $\hat{\boldsymbol{u}}^-_\infty$ are determined by enforcing (i) continuity of the displacement at $y_3 = x_3$, i.e.:

$$\hat{\boldsymbol{u}}^-_\infty(y_3 = x_3) = \hat{\boldsymbol{u}}^+_\infty(y_3 = x_3) \tag{4.13}$$

and (ii) satisfaction of equation (4.8) by (4.10), i.e.:

$$\boldsymbol{A}\hat{\boldsymbol{u}}_\infty + \boldsymbol{B}\hat{\boldsymbol{u}}'_\infty + \boldsymbol{C}\hat{\boldsymbol{u}}''_\infty + \boldsymbol{F}\delta(y_3 = x_3) = 0 \Longrightarrow \boldsymbol{C}(\hat{\boldsymbol{u}}^{+\prime}_\infty - \hat{\boldsymbol{u}}^{-\prime}_\infty)(y_3 = x_3) + \boldsymbol{F} = 0. \tag{4.14}$$

This leads, after some manipulation, to with

$$\boldsymbol{U}^+_\infty = \boldsymbol{Z}^{-1}_\infty \boldsymbol{F}, \quad \boldsymbol{U}^-_\infty = (\boldsymbol{Q}^-)^{-1}\boldsymbol{Q}^+\boldsymbol{U}^+_\infty, \tag{4.15}$$

$$\boldsymbol{Z}^{-1}_\infty = \frac{1}{2\mu s_{\mathrm{S}} k^2_{\mathrm{S}}} \begin{bmatrix} \mathrm{i}(k^2_{\mathrm{S}} - k^2_1) & -\mathrm{i}k_1k_2 & -k_1 s_{\mathrm{S}} \\ -\mathrm{i}k_1k_2 & \mathrm{i}(k^2_{\mathrm{S}} - k^2_2) & -k_2 s_{\mathrm{S}} \\ \mathrm{i}k_1 s_{\mathrm{S}} & \mathrm{i}k_2 s_{\mathrm{S}} & s_{\mathrm{P}} s_{\mathrm{S}} \end{bmatrix}.$$

Summing up, equations (4.12) and (4.15) define the free-space fundamental solution expressed in coordinates (k_1, k_2, y_3). The stress vector on free surface $y_3 = 0$ associated with $\hat{\boldsymbol{u}}_\infty$ is then given by

$$\hat{\boldsymbol{p}}^+_\infty = (\boldsymbol{D}\boldsymbol{Q}^+ + \boldsymbol{C}\boldsymbol{Q}^+\boldsymbol{\Lambda})\boldsymbol{E}(-x_3)\boldsymbol{Z}^{-1}_\infty \boldsymbol{F}$$

having set $\boldsymbol{\Lambda} = \mathrm{Diag}\big(s_{\mathrm{S}},\, s_{\mathrm{S}},\, s_{\mathrm{P}}\big)$ and

$$\boldsymbol{D} = \mu \begin{bmatrix} 0 & 0 & \mathrm{i}k_1 \\ 0 & 0 & \mathrm{i}k_2 \\ \mathrm{i}k_1\frac{-\zeta+1}{\zeta} & \mathrm{i}k_2\frac{-\zeta+1}{\zeta} & 0 \end{bmatrix}.$$

This corresponds to the following explicit expression, in Fourier space:

$$\hat{\boldsymbol{p}}_\infty^+ = \frac{1}{2\mu k_{\mathrm{S}}^2}\begin{bmatrix}(2k_1^2-k^2) & 2k_1k_2 & \mathrm{i}k_1\beta/s_{\mathrm{S}}\\ 2k_1k_2 & (2k_2^2-k^2) & \mathrm{i}k_2\beta/s_{\mathrm{S}}\\ -2\mathrm{i}k_1s_{\mathrm{S}} & -2\mathrm{i}k_2s_{\mathrm{S}} & -2k^2\end{bmatrix}\boldsymbol{F}e^{-s_{\mathrm{S}}x_3} + \frac{1}{2\mu k_{\mathrm{S}}^2}\begin{bmatrix}-2\mathrm{i}k_1^2 & -2\mathrm{i}k_1k_2 & 2\mathrm{i}k_1s_{\mathrm{P}}\\ -2\mathrm{i}k_1k_2 & -2\mathrm{i}k_2^2 & 2\mathrm{i}k_2s_{\mathrm{P}}\\ -\mathrm{i}k_1\beta/s_{\mathrm{P}} & -\mathrm{i}k_2\beta/s_{\mathrm{P}} & -\beta\end{bmatrix}\boldsymbol{F}e^{-s_{\mathrm{P}}x_3}$$

with β given by $\beta = k_{\mathrm{S}}^2 - 2k^2 = -(s_{\mathrm{S}}^2 + k^2)$.

Image full-space fundamental solution. Now, the image full-space fundamental solution, corresponding to a point source $\boldsymbol{SF}$ applied at the mirror image source point $\boldsymbol{Sx}$, is formulated in the Fourier space as:

$$\hat{\bar{\boldsymbol{u}}}_\infty = \boldsymbol{Q}^-\boldsymbol{E}(-y_3)\boldsymbol{E}(-x_3)\bar{\boldsymbol{U}}_\infty,$$

where $\boldsymbol{S} = \mathrm{Diag}\big(1,\ 1,\ -1\big)$ is the matrix associated with the symmetry with respect to plane $y_3 = 0$, $\bar{\boldsymbol{U}}_\infty = \bar{\boldsymbol{Z}}_\infty^{-1}\boldsymbol{SF}$, $\bar{\boldsymbol{Z}}_\infty = \boldsymbol{SZ}_\infty\boldsymbol{S}$. Finally, since $\boldsymbol{Q}^- = \boldsymbol{SQ}^+\boldsymbol{S}$, $\hat{\bar{\boldsymbol{u}}}_\infty$ is given by

$$\hat{\bar{\boldsymbol{u}}}_\infty = \boldsymbol{SQ}^+\boldsymbol{E}(-y_3)\boldsymbol{E}(-x_3)\boldsymbol{Z}_\infty^{-1}\boldsymbol{F}.$$

Note that, from the above formula, one has

$$\bar{\boldsymbol{U}}_\infty(\boldsymbol{x},\boldsymbol{y}) = \boldsymbol{SU}_\infty(\boldsymbol{Sx},\boldsymbol{y}).$$

The stress vector on the half-space boundary associated with $\hat{\bar{\boldsymbol{u}}}_\infty$ is found to be:

$$\hat{\bar{\boldsymbol{p}}}_\infty = -\boldsymbol{S}\hat{\boldsymbol{p}}_\infty^+.$$

Before formulating the complementary fundamental solutions, we note that the superposition of full-space and image fundamental solutions leads to:

$$\hat{\boldsymbol{p}}_\infty^+ + \hat{\bar{\boldsymbol{p}}}_\infty = (\boldsymbol{I}-\boldsymbol{S})\hat{\boldsymbol{p}}_\infty^+ = \frac{1}{\mu k_{\mathrm{S}}^2}\begin{Bmatrix}0\\0\\1\end{Bmatrix}\big(2\boldsymbol{V}'_{\mathrm{T}}e^{-s_{\mathrm{S}}x_3} + \beta\boldsymbol{V}'_{\mathrm{L}}e^{-s_{\mathrm{P}}x_3}\big)^{\mathrm{T}}\boldsymbol{F}$$

with

$$\boldsymbol{V}'_{\mathrm{T}} = \begin{Bmatrix}\mathrm{i}k_1s_{\mathrm{S}}\\ \mathrm{i}k_2s_{\mathrm{S}}\\ k^2\end{Bmatrix}, \qquad \boldsymbol{V}'_{\mathrm{L}} = \begin{Bmatrix}\mathrm{i}k_1/s_{\mathrm{P}}\\ \mathrm{i}k_2/s_{\mathrm{P}}\\ 1\end{Bmatrix}. \tag{4.16}$$

Complementary fundamental solution. Finally, the complementary fundamental solution in the Fourier space solves the homogeneous Navier equation in the region $y_3 \le 0$, i.e.

$$\boldsymbol{A}\hat{\boldsymbol{u}}_{\mathrm{C}} + \boldsymbol{B}\hat{\boldsymbol{u}}'_{\mathrm{C}} + \boldsymbol{C}\hat{\boldsymbol{u}}''_{\mathrm{C}} = 0, \qquad (y_3 \le 0) \tag{4.17}$$

and must hence have the form (4.9) for any $y_3 \le 0$. Moreover, $\hat{\boldsymbol{u}}_{\mathrm{C}}$ must decay in the limit $y_3 \to -\infty$, implying that it is in fact of the form (4.11b). On enforcing next that such $\hat{\boldsymbol{u}}_{\mathrm{C}}$ actually solves (4.17), one obtains

$$\hat{\boldsymbol{u}}_{\mathrm{C}} = \boldsymbol{Q}^-\boldsymbol{E}(-y_3)\boldsymbol{U}_{\mathrm{C}}$$

where the 3-vector $\boldsymbol{U}_{\mathrm{C}}$ of constants is to be determined from the free-surface condition

$$\hat{\boldsymbol{p}}_{\infty}^{+} + \hat{\bar{\boldsymbol{p}}}_{\infty} + \hat{\boldsymbol{p}}_{\mathrm{C}}^{-} = 0 \quad (y_3 = 0).$$

Enforcing this condition, the complementary fundamental solution takes the form

$$\boldsymbol{U}_{\mathrm{C}} = \boldsymbol{Z}_{\mathrm{C}}\boldsymbol{E}(-x_3)\boldsymbol{U}_{\infty}^{+}, \qquad \boldsymbol{Z}_{\mathrm{C}} = \frac{2}{\delta}\begin{Bmatrix} 2k_1 s_{\mathrm{S}} \\ 2k_2 s_{\mathrm{S}} \\ -\beta \end{Bmatrix}\begin{Bmatrix} 2k_1 s_{\mathrm{P}} & 2k_2 s_{\mathrm{P}} & -\beta \end{Bmatrix}$$

with $\boldsymbol{U}_{\infty}^{+}$ given by (4.15), and is thus found after some manipulation to have the explicit expression

$$\begin{aligned} \hat{\boldsymbol{u}}_{\mathrm{C}} &= \boldsymbol{Q}^{-}\boldsymbol{E}(-y_3)\boldsymbol{Z}_{\mathrm{C}}\boldsymbol{E}(-x_3)\boldsymbol{Z}_{\infty}^{-1}\boldsymbol{F} \\ &= \frac{s_{\mathrm{P}}}{\delta\mu k_{\mathrm{S}}^2}\big(2\boldsymbol{V}_{\mathrm{T}}e^{-s_{\mathrm{S}}y_3} + \beta\boldsymbol{V}_{\mathrm{L}}e^{-s_{\mathrm{P}}y_3}\big)\big(2\boldsymbol{V}'_{\mathrm{T}}e^{-s_{\mathrm{S}}x_3} + \beta\boldsymbol{V}'_{\mathrm{L}}e^{-s_{\mathrm{P}}x_3}\big)^{\mathrm{T}}\boldsymbol{F}, \end{aligned} \tag{4.18}$$

with δ defined by $\delta = \beta^2 - 4k^2 s_{\mathrm{P}} s_{\mathrm{S}}$, $\boldsymbol{V}'_{\mathrm{T}}, \boldsymbol{V}'_{\mathrm{L}}$ as given by (4.16), and

$$\boldsymbol{V}_{\mathrm{T}} = 2s_{\mathrm{P}}\begin{Bmatrix} \mathrm{i}k_1 s_{\mathrm{S}} \\ \mathrm{i}k_2 s_{\mathrm{S}} \\ -k^2 \end{Bmatrix}, \qquad \boldsymbol{V}_{\mathrm{L}} = \beta s_{\mathrm{P}}\begin{Bmatrix} \mathrm{i}k_1/s_{\mathrm{P}} \\ \mathrm{i}k_2/s_{\mathrm{P}} \\ -1 \end{Bmatrix}$$

Note that the unique (real, positive) value k_{R} of k such that $\delta(k_{\mathrm{R}}) = 0$ is the Rayleigh wavenumber (i.e. k_{R} is, as expected, a pole of $\hat{\boldsymbol{u}}_{\mathrm{C}}$), and that one has $k_{\mathrm{P}} < k_{\mathrm{S}} < k_{\mathrm{R}}$. Note also that (4.18) contains products of functions of y_3 and x_3, which is an essential feature for fast evaluation of (4.7).

Finally, the complementary Green's *tensor* $\hat{\boldsymbol{U}}_{\mathrm{C}}$ (expressed in Fourier space) is such that $\hat{\boldsymbol{U}}_{\mathrm{C}}\boldsymbol{F} = \hat{\boldsymbol{u}}_{\mathrm{C}}$, which implies

$$\hat{\boldsymbol{U}}_{\mathrm{C}} = \frac{s_{\mathrm{P}}}{\delta\mu k_{\mathrm{S}}^2}\big(2\boldsymbol{V}_{\mathrm{T}}e^{-s_{\mathrm{S}}y_3} + \beta\boldsymbol{V}_{\mathrm{L}}e^{-s_{\mathrm{P}}y_3}\big)\big(2\boldsymbol{V}'_{\mathrm{T}}e^{-s_{\mathrm{S}}x_3} + \beta\boldsymbol{V}'_{\mathrm{L}}e^{-s_{\mathrm{P}}x_3}\big)^{\mathrm{T}}.$$

4.3.3 Half-space fundamental solution

Once the complementary fundamental solution obtained in the Fourier space, $\boldsymbol{U}_{\mathrm{C}}(\boldsymbol{x}, \boldsymbol{y})$ is given in physical coordinates in terms of an inverse Fourier transform:

$$\boldsymbol{U}_{\mathrm{C}}(\boldsymbol{x}, \boldsymbol{y}) = \int_{\mathbb{R}^2} e^{\mathrm{i}(k_1(y_1 - x_1) + k_2(y_2 - x_2))}\hat{\boldsymbol{U}}_{\mathrm{C}}(k_1, k_2, y_3, x_3)\ \mathrm{d}k_1\mathrm{d}k_2.$$

On introducing polar coordinates in the Fourier space, i.e. setting $(k_1, k_2) = k(\cos\alpha, \sin\alpha)$, one gets

$$\boldsymbol{U}_{\mathrm{C}}(\boldsymbol{x}, \boldsymbol{y}) = \int_0^{+\infty}\int_0^{2\pi} e^{\mathrm{i}k(\cos\alpha(y_1 - x_1) + \sin\alpha(y_2 - x_2))}\hat{\boldsymbol{U}}_{\mathrm{C}}(k\cos\alpha, k\sin\alpha, y_3, x_3)k\ \mathrm{d}\alpha\mathrm{d}k \tag{4.19}$$

Importantly, the integrand of (4.19) involves the product of a function of $\boldsymbol{x}$ and a function of $\boldsymbol{y}$ (see remark after (4.18)).

Standard (Hankel transform) form. The angular integrations in (4.19) and in similar formulae available for $\boldsymbol{U}(\boldsymbol{x},\boldsymbol{y})$ can be performed analytically by means of integral representation formulae for Bessel functions, e.g.:

$$J_0(z) = \frac{1}{2\pi}\int_0^{2\pi} e^{\mathrm{i}z\cos\alpha}\,\mathrm{d}\alpha.$$

This leads to a previously proposed expression of $\boldsymbol{U}(\boldsymbol{x},\boldsymbol{y})$ in Hankel transform form, see e.g. [108]. However, this operation yields formulae that no longer involve products of functions of $\boldsymbol{y}$ and $\boldsymbol{x}$, making them unsuitable for the development of fast BEMs.

Multipole-expansion form. Let $\boldsymbol{x}^0$ and $\boldsymbol{y}^0$ denote local origins of $\boldsymbol{x}$-clusters and $\boldsymbol{y}$-clusters. The product form achieved by the Fourier-space representation (4.18) permits a decomposition reminiscent of the diagonal form:

$$\boldsymbol{U}_{\mathrm{C}}(\boldsymbol{x},\boldsymbol{y}) = \frac{1}{\mu k_{\mathrm{S}}^2}\sum_{a,b=\mathrm{L,T}}\int_0^{+\infty}\int_0^{2\pi} e^{\mathrm{i}k(\cos\alpha(y_1-y_1^0)+\sin\alpha(y_2-y_2^0))}e^{-\mathrm{i}s_a(y_3-y_3^0)}\,\boldsymbol{\mathcal{U}}_{ab}(k,\alpha,\boldsymbol{x}^0,\boldsymbol{y}^0)$$
$$e^{\mathrm{i}k(\cos\alpha(x_1^0-x_1)+\sin\alpha(x_2^0-x_2))}e^{-\mathrm{i}s_b(x_3-x_3^0)}\;\mathrm{d}\alpha\mathrm{d}k$$

where the transfer (tensor) functions $\boldsymbol{\mathcal{U}}_{ab}(k,\alpha,\boldsymbol{x}^0,\boldsymbol{y}^0)$ are defined by

$$\boldsymbol{\mathcal{U}}_{\mathrm{TT}}(k,\alpha,\boldsymbol{x}^0,\boldsymbol{y}^0) = \frac{4ks_{\mathrm{P}}}{\delta}\boldsymbol{V}_{\mathrm{T}}(k,\alpha)\boldsymbol{V}_{\mathrm{T}}'^{\mathrm{T}}(k,\alpha)e^{\mathrm{i}k(\cos\alpha(y_1^0-x_1^0)+\sin\alpha(y_2^0-x_2^0))}e^{-s_{\mathrm{S}}y_3^0}e^{-s_{\mathrm{S}}x_3^0}$$
$$\boldsymbol{\mathcal{U}}_{\mathrm{TL}}(k,\alpha,\boldsymbol{x}^0,\boldsymbol{y}^0) = \frac{2k\beta s_{\mathrm{P}}}{\delta}\boldsymbol{V}_{\mathrm{T}}(k,\alpha)\boldsymbol{V}_{\mathrm{L}}'^{\mathrm{T}}(k,\alpha)e^{\mathrm{i}k(\cos\alpha(y_1^0-x_1^0)+\sin\alpha(y_2^0-x_2^0))}e^{-s_{\mathrm{S}}y_3^0}e^{-s_{\mathrm{P}}x_3^0}$$
$$\boldsymbol{\mathcal{U}}_{\mathrm{LT}}(k,\alpha,\boldsymbol{x}^0,\boldsymbol{y}^0) = \frac{2k\beta s_{\mathrm{P}}}{\delta}\boldsymbol{V}_{\mathrm{L}}(k,\alpha)\boldsymbol{V}_{\mathrm{T}}'^{\mathrm{T}}(k,\alpha)e^{\mathrm{i}k(\cos\alpha(y_1^0-x_1^0)+\sin\alpha(y_2^0-x_2^0))}e^{-s_{\mathrm{P}}y_3^0}e^{-s_{\mathrm{S}}x_3^0}$$
$$\boldsymbol{\mathcal{U}}_{\mathrm{LL}}(k,\alpha,\boldsymbol{x}^0,\boldsymbol{y}^0) = \frac{k\beta^2 s_{\mathrm{P}}}{\delta}\boldsymbol{V}_{\mathrm{L}}(k,\alpha)\boldsymbol{V}_{\mathrm{L}}'^{\mathrm{T}}(k,\alpha)e^{\mathrm{i}k(\cos\alpha(y_1^0-x_1^0)+\sin\alpha(y_2^0-x_2^0))}e^{-s_{\mathrm{P}}y_3^0}e^{-s_{\mathrm{P}}x_3^0}$$

4.3.4 Numerical implementation

The evaluation of single-layer potentials of the form (4.7) typically involves three successive operations:

1. Computation of multipole moments

$$\boldsymbol{\mathcal{R}}_a(k,\alpha;\boldsymbol{y}^0) = \int_B e^{\mathrm{i}k(\cos\alpha(y_1-y_1^0)+\sin\alpha(y_2-y_2^0))}e^{-\mathrm{i}s_a(y_3-y_3^0)}\,\boldsymbol{p}(\boldsymbol{y})\,\mathrm{d}B_y \qquad (a=\mathrm{L,T})$$

2. Transfer

$$\boldsymbol{\mathcal{L}}_b(k,\alpha;\boldsymbol{x}^0) = \sum_{a=\mathrm{L,T}}\boldsymbol{\mathcal{U}}_{ab}(k,\alpha,\boldsymbol{x}^0,\boldsymbol{y}^0)\boldsymbol{\mathcal{R}}_a(k,\alpha;\boldsymbol{y}^0) \qquad (b=\mathrm{L,T})$$

3. Evaluation at observation points (numerical quadrature in Fourier space)

$$\boldsymbol{v}_{\mathrm{C}}(\boldsymbol{x}) = \sum_{b=\mathrm{L,T}}\int_0^{\infty}\int_0^{2\pi} w(k,\alpha)e^{\mathrm{i}k(\cos\alpha(x_1^0-x_1)+\sin\alpha(x_2^0-x_2))}e^{-\mathrm{i}s_b(x_3-x_3^0)}\,\boldsymbol{\mathcal{L}}_b(k,\alpha;\boldsymbol{x}^0)d\alpha dk$$

A key numerical issue is concerned with the definition of an efficient numerical quadrature in Fourier space to perform the integration involved in the third step (which plays the same role as the integration over the unit sphere involved in multipole expansions of free-space fundamental solutions). The method proposed to use is based on a singular value decomposition (SVD). This method is used for example in [60] and details on this decomposition and its numerical implementation are given in [210].

4.3.5 Conclusions on the formulation of multipole expansion of the half-space fundamental solutions

The use of the elastic half-space fundamental solutions in the FM-BEM is a very promising avenue for enhancing the computational performances of 3-D elastodynamic BEM. However, the multipole expansions of such fundamental solutions cannot be obtained in a simple way, and are not available in the current literature. In this section, in an effort towards bridging this gap, a formulation of the multipole expansions of the elastic half-space fundamental solutions was presented, in the form of a Fourier 2-D integral whose density is the product of a function of $\boldsymbol{x}$ and a function of $\boldsymbol{y}$, i.e. has the desired structure for defining fast BEMs. The derivation follows to a substantial extent that of the half-space fundamental solution expressed in terms of Hankel transforms. It is important to emphasize that exploitation of the proposed decomposition for fast BEM purposes still requires careful investigation and implementation of numerical quadrature methods along the lines of [60] and [210]. This essential step could not be done due to time limitations, but will be undertaken in the near future.

4.4 CONCLUSIONS

The introduction of the FM-BEM presented in Chapters 2 and 3 has substantially expanded the capabilities of 3-D elastodynamic BEM. This chapter has then presented, three possible ways to further improve the method. First, an efficient preconditioning strategy is presented and some possible improvements are given (Section 4.1). Then, the reduction of necessary moments is presented in Section 4.2. While not currently operational, this modification is simple to implement. Numerical experiments are additionally required to check the accuracy of the extrapolation pass in this new formulation. Last, the elastodynamic half-space fundamental solution has been formulated in a form suitable for FM-BEM. This is a promising avenue, but the numerical implementation requires the development of an efficient numerical quadrature for computing the inverse Fourier transform. Moreover, the complete implementation of this new FM-BEM will imply various modifications with respect to the present FM-BEM based on the elastic full-space fundamental solutions. The first step is to check that the actual computation of the half-space fundamental solutions (for N source points and N observation points) presented in Section 4.3 has a complexity lower that $O(N^2)$.

Part I: Summary

Part I of this dissertation was devoted to develop an efficient solver for frequency-domain elastodynamics using FM-accelerated BEM. Taking advantage of published recent developments for Helmholtz and Maxwell equations, the Fast Multipole Method has been successfully extended to elastodynamics in the frequency domain in Chapter 2. Combined with the BEM formulation, it permits to reduce the computational burden, in both CPU time and memory requirements, for the simulation of (e.g. seismic) wave propagation and allows to run models of size $N = O(10^6)$ on an ordinary PC. The accuracy of the method has been tested against exact, and previously-published numerical, solutions. In this first stage the formulation was limited to homogeneous media.

In Chapter 3, the ability to deal with alluvial-basin configurations has been introduced using a FM-based BE-BE approach suitable for 3-D piecewise-homogeneous media. Towards this end, the single-domain FMM has been applied independently in each homogeneous sub-domain. The accuracy of this multi-domain FM-BEM has also been extensively tested against available exact and numerical solutions. Additionally, the method has been successfully tested for higher frequencies and time-domain responses have been computed using Fourier synthesis.

The efficiency of the elastodynamic FM-BEM presented in Chapter 2 and 3 can still be improved in several ways. Three avenues for enhancing the computational performances have been proposed in Chapter 4: a simple preconditioning strategy, a method to reduce the number of necessary multipole moments and the formulation of a multipole expansion for the elastodynamic half-space fundamental solutions.

Part II

Seismological applications

Chapter 5

Seismic wave propagation in canonical canyons and basins

Contents

The work presented in this chapter is part of the research project "Quantitative Seismic Hazard Assessment" (QSHA, 2006-2009) funded by the French National Research Agency (ANR, http://qsha.unice.fr/). The project aims at (a) obtaining a better description of crustal structures, (b) improving the source characterization and the determination of earthquake scenarios, (c) developing more precise modelling of seismic waves, (d) improving empirical and semi-empirical techniques based on observed data and (e) obtaining a quantitative estimation of ground motion based on previous information. More specifically we have participated to the work package entitled "Developments of numerical tools for seismic wave propagation". Various partners are involved in this work package, each having expertise in a specific numerical method. Because various methods are available within this group of participants (finite difference method, finite volume method, finite element method, spectral element method, discrete element method and boundary element method), each one having specific advantages and limitations, comparisons in terms of numerical accuracy and efficiency on canonical examples were proposed as a part of the QSHA project. Four canonical problems have been defined for the purpose of such comparisons: semi-spherical and semi-ellipsoidal canyons, and corresponding basins. Various wave types were proposed as incident wavefields, in the frequency domain or in the time domain. Because of the specificity of our solver, we have treated examples involving incident plane P– and SV–waves, in the frequency domain. The examples treated in this framework (with and without preconditioning strategy) are presented in this chapter. Unfortunately, comparisons with other methods are not available at the time of this writing. Several papers nevertheless deal with some of theses cases [63, 183, 169].

5.1 DEFINITION OF CANONICAL PROBLEMS

The examples proposed in this chapter are concerned with the diffraction, by a semi-ellipsoidal canyon (Fig. 5.1) or a semi-ellipsoidal basin (Fig. 5.2), of an oblique incident plane P– or SV–wave of unit amplitude travelling in an elastic half-space. A right-handed Cartesian frame (x, y, z) is defined so that the elastic half-space occupies the region $\{(x, y, z)|z \leq 0\}$. The surface of the canyon or basin is ellipsoidal, with semiaxes b, a, a respectively aligned along the coordinate directions x, y, z. The incident plane wave travels along direction $\sin\theta\boldsymbol{e_y} + \cos\theta\boldsymbol{e_z}$ (θ being defined on Figs. 5.1 and 5.2). The semi-ellipsoidal surface of the canyon or basin and the surrounding portion of the free surface lying inside a disk of radius $D > a, b$ are discretized using boundary elements. For each geometry, four types of incident waves are always considered: vertical ($\theta = 0^\circ$) or oblique ($\theta = 30^\circ$) incident plane P–waves and vertical or oblique incident plane SV–waves. For each incident plane wave, various non-dimensional frequencies are considered to show the capabilities of the FM-BEM in the "low" or "high" frequency range. For each configuration (combining given geometry and incident wave), the modulus of the three components of surface displacement are displayed as isovalue plots arranged in tabular fashion, where each line corresponds to the modulus of a displacement component and each column to a non-dimensional frequency. All results in a given tabular set are plotted using the same color scale to emphasize the predominant components and facilitate visual comparisons. The numerical data (number of DOFs, leaf levels, CPU time per iteration and iteration counts) are also given for each configuration to show the effects of the geometry, incident wave and frequency on the efficiency. The efficiency of the preconditioning strategy defined in Section 4.1 is also demonstrated on this set of examples, with iteration counts with and without preconditioning systematically provided. For a good compromise between accuracy and CPU time per iteration, all meshes used in this chapter have a density of about ten points per S–

wavelength. All results presented in this chapter have been obtained on a 8-processor PC (RAM: 64GB, CPU frequency: 2.33 GHz), each FMM analysis being performed independently on a single processor.

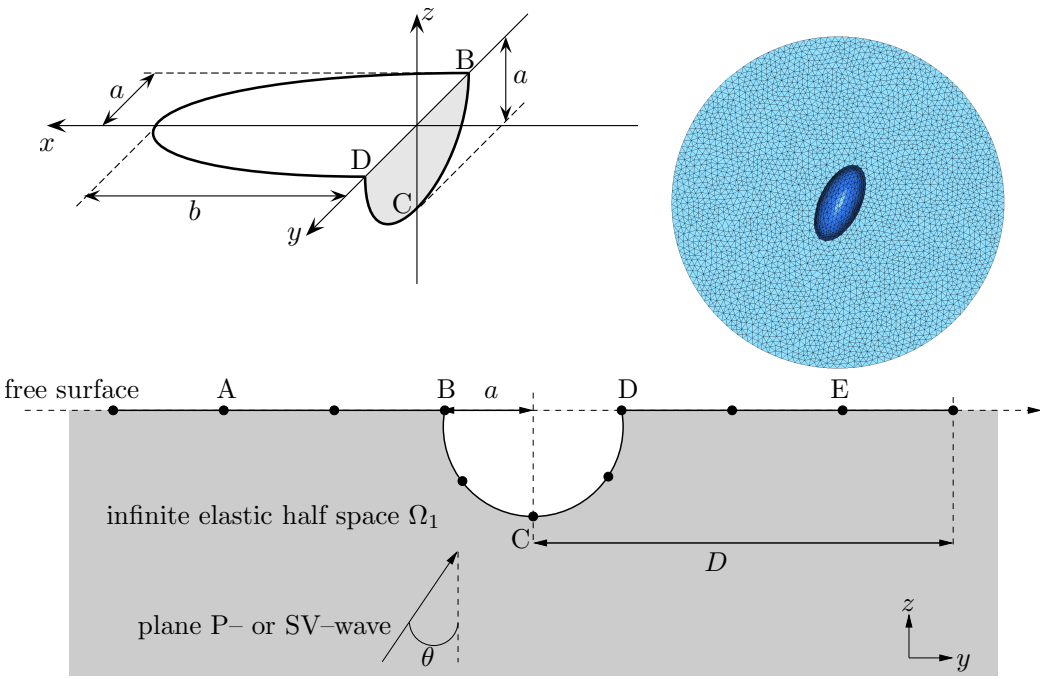

Figure 5.1: *Diffraction of an oblique incident plane P– or SV–wave by a semi-ellipsoidal canyon: notation (top left and bottom); sample BEM mesh, with $N = 9,642$ (top right).*

5.2 SEMI-SPHERICAL CANYON

Problem definition. The first configuration deals with a special case of semi-ellipsoidal canyon: a semi-spherical canyon of radius a, with $\nu = 0.25$. The free surface lies inside a disk of radius $D = 5a$. This case is studied in [183] for $k_{\mathrm{P}}a/\pi = 0.25;\ 0.5;\ 0.75;\ 1.5$ and in [169] for $k_{\mathrm{P}}a/\pi = 0.25;\ 0.5$. In Figure 2.22, our results using the FMM (with $D = 3a$) for $k_{\mathrm{P}}a/\pi = 0.25$ are seen to be in good agreement with the results of [183, 169]. In Table 5.1, the number of DOFs N, the leaf level $\bar{\ell}$ are given for three non-dimensional frequencies ($k_{\mathrm{P}}a/\pi = 0.25;\ 0.5;\ 2$), together with the CPU time per iteration recorded (without preconditioning). These data are applicable for all the types of incident plane waves considered. When the incident plane wave is changed, only the right-hand side is modified, which in turn only influences the iteration count. The latter will be given in the following for each wave type. We note that the two first non-dimensional frequencies are low (i.e. the canyon spans a fraction of P–wavelength), with the octree featuring only two active levels ($\bar{\ell} = 3$ as a result). The last example, which features four active octree levels ($\bar{\ell} = 5$), is characterized by a low CPU time per iteration given the problem size (40 s per iteration, $N = 111,237$).

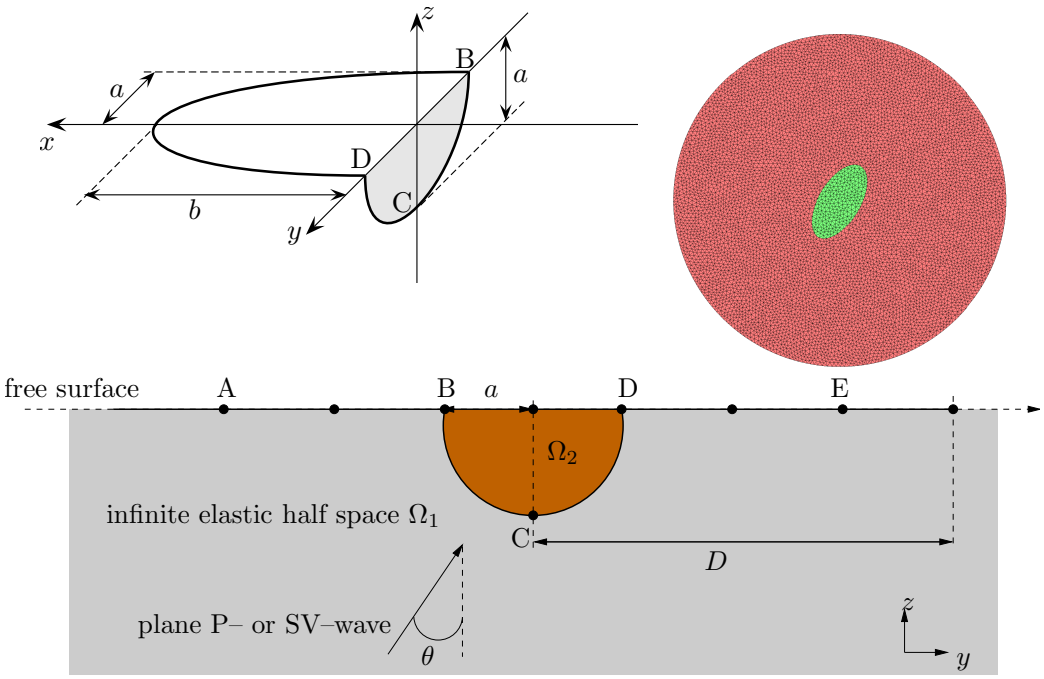

Figure 5.2: *Diffraction of an oblique incident plane P– or SV–wave by a semi-ellipsoidal basin: notation (top left and bottom); sample BEM mesh, with $N = 27,144$ (top right).*

Table 5.1: *Diffraction of incident plane waves by a semi-spherical canyon: computational data.*

$k_{\mathrm{P}}a/\pi$	N	$\bar{\ell}$	CPU / iter (s)
0.25	23,903	3	6.5
0.5	27,903	3	14
2	111,237	5	40

Vertical incident plane P–wave. The first configuration is concerned with the diffraction of a vertical ($\theta = 0°$) incident plane P–wave. In Figure 5.4, the modulus of the x-, y- and z-components are displayed for the three non-dimensional frequencies. Because the canyon is semi-spherical and the incident wave is vertical, the displacement solution must be axisymmetric. The numerical results are consistent with this symmetry. We note for example the symmetry with respect to the $x = 0$ (resp. $y = 0$) plane for the x- (resp. y-) component, while the x-component can be obtained from applying a $\pi/2$ rotation to the y-component, as expected. Also, the z-component is axisymmetric. None of these expected symmetries is embedded in the computational procedure although this might be done for many types of symmetry, adapting the approach of [32]. When the frequency is increased, the reduction of the wavelengths is easily observed. For these three frequencies, the predominant component is the z-component. Moreover, the maximum amplitude of the z-component occurs away from the canyon for the lower considered frequency but at the canyon center for the two higher frequencies.

Oblique incident plane P–wave. The diffraction of an oblique ($\theta = 30°$) incident plane P–wave by the same semi-spherical canyon is now considered. In Figure 5.5, the modulus of the x-, y- and z-components are displayed for the three non-dimensional frequencies. Because the direction of propagation lies in the Oyz plane, all the components are symmetric with respect to the $x = 0$ plane. The z-component is still predominant but the y- component is also significant in this case. The maximum amplitude increases with the non-dimensional frequency (from 2.07 to 2.98).

Vertical incident plane SV–wave. The diffraction of a vertical ($\theta = 0°$) incident plane SV–wave by the same semi-spherical canyon is displayed in Figure 5.6 (modulus of the x-, y- and z-components for the three non-dimensional frequencies). In this case, contrary to the plane P–wave case, the displacement response is symmetrical with respect to the planes $x = 0$ and $y = 0$ rather than axisymmetric, and hence is fully 3-D. The y-component is predominant, with a maximum amplitude ranging between 2.55 and 3.38. For the case $k_{\mathrm{P}}a/\pi = 2$, the z-component also reaches a large value and the y-component contribution is smaller than for the two other frequencies.

Oblique incident plane SV–wave. The last case is concerned with the diffraction of an oblique ($\theta = 30°$) incident plane SV–wave by the same semi-spherical canyon. In Figure 5.7, the modulus of the x-, y- and z-components are displayed for the three non-dimensional frequencies. In this case, the y-component is predominant but the contribution of the z-component is also significant. The maximum amplitude ranges between 3.05 and 3.69 and is larger than for the vertical incidence. Because the direction of propagation lies in the plane Oyz, the displacement response is symmetric with respect to the $x = 0$ plane. As the non-dimensional frequency increases, the maximum amplitude becomes localized in a small region near the rear part ($y \leq 0$) of the canyon.

Iteration counts. In Table 5.2, the iteration counts recorded for the twelve configurations are given. When no preconditioning strategy is used the number of iterations and CPU time for the complete solution are given. When the preconditioning strategy of Section 4.1 is used, the total number of inner iterations, the number of outer iterations and the cumulative CPU time are given.

The first remark is that the iteration counts are similar for the cases of P– and SV–waves. For both wave types, the oblique incidence requires more iterations than the vertical incidence if no preconditioning strategy is used. This can be explained by the lower degree of symmetry for the oblique incidence case. This effect seems to be reduced when the preconditioning strategy is used.

As already noticed in Section 2.6.3, if the frequency increases, the iteration count also increases. But, even if no preconditioning strategy is used, the iteration counts are still moderate for canyon problems featuring about $N = O(10^5)$ DOFs. The preconditioning strategy is however seen to drastically reduce the number of outer iterations for high frequency problems. To emphasize the efficiency of the preconditioning with respect to the non-dimensional frequency, the number of iterations without preconditioning and the number of outer iterations with preconditioning are represented against the non-dimensional frequency in Fig. 5.3a. The increase of the number of outer iterations with the non-dimensional frequency is seen to be slower than without preconditioning. The same trend is observed in Figure 5.3b, where the number of iterations is replaced by the cumulative CPU time.

Table 5.2: *Diffraction of incident plane waves by a semi-spherical canyon: iteration counts and CPU time (with and without preconditioning).*

	without prec.		with prec.		
	nb iter.	CPU time	nb iter. (inner)	nb iter. (outer)	CPU time
vertical P–wave					
$k_{\mathrm{P}}a/\pi = 0.25$	8	$4'51''$	17	5	$5'39''$
$k_{\mathrm{P}}a/\pi = 0.5$	10	$6'16''$	25	6	$6'29''$
$k_{\mathrm{P}}a/\pi = 2$	31	$25'02''$	65	16	$23'54''$
oblique P–wave					
$k_{\mathrm{P}}a/\pi = 0.25$	9	$4'52''$	19	6	$5'50''$
$k_{\mathrm{P}}a/\pi = 0.5$	13	$6'44''$	24	6	$6'43''$
$k_{\mathrm{P}}a/\pi = 2$	43	$33'19''$	70	17	$25'36''$
vertical SV–wave					
$k_{\mathrm{P}}a/\pi = 0.25$	8	$4'35''$	17	5	$5'31''$
$k_{\mathrm{P}}a/\pi = 0.5$	11	$6'04''$	27	6	$6'39''$
$k_{\mathrm{P}}a/\pi = 2$	38	$29'54''$	68	16	$26'10''$
oblique SV–wave					
$k_{\mathrm{P}}a/\pi = 0.25$	10	$5'00''$	19	6	$5'24''$
$k_{\mathrm{P}}a/\pi = 0.5$	13	$6'32''$	31	7	$7'26''$
$k_{\mathrm{P}}a/\pi = 2$	45	$34'19''$	73	18	$27'04''$

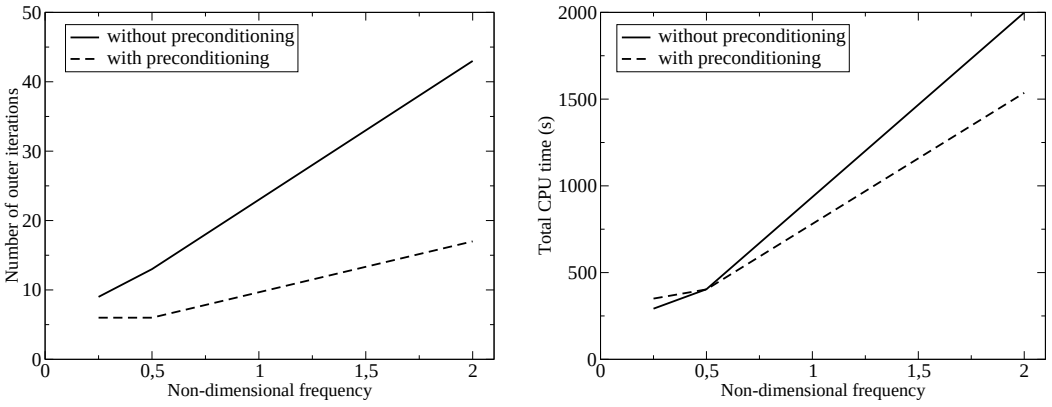

(a) (b)

Figure 5.3: *Number of outer iterations (a) and total CPU time (b) with or without preconditioning, against the non-dimensional frequency, for the problem of the diffraction of an oblique incident plane P–wave by a semi-spherical canyon.*

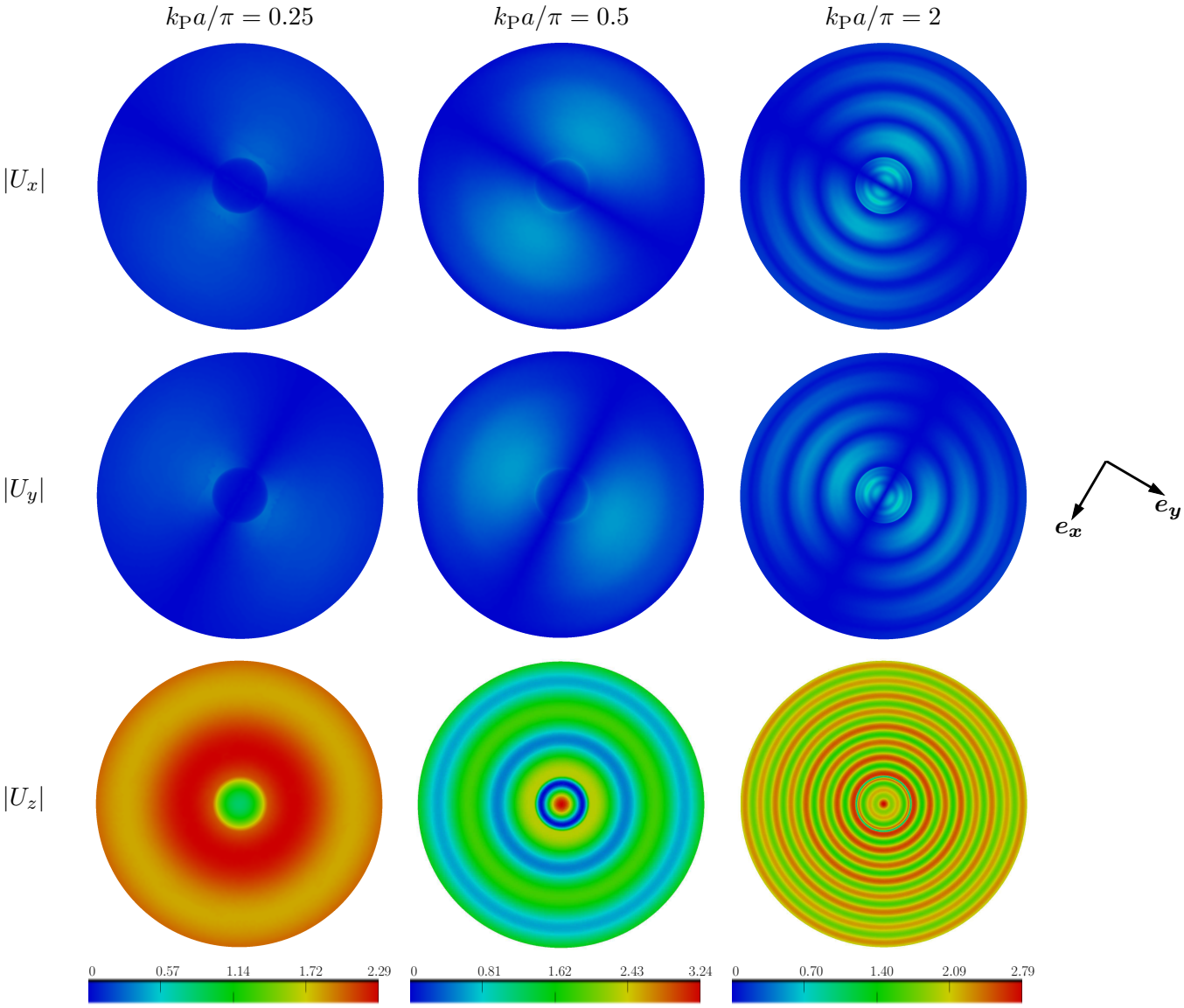

Figure 5.4: *Diffraction of a vertical incident plane P–wave by a semi-spherical canyon: modulus of the x- (top), y- (middle) and z- (bottom) components of displacement for the normalized frequencies* $k_P a/\pi = 0.25$ *(left),* $k_P a/\pi = 0.5$ *(middle) and* $k_P a/\pi = 2$ *(right).*

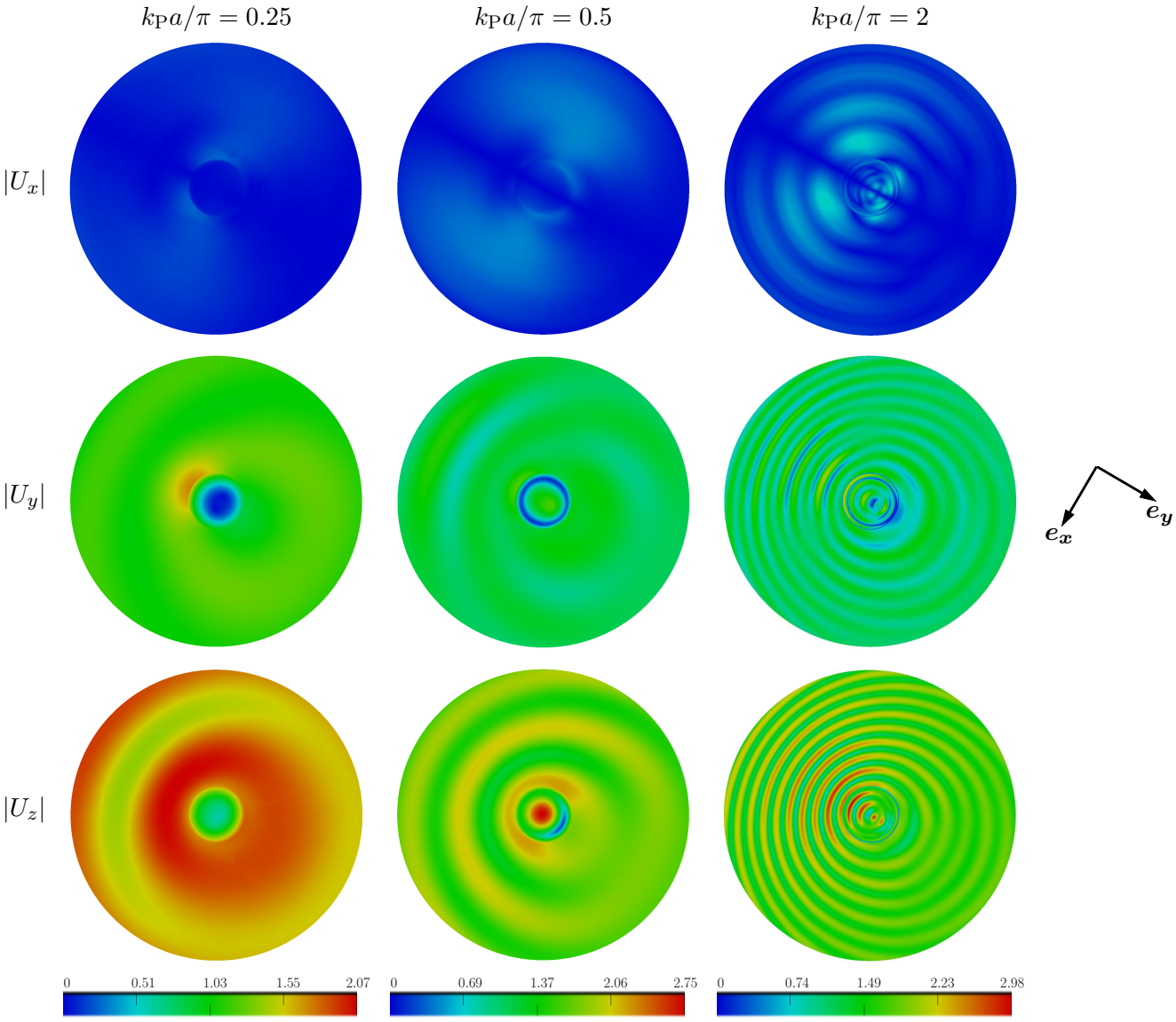

Figure 5.5: *Diffraction of an oblique ($\theta = 30°$) incident plane P–wave by a semi-spherical canyon: x- (top), y- (middle) and z- (bottom) components of displacement for the normalized frequencies $k_P a/\pi = 0.25$ (left), $k_P a/\pi = 0.5$ (middle) and $k_P a/\pi = 2$ (right).*

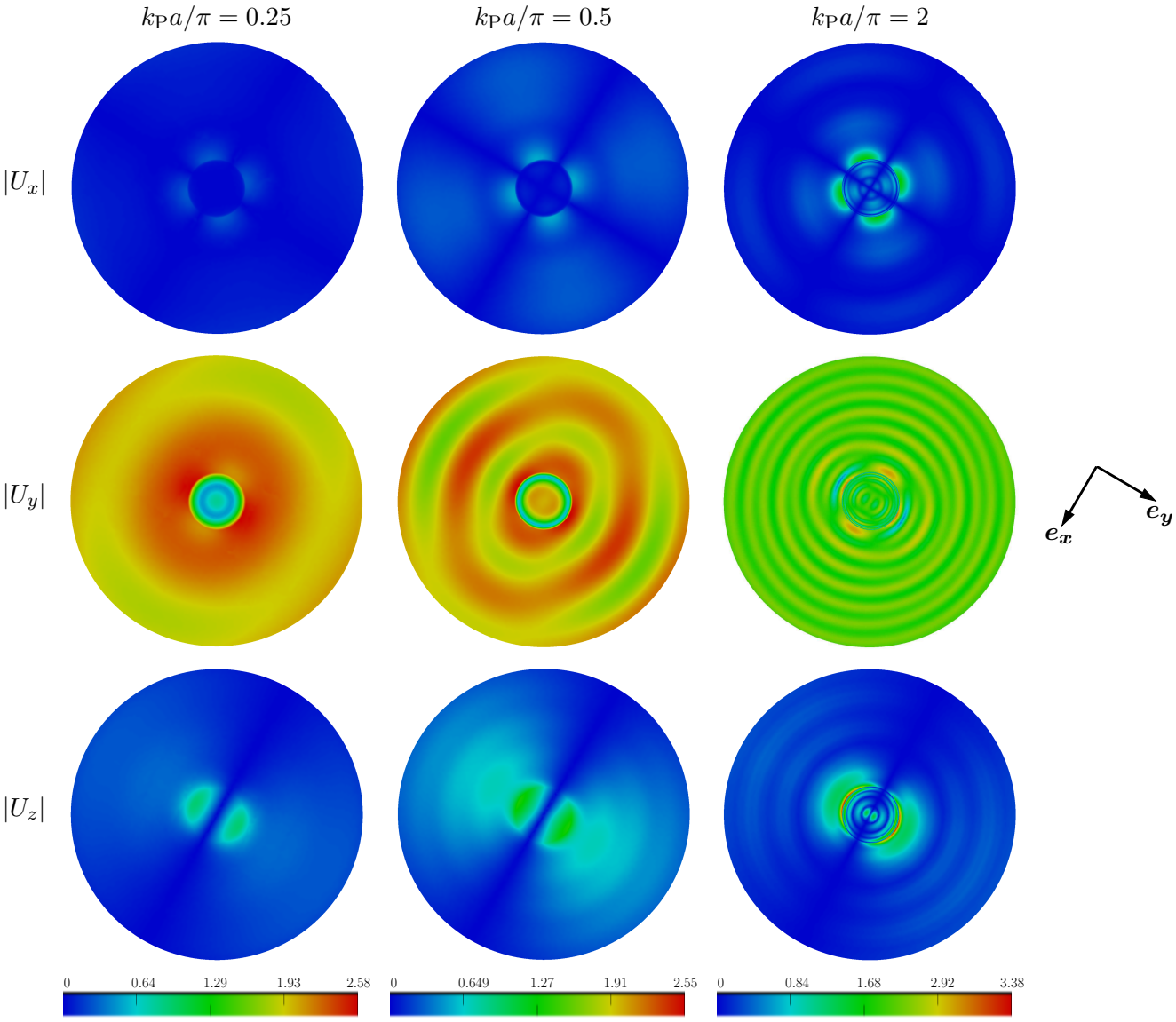

Figure 5.6: *Diffraction of a vertical incident plane SV–wave by a semi-spherical canyon: x- (top), y- (middle) and z- (bottom) components of displacement for the normalized frequencies* $k_{\mathrm{P}}a/\pi = 0.25$ *(left),* $k_{\mathrm{P}}a/\pi = 0.5$ *(middle) and* $k_{\mathrm{P}}a/\pi = 2$ *(right).*

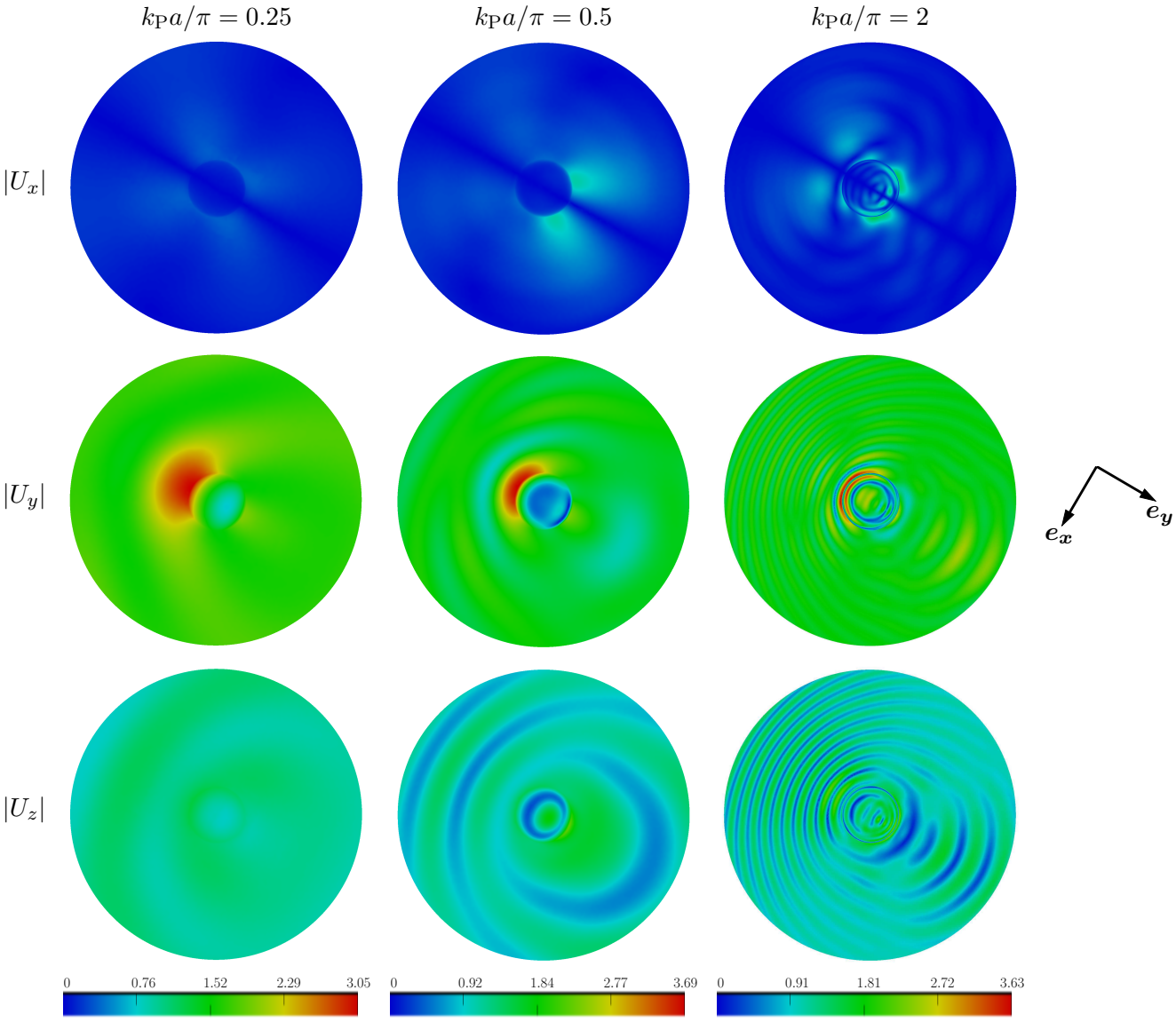

Figure 5.7: *Diffraction of an oblique ($\theta = 30°$) incident plane SV–wave by a semi-spherical canyon: x- (top), y- (middle) and z- (bottom) components of displacement for the normalized frequencies $k_{\mathrm{P}}a/\pi = 0.25$ (left), $k_{\mathrm{P}}a/\pi = 0.5$ (middle) and $k_{\mathrm{P}}a/\pi = 2$ (right).*

5.3 SEMI-ELLIPSOIDAL CANYON

The diffraction of plane waves by a semi-ellipsoidal canyon, with semi-axes defined by $b = 2a$ and $\nu = 1/3$, is now considered. The free surface lies inside a disk of radius $D = 8a$. In Table 5.3, the number of DOFs N and the leaf level $\bar{\ell}$ are given for two non-dimensional frequencies ($k_{\mathrm{P}}a/\pi = 0.25$ and $k_{\mathrm{P}}a/\pi = 2$), together with the CPU time per iteration recorded (without preconditioning). For this configuration, the largest problem features $290,715$ DOFs and the solution of this large scale problem only takes 105 s per iteration.

Table 5.3: *Diffraction of incident plane waves by a semi-ellipsoidal canyon: computational data.*

$k_{\mathrm{P}}a/\pi$	N	$\bar{\ell}$	CPU / iter (s)
0.25	$9,642$	3	3.5
2	$290,715$	6	105

Vertical incident plane P–wave. In Figure 5.8, the modulus of the x-, y- and z-components are displayed for the two non-dimensional frequencies. Because of the symmetry of the canyon with respect to the $x = 0$ and $y = 0$ planes, the results are symmetric with respect to the $x = 0$ and $y = 0$ planes. The z-component is predominant. At the highest frequency, the maximum amplitude is not much higher than for the lowest frequency. This maximum occurs at several places, due to the short wavelength, whereas it was more localized for the low frequency case.

Oblique incident plane P–wave. If an oblique ($\theta = 30^\circ$) incident plane P–wave is considered, the z-component is still predominant but the y-component is significant (Fig. 5.9). As in the semi-spherical case, the maximum amplitude is localized on the rear part ($y \leq 0$) of the canyon. The maximum amplitudes are higher than in the semi-spherical case (2.66 and 3.28 compared to 2.07 and 2.98 in the semi-spherical case).

Vertical incident plane SV–wave. In the case of a vertical incident plane SV–wave, the y-component is now predominant (see Fig. 5.10) but some significant displacements also appear on the z-component. Because of the vertical incidence and symmetry of the geometry, the displacement response is symmetric with respect to the $x = 0$ and $y = 0$ planes. The maximum amplitude is increased between the lower and the higher frequencies and when compared to the case of a vertical incident plane P–wave.

Oblique incident plane SV–wave. The last case considered for this geometry is concerned with the diffraction of an oblique ($\theta = 30^\circ$) incident plane SV–wave. In Figure 5.11, the modulus of the x-, y- and z-displacement components are displayed for the two non-dimensional frequencies. In that case, the y-component is predominant and the contribution of the z-component is seen to be lower than for the vertical incidence case. The maximum amplitude is similar between the two non-dimensional frequencies but is twice higher than for the vertical incidence. This phenomenon

is not observed in the semi-spherical case. A possible explanation is that, because of the non-axisymmetric of the canyon, incident waves are more trapped in one side of the canyon than in the semi-spherical case.

Iteration counts. In Table 5.4, the iteration counts recorded for the four kinds of incident plane waves and the two non-dimensional frequencies are given, using the same convention as in Table 5.2. Contrary to the semi-spherical case, the four types of incident plane waves lead to similar iteration counts even if no preconditioning is used. This can be explained by the non-axisymmetry of the geometry. Once again, both the iteration count and the total CPU time increase with the frequency, but this increase is slower when the preconditioning strategy is used.

The last remark is that, if the iteration counts are similar for the lower fequency cases, the number of iterations is doubled compared to the semi-spherical case (even if a preconditioning strategy is used). The geometry seems to influence the iteration counts. A non-axisymmetric geometry leads to higher iteration counts than an axisymmetric geometry.

Table 5.4: *Diffraction of incident plane waves by a semi-ellipsoidal canyon: iteration counts and CPU time (with and without preconditioning).*

	without prec.		with prec.		
	nb iter.	CPU time	nb iter. (inner)	nb iter. (outer)	CPU time
vertical P–wave					
$k_{\mathrm{P}}a/\pi = 0.25$	10	$1'04''$	21	6	$55''$
$k_{\mathrm{P}}a/\pi = 2$	88	$2\mathrm{h}47'55''$	108	32	$1\mathrm{h}24'27''$
oblique P–wave					
$k_{\mathrm{P}}a/\pi = 0.25$	11	$1'02''$	27	7	$1'00''$
$k_{\mathrm{P}}a/\pi = 2$	90	$2\mathrm{h}50'21''$	120	32	$1\mathrm{h}25'09''$
vertical SV–wave					
$k_{\mathrm{P}}a/\pi = 0.25$	11	$1'06''$	27	7	$1'00''$
$k_{\mathrm{P}}a/\pi = 2$	91	$2\mathrm{h}53'07''$	106	31	$1\mathrm{h}22'43''$
oblique SV–wave					
$k_{\mathrm{P}}a/\pi = 0.25$	11	$1'06''$	27	7	$1'02''$
$k_{\mathrm{P}}a/\pi = 2$	96	$3\mathrm{h}05'55''$	118	32	$1\mathrm{h}30'04''$

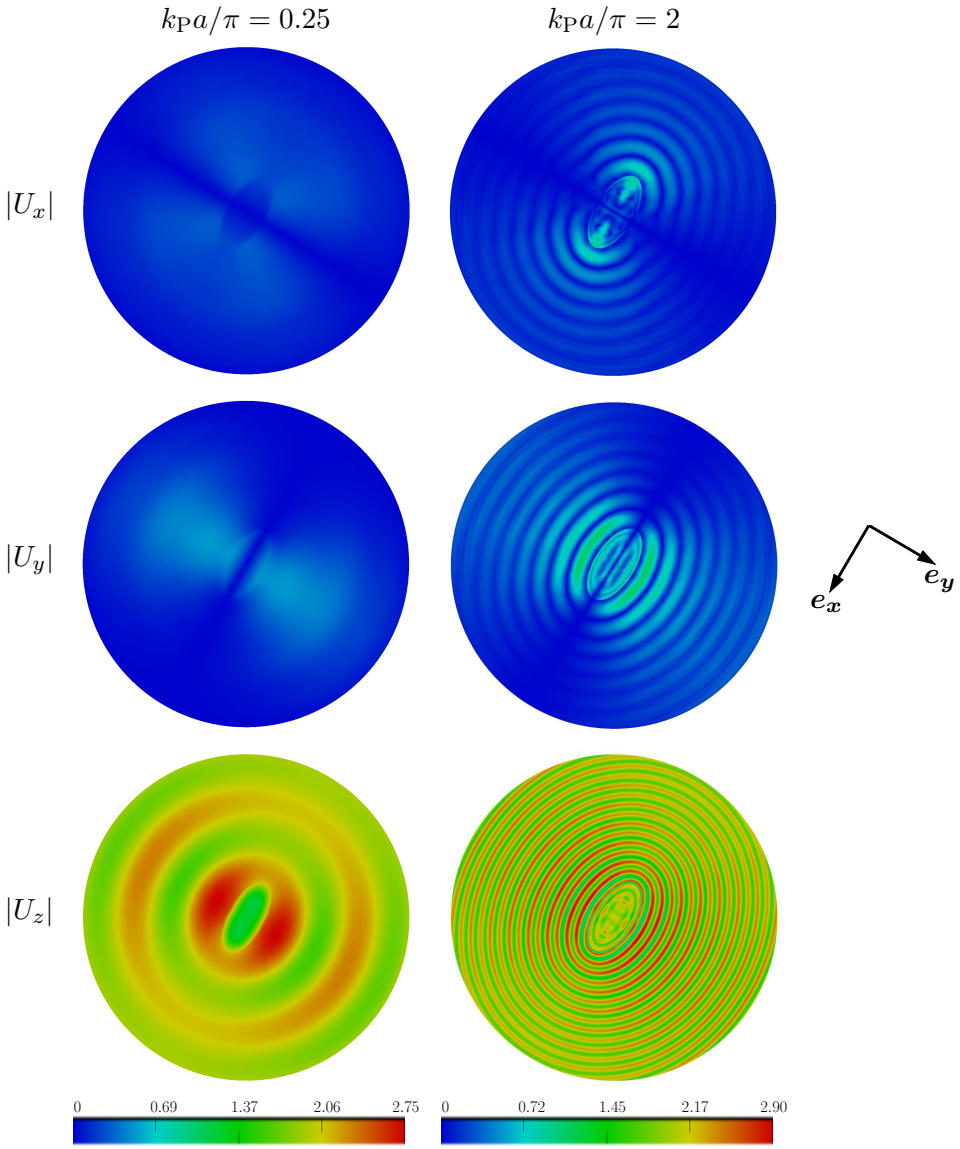

Figure 5.8: *Diffraction of a vertical incident plane P–wave by a semi-ellipsoidal canyon: x- (top), y- (middle) and z- (bottom) components of displacement for the normalized frequencies* $k_{\mathrm{P}}a/\pi = 0.25$ *(left) and* $k_{\mathrm{P}}a/\pi = 2$ *(right).*

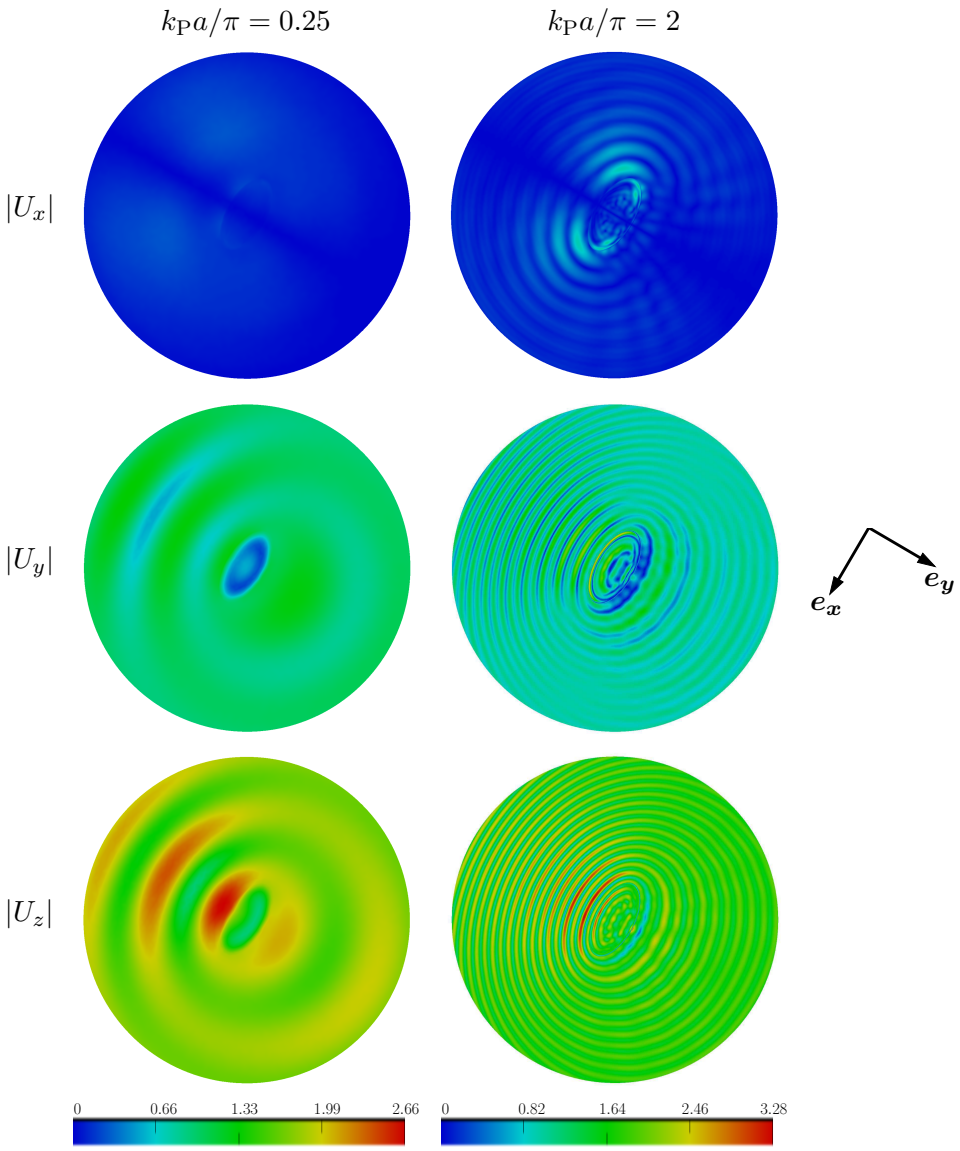

Figure 5.9: *Diffraction of an oblique ($\theta = 30°$) incident plane P–wave by a semi-ellipsoidal canyon: x- (top), y- (middle) and z- (bottom) components of displacement for the normalized frequencies $k_{\mathrm{P}}a/\pi = 0.25$ (left) and $k_{\mathrm{P}}a/\pi = 2$ (right).*

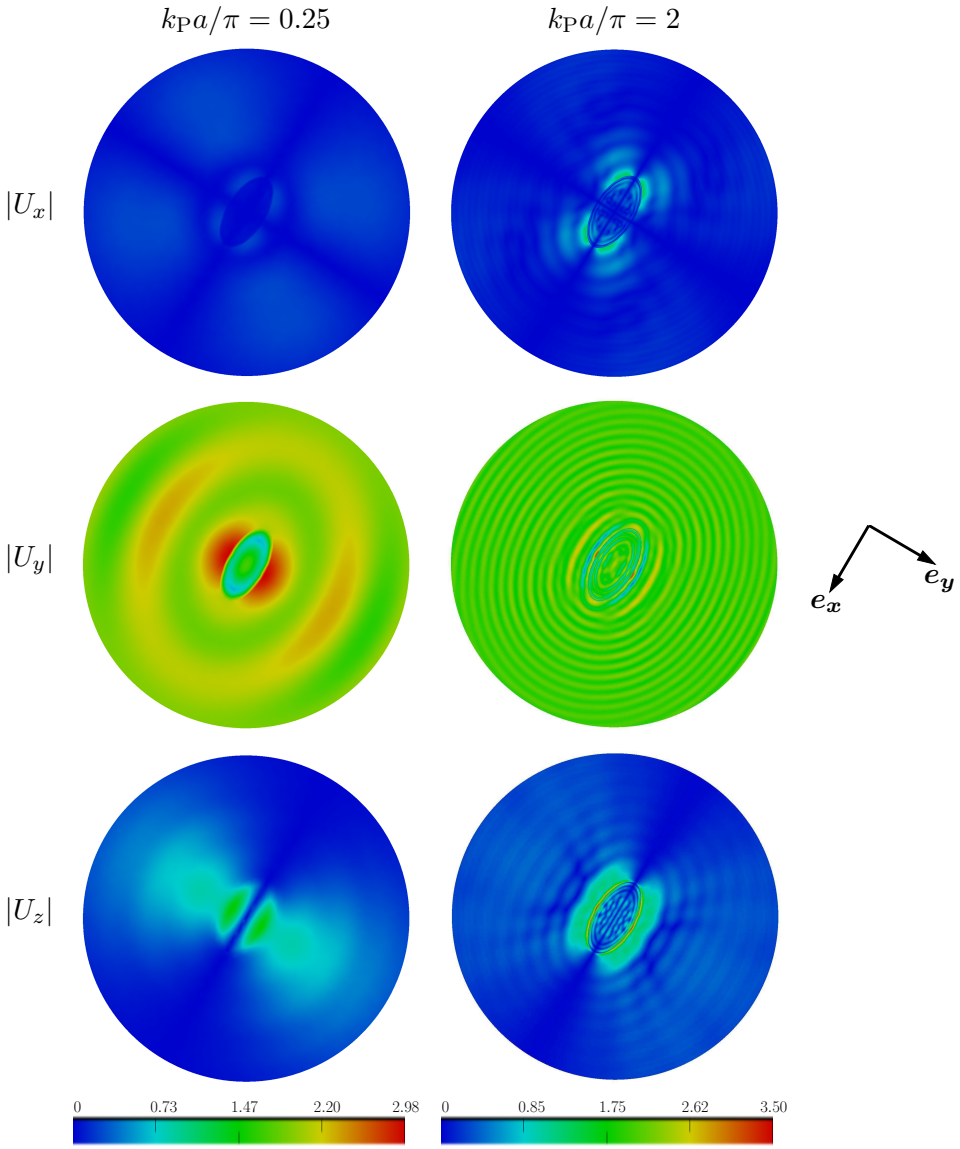

Figure 5.10: *Diffraction of a vertical incident plane SV–wave by a semi-ellipsoidal canyon: x- (top), y- (middle) and z- (bottom) components of displacement for the normalized frequencies* $k_{\mathrm{P}}a/\pi = 0.25$ *(left) and* $k_{\mathrm{P}}a/\pi = 2$ *(right).*

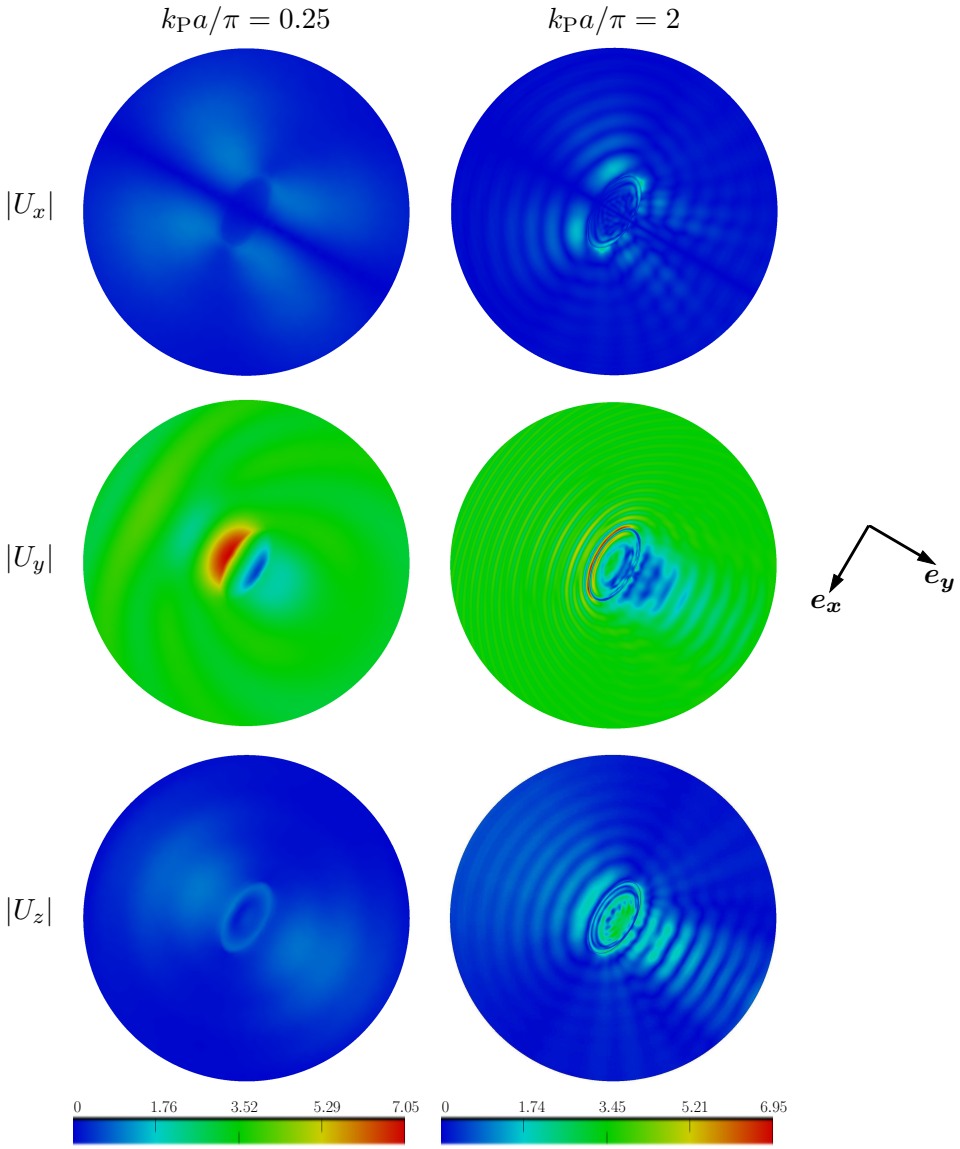

Figure 5.11: *Diffraction of an oblique ($\theta = 30°$) incident plane SV–wave by a semi-ellipsoidal canyon: x- (top), y- (middle) and z- (bottom) components of displacement for the normalized frequencies $k_{\mathrm{P}}a/\pi = 0.25$ (left) and $k_{\mathrm{P}}a/\pi = 2$ (right).*

5.4 SEMI-SPHERICAL BASIN

After the study of the diffraction of plane waves by canonical canyons, the following two sections are devoted to the diffraction of plane waves by sedimentary basins. In this section, a semi-spherical basin of radius a is considered. The free surface lies in a disk of radius $D = 5a$. The material parameters are $\nu^{(1)} = 0.25$, $\mu^{(2)} = 0.3\mu^{(1)}$, $\rho^{(2)} = 0.6\rho^{(1)}$ and $\nu^{(2)} = 0.3$. In Table 5.5, the number of DOFs N, the leaf levels $\bar{\ell}_1$ and $\bar{\ell}_2$ are given for three non-dimensional frequencies ($k_{\mathrm{P}}^{(1)}a/\pi = 0.5$; 1; 2), together with the CPU time per iteration recorded (without preconditioning). For $k_{\mathrm{P}}^{(1)}a/\pi = 2$, the mesh features $N = 190,299$ DOFs and only requires 11.3 s per iteration. The numerical efficiency of the present implementation of the FM-BEM is once again illustrated. The lower CPU time per iteration for the case $k_{\mathrm{P}}^{(1)}a/\pi = 2$ than for the case $k_{\mathrm{P}}^{(1)}a/\pi = 1$ is explained by the change of number of levels.

Table 5.5: *Diffraction of incident plane waves by a semi-spherical basin: computational data.*

$k_{\mathrm{P}}^{(1)}a/\pi$	N	$\bar{\ell}_1;\bar{\ell}_2$	CPU / iter (s)
0.5	17,502	3;3	7.3
1	90,057	4;3	40
2	190,299	5;4	11.3

Vertical incident plane P–wave. First, the diffraction of a vertical incident plane P–wave is considered. In Chapter 3, in Figure 3.12 our results using the FMM are shown to be in good agreement with previously published ones [183, 63] for $k_{\mathrm{P}}^{(1)}a/\pi = 0.5$ (resp. $k_{\mathrm{P}}^{(1)}a/\pi = 0.5$). In Figure 5.13, the modulus of the x-, y- and z-components of the surface displacements are displayed for the three non-dimensional frequencies. Due to the axisymmetry of the basin, the x- and y-components are symmetric with respect to the $x = 0$ and $y = 0$ planes and the y-component is obtained from applying a $\pi/2$ rotation to the x-component, as expected. The maximum amplitude occurs inside the basin (Ω_2) and increases with the frequency. Comparing with the amplitudes in the canyon case in Section 5.2, for $k_{\mathrm{P}}^{(1)}a/\pi = 2$, this maximum is more than doubled (6.13 instead of 2.79 in the canyon case). Moreover, on the flat surface, outside of the basin, the modulus of the z-component is about 50% (or less) of the maximum amplitude whereas in the canyon case, this value is higher (at least 50%). As expected, the waves are trapped inside the sedimentary basin and only a small faction propagates outwards.

Oblique incident plane P–wave. If we consider an oblique plane P–wave (Fig. 5.14), the z-component is still predominant but the y-component contributes more than in the vertical incident case and the maximum amplitudes are lower than in the vertical incident case (for example 5.31 instead of 6.13 for $k_{\mathrm{P}}^{(1)}a/\pi = 2$). As the frequency increases, so does the contribution of the y-component and the maximum on the z-component becomes localized in a small region inside the basin. But, comparing the results with those obtained in Section 5.2, the maximum amplitude is about twice higher than in the canyon case (5.31 instead of 2.98 in the canyon case for $k_{\mathrm{P}}^{(1)}a/\pi = 2$). The incident waves are trapped in the basin and the multiple reflections lead to higher amplitude.

Vertical incident plane SV–wave. In the case of a vertical incident plane SV–wave (Fig. 5.15), the y-component is predominant. The maximum amplitude increases with the frequency. Doing some comparisons with the semi-spherical case (Section 5.2), it is seen that the maximum amplitude is about twice higher than in the canyon case (7.90 instead of 3.38 in the canyon case for $k_{\mathrm{P}}^{(1)}a/\pi = 2$), and also that this maximum is localized inside the basin (Ω_2) instead of occurring at several places outside the cavity (on the planar surface surrounding it) in the canyon case.

Oblique incident plane SV–wave. In the case of an oblique incident plane SV–wave (Fig. 5.16), the y-component is predominant. Compared to the vertical incident case, the maximum amplitude is increased (8.65 instead of 7.90 in the vertical case for $k_{\mathrm{P}}^{(1)}a/\pi = 2$) and this maximum is more localized in the rear part ($y \geq 0$) of the basin. The maximum amplitude for $k_{\mathrm{P}}^{(1)}a/\pi = 2$ is more than twice higher than in the semi-spherical canyon (8.65 instead of 3.63).

Iteration counts. In Table 5.6, the iteration counts recorded for the twelve studied configurations are given. A first remark is that the number of iterations, if the incident wave is oblique, is larger than if the incident wave is vertical. As in Section 5.2, this is presumably due to the lower degree of symmetry for the oblique incidence case and possibly the influence of wave conversions. This effect seems to be reduced when the preconditioning strategy is used. A comparison with the iteration counts obtained for the semi-spherical canyon shows that the iteration count is about ten times higher in the basin case if no preconditioning strategy is used. Contrary to the canyon case, to deal with basin problems at higher frequency, a preconditioning strategy is necessary to overcome the bad conditioning. If such approach is used, the number of outer iterations for the basin problems is only twice that for the canyon.

Once again, the iteration count increases with the frequency (even if the preconditioning strategy is used). But, as in the canyon case, for problems featuring about $O(10^5)$ DOFs, the preconditioning strategy is very efficient. The total CPU is reduced by about 69% for the problem of the propagation of an oblique incident plane P–wave at $k_{\mathrm{P}}^{(1)}a/\pi = 2$. To emphasize the efficiency of the preconditioning strategy, the number of iterations without preconditioning and the number of outer iterations with preconditioning are plotted against the non-dimensional frequency in Fig. 5.12a. The increase of the number of outer iterations with the frequency is seen to be slower than without preconditioning. The same trend is observed in Figure 5.12b, where the number of outer iterations is replaced by the total CPU time.

Table 5.6: *Diffraction of incident plane waves by a semi-spherical basin: iteration counts and CPU time (with and without preconditioning).*

	without prec.		with prec.		
	nb iter.	CPU time	nb iter. (inner)	nb iter. (outer)	CPU time
vertical P–wave					
$k_{\mathrm{P}}^{(1)} a/\pi = 0.5$	28	$6'07''$	65	10	$5'12''$
$k_{\mathrm{P}}^{(1)} a/\pi = 1$	52	$45'01''$	122	13	$55'51''$
$k_{\mathrm{P}}^{(1)} a/\pi = 2$	325	$6\mathrm{h}55'55''$	223	25	$2\mathrm{h}25'25''$
oblique P–wave					
$k_{\mathrm{P}}^{(1)} a/\pi = 0.5$	31	$5'49''$	80	12	$5'45''$
$k_{\mathrm{P}}^{(1)} a/\pi = 1$	78	$1\mathrm{h}01'25''$	157	16	$1\mathrm{h}10'55''$
$k_{\mathrm{P}}^{(1)} a/\pi = 2$	388	$7\mathrm{h}59'27''$	231	26	$2\mathrm{h}30'54''$
vertical SV–wave					
$k_{\mathrm{P}}^{(1)} a/\pi = 0.5$	24	$4'53''$	73	11	$5'27''$
$k_{\mathrm{P}}^{(1)} a/\pi = 1$	50	$42'40''$	138	15	$1\mathrm{h}07'20''$
$k_{\mathrm{P}}^{(1)} a/\pi = 2$	307	$6\mathrm{h}24'52''$	215	25	$2\mathrm{h}40'50''$
oblique SV–wave					
$k_{\mathrm{P}}^{(1)} a/\pi = 0.5$	34	$6'05''$	82	12	$6'04''$
$k_{\mathrm{P}}^{(1)} a/\pi = 1$	82	$1\mathrm{h}03'18''$	153	16	$1\mathrm{h}12'24''$
$k_{\mathrm{P}}^{(1)} a/\pi = 2$	418	$8\mathrm{h}44'24''$	252	29	$3\mathrm{h}06'57''$

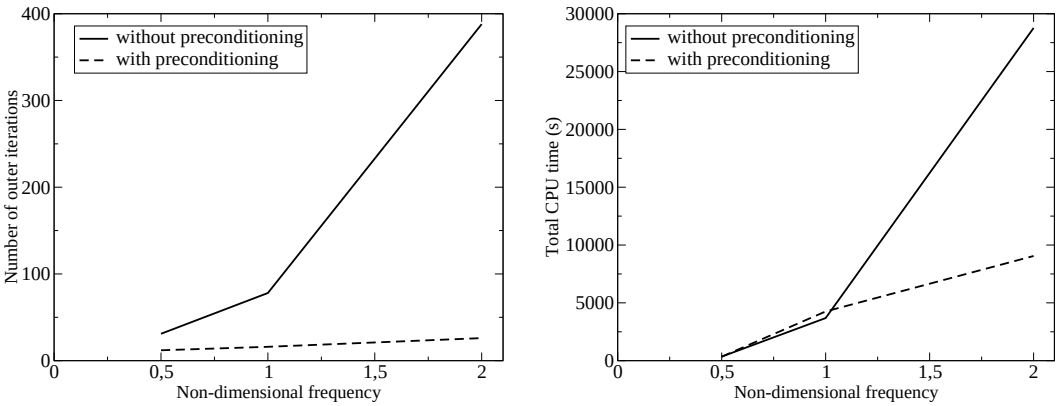

(a) (b)

Figure 5.12: *Number of outer iterations (a) and total CPU time (b) with or without preconditioning, against the non-dimensional frequency, for the problem of the diffraction of an oblique incident plane P–wave by a semi-spherical basin.*

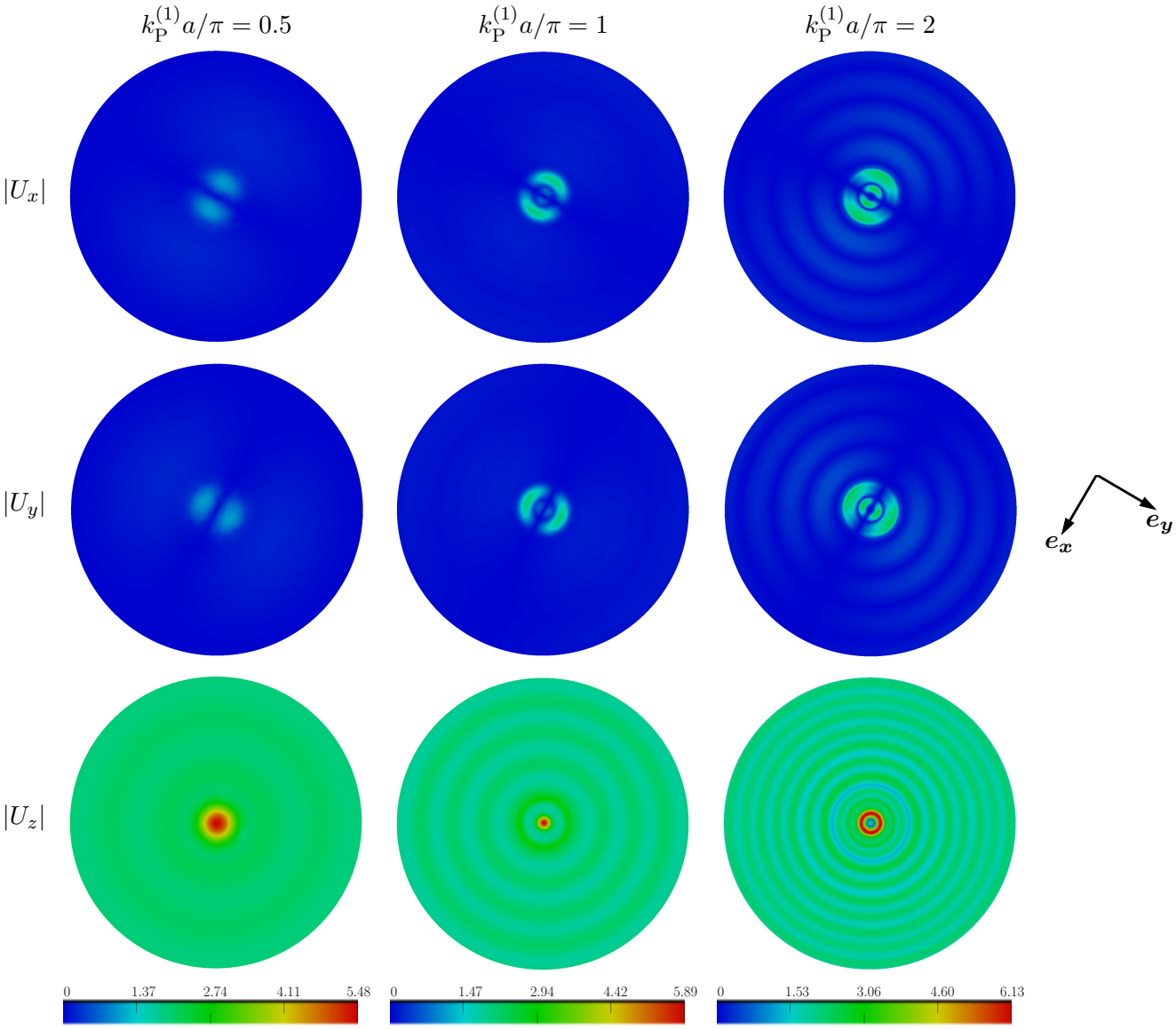

Figure 5.13: *Diffaction of a vertical incident plane P–wave by a semi-spherical basin: x- (top), y- (middle) and z- (bottom) components of surface displacement for the normalized frequencies* $k_{\mathrm{P}}a/\pi = 0.5$ *(left),* $k_{\mathrm{P}}a/\pi = 1$ *(middle) and* $k_{\mathrm{P}}a/\pi = 2$ *(right).*

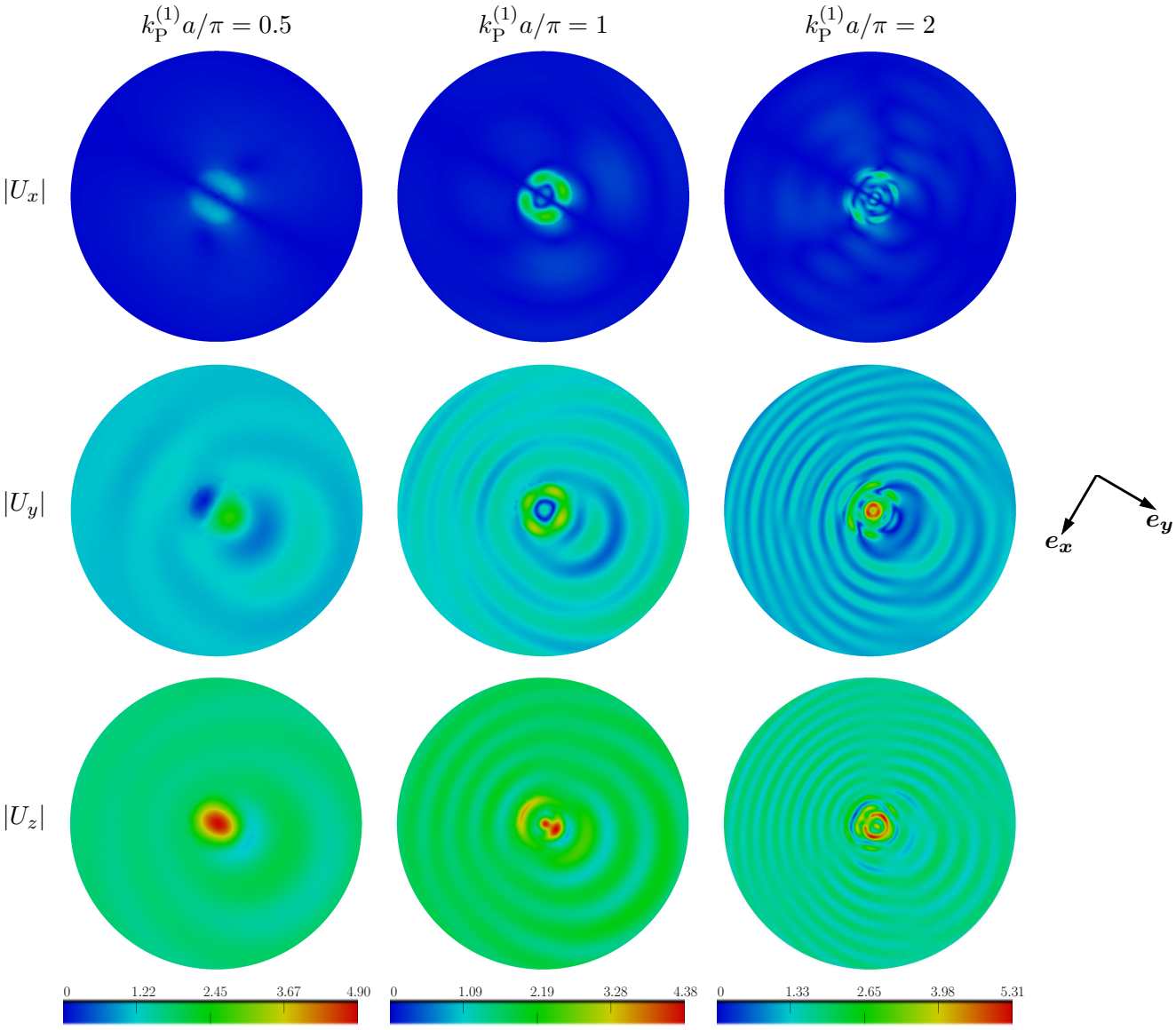

Figure 5.14: *Diffraction of an oblique ($\theta = 30°$) incident plane P–wave by a semi-spherical basin: x- (top), y- (middle) and z- (bottom) components of surface displacement for the normalized frequencies $k_{\mathrm{P}}a/\pi = 0.5$ (left), $k_{\mathrm{P}}a/\pi = 1$ (middle) and $k_{\mathrm{P}}a/\pi = 2$ (right).*

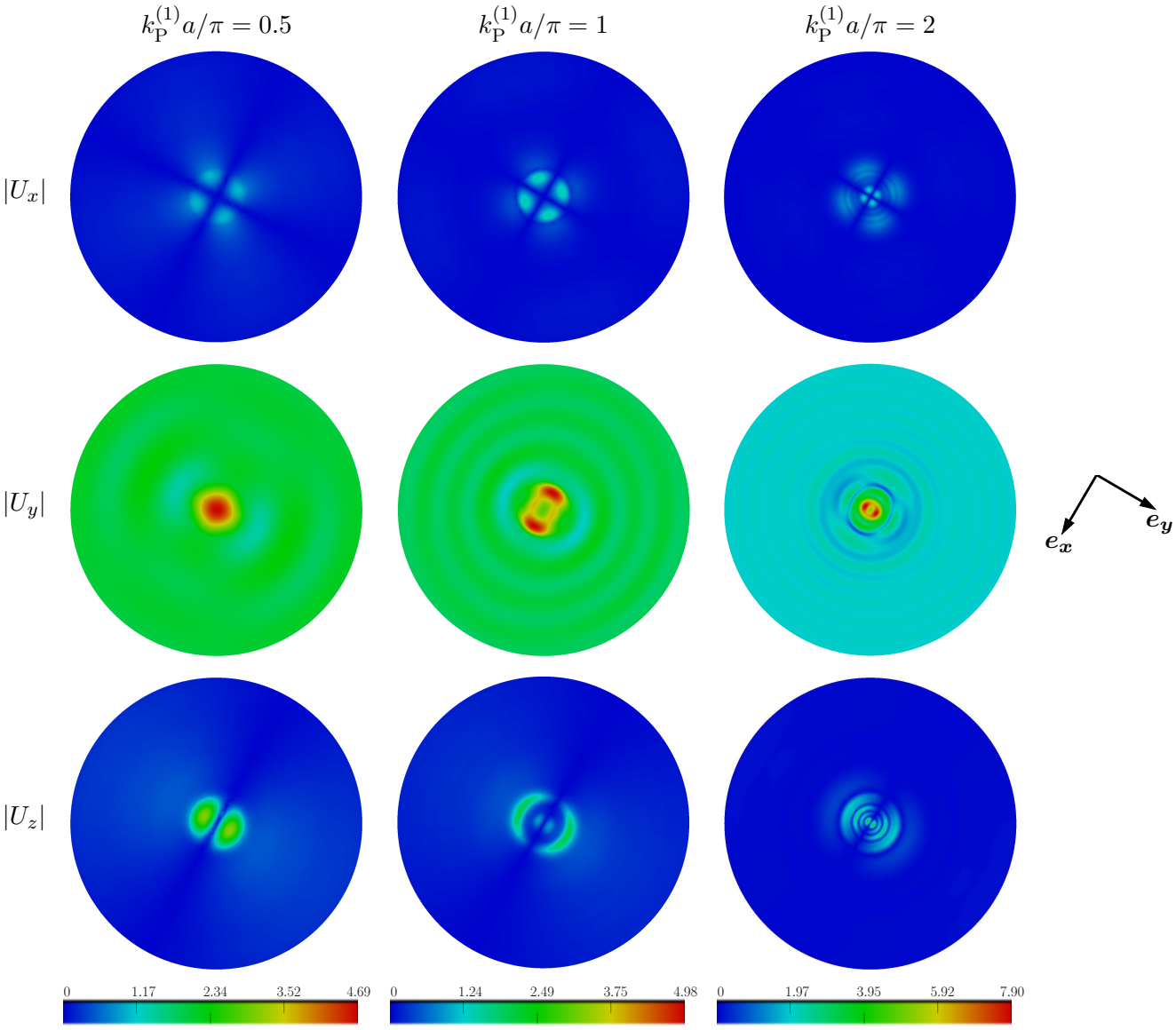

Figure 5.15: *Diffraction of a vertical incident plane SV–wave by a semi-spherical basin: x- (top), y- (middle) and z- (bottom) components of surface displacement for the normalized frequencies* $k_{\mathrm{P}}a/\pi = 0.5$ *(left),* $k_{\mathrm{P}}a/\pi = 1$ *(middle) and* $k_{\mathrm{P}}a/\pi = 2$ *(right).*

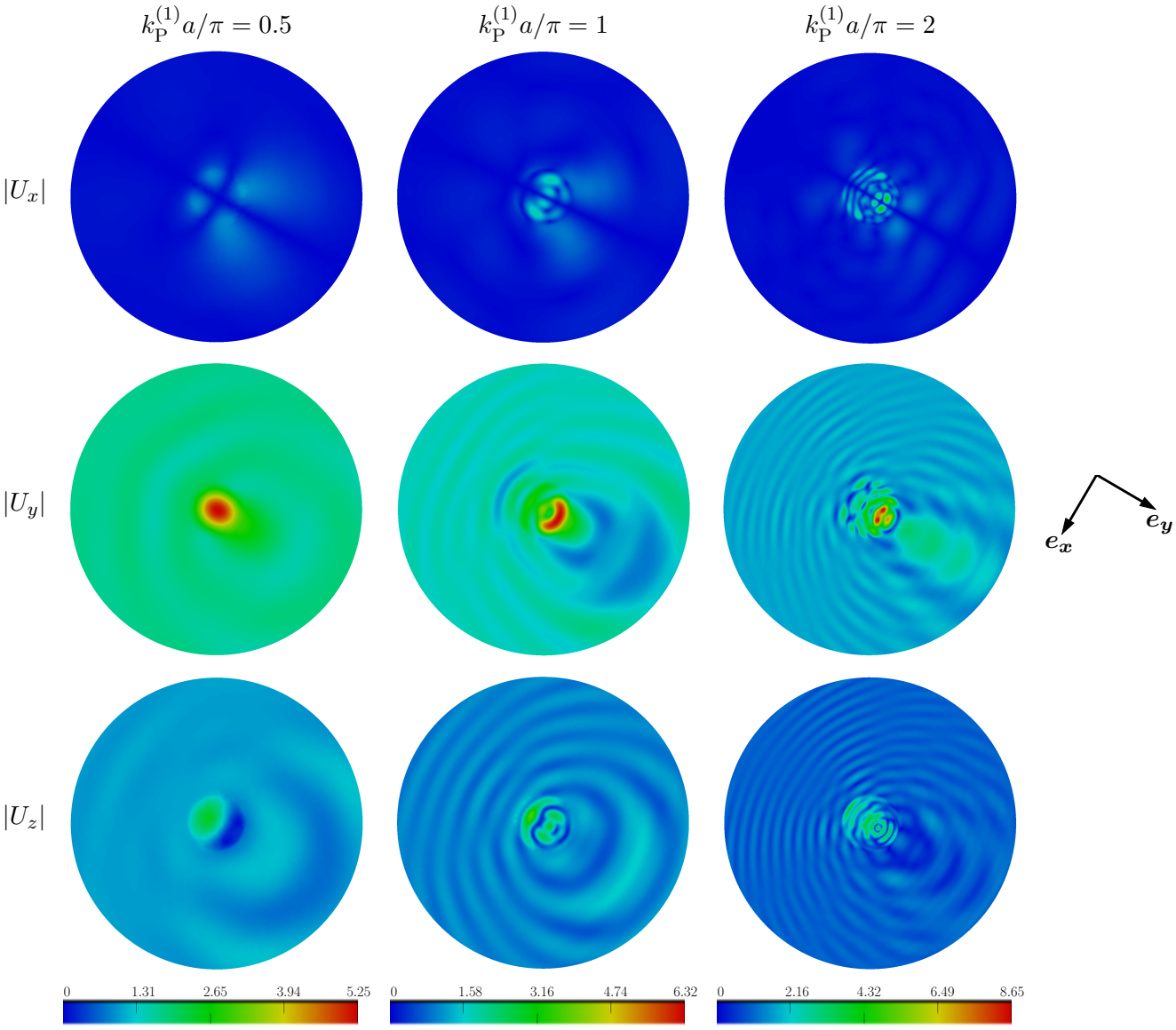

Figure 5.16: *Diffraction of an oblique ($\theta = 30°$) incident plane SV–wave by a semi-spherical basin: x- (top), y- (middle) and z- (bottom) components of surface displacement for the normalized frequencies $k_{\mathrm{P}}a/\pi = 0.5$ (left), $k_{\mathrm{P}}a/\pi = 1$ (middle) and $k_{\mathrm{P}}a/\pi = 2$ (right).*

5.5 SEMI-ELLIPSOIDAL BASIN

The last geometry is a semi-ellipsoidal basin, with semi-axes defined by $b = 2a$. The mechanical parameters are $\nu^{(1)} = 1/3$, $\mu^{(2)} = 1/4\mu^{(1)}, \rho^{(2)} = \rho^{(1)}$ and $\nu^{(2)} = 1/3$. The free surface lies inside a disk of radius $D = 8a$. In Table 5.7, the number of DOFs N, leaf levels $\bar{\ell}_1$ and $\bar{\ell}_2$ are given for four non-dimensional frequencies ($k_{\mathrm{P}}^{(1)}a/\pi = 0.25;\ 1;\ 1.5;\ 2$) together with the CPU time per iteration recorded (without preconditioning).

Table 5.7: *Diffraction of incident plane waves by a semi-ellipsoidal basin: computational data.*

$k_{\mathrm{P}}^{(1)}a/\pi$	N	$\bar{\ell}_1; \bar{\ell}_2$	CPU / iter (s)
0.25	$27,144$	$3;3$	12.4
1	$278,304$	$4;3$	111.4
1.5	$685,830$	$6;5$	199
2	$1,117,080$	$6;5$	452.5

Vertical incident plane P–wave. In Figure 5.17, the modulus of the x-, y- and z-components of surface displacements are represented for the three non-dimensional frequencies ($k_{\mathrm{P}}^{(1)}a/\pi = 0.25;\ 1;\ 1.5$). The z-component is predominant and if the frequency is increased, the x- and y-components are also significant. Four regions, with very high amplitudes occur on the x-component for $k_{\mathrm{P}}^{(1)}a/\pi = 1$. The maximum amplitude strongly increases with the frequency, and is twice higher than in the canyon case.

Oblique incident plane P–wave. If an oblique ($\theta = 30^\circ$) incident plane P–wave is considered (Fig. 5.18), the z-component is still predominant but the x- and y-components are also significant (more if the frequency is increased). As expected, the displacement response is symmetric with respect to the $x = 0$ plane because the direction of propagation lies in the Oyz plane. Compared to the semi-ellipsoidal canyon, the maximum amplitude is doubled.

Vertical incident plane SV–wave. In the case of a vertical incident plane SV–wave, the y-component is now predominant (Fig. 5.19) but the contributions of the x- and z-components increase with the frequency. The maximum amplitude is larger than 10 (i.e. amplification higher than 5) for $k_{\mathrm{P}}^{(1)}a/\pi = 1$ and $k_{\mathrm{P}}^{(1)}a/\pi = 1.5$.

Oblique incident plane SV–wave. The last case is concerned with the diffraction of an oblique ($\theta = 30^\circ$) incident plane SV–wave. In Figure 5.20, the modulus of the x-, y- and z-surface displacement components are displayed for the three non-dimensional frequencies. The y-component is predominant but once again the contributions of the x- and z-components increase with the non-dimensional frequency. The maximum amplitude reaches 18.82 for $k_{\mathrm{P}}^{(1)}a/\pi = 1.5$ leading to a strong spectral amplification.

Iteration counts. In Table 5.8, the iteration counts recorded for the twelve configurations are given. Again, the iteration count is found to be influenced not only be the frequency but also by the symmetry of the geometry and the mesh size. The influence of scattering phenomena and wave conversion is probably significant depending on the velocity contrast between the basin and the bedrock.

Once again, the iteration count increases with the frequency. Compared to the semi-ellipsoidal canyon, the iteration counts are significantly higher, reflecting the fact that basin problems are more badly conditioned than canyon problems. The use of the preconditioning strategy of Section 4.1 nonetheless drastically reduces the number of outer iterations and the total CPU time. As a result, basin problems featuring $N = 685,830$ DOFs were solved in about 36h using preconditioning, whereas they could not be solved without preconditioning.

A mesh featuring $N = 1,117,080$ DOFs is required to deal with the $k_{\mathrm{P}}^{(1)} a/\pi = 2$ case. For this computation about 6GB of RAM and 70GB on the hard drive (for storing the matrix K^{near} of near contributions) are required. Unfortunately, the preconditioning strategy was not efficient enough to solve the complete problem in this case. With our preconditioning strategy, the complete matrix K^{near} is read at each inner and outer iteration. This operation is not CPU-consuming because the time spent to read the matrix (of 70GB) is not taken into account, but requires a significant amount of elapsed time thus slowing down the overall solution procedure. Moreover, the average number of inner iterations at each outer iterations is large (sometimes over 50), and the estimated number of required outer iterations is higher than 200. This problem is thus still difficult to solve on a single-processor PC. A preconditioning strategy that does not need to read at each iteration, the complete matrix K^{near} needs to be developed to solve, on a single-processor PC, problems with $N = O(10^6)$ DOFs.

Table 5.8: *Diffraction of incident plane waves by a semi-ellipsoidal basin: iteration counts and CPU time (with and without preconditioning).*

	without prec.		with prec.		
	nb iter.	CPU time	nb iter. (inner)	nb iter. (outer)	CPU time
vertical P–wave					
$k_{\mathrm{P}}^{(1)} a/\pi = 0.25$	27	$10'37''$	108	13	$16'42''$
$k_{\mathrm{P}}^{(1)} a/\pi = 1$	734	$24\mathrm{h}07'05''$	616	44	$10\mathrm{h}27'49''$
$k_{\mathrm{P}}^{(1)} a/\pi = 1.5$	/	/	1026	128	$31\mathrm{h}26'50''$
oblique P–wave					
$k_{\mathrm{P}}^{(1)} a/\pi = 0.25$	30	$11'00''$	115	14	$16'29''$
$k_{\mathrm{P}}^{(1)} a/\pi = 1$	681	$22\mathrm{h}21'35''$	645	45	$11\mathrm{h}54'12''$
$k_{\mathrm{P}}^{(1)} a/\pi = 1.5$	/	/	1130	143	$36\mathrm{h}04'47''$
vertical SV–wave					
$k_{\mathrm{P}}^{(1)} a/\pi = 0.25$	24	$09'47''$	92	12	$15'14''$
$k_{\mathrm{P}}^{(1)} a/\pi = 1$	408	$13\mathrm{h}51'30''$	559	40	$9\mathrm{h}34'15''$
$k_{\mathrm{P}}^{(1)} a/\pi = 1.5$	/	/	857	105	$27\mathrm{h}09'09''$
oblique SV–wave					
$k_{\mathrm{P}}^{(1)} a/\pi = 0.25$	31	$10'50''$	115	14	$16'39''$
$k_{\mathrm{P}}^{(1)} a/\pi = 1$	608	$19\mathrm{h}36'25''$	653	46	$11\mathrm{h}57'55''$
$k_{\mathrm{P}}^{(1)} a/\pi = 1.5$	/	/	1077	133	$35\mathrm{h}22'41''$

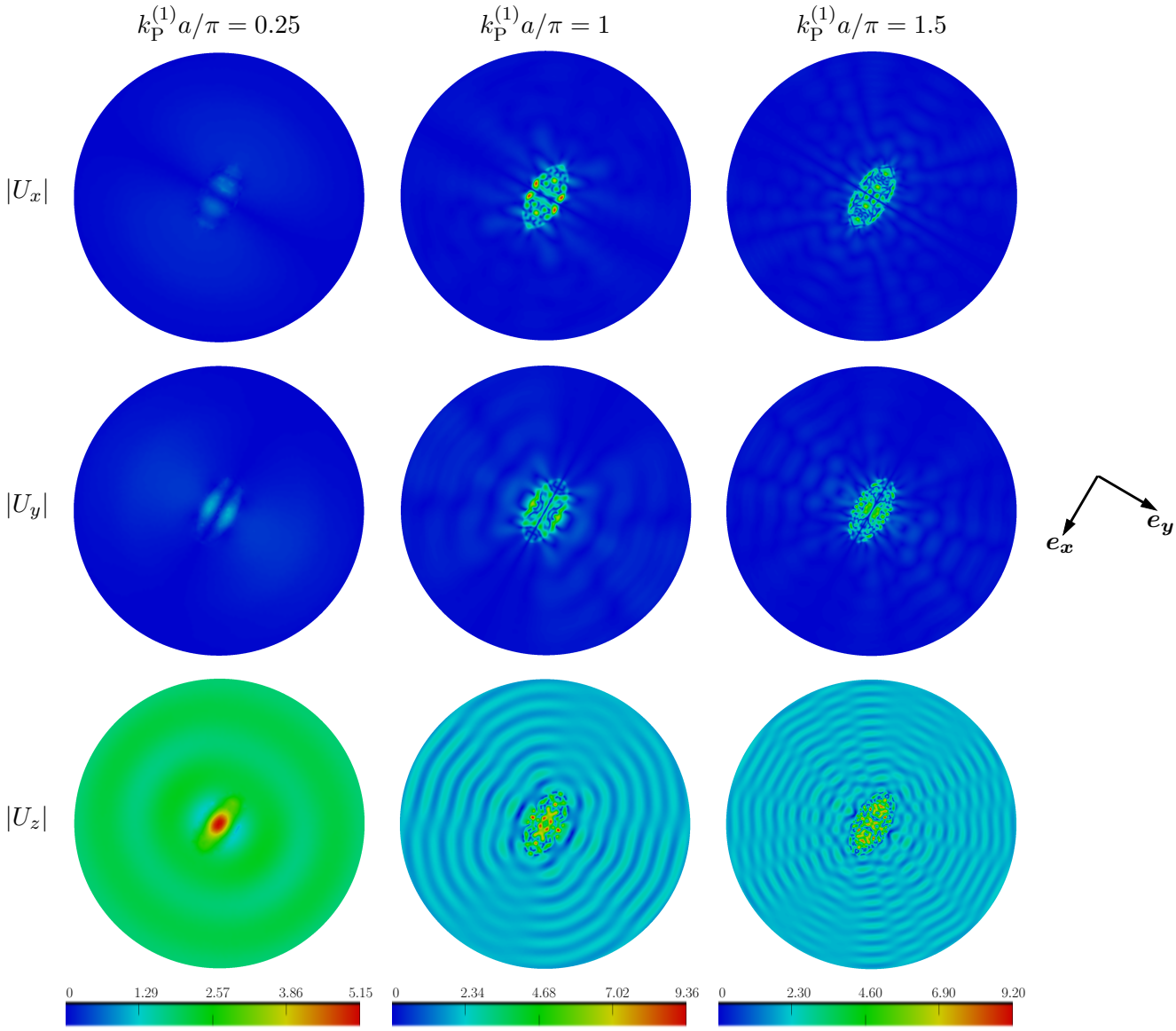

Figure 5.17: *Diffraction of a vertical incident plane P–wave by a semi-ellipsoidal basin: x- (top), y- (middle) and z- (bottom) components of surface displacement for the normalized frequencies* $k_{\mathrm{P}}a/\pi = 0.25$ *(left),* $k_{\mathrm{P}}a/\pi = 1$ *(middle) and* $k_{\mathrm{P}}a/\pi = 1.5$ *(right).*

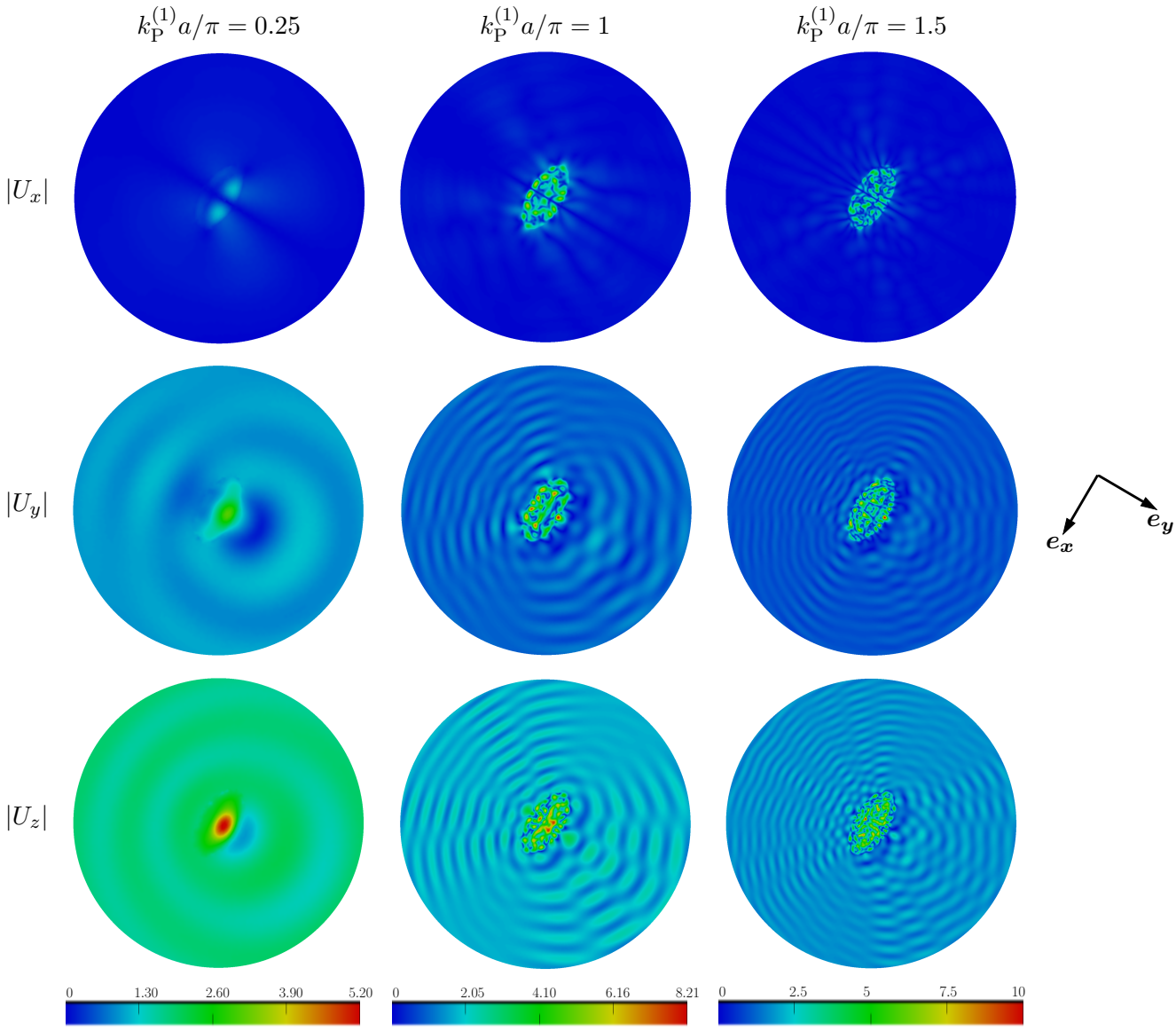

Figure 5.18: *Diffraction of an oblique ($\theta = 30°$) incident plane P–wave by a semi-ellipsoidal basin: x- (top), y- (middle) and z- (bottom) components of surface displacement for the normalized frequencies $k_{\mathrm{P}}a/\pi = 0.25$ (left), $k_{\mathrm{P}}a/\pi = 1$ (middle) and $k_{\mathrm{P}}a/\pi = 1.5$ (right).*

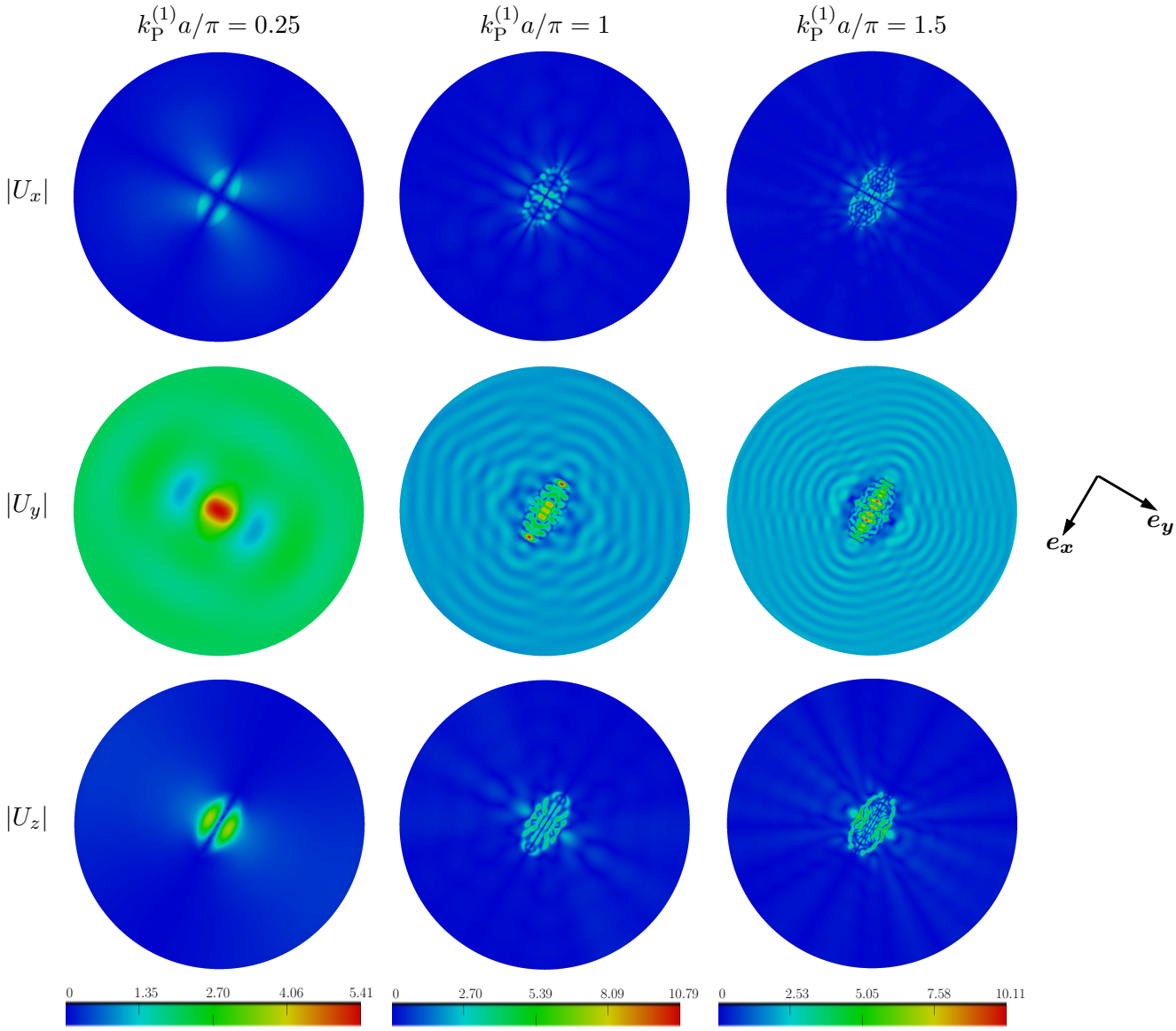

Figure 5.19: *Diffraction of a vertical incident plane SV–wave by a semi-ellipsoidal basin: x- (top), y- (middle) and z- (bottom) components of surface displacement for the normalized frequencies* $k_{\mathrm{P}}a/\pi = 0.25$ *(left),* $k_{\mathrm{P}}a/\pi = 1$ *(middle) and* $k_{\mathrm{P}}a/\pi = 1.5$ *(right).*

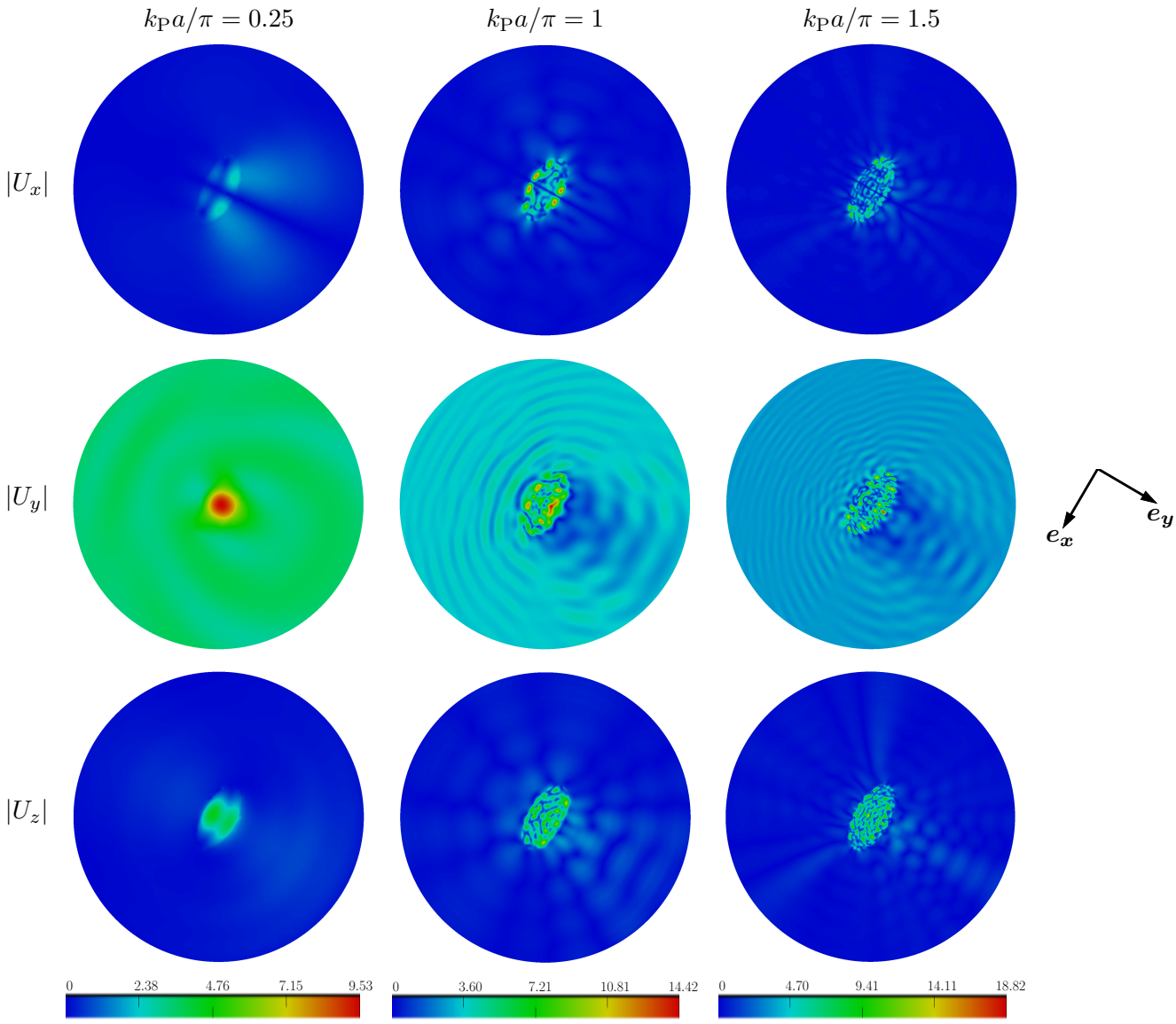

Figure 5.20: *Diffraction of an oblique ($\theta = 30°$) incident plane SV–wave by a semi-ellipsoidal basin: x- (top), y- (middle) and z- (bottom) components of surface displacement for the normalized frequencies $k_{\mathrm{P}}a/\pi = 0.25$ (left), $k_{\mathrm{P}}a/\pi = 1$ (middle) and $k_{\mathrm{P}}a/\pi = 1.5$ (right).*

5.6 CONCLUSIONS

In this chapter, the capabilities of the FM-BEM formulation presented in the first Part of this dissertation has been used to study various canonical seismological examples. Namely, the diffraction of oblique incident plane P– or SV–wave by a semi-ellipsoidal canyon or basin, have been studied. These results are our contribution to the QSHA research project. The results on the complete surface have been shown even if some results are axisymmetric, to show the good "quality" of the results obtained by our new 3-D elastodynamic solver. Moreover, this choice of representation enable quick comparisons between various kinds of incident waves or various kinds of geometries. In particular, the amplification induced by the introduction of an alluvial deposit in a canyon is easily seen. These examples also enable the presentation of the numerical performances of the present method in terms of CPU time per iteration, BE model sizes and iteration counts. Problems of size up to $N = O(7\,10^5)$ have been solved on a single-processor PC. The necessity of the development of a preconditioning strategy is also pointed out, to be able to solve higher frequency basin problems since the memory requirements and CPU time per iteration are no longer a limiting factor. The eficiency of the preconditioning strategy defined in Section 4.1 is also illustrated on these examples. However, the necessity of an improvement of this preconditioning strategy is shown. Even if it is possible to perform some iterations for problems featuring $N = O(10^6)$ DOFs, due to the need to read the complete matrix of the near contributions, this problem cannot be solved completely. The motivation of these canonical examples was not to perform an exhaustive study on the effect of the geometry or type of incident wave. The motivation was to define some simple examples to do some comparisons in terms of accuracy and numerical efficiency between the various methods proposed in the QSHA project. Unfortunately, such comparisons are not possible at the time of this writting. But, we think that these results needed to be presented in this dissertation to give a set of simple examples to validate a numerical method dealing with seismic wave propagation.

Chapter 6

Diffraction of a vertical incident plane P–wave by an Alpine valley (Grenoble)

Contents

In Chapter 5, the numerical efficiency of the present FM-BEM has been shown on canonical examples (diffraction of oblique incident plane P– and SV–waves by various canonical canyons and basins). Now, the method is applied to a more realistic seismological application, namely the diffraction of a vertical incident plane P–wave by an Alpine valley (Grenoble).

6.1 MODELLING OF AN ALPINE VALLEY: GRENOBLE

Choice of the Grenoble site

As explained in the introductory Chapter 1, the geological configuration, basin geometry and edges can modify the incident wave field and lead to large amplifications and higher signal duration. In Figure 6.1, the records for the Laffrey 1998 earthquake, at the bedrock and at the sedimentary basin surface are compared. The signal amplitude is multiplied by 8 between the bedrock (OGMU station) and the sedimentary basin (OGDH station). Moreover, the signal duration is multiplied by 3. This earthquake illustrates the negative effects of a sedimentary basin on an earthquake, even a moderate one (magnitude 3.5 in the case of the Laffrey earthquake).

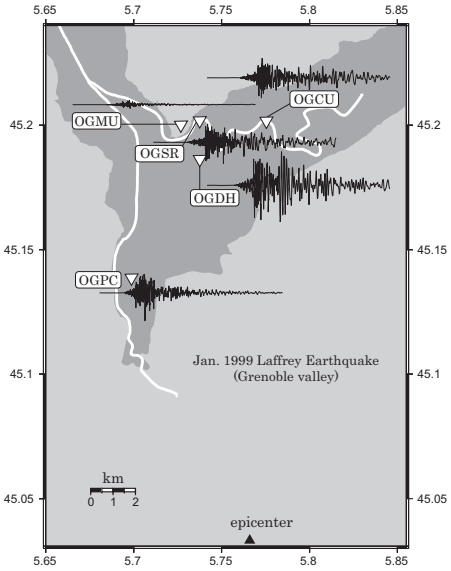

Figure 6.1: *Seismic wave amplification in deep alluvial deposits (Grenoble, France): velocities (N-S component) recorded at various locations during the 1999 Laffrey earthquake (data: French accelerometric network, www-rap.obs.ujf-grenoble.fr), from Semblat and Pecker [193] (repeats Fig. 1.2 for convenience).*

The Alpine valley case is considered in this chapter because it was proposed in the QSHA project, and has also previously been the subject of a numerical benchmark during the Third International Symposium on the Effects of Surface Geology on Seismic Motion (ESG 2006 [14]). As a result, the mechanical parameters and topographical data are available. This case also allows to show the improvement obtained by the present FM-BEM compared to standard BEM used in previous studies of this case (see thesis dissertation by N. Delépine [64] and [65]). While the main part of Delépine's work was on a 2-D profile (Fig. 6.2) of the Alpine valley proposed for the benchmark

at the ESG, he also studied in 3-D conditions the diffraction of a vertical incident plane P–wave by the 3-D profile of this Alpine valley. Due to the limitations of standard BEM, Delépine's mesh featured $8,600$ vertices and a single homogeneous layer. Moroeover, the size of the discretized free surface was set not much larger than the radius of the circle enclosing the basin (Fig. 6.3), although this size has been shown in Section 3.5.1 to influence the results. Numerical results are presented in [64] for a frequency $f = 0.4$ Hz, but to deal with such a "high" frequency using standard BEM, only about 5 points per S–wavelength were used, which is usually insufficient for BEMs. Using the capabilities of the present FM-BEM, finer meshes can be used.

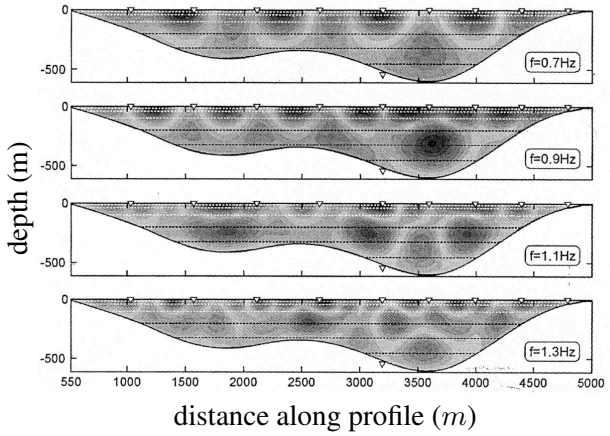

Figure 6.2: *2-D amplification in the basin, for various frequencies, from Delépine [64].*

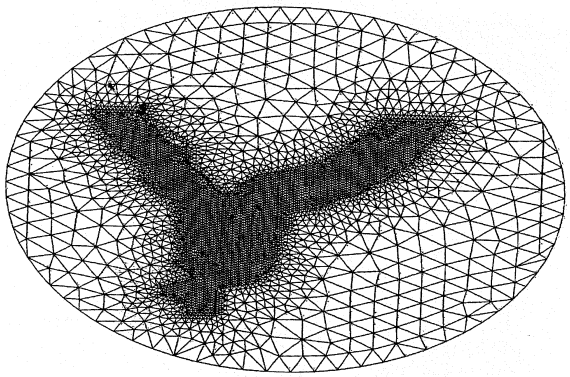

Figure 6.3: *Mesh of the Alpine valley used in [64].*

Geometry definition and mesh generation

Mesh generation is a significant issue when dealing with realistic seismological applications. For this preliminary study of a realistic site, the topography of the valley outside the sedimentary basin is not considered, for two reasons. The first one is to keep the BEM model size within manageable

limits. The second one is that the ESG numerical benchmark study showed that this topography does not affect the seismic motion. The bedrock/sediment interface is given by the inversion of gravimetric anamolies performed by Vallon [206]. A regular grid of points (every 250m) defining the topographical coordinates of the bedrock/sediment interface is provided.

The horizontal geometry of the Alpine valley is depicted on Figure 6.4a. The valley, which is Y-shaped when seen from above, is enclosed in a circle of radius $a \simeq 11.7$ km. For this study, the meshed surrounding portion of the free surface is circumscribed within a disk of radius $D = 30$ km ($\simeq 3a$). No topographical data are available at Γ_{12}^a and Γ_{12}^b. Consequently, the North ends of the Y-shaped valley are closed artificially (see Fig. 6.5), although the steep slopes thus introduced may induce artificial reflections at the basin edges. A study comparing various artificial valley closures should be done to evaluate their effects on the simulated seismic motion. However, for now we use this simple closure method in this study.

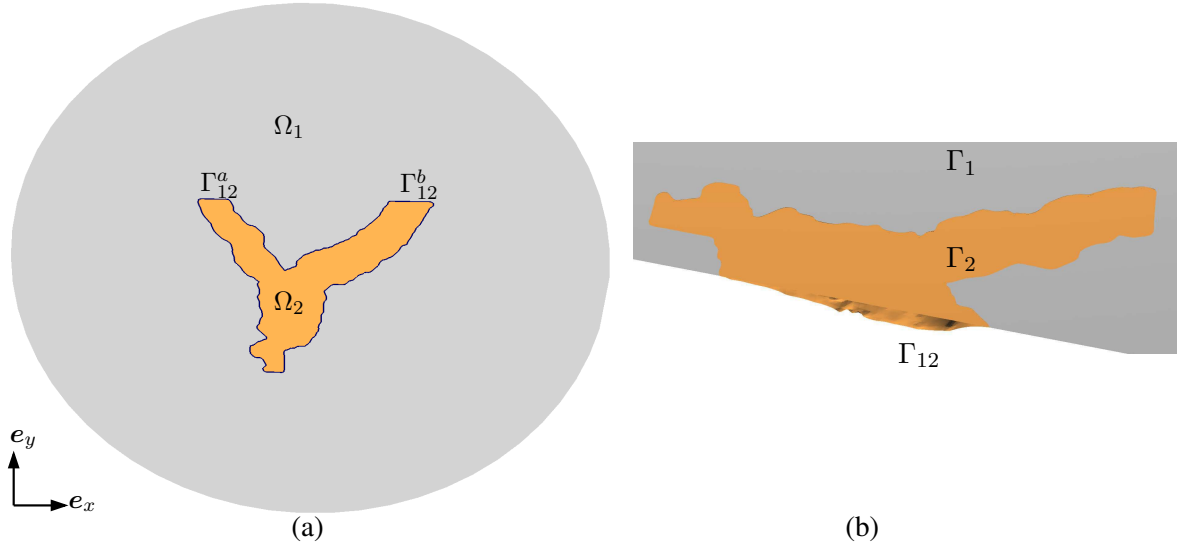

Figure 6.4: *Geometry of the Alpine valley.*

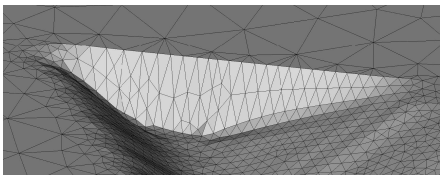

Figure 6.5: *Close up of the mesh at* Γ_{12}^a.

The mesh was generated with the help of Adrien Loseille (GAMMA team, INRIA Rocquencourt, www-c.inria.fr/gamma/) and using software developed by this team. The notations Γ_1, Γ_2 and Γ_{12} are defined in Fig. 6.4b. The methodology used is to first define the 2-D geometries of Γ_1 and Γ_2 from topographical data (Figs. 6.6a,b). Then, the 2-D mesh is generated using `BL2D` [219] (Figs. 6.6c,d). Γ_1 and Γ_2 are then merged (Fig. 6.6e) using `Spider` (code provided by Adrien Loseille). Using topographical data, Γ_{12} (Fig. 6.6f) is obtained from Γ_2 (using `Spider`). Finally, $\Gamma_1 \cup \Gamma_2$ is merged to Γ_{12} (Fig. 6.6g). `Yams` [223] is used to optimize the mesh to the frequency.

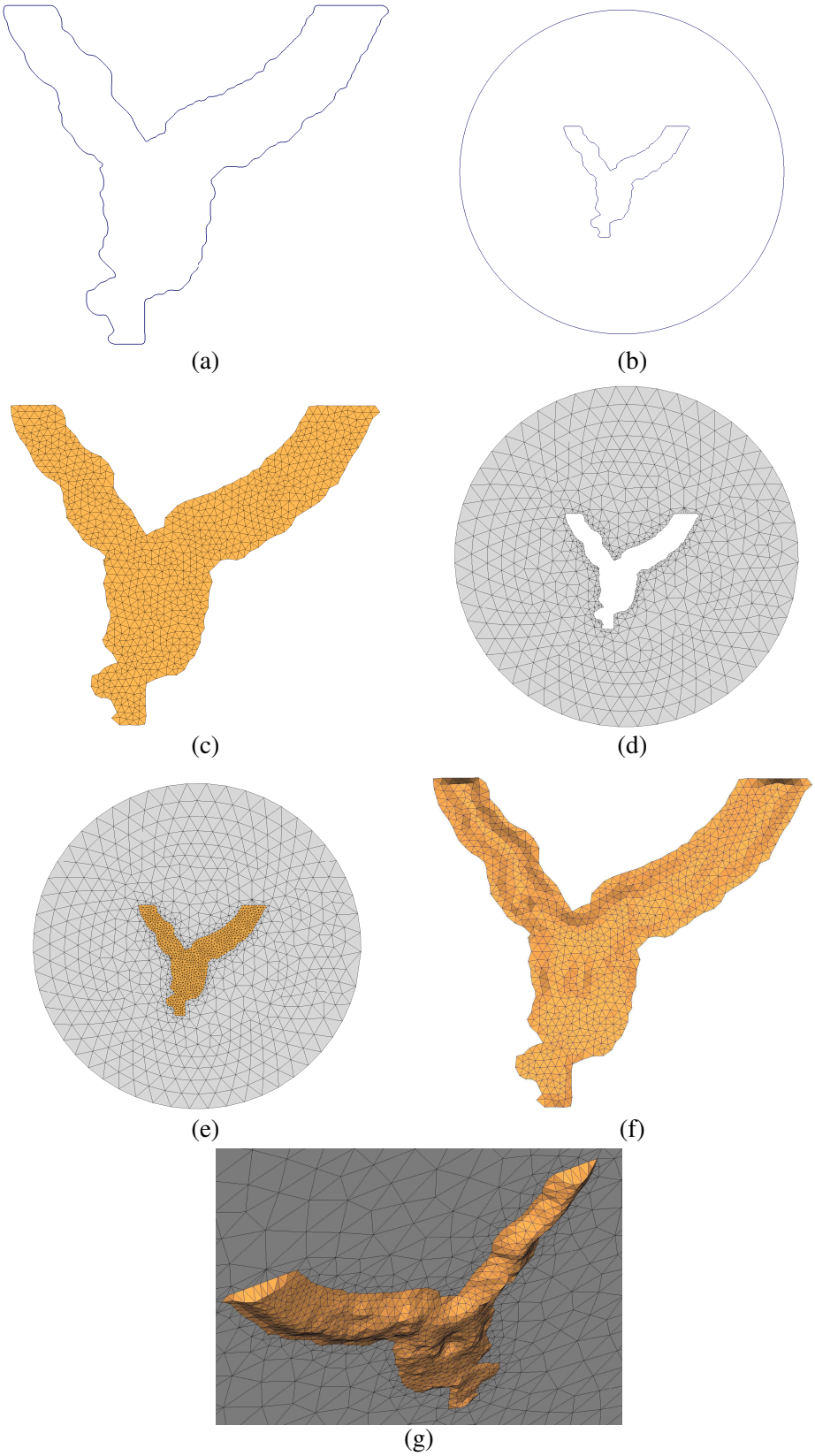

Figure 6.6: *Alpine valley: mesh generation.*

Mechanical parameters

The bedrock and sedimentary basin models are as proposed in [43]. In the bedrock, denoted Ω_1 (Fig. 6.4a), the P– and S–velocities and mass density are set to constant values:

$$c_{\mathrm{P}}^{(1)} = 5,600 \text{ m.s}^{-1}, \quad c_s^{(1)} = 3,200 \text{ m.s}^{-1} \text{ and } \rho^{(1)} = 2,720 \text{ kg.m}^{-3}.$$

In the sedimentary basin, as proposed for the numerical benchmark (ESG 2006), the velocity profile increases with depth z. The models proposed are:

$$c_p(z) = 1450 + 1.2z, \quad c_s(z) = 300 + 19\sqrt{z} \text{ and } \rho(z) = 2140 + 0.125z.$$

In this work, of a preliminary nature, only a single homogeneous layer Ω_2 is used, with mechanical parameters set to:

$$c_{\mathrm{P}}^{(2)} = 1,988 \text{ m.s}^{-1}, \quad c_s^{(2)} = 526 \text{ m.s}^{-1} \text{ and } \rho^{(2)} = 2,206 \text{ kg.m}^{-3}.$$

6.2 SURFACE DISPLACEMENTS FOR A VERTICAL INCIDENT PLANE P–WAVE

All examples presented in this chapter have been run on the same 8-processor PC (RAM: 64 GB, CPU frequency: 2.33 GHz), with each FMM analysis performed independently on a single processor.

The diffraction of a vertical incident plane P–wave by an Alpine valley is considered for two frequencies: $f = 0.3$ Hz and $f = 0.6$ Hz. In Table 6.1, the number of DOFs N and the leaf levels $\bar{\ell}_1$ and $\bar{\ell}_2$ are given for the two frequencies together with the CPU time per iteration (without preconditioning), the number of iterations and the cumulative CPU time (with preconditioning strategy). In Figure 6.7, the modulus of the x-, y-, z- surface displacement components are displayed for the two frequencies. This realistic example shows the possibility of very high amplifications inside the alluvial basin (about 15.5 for $f = 0.6$ Hz). As noted in [64], the major part of the amplification is observed at the north of the basin, for the z-component.

Table 6.1: *Propagation of an incident plane P–wave in an Alpine valley: computational data.*

f	N	$\bar{\ell}_1; \bar{\ell}_2$	CPU time (s) per iter.	nb iter. with prec.	total CPU time
0.3 Hz	95,142	4;5	86.6	253	39h55′31″
0.6 Hz	141,288	5;6	77	747	75h45′44″

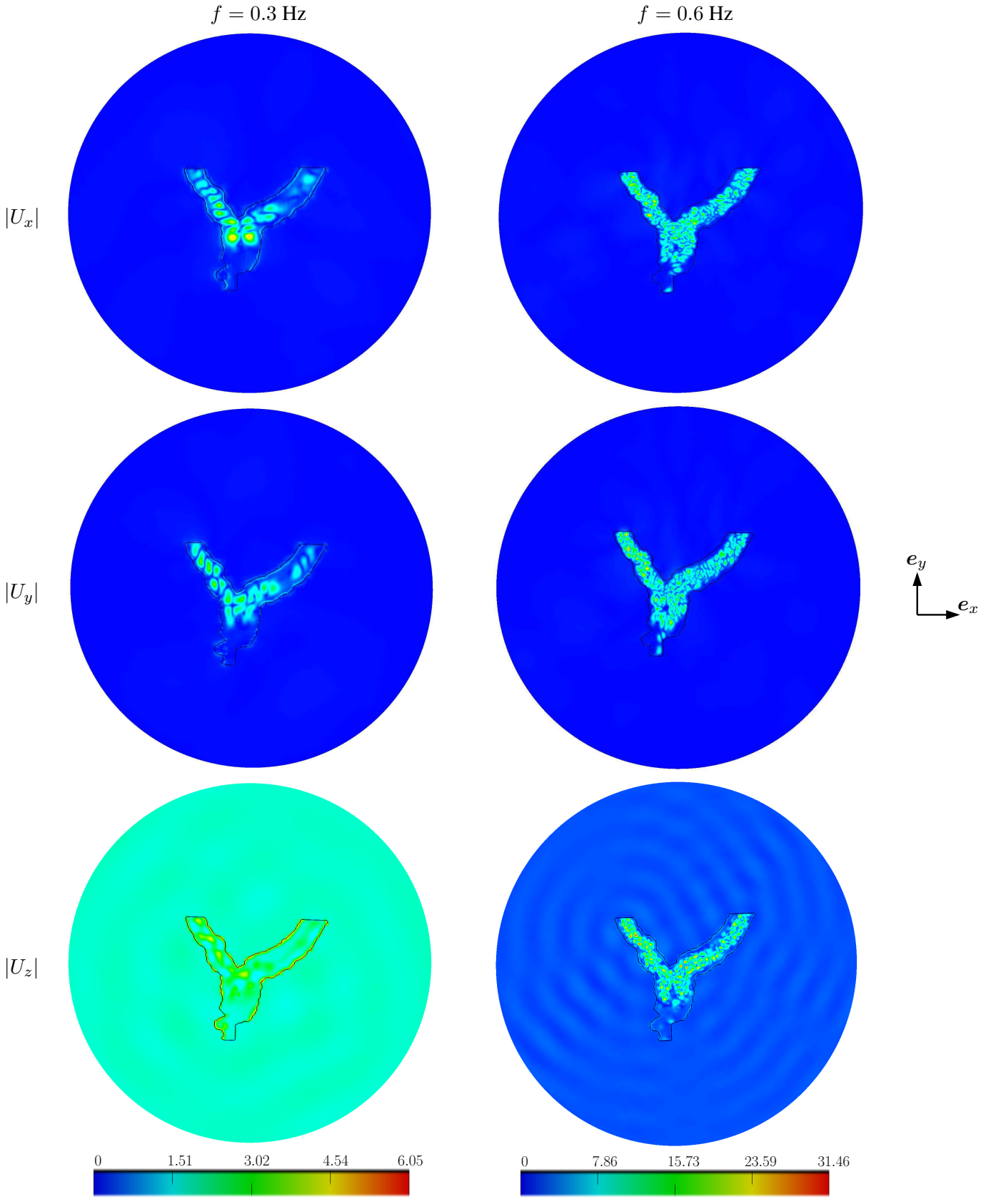

Figure 6.7: *Propagation of a vertical incident plane P–wave in the Alpine valley: modulus of the x- (top), y- (middle) and z- (bottom) components of displacement for frequencies $f = 0.3$ Hz (left) and $f = 0.6$ Hz (right).*

6.3 LIMITATIONS OF PRESENT FM-BEM FOR REALISTIC SEISMIC APPLICATIONS

The meshes used in this chapter feature a relatively low number of degrees of freedom (and so the frequencies studied are relatively low) compared to examples treated in the previous chapters. This example highlights the limitations induced by a high velocity contrast between two layers (in this example, the velocity contrast is about 6). Usually, the mesh is generated to obtain about 10 points per S–wavelength. But for basin problems, mesh conformity requirements at interfaces induce densities of about 10 points per *smallest* S–wavelength near the interfaces. As a result, on the interface Γ_{12}, the mesh is adapted to Ω_2 but is about 6 times too dense for the domain Ω_1. For example, for $f = 0.6$ Hz, in Figures 6.8a,c, the mesh is seen adapted to about 8-10 points per S–wavelength on Γ_1 and Γ_2. But, in Figure 6.9b, the mesh on Γ_{12} is seen to be too dense compared to the wavelength.

This is sub-optimal for the present FM-BEM. The evaluation of memory and CPU time complexities presented in Section 2.5.2 is based on the assumption that the number of DOFs per wavelength is roughly uniform, resulting in roughly equal numbers of DOFs per leaf cell (due to the stopping criteria $d^{\min} \geq 0.30\lambda_S$). Here, the combined effect of highly heterogeneous mesh densities and cell size threshold leads to leaf cells containing large numbers of DOFs in regions close to the interface. This in turn leads to a large matrix K^{near}. As a result, memory requirements are high (compared to a uniform mesh) in terms of RAM and space on the hard drive. The other consequence is that the CPU time and memory requirements are very sensitive to the number of levels. For the two frequencies studied $f = 0.3$ Hz and $f = 0.6$ Hz, the size of the matrix K^{near} are respectively of about 20 GB and 25 GB. The first remark is that the size of K^{near} is larger for $f = 0.3$ Hz than for $f = 0.6$ Hz even though the number of DOFs is smaller. The explanation is that the number of levels is larger in the second case. If the mesh featuring $N = 141,288$ is used for $f = 0.5$ Hz instead of $f = 0.6$ Hz, the leaf levels are $\bar{\ell}_1 = 4$ and $\bar{\ell}_2 = 5$. As a result, this problem is difficult to solve since K^{near} is very large: 52 GB. This sensitivity to the number of levels also explained why the CPU time per iteration is larger for $f = 0.3$ Hz than for $f = 0.6$ Hz. The proportion of near contributions is larger for the first case than for the second one, leading to larger CPU time per iteration.

Concerning the preconditioning strategy, because K^{near} is very large, it is less efficient. The cost of the inner iterations is high since the matrix K^{near} needs to be inverted at each inner iteration. For that reason, for the two examples presented in this chapter, the value of the stopping criteria is set to $\varepsilon_{\text{inner}} = 5\,10^{-1}$ instead of the recommended value $\varepsilon_{\text{inner}} = 10^{-1}$.

To enable the computation $f = 0.6$ Hz, only about 8 points per S–wavelength are used in Ω_2 whereas 10 points per S–wavelength are used for $f = 0.3$ Hz. This explains that the number of DOFs is not twice higher for $f = 0.6$ Hz than for $f = 0.3$ Hz.

6.4 CONCLUSIONS AND DIRECTIONS FOR FUTURE WORK

In this chapter, the FM-BEM is used to study a more realistic example: the diffraction of a vertical incident plane P–wave by an Alpine valley (Grenoble). It has been shown that the FM-BEM allows computations for higher frequencies and with a larger discretized free surface than using standard BEM [64]. This example also underlines the current limitation of the present FM-BEM to deal with basin problems featuring a high velocity contrast between two layers. Due to the non-uniform mesh, the method loses efficiency.

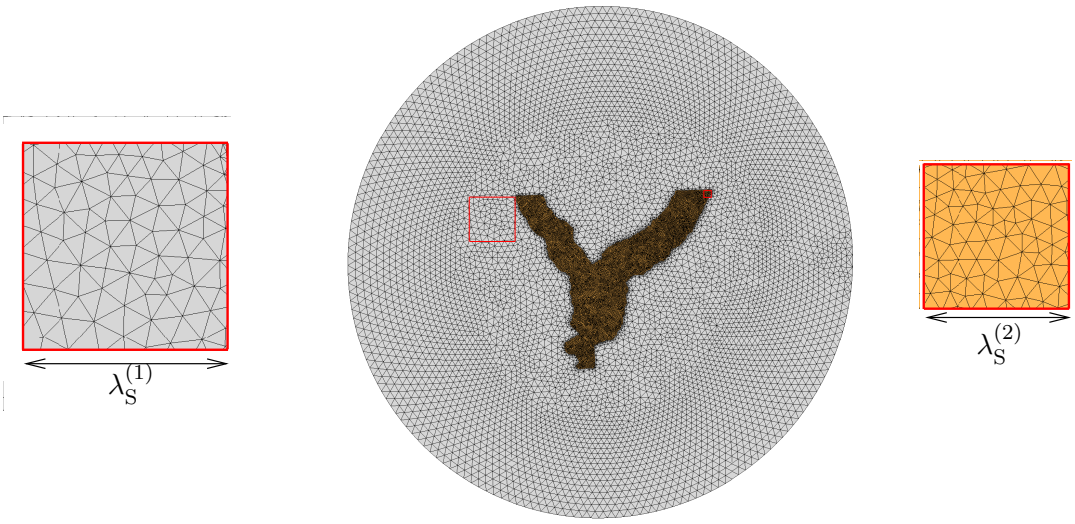

Figure 6.8: *Density of points per S–wavelength (b) and close-ups on cells of size* $\lambda_S^{(i)}$ *(a and c), for* $N = 141,288$ *and* $f = 0.6$ *Hz.*

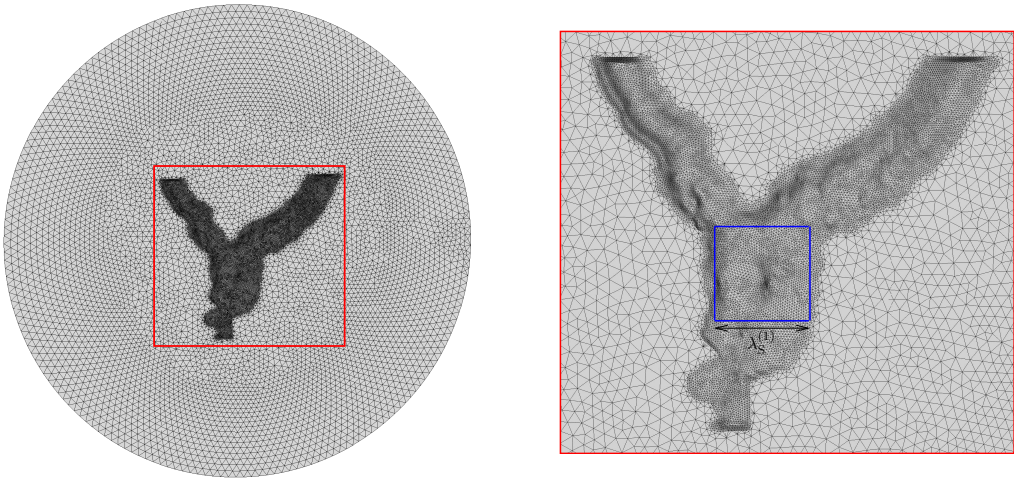

Figure 6.9: *Density of points per S–wavelength in* $\Omega^{(1)}$ *(a) and close-up on the density of points per* $\lambda_S^{(1)}$ *on the interface* Γ_{12} *(b), for* $N = 141,288$ *and* $f = 0.6$ *Hz.*

To overcome this limitation, a method stable at all frequencies (combining low and mid frequency FMM) could be used [117, 164]. This method removes the $0.30\lambda_S$ lower bound for linear cell size (the subdivision-stopping criterion used for the mid frequency FMM), allowing to adapt the number of DOFs per cell to a constant value. Another possibility is to use non-conforming meshes and develop a weak coupling formulation [177].

Moreover, in this example, only a single layer is used, whereas velocities of alluvial deposits usually have vertical gradients. For example, for the 2-D profile studied using standard BEM

in [64], the velocity gradient proposed for the numerical benchmark is approximated by seven layers (Fig. 6.10). As a result, more layers may be used in our simulation and the efficiency of the present FM-BEM may be increased if the contrasts are smaller. The difficulty is then to generate the mesh with various layers. Other possibilities include (i) resorting to fundamental solutions for layered [108, 49] or vertically-heterogeneous [107] media, for which multipole expansions may conceivably be set up along the lines of Section 4.3, and (ii) use FEM or other domain discretization methods for modelling thin layers.

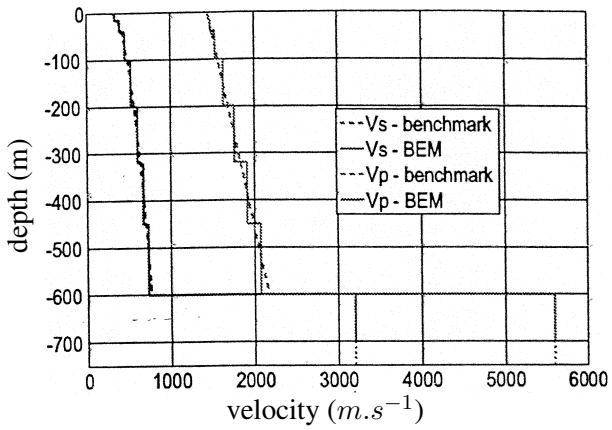

Figure 6.10: *Velocity profile for P– and S–waves used in [64].*

In this preliminary set of results, only plane waves are considered. The last point to deal with realistic seismological problems is to implement more complex sources. The BEM needs to be provided with the value of the incident wavefield, which may require preliminary FM-BEM analyses on simpler domains.

Conclusions

Conclusions and directions for future work

CONCLUSIONS

The main aim of this work, to which Part I of this dissertation was devoted, was to develop an efficient solver for frequency-domain elastodynamics using FM-accelerated BEM. Taking advantages of recent published developments for Helmholtz and Maxwell equations, the Fast Multipole Method has been successfully extended to elastodynamics in the frequency domain in Chapter 2. Combined with the BEM formulation, it permits to reduce the computational burden, in both CPU time and memory requirements, for the simulation of (e.g. seismic) wave propagation and allows to run models of size $N = O(10^6)$ on an ordinary PC. The theoretical complexity estimates of the method were derived and corrobated by numerical experiments. The accuracy of the method has been tested on exact, and previously-published numerical, solutions. In this first stage the formulation was limited to homogeneous media.

Next, as the other aim of this thesis was to develop a seismic wave-oriented solver, the ability to deal with alluvial-basin configurations has been introduced in Chapter 3 using a FM-based BE-BE approach suitable for 3-D piecewise-homogeneous media. Towards this end, the single-domain FMM was applied independently in each homogeneous sub-domain. Various implementation issues raised by the BE-BE coupling have been adressed, and the accuracy of this multi-domain FM-BEM has also been extensively tested on exact and previously published problems.

The efficiency of the elastodynamic FM-BEM presented in Chapter 2 and 3 can still be improved in several ways. Three avenues for enhancing computational performance have been proposed in Chapter 4. First, a simple preconditioning strategy has been presented, and its efficiency demonstrated on canonical examples. Then, a method to reduce the number of necessary multipole moments has been discussed. Finally, the formulation of a multipole expansion for the elastodynamic half-space fundamental solutions has been presented.

Then, Part II of this dissertation was devoted to some seismological examples. First, results on the propagation of plane waves in various canonical canyons and basins have been presented in Chapter 5. These examples, performed in the context of the QSHA project, will be compared to results using other numerical methods. The efficiency of the method has been used in Chapter 6 to deal with a more realistic application: the diffraction of an incident plane P–wave by an Alpine valley (Grenoble).

DIRECTIONS FOR FUTURE WORK

This work was the first stage of the development of a fast solver for frequency-domain elastodynamics, using FM-BEM, at the École Polytechnique and LCPC. Before this thesis, no efficient BEM solver for large 3-D elastodynamic problems was available. In view of the encouraging results obtained in this thesis, further work will be devoted to increase the capabilities and possibilities of this elastodynamic solver. Some possible directions for future work are now briefly discussed.

Parallelization. The present implementation of the elastodynamic FMM has been done for single-processor platforms. The introduction of the FMM has been shown in this thesis to greatly enhance the capabilities of the standard BEM. Now, with the increasing performance of computers, the parallelization of the code would further extend the capabilities of the method in terms of e.g. BEM model size or frequency range. The parallelization of the FMM is a difficult task. A natural idea is to associate a cell to a single processor. However, various stages of the algorithm link at least two cells:

- near contributions,
- upward and downward passes,
- transfers.

As a result, the distribution of the cells to the various processors is an important issue in order to minimize communication time between processors. This issue has been studied, for the Maxwell's equations, in [200].

When dealing with piecewise-homogeneous media, computation of the matrix-vector product at each iteration is naturally decomposed into independent tasks (one per sub-domain). When dealing with many sub-domains, an obvious approach is to associate each sub-domain to a processor. Using this method, the communication between the processors will be reduced to the transfer of the resulting vector after the matrix-vector product (before the GMRES step).

Preconditioning. In Chapters 4 and 5, a simple preconditioning strategy, based on the complete matrix of near contributions K^{near} used as preconditioner and two nested GMRES solvers, has been presented and its efficiency demonstrated. However, for BEM models of size $N = O(10^6)$ or more, the iteration count was found to remain a major limiting factor. The definition of an effective preconditioner is crucial for developing an efficient iterative solver. To improve on the admittedly simple approach currently implemented, one possibility is to introduce a theshold on the entries of K^{near}. Moreover, a comparative study with the other usual preconditioning strategy used in electromagnetic FMM (SPAI, incomplete LU, ...) is expected to bring worthwhile insight on this issue.

All preconditioners discussed so far are purely algebraic. A completely different approach, however less developed and more intrusive in the code, consists in taking into account the mathematical properties of the continuous operator. In electromagnetism, some works are dealing with the reformulation of the integral operator, at the continuous level, to obtain stable formulations (e.g. [8]). Another approach consists in determining a good preconditioner using a regularization at the continuous level of the boundary integral equations. Such formulations, based on Calderón identities for integral operators, have produced good results in electromagnetics [47, 9].

Other refinements related to time-domain response computation. In Chapters 2 and 3, time-domain results have been obtained via frequency-domain analyses at sampling frequencies and a Fourier transform. For results presented in Sections 2.6.4 and 3.6, the FM-BEM solution for each frequency has been computed independently, i.e. without using previously-obtained solutions at lower frequencies. The iteration counts, and hence the cumulative CPU time, may be reduced when performing time-domain computations, by using the result at the previous frequency as an initial guess of the GMRES iterative solver. As, frequency steps are usually small, frequency-domain solutions at two consecutive frequencies are expected to be similar. This trick should thus speed up the overall convergence. This method can be used because, as explained in Section 3.6, a hierarchical sequence of meshes is used. Another possibility is to adapt the FM-BEM to the Convolution Quadrature Method [136, 137], which has already been applied for elastodynamic [186] and viscoelastic [187] BEMs.

Viscoelasticity. In this work, only linear elastodynamics has been considered. But, in seismology, the ideal model of an elastic soil is often insufficiently realistic. The introduction of damping, using a viscoelastic law is needed. From (1.12), we see that viscoelasticity can be easily derived from elastodynamics. For standard BEM, the classical method consists in introducing complex-valued elastic constants (see Section 1.4). But no convergence theorem is known, at this time, for the multipole expansion of the Helmholtz fundamental solutions, eq. (2.8) for a complex value of the wavenumber k. I have participated to the supervision of the master thesis of Régis Bost [35] on this subject, in which numerical experiments have been performed to determine how to adapt the truncation parameter of the transfer function (2.9) in the case of a complex value of k. It appears that, as in the elastic case, the truncation parameter can be determined using a relation of the type: $L = O(|kd|)$. But, a limiting factor is concerned with the definition of the adjacent cells. In elastodynamics, as for Helmholtz equation, the criterion to achieve convergence in the transfer function is to have non adjacent cells (that do not share a corner). But, in this numerical experiment, it seems that for damping ratios larger than 5%, convergence of the multipole expansion is not always achievable for interaction between cells that are separated by only one same-level cell. Satisfactory extension of the elastodynamic FMM to viscoelastic media requires deeper mathematical examination of expansions such as (2.15) to gain better understanding on how complex wavenumbers affect convergence as $L \to \infty$. Such issues will be addressed in the PhD thesis of Eva Grasso (2008-2011) and COFFEE will be extended in the future to viscoelastic materials.

Coupling with other numerical methods. In this work, an efficient solver for elastodynamic problems has been developed. But, due to the BIE formulation with the fundamental solutions of the infinite half-space, only piecewise-homogeneous medium can be studied. An interesting perspective of this work is to implement a FE/BE coupling. The first possible application of such coupling is to deal with soil-structure interactions. With this new formulation, it could be possible, for example, to study the influence of the traffic induced waves propagating into the soil on the vibrations of structures and potential nuisances. The second possible application is to take into account non-linear constitutive behaviour in a bounded region of the soil, modelled using the FEM, while a complementary infinite region is modelled using the FM-BEM.

Such coupling strategy would use the adequateness of the BEM to deal with unbounded media, the numerical efficiency of the FMM, and the flexibility of FEM to deal with non-linear materials. Moreover, such formulation avoids the major drawbacks of BEM (simple linear material properties) and of FEM (artificial truncation of the infinite domain and cost of the volume mesh).

Inverse problems. Another possible application of this work concerns the solution of inverse problems. There exists various methods to solve inverse problems. An active research field is concerned with defect identification problems in geophysics or in medical imaging. Usually, iterative gradient-based minimization methods are used to minimize a cost function used for formulating the inversion problem, because global search algorithms are overly CPU consuming. Because these methods are sensitive to the initial conditions, sampling or probe non-iterative methods have been recently developed [168, 158]. For example, the topological sensitivity method evaluates the pointwise sensitivity of the error functional to an infinitesimal obstacle [106, 33]. Such method requires the values of displacements and stresses for a direct and adjoint problem at a large number of sampling points, which makes the FM-BEM quite useful for such computations. In [158], the FM-BEM is successfully applied to 3-D acoustic inverse scattering. The present implementation may similarly be applied to 3-D elastodynamics inverse scattering.

MAIN PUBLICATIONS ASSOCIATED WITH THIS WORK

Articles. The work presented in the dissertation has lead to several journal articles:

- S. Chaillat, M. Bonnet and J. F. Semblat. A new fast multi-domain BEM to model seismic wave propagation and amplification in 3D geological structures. *Geophys. J. Int.*, accepted, 2008.
- S. Chaillat, M. Bonnet and J. F. Semblat. A fast multipole accelerated BEM for 3-D elastic wave computation. *Revue Européenne de Mécanique Numérique*, 17: 701–712, 2008.
- S. Chaillat, M. Bonnet and J. F. Semblat. A multi-level fast multipole BEM for 3-D elastodynamics in the frequency domain. *Comp. Meth. Appl. Mech. Engng.*, 197:4233–4249, 2008.
- S. Chaillat and H. D. Bui. Resolution of linear viscoelastic equations in the frequency domain using real Helmholtz boundary integral equations. *C. R. Mecanique*, 335:746–750, 2007.
- S. Chaillat, M. Bonnet and J. F. Semblat. A fast multipole method formulation for 3D elastodynamics in the frequency domain. *C. R. Mecanique*, 335:714–719, 2007.

Book chapter. A chapter in a scientific book has also been written following this work:

- M. Bonnet, S. Chaillat and J. F. Semblat. Multi-level fast multipole BEM for 3-D elastodynamics. *In Recent Advances in BEM* (D. Polyzos and G. Manolis, eds.), to appear, 2008.

Conferences. This work has been presented in 5 international conferences and 3 national (French) conferences.

Appendices

Appendix A

Standard Boundary Element Method: implementation details

Contents

In Chapter 1, the formulation of the elastodynamic boundary integral equations and boundary element method have been briefly recalled. In this appendix, we give more details on the implementation. Moreover, a large part of this appendix is devoted to the numerical integration of the various integrals present in the formulation.

A.1 DISCRETIZATION OF THE INTEGRAL EQUATION

This first section addresses the boundary element discretization method for the elastodynamic equation (1.5) on a domain Ω of boundary $\partial\Omega$. The displacement $\boldsymbol{u}$ and traction $\boldsymbol{t}$ are governed by the boundary integral equation:

$$c_{ik}(\boldsymbol{x})u_i(\boldsymbol{x}) + (\text{P.V.}) \int_{\partial\Omega} u_i(\boldsymbol{y}) T_i^k(\boldsymbol{x},\boldsymbol{y},\omega) dS_y - \int_{\partial\Omega} t_i(\boldsymbol{y}) U_i^k(\boldsymbol{x},\boldsymbol{y},\omega) dS_y = 0 \qquad \text{(A.1)}$$

A.1.1 Definition of the boundary elements

The numerical solution of boundary integral equation (A.1) is based on a discretization of the boundary surface $\partial\Omega$ into N_E non-intersecting boundary elements $E_1, E_2, \ldots$ Equation (A.1) then takes the form of a sum of elementary integrals:

$$c_{ik}(\boldsymbol{x})u_i(\boldsymbol{x}) + \sum_{e=1}^{N_e} \left[(\text{P.V.}) \int_{E_e} u_i(\boldsymbol{y}) T_i^k(\boldsymbol{x},\boldsymbol{y},\omega) dS_y - \int_{E_e} t_i(\boldsymbol{y}) U_i^k(\boldsymbol{x},\boldsymbol{y},\omega) dS_y \right] = 0$$

Actual evaluation of those element integrals requires that each element E_e be analytically described. Usually a mapping of each physical element E_e onto a parent element Δ_e (triangle in the (ξ_1, ξ_2)

plane), in a parameter space, is introduced:

$$\boldsymbol{\xi} \in \Delta_e \rightarrow \boldsymbol{y}(\boldsymbol{\xi}) = \sum_{m=1}^{N_e} N^m(\boldsymbol{\xi}) \boldsymbol{y^m} \in E_e \;\; (1 \leq e \leq N_E) \tag{A.2}$$

where the $\boldsymbol{y^m}$ are the N_e geometrical nodes and N^m are the N_e shape functions.

A.1.2 Discretization of the unknowns

N_I interpolation points are used to discretize the unknowns. The variables $\boldsymbol{u}$ and $\boldsymbol{t}$ are approximated on E_e by:

$$\tilde{\boldsymbol{u}}(\boldsymbol{y}) = \sum_{k=1}^{N_I(e)} M_u^k(\boldsymbol{\xi}) \boldsymbol{u}^k; \qquad \tilde{\boldsymbol{t}}(\boldsymbol{y}) = \sum_{k=1}^{N_I(e)} M_t^k(\boldsymbol{\xi}) \boldsymbol{t}^k \; \boldsymbol{\xi} \in \Delta_e \tag{A.3}$$

where $(\boldsymbol{u}^k, \boldsymbol{t}^k)$ $(1 \leq k \leq N_I(e))$ are the nodal values of the approximations $\tilde{\boldsymbol{u}}$, $\tilde{\boldsymbol{t}}$ of $(\boldsymbol{u}, \boldsymbol{t})$ on the element E_e and $M_\alpha^k(\xi)$ $(\alpha = u, t)$ are the interpolation functions.

A.1.3 Discretized form of the integral equation

In order to solve the integral equation (A.1), the *collocation method* is applied. N_c equations are generated from eq. (A.1) by enforcing eq. (A.1) at N_c collocation points $\boldsymbol{x}^c \in \partial\Omega$ $(1 \leq c \leq N_c)$:

$$c_{ik}(\boldsymbol{x}^c)\tilde{u}_i(\boldsymbol{x}^c) + \sum_{e=1}^{N_e} \left[(\text{P.V.}) \int_{E_e} \tilde{u}_i(\boldsymbol{y}) T_i^k(\boldsymbol{x}^c, \boldsymbol{y}, \omega) dS_y - \int_{E_e} \tilde{t}_i(\boldsymbol{y}) U_i^k(\boldsymbol{x}^c, \boldsymbol{y}, \omega) dS_y \right] = 0 \tag{A.4}$$

For more details about this classical procedure, the reader is referred to [31, 6]. The computation of the near contributions (2.18a,b) involves the numerical evaluation of CPV-singular, weakly-singular and non-singular element integrals. Details on the methods used in our implementation are given later in Section A.2.

A.1.4 Implementation choices

In this work, only 3-noded triangular boundary elements have been used (Fig. A.1). This choice is driven by the fact that the simplest interpolations are the most efficient in a FM-BEM context, as they allow to "streamline" the non-FMM part of the computations. An important technical issue in

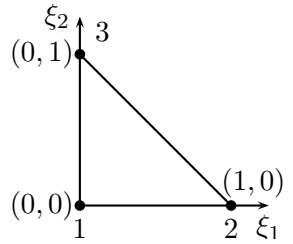

Figure A.1: *Triangular boundary elements (T3).*

BEMs is the normal orientation. The usual convention, adopted here, is that the normals are always exterior to the domain. The normal orientation is, in practice, determined by the ordering of the element nodes. For example, in Fig. A.1, the node orderings (1,2,3) and (2,1,3) yield normals with opposite orientations.

The relevant linear shape functions are:

$$N^1(\xi_1,\xi_2) = 1-\xi_1-\xi_2 = \xi_3; \quad N^2(\xi_1,\xi_2) = \xi_1; \quad N^3(\xi_1,\xi_2) = \xi_2. \tag{A.5}$$

Traction values are assumed to be constant over each element (noted $\boldsymbol{t}^e$), i.e. $M_t^1(\boldsymbol{\xi}) = 1$ in (A.3).

Finally, equation (A.4) becomes:

$$\begin{aligned}\sum_{e=1}^{N_e}\Big[c_{ik}(\boldsymbol{x}^c)\sum_{p=1}^{N_I(e)} u_i^{m(e,p)} N^p(\boldsymbol{\eta_e}) \quad &+\sum_{p=1}^{N_I(e)}\Big((\text{P.V.})\int_{E_e} N^p(\xi)T_i^k(\boldsymbol{x}^c,\boldsymbol{y},\omega)dS_y\Big)u_i^{m(e,p)} \\ &-\Big(\int_{E_e} U_i^k(\boldsymbol{x}^c,\boldsymbol{y},\omega)dS_y\Big)t_i^e\Big] = 0 \;\; (1\le c\le N_c)\end{aligned} \tag{A.6}$$

where $\boldsymbol{\eta_e}$ denotes the antecedent of $\boldsymbol{x}^c$ on element E_e under the mapping (A.2). As a result, to obtain the required number of equations, the collocation is performed:

- at the nodes if the nodal value of the displacement is unknown at that node ("nodal collocation");
- at the element center if the traction is unknown on this element ("element collocation");
- at the nodes *and* the center of interfacial elements (multi-domain problems).

A.1.5 Implementation of the near contributions: summary

In Chapters 2 and 3, the linear integral operator $(\mathcal{K}u)$ (resp. $(\mathcal{K}t)$) in equation (2.4) has been reformulated into $(\mathcal{K}u) = (\mathcal{K}u)^{\text{near}} + (\mathcal{K}u)^{\text{FMM}}$ (resp. $(\mathcal{K}t) = (\mathcal{K}t)^{\text{near}} + (\mathcal{K}t)^{\text{FMM}}$). The algorithm used to numerically compute the stored sparse matrix $[K]^{\text{near}}$, corresponding to near contributions, is summarized for convenience in Fig. A.2.

A.2 NUMERICAL PROCEDURE FOR THE EVALUATION OF THE VARIOUS INTEGRALS

A.2.1 General overview

It is now necessary to define numerical procedures to evaluate the element integrals encountered in eq. (A.6). In elastodynamics, two such integrals arise:

$$\int_{E_e} U_i^k(\boldsymbol{x}^c,\boldsymbol{y};\omega)dS_y \tag{A.7}$$

$$(\text{P.V.})\int_{E_e} N^p(\boldsymbol{\xi})T_i^k(\boldsymbol{x}^c,\boldsymbol{y};\omega)dS_y \tag{A.8}$$

where, in this work, $N^p(\xi)$ are linear shape functions (A.5). Two cases must be distinguished. The simpliest case is when $\boldsymbol{x}^c \notin E_e$: the two integrals (A.7) and (A.8) are non-singular. The standard method, recalled in Section A.2.2.1, is used. On the other hand, if $\boldsymbol{x}^c \in E_e$, a singularity occurs in (A.7) and (A.8) due to the definition of the fundamental solutions (1.17). The singularity

for all leaf cells $\mathcal{C}_x^{(\bar{\ell})}$,
  for all collocation points $\boldsymbol{x^c} \in \mathcal{C}_x^{(\bar{\ell})}$ (nodal or element collocation),
    for all elements E_e in $\mathcal{C}_x^{(\bar{\ell})}$
      compute the integrals (A.7) and (A.8) (Section A.2)
      multiply by known values to compute $\{f^{\text{near}}\}$ or store in matrix $[K]^{\text{near}}$
    end for
    compute free term $c_{ik}(\boldsymbol{x}^c)$,
    multiply by known values to compute $\{f^{\text{near}}\}$ or store in matrix $[K]^{\text{near}}$
    for all adjacent cells $\mathcal{C}_y^{(\bar{\ell})} \in \mathcal{A}(\mathcal{C}_x^{(\bar{\ell})})$
      for all elements E_e in $\mathcal{C}_y^{(\bar{\ell})}$
        compute the integrals (A.7) and (A.8) (Section A.2)
        multiply by known values to compute $\{f^{\text{near}}\}$ or store in matrix $[K]^{\text{near}}$
      end for
    end for

  write on the hard drive the fully-populated block matrix
    corresponding to cell $\mathcal{C}_x^{(\bar{\ell})}$ (Section 2.4.6)
end for

Figure A.2: *Elastodynamic multi-level FM-BEM: schematic description of the algorithm used to compute the near contributions with standard BEM.*

in (A.7) is of order $1/||\boldsymbol{x}^c - \boldsymbol{y}||$. The integral is weakly singular and a simple method, presented in Section A.2.2.2, is applied to eliminate this singularity. In contrast, integral (A.8) involve a strong singularity of order $1/||\boldsymbol{x}^c - \boldsymbol{y}||^2$, so that the previous approach does not apply. Since the singularities in the static and dynamic fundamental solutions are known [31] to be identical, the integral (A.9) below (where $T_i^k(\boldsymbol{x}^c, \boldsymbol{y})$ denotes the static Kelvin fundamental solution) is non-singular and its numerical integration is performed using the standard method (Section A.2.2.1).

$$\int_{E_e} N^p(\boldsymbol{\xi})[T_i^k(\boldsymbol{x}^c, \boldsymbol{y}; \omega) - T_i^k(\boldsymbol{x}^c, \boldsymbol{y})]dS_y \tag{A.9}$$

The remaining integral involving the static fundamental solution is strongly singular, but has a form simpler than (A.8) which allows its exact analytical evaluation (Section A.2.3).

A.2.2 Numerical evaluation of integrals

A.2.2.1 Non-singular integrals

If $\boldsymbol{x}^c \notin E_e$, or for the computation of (A.9), a standard numerical quadrature rule is adopted, of Gaussian type [62, 199]. Numerical evaluation of integrals over a triangle E_e are made according to:

$$\int_{E_e} g(x, y)dxdy \simeq \sum_{i=1}^{N} w_i g(x_i, y_i)$$

where x_i, y_i and w_i denote the abscissae and weights of the Gauss points. The values of (x_i, y_i, w_i) have been designed for the triangle in [138], for several values of N.

A.2.2.2 Weakly-singular integrals

Accurate evaluation of singular integrals is a crucial point to guarantee the accuracy of the result. Gaussian quadrature will lead to significant errors in such cases. The integral (A.7) presents a weak singularity when $\boldsymbol{x}^c \to \boldsymbol{y}$. A change of variables following a subdivision of E_e into triangular subregions (if required) enables to work around this problem. For a three-noded triangular boundary element, if the singularity is at a node, no subdivision is needed, while three subtriangles are used if the singularity is at the element center (Fig. A.3). Then, on every triangular subregion E_e: $\xi_1 \geq 0$, $\xi_2 \geq 0$, $1 - \xi_1 - \xi_2 \geq 0$, the change of variables $\xi_1 = 0.25(1+u)(1-v)$, $\xi_2 = 0.5(1+v)$ maps the triangle E_e onto the unit square $(u, v) \in [-1, 1] \times [-1, 1]$. As a result, the Jacobian of the transformation, of order $||\boldsymbol{x}^c - \boldsymbol{y}||$, exactly cancels the singularity, of order $1/||\boldsymbol{x}^c - \boldsymbol{y}||$. A classical Gaussian integration rule can thus be applied in $(u, v)-$space.

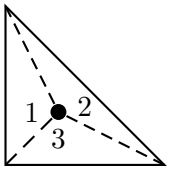

Figure A.3: *Numerical integration of weakly-singular integrals if singularity at the element center.*

A.2.2.3 Free term

Another integral to evaluate is the free term. In the usual case where the surface is smooth, the free term $c_{ik}(\boldsymbol{x}^c)$ is equal to $\frac{1}{2}\delta_{ik}$. The other cases are handled in this work using the method proposed in [145].

A.2.3 Analytical computation of the integral of the (static) Kelvin traction vector

We have seen that, to isolate the singularity in (A.8) into a simpler contribution, the (strongly-singular) Kelvin traction vector has been introduced. This section presents an analytical procedure to compute:

$$\text{(P.V.)} \int_E N^p(\boldsymbol{\xi}) T_i^k(\boldsymbol{x}, \boldsymbol{y}) dS_y \tag{A.10}$$

over a generic planar triangular element E, where $T_i^k(\boldsymbol{x}^c, \boldsymbol{y})$, the static Kelvin fundamental solution for the infinite body, is given by:

$$T_i^k(\boldsymbol{x}^c, \boldsymbol{y}) = \frac{-1}{8\pi(1-\nu)r^2}\Big\{\big[3r_{,i}r_{,k} + (1-2\nu)\delta_{ik}\big]r_{,n} + (1-2\nu)(n_k r_{,i} - n_i r_{,k})\Big\} \tag{A.11}$$

with $r = ||\boldsymbol{x}^c - \boldsymbol{y}||$. We note the presence of the strongly singular term $1/r^2$, due to which the method of Section A.2.2.2 is not applicable. There exist numerical methods to deal with such integrals [104, 203]. In this work, integral (A.10) is evaluated analytically, taking advantage of the fact that only three-noded planar triangular boundary elements (T3) are used. T3 elements

have constant unit normal and Jacobian, and are such that $r_{,n} = r_{,j}n_j = 0$, so the integral (A.11) becomes:

$$(P.V.)\int_E N^p(\boldsymbol{\xi})T_i^k(\boldsymbol{x}^c,\boldsymbol{y})dS_y = f\ (P.V.)\int_E \frac{1}{r^2}(n_k r_{,i} - n_i r_{,k})N^p(\boldsymbol{\xi})dS_y \tag{A.12}$$

where $f = \frac{-(1-2\nu)}{8\pi(1-\nu)}$. The integral (A.12) being evaluated as a Cauchy Principal Value, let $E_\varepsilon = E - c_\varepsilon$, where $c_\varepsilon(\boldsymbol{x}^c)$ is a neighbourhood of $\boldsymbol{x}^c$ ($\varepsilon > 0$, small; see Fig. A.4).

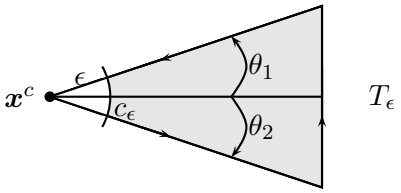

Figure A.4: *Analytical integration of Kelvin traction vector: configuration.*

Letting D_{ik} denote the tangential differential operator: $D_{ik}g = n_i g_{,k} - n_k g_{,i}$, (A.12) becomes:

$$\lim_{\varepsilon\to 0}\int_{E_\varepsilon} N^p(\boldsymbol{\xi})T_i^k(\boldsymbol{x}^c,\boldsymbol{y})dS_y = f\lim_{\varepsilon\to 0}\int_{E_\varepsilon}[D_{ik}\frac{1}{r}]N^p(\boldsymbol{\xi})dS_y \tag{A.13}$$

Denoting by τ the unit tangent to ∂E_ε and performing integrations by parts via a variant of the Stokes formula, (A.13) can be rewritten:

$$\lim_{\varepsilon\to 0}\int_{E_\varepsilon} N^p(\boldsymbol{\xi})T_i^k(\boldsymbol{x}^c,\boldsymbol{y})dS_y = f\Big[e_{ik\ell}\lim_{\varepsilon\to 0}\oint_{\partial E_\varepsilon}\tau_\ell(\boldsymbol{y})N^p(\boldsymbol{\xi})\frac{ds_y}{r} + \lim_{\varepsilon\to 0}\int_{E_\varepsilon} D_{ik}N^p(\boldsymbol{\xi})\frac{dS_y}{r}\Big] \tag{A.14}$$

Now, two cases have to be considered: (i) singularity at a node (nodal collocation), and (ii) singularity at the element center (element collocation). In case (i), linear interpolation implies that $D_{ik}N^p(\boldsymbol{\xi})$ is a constant so equation (A.14) is reduced to:

$$\lim_{\varepsilon\to 0}\int_{E_\varepsilon} T_i^k(\boldsymbol{x}^c,\boldsymbol{y})N^p(\boldsymbol{\xi})dS_y = f\Big[e_{ik\ell}\lim_{\varepsilon\to 0}\oint_{\partial E_\varepsilon}\tau_\ell(\boldsymbol{y})N^p(\boldsymbol{\xi})\frac{ds_y}{r} + D_{ik}N^p(\boldsymbol{\eta_e})\lim_{\varepsilon\to 0}\int_{E_\varepsilon}\frac{dS_y}{r}\Big] \tag{A.15}$$

Since $\partial E_\varepsilon = c_\varepsilon + (\partial E_\varepsilon - c_\varepsilon)$, the contour integral in (A.15) can be decomposed into two parts. The first part is the computation of:

$$\lim_{\varepsilon\to 0}\oint_{c_\varepsilon} N^p(\boldsymbol{\xi})\tau_\ell(\boldsymbol{y})\frac{ds_y}{r} = \lim_{\varepsilon\to 0}\int_{\theta_1}^{\theta_2} N^p(\boldsymbol{y})(-\boldsymbol{e_\theta})_\ell d\theta \tag{A.16}$$

when $\varepsilon \to 0$, $N^p(\boldsymbol{\xi}) = N^p(\boldsymbol{\eta_e}) + O(||\varepsilon||^\alpha)$, so (A.16) is equivalent to:

$$\lim_{\varepsilon\to 0}\oint_{c_\varepsilon} N^p(\boldsymbol{\xi})\tau_\ell(\boldsymbol{y})\frac{ds_y}{r} = N^p(\boldsymbol{\eta_e})\int_{\theta_1}^{\theta_2}(-\boldsymbol{e_\theta})_\ell d\theta = N^p(\boldsymbol{\eta_e})\Big[\boldsymbol{e}_r(\theta_1) - \boldsymbol{e}_r(\theta_2)\Big]_\ell \tag{A.17}$$

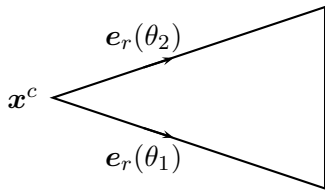

Figure A.5: *Analytical integration of Kelvin traction vector: definition of the $\boldsymbol{e}_r$ vectors.*

where $\boldsymbol{e}_r(\theta_1)$ and $\boldsymbol{e}_r(\theta_2)$ are defined in Fig. A.5.

Clearly, the sum of contributions (A.17) for all the triangles that share $\boldsymbol{x}^c$ node cancels out whenever $\boldsymbol{x}^c$ is *interior* to $\partial\Omega$. Conversely, the sum is not zero in general when $\partial\Omega$ is an open surface and lies on its edge (this typically may occur when an unbounded free surface is truncated, see Section 3.2). In the current state of implementation, such special situations are ignored, i.e. it is always considered that the sum of contributions cancels out, so that:

$$\sum_{E\in\mathcal{T}(\boldsymbol{x}^c)} \oint_{\partial E_\varepsilon} \tau_\ell(\boldsymbol{y}) N^p(\boldsymbol{\xi}) \frac{ds_y}{r} = \sum_{E\in\mathcal{T}(\boldsymbol{x}^c)} \oint_{(\partial E_\varepsilon - c_\varepsilon)} \tau_\ell(\boldsymbol{y}) N^p(\boldsymbol{\xi}) \frac{ds_y}{r} \tag{A.18}$$

where $\mathcal{T}(\boldsymbol{x}^c)$ is the set of triangles that share the node $\boldsymbol{x}^c$. For the contour integral over $\partial E_\varepsilon - c_\varepsilon$, contributions from edges emanating from $\boldsymbol{x}^c$ (i.e. shared by two adjacent triangles of $\mathcal{T}(\boldsymbol{x}^c)$) cancel out. Thus, only contributions for edges opposite to $\boldsymbol{x}^c$ (denoted C for the generic triangle E) need to be considered (see Fig. A.6).

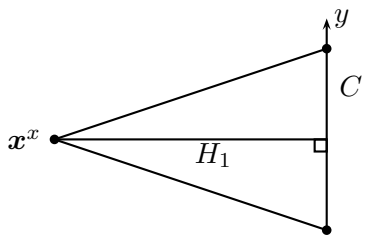

Figure A.6: *Analytical integration of Kelvin traction vector: definition of C.*

But N^p is affine and $\boldsymbol{\tau}$ is a constant vector $\boldsymbol{\tau}^C$ on C, so:

$$\oint_C \tau_\ell(\boldsymbol{y}) N^p(\boldsymbol{\xi}) \frac{ds_y}{r} = \tau_\ell^C \oint_C (\beta_p y + \gamma_p) \frac{dy}{\sqrt{y^2 + H_1^2}} \tag{A.19}$$

where the coefficients β_p and γ_p are defined by

$$\begin{aligned} \beta_1 &= 0, \quad \beta_2 = \frac{1}{|D_2| + |D_1|}, \quad \beta_3 = \frac{-1}{|D_2| + |D_1|}, \\ \gamma_1 &= 0, \quad \gamma_2 = \frac{|D_1|}{|D_2| + |D_1|}, \quad \gamma_3 = \frac{|D_2|}{|D_2| + |D_1|}, \end{aligned}$$

with the nodes and algebraic distances D_1, D_2 defined in Fig. A.7.

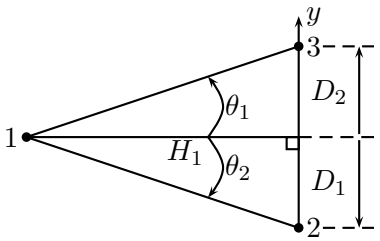

Figure A.7: *Analytical integration of Kelvin traction vector: various nodes for the definition of the interpolation functions and definition of H_1,D_1 and D_2.*

It is possible to calculate exactly integral (A.19) using the fact that:

$$\text{(a)} \int \frac{dx}{\sqrt{x^2+1}} = \ln(|x+\sqrt{x^2+1}|) \qquad \text{and} \qquad \text{(b)} \int \frac{xdx}{\sqrt{x^2+1}} = \sqrt{1+x^2}. \tag{A.20}$$

Using (A.20a,b), we obtain:

$$\begin{aligned} \oint_C \tau_\ell(\boldsymbol{y}) N^p(\boldsymbol{\xi}) \frac{ds_y}{r} &= \tau_\ell^C \gamma_p \Big[\ln \frac{|y+\sqrt{y^2+H_1^2}|}{|H_1|} \Big]_{D_1}^{D_2} + \tau_\ell^C \beta_p \Big[\sqrt{H_1^2+y^2} \Big]_{D_1}^{D_2} \\ &= \tau_\ell^C \gamma_p a_1 + \tau_\ell^C \beta_p a_2 \end{aligned}$$

where H_1,D_1 and D_2 are defined in Fig. A.7, $a_1 = \ln \dfrac{|D_2+\sqrt{D_2^2+H_1^2}|}{|D_1+\sqrt{D_1^2+H_1^2}|}$ and $a_2 = \sqrt{H_1^2+D_2^2} - \sqrt{H_1^2+D_1^2}$.

The second term to compute is $\lim\limits_{\varepsilon\to 0} \int_{E_\varepsilon} \dfrac{dS_y}{r}$. Using the fact that, when $\varepsilon \to 0$, $E_\varepsilon \to E$ and the polar coordinates:

$$\begin{aligned} \lim_{\varepsilon\to 0} \int_{E_\varepsilon} \frac{dS_y}{r} &= \int_{-\theta_1}^{\theta_2} d\theta \int_0^{H_1/\cos\theta} dr = H_1 \Big[\ln|\tan(\frac{\pi}{4}+\frac{x}{2})| \Big]_{\theta_1}^{\theta_2} \\ &= H_1 \Big[\ln|\tan(\frac{\pi}{4}+\frac{\theta_2}{2})| - \ln|\tan(\frac{\pi}{4}+\frac{\theta_1}{2})| \Big] \end{aligned} \tag{A.21}$$

But, it is known that $\tan\dfrac{\theta_i}{2} = \dfrac{1-\cos\theta_i}{\sin\theta_i}$ and so $\tan(\dfrac{\pi}{4}+\dfrac{\theta_i}{2}) = \dfrac{1+\sin\theta_i}{\cos\theta_i} = \dfrac{D_i+\sqrt{D_i^2+H_1^2}}{H_1}$.
So, (A.21) can be simplified to:

$$\lim_{\varepsilon\to 0} \int_{E_\varepsilon} \frac{dS_y}{r} = H_1 a_1$$

Finally, we obtain:

$$\begin{aligned} \int_{E_\varepsilon} T_i^k(\boldsymbol{x}^c,\boldsymbol{y}) N^p(\boldsymbol{\xi}) dS_y &= f\Big\{ s(i,k)\gamma_p a_1 + s(i,k)\beta_p a_2 + D_{ik} N^p(\boldsymbol{\eta_e}) H_1 a_1 \Big\} \\ \int_{E_\varepsilon} T_i^k(\boldsymbol{x}^c,\boldsymbol{y}) N^1(\boldsymbol{\xi}) dS_y &= f D_{ik} N^1(\boldsymbol{\eta_e}) H_1 a_1 \\ \int_{E_\varepsilon} T_i^k(\boldsymbol{x}^c,\boldsymbol{y}) N^2(\boldsymbol{\xi}) dS_y &= f\Big\{ \frac{s(i,k)}{|D_2|+|D_1|} \Big(|D_1| a_1 + a_2 \Big) + D_{ik} N^2(\boldsymbol{\eta_e}) H_1 a_1 \Big\} \\ \int_{E_\varepsilon} T_i^k(\boldsymbol{x}^c,\boldsymbol{y}) N^3(\boldsymbol{\xi}) dS_y &= f\Big\{ \frac{s(i,k)}{|D_2|+|D_1|} \Big(|D_2| a_1 - a_2 \Big) + D_{ik} N^3(\boldsymbol{\eta_e}) H_1 a_1 \Big\} \end{aligned}$$

where $s(i,k) = e_{ik\ell}\tau_\ell^C$.

Finally, a procedure for the computation of $D_{ik}N^p(\boldsymbol{\eta_e})$ is needed. Using the definition of D_{ik}, it is clear that:

$$\begin{aligned} D_{ik}N^p &= (\boldsymbol{n}\otimes\nabla N^p - \nabla N^p\otimes\boldsymbol{n})_{ik} \\ &= \frac{1}{H_p}(\boldsymbol{n}\otimes\boldsymbol{d}_p - \boldsymbol{d}_p\otimes\boldsymbol{n})_{ik} \end{aligned}$$

where the distances H_1, H_2, H_3 and unit vectors $\boldsymbol{d}_1$, $\boldsymbol{d}_2$, $\boldsymbol{d}_3$ are defined on Fig. A.8.

The remaining task is to express the unit vectors $\boldsymbol{d_1}$, $\boldsymbol{d_2}$ and $\boldsymbol{d_3}$ in the global system of coordinates. It is easy to see that:

$$\boldsymbol{d}_i = \frac{\boldsymbol{OM_i} - \boldsymbol{OM}}{||\boldsymbol{OM_i} - \boldsymbol{OM}||} \; 0 \leq i \leq 3$$

If the singularity lies at the center of the element, the triangle is subdivided into 3 sub-domains and the previously defined method is applied in each sub-domain.

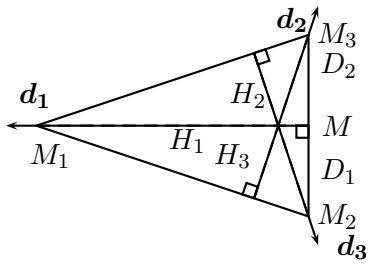

Figure A.8: *Analytical integration of Kelvin traction vector: definition of unit vectors and distances used in the computation of $D_{ik}N^p$.*

A.2.4 Schematic representation of the computation of the integrals.

The algorithm used to numerically computed the various integrals is summarized for convenience in Fig. A.9.

if **nodal collocation**
  if the collocation point is a node of the element on which the integral is performed,
    the integral is **singular**
  else
    the integral is **non-singular**
  end if
else **element collocation**
  if the element to which belongs the collocation point is the element
    on which the integral is performed, the integral is **singular**
  else
    the integral is **non-singular**
  end if
end if

if **non-singular integral**
  compute integrals in eq. (A.7) and eq. (A.8) using
    standard method defined in Section A.2.2.1
else **singular integral**
  if **nodal collocation**
    (a) compute the **non-singular integral** in eq. (A.9) using
      the **standard method** defined in Section A.2.2.1
    (b) compute the **singular integral** in eq. (A.7) using
      the method defined in Section A.2.2.2 (with 2 triangular **sub-elements**)
    (c) compute the **CPV integral** in eq. (A.10) using the **analytical method**
      defined in Section A.2.3
  else **element collocation**
    (a) compute the **non-singular integral** in eq. (A.9) using
      the **standard method** defined in Section A.2.2.1
    (b) compute the **singular integral** eq. (A.7) using
      the method defined in Section A.2.2.2 (with 3 triangular **sub-elements**)
    (c) compute the **CPV integral** in eq. (A.10) using the **analytical method**
      defined in Section A.2.3 (using 3 triangular **sub-elements**)
  end if
end if

Figure A.9: *Elastodynamic multi-level FM-BEM: schematic description of the algorithm used to compute the integrals in the near part.*

Appendix B

Analytical expressions of the free-field displacement vectors for incident plane P– and SV–waves

Contents

In the case of seismic problems, the value of the scattered free-field $\boldsymbol{u}^F$ needs to be prescribed on the domain boundary. In the case of the diffraction of an oblique incident plane wave, $\boldsymbol{u}^F$ has a known analytical expression. In this Appendix, such expressions are recalled for plane P–waves and plane SV–waves, which are involved in many of the numerical tests presented in this thesis.

B.1 REFLECTION OF PLANE WAVES BY HALF-SPACE

We consider an incoming plane wave propagating from infinity. In that case, the free-field includes the incident displacement vector and the resulting reflected plane P– and SV–wave at the free surface ($z = 0$). The wave system and coordinates are represented in Fig. B.1. For clarity, we introduce the new axis $\boldsymbol{e_{y'}}$, with $\boldsymbol{e_{y'}} = \cos\phi_0 \boldsymbol{e_x} + \sin\phi_0 \boldsymbol{e_y}$.

We know that the general formulation of a plane wave propagating with a phase velocity c is:

$$\boldsymbol{u} = A\boldsymbol{d}e^{ik(\boldsymbol{x}.\boldsymbol{p}-ct)} \tag{B.1}$$

where $\boldsymbol{d}$ and $\boldsymbol{p}$ are the unit vectors defining the directions of motion and propagation respectively, A is the wave amplitude (independent of $\boldsymbol{x}$ and t), k is the wavenumber and $\boldsymbol{x}$ is the position vector.

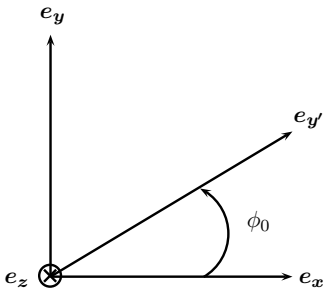

Figure B.1: *Definition of the new axis* $e_{y'}$.

B.2 PLANE P–WAVE

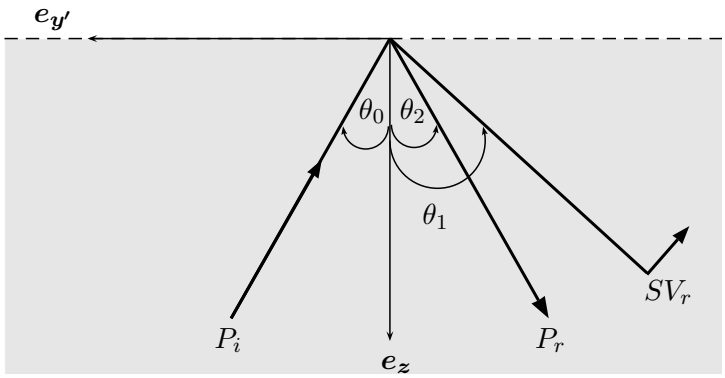

Figure B.2: *Diffraction of a plane P–wave by the free surface.*

First, we consider the case of an oblique incident plane P–wave. This incident plane P–wave (P_i) is reflected into a P–wave (P_r) and a SV–wave (SV_r) (Fig. B.2). Because of the phase-matching condition, we have $\theta_2 = \theta_0$ and $\sin\theta_1 = (c_S/c_P)\sin\theta_2$. The various unit vectors defining the directions of motion and propagation, are given by:

- for P_i: $\left\{ \begin{array}{ll} \boldsymbol{p}_I = \boldsymbol{d}_I & = -\sin\theta_0 \boldsymbol{e_{y'}} - \cos\theta_0 \boldsymbol{e_z} \\ & = -(\sin\theta_0\cos\phi_0 \boldsymbol{e_x} + \sin\theta_0 \sin\phi_0 \boldsymbol{e_y} + \cos\theta_0 \boldsymbol{e_z}) \end{array} \right.$

- for P_r: $\left\{ \begin{array}{ll} \boldsymbol{p}_P = \boldsymbol{d}_P & = -\sin\theta_0 \boldsymbol{e_{y'}} + \cos\theta_0 \boldsymbol{e_z} \\ & = -\sin\theta_0\cos\phi_0 \boldsymbol{e_x} - \sin\theta_0 \sin\phi_0 \boldsymbol{e_y} + \cos\theta_0 \boldsymbol{e_z} \end{array} \right.$

- for SV_r: $\left\{ \begin{array}{ll} \boldsymbol{p}_{SV} & = -\sin\theta_1 \boldsymbol{e_{y'}} + \cos\theta_0 \boldsymbol{e_z} \\ & = -\sin\theta_1\cos\phi_0 \boldsymbol{e_x} - \sin\theta_1 \sin\phi_0 \boldsymbol{e_y} + \cos\theta_0 \boldsymbol{e_z} \\ \boldsymbol{d}_{SV} & = -\cos\theta_1 \boldsymbol{e_{y'}} - \sin\theta_1 \boldsymbol{e_z} \\ & = -\cos\theta_1\cos\phi_0 \boldsymbol{e_x} - \cos\theta_1 \sin\phi_0 \boldsymbol{e_y} - \sin\theta_1 \boldsymbol{e_z} \end{array} \right.$

Using eq. (B.1), we obtain:

$$\boldsymbol{u}^F = A_0\Big[\boldsymbol{d}_{\rm I}\exp ik_{\rm P}(\boldsymbol{x}.\boldsymbol{p}_{\rm I} - c_{\rm P}t) + \gamma_{\rm P}\boldsymbol{d}_{\rm P}\exp ik_{\rm P}(\boldsymbol{x}.\boldsymbol{p}_{\rm P} - c_{\rm P}t) + \gamma_{\rm SV}\boldsymbol{d}_{\rm SV}\exp ik_{\rm S}(\boldsymbol{x}.\boldsymbol{p}_{\rm SV} - c_{\rm S}t)\Big]$$

where the amplitude ratios $\gamma_{\rm P} = A_{\rm P}/A_0$ and $\gamma_{\rm SV} = A_{\rm SV}/A_0$, deduced from the traction-free surface condition at $z = 0$, are found to be given by

$$\gamma_{\rm P} = \frac{\gamma^2\sin(2\theta_0)\sin(2\theta_1) - \cos^2(2\theta_1)}{\gamma^2\sin(2\theta_0)\sin(2\theta_1) + \cos^2(2\theta_1)}; \qquad \gamma_{\rm SV} = \frac{2\gamma\sin(2\theta_0)\sin(2\theta_1)}{\gamma^2\sin(2\theta_0)\sin(2\theta_1) + \cos^2(2\theta_1)}$$

where $\gamma^{-1} = \sqrt{\dfrac{2(1-\nu)}{1-2\nu}} = c_{\rm P}/c_{\rm S}$.

B.3 PLANE SV–WAVE

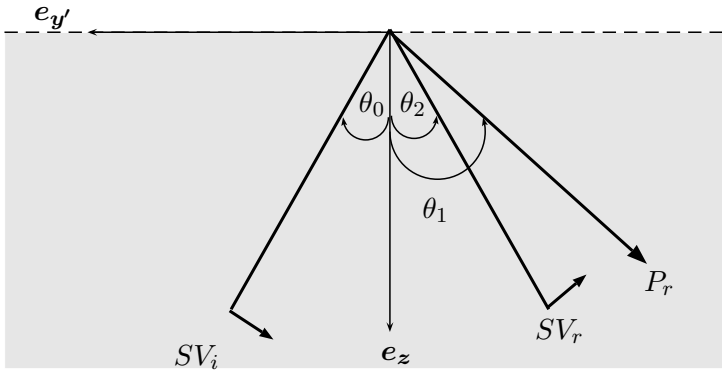

Figure B.3: *Diffraction of a plane SV–wave by the free surface.*

Then, we consider the case of an oblique incident plane SV–wave. This incident plane SV–wave (SV_i) is reflected into a SV–wave (SV_r) and a P–wave (P_r) (Fig. B.3). The various unit vectors defining the directions of motion and propagation, are given by:

- for SV_i:
$$\begin{cases} \boldsymbol{p}_{\rm I} &= -\sin\theta_0\boldsymbol{e}_{y'} - \cos\theta_0\boldsymbol{e}_z \\ &= -\sin\theta_0\cos\phi_0\boldsymbol{e}_x - \sin\theta_0\sin\phi_0\boldsymbol{e}_y - \cos\theta_0\boldsymbol{e}_z \\ \boldsymbol{d}_{\rm I} &= -\cos\theta_0\boldsymbol{e}_{y'} + \sin\theta_0\boldsymbol{e}_z \\ &= -\cos\theta_0\cos\phi_0\boldsymbol{e}_x - \cos\theta_0\sin\phi_0\boldsymbol{e}_y + \sin\theta_0\boldsymbol{e}_z \end{cases}$$

- for SV_r:
$$\begin{cases} \boldsymbol{p}_{\rm SV} &= -\sin\theta_0\boldsymbol{e}_{y'} + \cos\theta_0\boldsymbol{e}_z \\ &= -\sin\theta_0\cos\phi_0\boldsymbol{e}_x - \sin\theta_0\sin\phi_0\boldsymbol{e}_y + \cos\theta_0\boldsymbol{e}_z \\ \boldsymbol{d}_{\rm SV} &= -\cos\theta_0\boldsymbol{e}_{y'} - \sin\theta_0\boldsymbol{e}_z \\ &= -\cos\theta_0\cos\phi_0\boldsymbol{e}_x - \cos\theta_0\sin\phi_0\boldsymbol{e}_y - \sin\theta_0\boldsymbol{e}_z \end{cases}$$

- for P_r:
$$\begin{cases} \boldsymbol{p}_{\rm P} = \boldsymbol{d}_{\rm P} &= -\sin\theta_1\boldsymbol{e}_{y'} + \cos\theta_1\boldsymbol{e}_z \\ &= -\sin\theta_1\cos\phi_0\boldsymbol{e}_x - \sin\theta_1\sin\phi_0\boldsymbol{e}_y + \cos\theta_1\boldsymbol{e}_z \end{cases}$$

Using eq. (B.1), we obtain:

$$\boldsymbol{u}^F = A_0 \Big[\boldsymbol{d}_{\mathrm{I}} \exp ik_{\mathrm{S}}(\boldsymbol{x}.\boldsymbol{p}_{\mathrm{I}} - c_{\mathrm{S}}t) + \gamma_{\mathrm{SV}} \boldsymbol{d}_{\mathrm{SV}} \exp ik_{\mathrm{S}}(\boldsymbol{x}.\boldsymbol{p}_{\mathrm{SV}} - c_{\mathrm{S}}t) \\ + \gamma_{\mathrm{P}} \boldsymbol{d}_{\mathrm{P}} \exp ik_{\mathrm{P}}(\boldsymbol{x}.\boldsymbol{p}_{\mathrm{P}} - c_{\mathrm{P}}t) \Big]$$

where the amplitude ratios $\gamma_{\mathrm{SV}} = A_{\mathrm{SV}}/A_0$ and $\gamma_{\mathrm{P}} = A_{\mathrm{P}}/A_0$, deduced from the traction-free surface condition at $z = 0$, are found to be given by

$$\gamma_{\mathrm{SV}} = \frac{-\gamma^2 \sin(2\theta_0)\sin(2\theta_1) + \cos^2(2\theta_1)}{\gamma^2 \sin(2\theta_0)\sin(2\theta_1) + \cos^2(2\theta_1)}; \qquad \gamma_{\mathrm{P}} = \frac{\gamma \sin(4\theta_0)}{\gamma^2 \sin(2\theta_0)\sin(2\theta_1) + \cos^2(2\theta_1)}.$$

Appendix C

COFFEE user's guide

Contents

During this thesis, the multi-domain multi-level FM-BEM for frequency-domain elastodynamics has been implemented into a computer code named COFFEE. The code includes more than $30,000$ Fortran 90 instructions, split into about 90 source files. This Appendix aims at describing the capabilities offered by COFFEE and explaining how to prepare data and use the code.

C.1 GENERAL OVERVIEW OF THE CODE

Assumptions and basic concepts. This program solves 3-D problems of linear elastodynamics using the boundary element method, accelerated by the fast multipole method. The solution is performed in the frequency domain. Time-domain solutions may be recovered using Fourier synthesis (see for example Sections 2.6.4 or 3.6).

Orientation towards seismic wave problems. One of the main goals of this thesis is to develop a fast solver for seismic wave propagation. Therefore, some routines have been specially developed to deal with seismic wave propagation in canyons or alluvial basins. Moreover, because the BEM formulation (1.19), upon which this work is based, is valid only for homogeneous media, the BE-BE coupling strategy of Chapter 3 has been incorporated in COFFEE for the purpose of dealing with piecewise-homogeneous media. With such a formulation, problems with layers in an alluvial basin can be solved. This code is nevertheless not just a seismic wave propagation solver, but rather a general solver for linear elastodynamics. The type of problem to be solved is dictated by the prescribed excitation and boundary conditions. For example, for seismic problems, the incident free field is not included in the code but computed from analytical formulae (see Appendix B for some examples) in a pre-processing step, using e.g. MATLAB, and then prescribed on the domain boundary as an input data of the solver. As a result, the solver is fully generic.

Preliminaries for the installation. In addition to the GMRES (`zPackgmres.f`) and FGMRES (`zPackfgmres.f`) routines provided by the CERFACS [221, 220], some other libraries need to be installed to be able to compile COFFEE. The usual BLAS and LAPACK libraries [218] are needed as they are involved in the computation of e.g. the eigenvalues of a vector (quadrature over the unit sphere: Section 2.4.3) or small matrix-vector products (near part: Section 2.4.6). The other important library is the Math Kernel Library (MKL) [217] for its implementation of the Fast Fourier Transform, a key step in extrapolation (2.33) and inverse extrapolation (2.34) that allows to keep a $O(N \log N)$ complexity. While a lot of FFT libraries are available for discrete sample sizes that are a power of two (an assumption which is not acceptable in this work), the FFT provided in MKL is not constrained by this restriction, and hence suitable. The author is aware about the loss of portability implied by the use of those libraries, motivated by computing efficiency. A sensible alternative approach would consist in re-coding the small number of routines needed in those libraries directly in COFFEE. Such time-consuming recoding was not possible within the time available for this work.

COFFEE has been compiled on Intel-based (Linux and Mac) 32 and 64 bits architectures. The following set of compilation options of the Intel Fortran Compiler has been found to increase the performance of the code:

```
-O3 -fast -axW
```

C.2 INPUT AND OUTPUT FILES

In this section, the input and output files of the solver are described. Each file is divided into sections, with the character # conventionally indicating the end of a section.

C.2.1 Input files

First, the input files which define the problem are described. Three separate input files are required, respectively defining the numerical parameters of the solver, the problem geometry, and finally the problem definition.

Numerical parameters. Some algorithmic parameters can be set by the user; they are listed in the file `Parameter.txt` (see sample file in Fig. C.1). This file is composed of five sections:

- `DIRECTORY` section. The path of the directory where the temporary files (created by the program) are stored, is given. The input and output files are always read and written in the current directory but it is possible to define another directory where the large temporary files (for example the stored matrix of the near contributions) are stored (e.g. `'./'`).

- `INTEGRATION` section. This section is devoted to the definition of the number of Gauss points used for the various integrals. The four numbers correspond respectively to:
  - the number of Gauss points for the computation of the CPV integrals in the near contributions eq. (A.10) (recommended value: 8);
  - the number of Gauss points for the computation of the weakly-singular integrals in the near contributions (recommended value: 4);

- the number of Gauss points for the computation of the non-singular integrals in the near contributions for triangular boundary elements (possible values: 3, 7 or 13; recommended value: 3);
- the number of Gauss points for the computation of the integrals in the FMM computations for triangular boundary elements (possible values: 3, 7 or 13; recommended value: 3).

- `SOLVER` section. This section sets all the parameters needed by the iterative solver. First it is, in principle, possible to define another solver than GMRES, although only GMRES is currently available in the code. Then, the tolerance used to stop GMRES is defined in the variable `PRECISION` (recommended value: 10^{-3}). In the variable `PRECONDITION`, the type of preconditioner is defined: `NO`, `LEFT` or `RIGHT` (no left preconditioner is currently implemented). `ORTH` is the orthogonalization procedure used by the solver. The possible values are: modified Gram-Schmidt (`MODIF_G-S`, recommended value), iterative modified Gram-Schmidt (`ITER_MODIF_G-S`), classical Gram-Schmidt (`CLASS_G-S`) and iterative classical Gram-Schmidt (`ITER_CLASS_G-S`). Then, `MAX ITERATIONS` defines the maximum number of iterations allowed for GMRES (in the outer GMRES if FGMRES is used). A restarted version of GMRES can be used with restart occuring every `RESTART PARAMETER` iterations (of the outer GMRES if FGMRES is used, recommended value: 50). Finally, the method used for the post-processing, evaluation of field variables at interior or exterior points using the boundary integral representation (Section 2.4.8), is defined in `POST_PROC`, whose possible values are: `NO` (solution needed only on the boundary), `BEM` (post-processing performed using standard BEM) or `FMM` (post-processing performed using FM-accelerated BEM).

- `OCTREE` section. In this section, all the variables related to the FMM are given. First, parameter `LOW FREQ` flags low-frequency problems, for which a little trick is used: the number of terms in the transfer function (2.14a,b) is increased to the number of terms in the transfer functions (2.13a,b). This option was developed to make some validations with previously published results at low frequency. We suggest to always put the key word `LOW FREQ` to `NO` and to avoid using COFFEE in the low-frequency regime. Then, the value of the constant C_ϵ, needed in the truncation of the transfer function, eq. (2.30), is defined in `CONS_C` (recommended value: 7.5). Next, the leaf cell size, which determines the number of levels in the octree, is set in `STOP_SIZE_PARAM` (recommended value: 0.30).

  The next two variables deal with the out-of-core part of the code (Section 2.4.7). They are assigned according to the RAM available on the computer. `MAX_GROUP` prescribes the maximum number of groups allowed in the out-of-core version of the program. The variable `MAX_MEM` defines the maximum size available on the computer and is defined on each computer by doing some numerical experiments.

- `PROBLEM` section. The first variable in this section is a special flag for problems of seismic wave propagation in an alluvial basin. When `BASIN PROBLEM` is equal to `FMM` or `BEM`, a routine which computes an integral specific to this type of problem (Section 3.4.5) is called. Three key words are possible for this variable: `NO` (no need to use the total field basin formulation), `BEM` (computation of this integral using standard BEM) or `FMM` (computation of this integral using FM-BEM). The last variable `VERBOSE` is a flag for helping debugging the program, with `VERBOSE=TRUE` triggering runtime comments displayed on the screen.

```
*DIRECTORY
  TEMP_PATH='./'
#
*INTEGRATION
  NBGAUSS=8,4,3,3
#
*SOLVER
  SOLVER TYPE=GMRES
  PRECISION=0.001000
  PRECONDITION=NO
  ORTH=MODIF_G-S
  MAX ITERATIONS=1000
  RESTART PARAMETER=50
  POST_PROC=FMM
#
*OCTREE
  LOW FREQ=NO
  CONS_C=7.500000
  STOP_SIZE_PARAM=0.30000
  MAX_GROUP=100
  MAX_MEM=2000000
#
*PROBLEM
  BASIN PROBLEM=NO
  VERBOSE=FALSE
#
```

Figure C.1: *Example of the input file:* `Parameter.txt`.

Geometry definition. The geometry of the problem is prescribed in the file `problem.GEO` (extensions in all input file names must be set using uppercase letters), see the sample file presented in Fig. C.3. The structure of this file is inspired by the "`.mesh`" format of the scientific visualization software MEDIT [222]. Three sections are defined in this file:

- `Zones` section. The number of sub-domains for the problem is set.
- `Vertices` section. The total number of nodes in the problem is followed by a list of all nodal coordinates (one line per node). For each node, the number of entries is $3+$ number of sub-domains: the three node coordinates, then the references of the node (i.e. sub-domains to which the node belongs), are listed. When a node belongs to less than the total number of sub-domains, the remaining references are set to 0.
- `Triangles` section. This section is devoted to the definition of the elements. The number of triangles in each sub-domain are listed in a single line. The next line defines the element type with the only currently available value being 4 (meaning three-noded triangular boundary elements). Then, the key word `Zone`, following by a sub-domain number, is used to specify that the elements given next define this sub-domain. For example, if we consider the geometry represented in Fig. C.2, after `Zone 1`, all the elements of $\partial\Omega_1 = \Gamma_1 \cup \Gamma_{12}$ are defined and, after `Zone 2`, all the elements of $\partial\Omega_2 = \Gamma_2 \cup \Gamma_{21}$ are defined. Elements are always simply defined by the list of their nodes (with implicit sequential element numbering assumed). The reader's attention is drawn to the convention used for the definition of the elements in the case of multi-domain problems. To ensure that normals are always exterior to a given sub-domain,

the interface elements (between Ω_1 and Ω_2 for example) are listed for both sub-domains (Γ_{12} in Ω_1 and Γ_{21} in Ω_2) to which they belong using opposite node orderings (Section 3.4.4). The normal orientation is then determined by the node ordering, via the evaluation of a cross product.

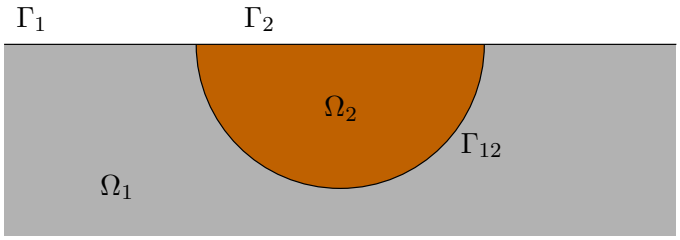

Figure C.2: *Illustrative geometry to explain the input file:* `problem.GEO`.

```
Zones
2
#
Vertices
324
0.850651 0.525731 -0.000000 1 0
-0.850650 0.525732 -0.000000 1 0
-0.850650 -0.525732 -0.000000 1 0
...
1.701300 1.051460 -0.000000 1 2
-1.701300 1.051460 -0.000000 1 2
-1.701300 -1.051460 -0.000000 1 2
#
Triangles
640 320
4
Zone
1
43 45 5
46 43 5
48 50 6
50 52 6
...
Zone
2
205 207 167
208 205 167
210 212 168
212 214 168
...
#
```

Figure C.3: *Example of the input file:* `problem.GEO`.

Problem definition. Once the geometry is defined, it is necessary to assign the mechanical parameters, boundary conditions and unknown variables. This is done in the file `problem.DAT` (see the sample file presented in Fig. C.4). Distinct files `.GEO` and `.DAT` are used because the same geometry can correspond to various problem definitions (e.g. scattering of a plane SV–wave or of a plane P–wave). Moreover, the generation of the `.GEO` file can be CPU-intensive for large meshes, making its re-usability advantageous. Eight sections are defined in the `.DAT` file:

- `Problem` section. The problem circular frequency ω is assigned.
- `Material properties` section. The mechanical parameters, for each sub-domain, are defined. The three entries of the i-th line correspond respectively to $\mu^{(i)}$ (shear modulus), $\nu^{(i)}$ (Poisson's ratio) and $\rho^{(i)}$ (mass density).
- `DISP_UNK` (resp. `TRAC_UNK`) section. The displacement (resp. traction) unknowns are listed (node (resp. element) number j and direction i):

```
DIR
i
        j
```

  This section allows maximum flexibility in setting boundary conditions, and in particular permits using the code in situations other than the typical seismological computations featuring given incident fields. To generate this data, the user may need to develop separate pre- and post-processing routines as explained in the following.

- `DISP_B` and `TRAC_B` sections. The same convention as in the `DISP_UNK` and `TRAC_UNK` sections is used to specify the nodes (resp. elements) at which the displacement (resp. traction) is (partially or completely) prescribed. The value of this prescribed displacement (resp. traction) is also set:

```
DIR
i           val
        j
```

  where val is the complex-valued prescribed displacement (resp. traction) and has to be written: ($\mathcal{R}$e(val), $\mathcal{I}$m(val)).

- `NODE_RHS` and `ELEM_RHS` sections. It is also possible to directly add some values to the right hand side (`NODE_RHS` for values at nodal collocation points and `ELEM_RHS` for values at element collocation points). This is useful for entering free-field values appearing in the right-hand side of scattering problems formulated in terms of total field (Section 3.2.2). The convention is the same that for the `DISP_B` and `TRAC_B` sections.

```
Problem
6.835000e-01
#
Material properties
4.000000e+00           2.500000e-01     3.000000e+00
1.000000e+00           3.333333e-01     2.000000e+00
#
DISP_UNK
DIR
1
        1
DIR
1
        2
DIR
1
        3
...
#
TRAC_UNK
ZONE
1
DIR
2
        321
DIR
2
        322
DIR
2
        323
...
ZONE
2
DIR
3
        1
DIR
3
        2
DIR
3
        3
...
#
DISP_B
#
TRAC_B
ZONE
1
DIR
1               (0.416922,0.000000)
        1
DIR
1               (0.416922,0.000000)
        2
DIR
1               (0.416922,0.000000)
        3
...
#
NODE_RHS
#
ELEM_RHS
#
```

Figure C.4: *Example of the input file:* `problem.DAT`.

Optional files. In the special case of the propagation of an elastic wave in a basin, the contribution of the free-surface to the right hand side is computed by means of a particular integral over the truncated planar free surface (Section 3.4.5, eq. (3.21)). The mesh of the free-surface is prescribed in the file `problem.GEO2`. The structure of this file is the same as `problem.GEO`. The only difference is that the number in the `Zones` section now defines the sub-domain for which this integral is computed. A `problem.DAT2` file is also required in this case; it only contains the `DISP_B` section of the file `problem.DAT` since this integral involves prescribed displacements only (Section 3.2.2).

If a post-processing step is needed, the number of observation points, sub-domains identifier, and point coordinates for which this integral representation is to be computed are defined in the file `problem.POSTGEO`, see example in Fig. C.5.

```
Vertices
100
Zone
1
0.000000 0.000000 1.100000
0.000000 0.000000 1.200000
0.000000 0.000000 1.300000
...
#
```

Figure C.5: *Example of the input file:* `problem.POSTGEO`.

C.2.2 Output files

Upon completion of the execution, COFFEE generates several files with the results and information about the computational process.

Results of the computation. Once the computation is performed, two output files are always created. The first one, `problem.DISP_NODES.txt`, contains, for each node on the domain boundary, the three components of the displacement (real and imaginary parts) given following the convention:

$$\texttt{node\_number}\ \mathcal{R}\mathrm{e}(u_x)\ \mathcal{R}\mathrm{e}(u_y)\ \mathcal{R}\mathrm{e}(u_z)\ \mathcal{I}\mathrm{m}(u_x)\ \mathcal{I}\mathrm{m}(u_y)\ \mathcal{I}\mathrm{m}(u_z)$$

The second file, `problem.TRAC_ELEM.txt`, gives the element traction values following the convention:

$$\texttt{element\_number}\ \mathcal{R}\mathrm{e}(t_x)\ \mathcal{R}\mathrm{e}(t_y)\ \mathcal{R}\mathrm{e}(t_z)\ \mathcal{I}\mathrm{m}(t_x)\ \mathcal{I}\mathrm{m}(t_y)\ \mathcal{I}\mathrm{m}(t_z)$$

Information about the computation. In addition to those two result files, two other files containing information about the computation are created.

- `ERROR.err` which contains some description and localization of errors encountered during the computation, if any, that possibly caused the program to stop prematurely.
- `STATUS.log` which contains details on the computational steps (see the sample file of Fig. C.6). First, the names of the problem file and of the directory where the temporary files are stored are recalled. Then, the number of octree levels in each sub-domain and the number of groups

for the out-of-core version are written. The CPU time spent in each part of the program is also recorded in this file. The remainder of the file is devoted to the convergence history of GMRES.

Optional files. If post-processing (computation of the boundary integral representation) is required, a new file is created: `problem.INT_REG.txt`. In this file, the three components of the displacement at interior (or exterior) points are saved. The convention is the same as for the file `problem.DISP_NODES.txt`.

C.3 HOW TO PERFORM A COMPUTATION WITH COFFEE

After this description of the input and output files, we give some information on how to run a seismology-oriented example. The complete resolution of an elastodynamic problem, using COFFEE, is usually decomposed into three steps:

1. pre-processing: domain geometry and surface mesh generation, definition of input files (Section C.2.1);
2. solution of the problem using COFFEE, creation of output files (Section C.2.2);
3. post-processing: creation of graphics, synthesis in the time domain, ...

In the following, a generic example of the method adopted in these three steps is given, and all softwares used for creating data and studying results are listed and credited.

Pre-processing. For all the geometries of canyons or multi-layered basins used in Chapters 2, 3, 4 and 5 of this thesis, a shell script has been written to generate the geometry and the mesh. All meshes have been created with the help of Adrien Loseille from the GAMMA team, INRIA Rocquencourt (www-c.inria.fr/gamma/), and using softwares developed by this team. We now illustrate with the case of a two-layer ellipsoidal basin the mesh generation method used. First, three regions are defined in the plane free-surface (Fig. C.7a). The boundaries of this plane geometry (namely ellipses) are generated using MATLAB and this simple geometry is then meshed using BAMG [224] (Fig. C.7b).

Then, with MATLAB, the nodes of the 2-D mesh (x, y) of Ω_2 and Ω_3 (Fig. C.7c) are transformed into nodes (x, y, z) of the 3-D mesh using the parametrization

$$\begin{aligned}
&\text{for all vertices in } \Omega_1 \quad && z = 0 \text{ (free surface)} \\
&\text{for all vertices in } \Omega_2 \quad && z = -c\sqrt{1 - x^2/a^2 - y^2/b^2} \text{ (interface } \Gamma_{12} \text{ with the infinite medium)} \\
&\text{for all vertices in } \Omega_3 \quad && z = z_{layer} \text{ (interface } \Gamma_{23} \text{ between two layers)} \\
& && z = -c\sqrt{1 - x^2/a^2 - y^2/b^2} \text{ (interface } \Gamma_{13} \text{with the infinite medium)}
\end{aligned} \tag{C.1}$$

where (a, b, c) define the ellipsoid semi-axes (Fig. C.7d). Finally, the various parts of the mesh (interface between the two layers, Fig. C.7e; interface with the infinite medium, Fig. C.7d, and free surface, Fig. C.7f) are geometrically merged (Fig. C.7g) using SPIDER (code provided by Adrien Loseille).

```
 bassin05_Ut          /grosdisque/chaillat/fichiers_tmp/
 ============================================================================
 BEGIN ANALYSIS                        time= 0.0
 READING INPUT FILE                    time= 0.0
 INPUT FILE  READ                      time= 0.3   step= 0.3
 ----------------------------------------------------------------------------
 GENERATING STRUCTURE FOR FMM (zone:1) time= 0.4
 GENERATING STRUCTURE FOR FMM (zone:2) time= 0.4
 NB LEVELS: 4  ; NB LEVELS: 4
 NB GOUPF,NB GROUPG: 0           0
 ...
 STRUCTURE GENERATED                   time= 3.3   step= 2.9
 ----------------------------------------------------------------------------
 EVALUATION FAR CONTRIBUTIONS TO RHS   time= 3.3
 RHS CONTRIBUTIONS EVALUATED           time= 6.5   step= 3.1
 ----------------------------------------------------------------------------
 ...
 ----------------------------------------------------------------------------
 EVALUATION NEAR CONTRIBUTIONS         time= 209.4
 NEAR CONTRIBUTIONS EVALUATED          time= 277.4 step= 68.1
 ----------------------------------------------------------------------------
 ...
 ----------------------------------------------------------------------------
  WARNING GMRES :
       For M= 17502  optimal value for LWORK = 612815029
                  CONVERGENCE HISTORY FOR GMRES
Errors are displayed in unit:   22
Warnings are displayed in unit: 21
Matrix size:       17502; Local matrix size: 17502
Restart:           17502
No preconditioning; Modified Gram-Schmidt
Default initial guess x_0 = 0; True residual computed at restart
Maximum number of iterations: 20000; Tolerance for convergence: 0.10E-02
Backward error on the unpreconditioned system Ax = b:
    the residual is normalised by ||b||
Backward error on the preconditioned system (P1)A(P2)y = (P1)b:
     the preconditioned residual is normalised by ||(P1)b||
Optimal size for the workspace:*******

Convergence history: b.e. on the preconditioned system
 Iteration   Arnoldi b.e.    True b.e.
 EVALUATION FAR CONTRIBUTIONS ZONE 1  time= 279.5
   -WRITTING           step= 0.0
   -INITIALIZATIONS    step= 4.6
   -TRANSFERS          step= 0.0
   -INTEGRATIONS       step= 2.8
   -UPWARD             step= 0.0
   -DOWNWARD           step= 0.1
MATRIX-VECTOR PRODUCT EVALUATED       time= 287.0 step= 7.5
----------------------------------------------------------------------------
 EVALUATION FAR CONTRIBUTIONS  ZONE 2 time= 287.0
   -WRITTING           step= 0.0
   -INITIALIZATIONS    step= 0.1
   -TRANSFERS          step= 0.0
   -INTEGRATIONS       step= 0.0
   -UPWARD             step= 0.0
   -DOWNWARD           step= 0.1
MATRIX-VECTOR PRODUCT EVALUATED       time= 287.4 step= 0.3
----------------------------------------------------------------------------
    1           0.4228E+00         --
...
----------------------------------------------------------------------------
   39           0.8919E-03       0.8919E-03
Convergence achieved
B.E. on the preconditioned system:   0.89E-03
B.E. on the unpreconditioned system: 0.89E-03
info(1)= 0;  Number of iterations (info(2)): 39 ; GMRES converged in 39 iterations
Backward error - preconditioned system:   8.9188620E-04
Backward error - unpreconditioned system: 8.9188620E-04
----------------------------------------------------------------------------
WRITE RESULTS                         time= 597.0
END WRITE RESULTS                     time= 597.1 step= 0.1
----------------------------------------------------------------------------
```

Figure C.6: *Example of the output file `STATUS.log`.*

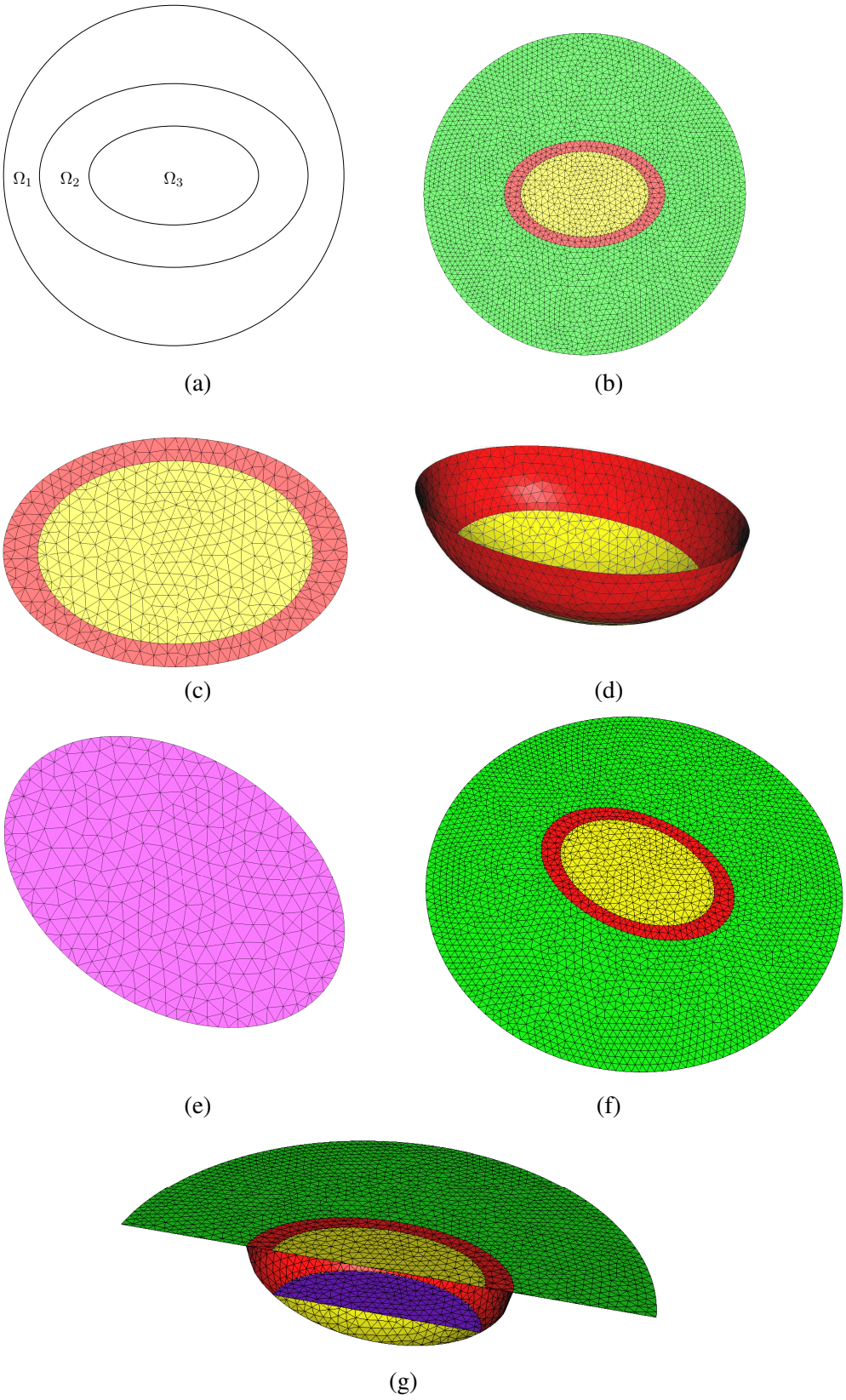

Figure C.7: *Two-layer ellipsoidal basin: mesh generation.*

This mesh is then optimized to the domain geometry and problem frequency using YAMS [223]. Because COFFEE is an elastodynamic solver in the frequency domain, the mesh size is determined by the frequency of the computation. Usually, for BEMs, about 10 nodes per λ_s are used. Once the `problem.mesh` file is generated, two MATLAB functions create the `problem.GEO` and `problem.DAT` files.

Run COFFEE. One must first check whether all the required files are in the directory chosen for the computation: `problem.GEO`, `problem.DAT` and `Parameter.txt` (in all cases), `problem.GEO2` and `problem.DAT2` (for seismic wave propagation in a basin), and `problem.POSTPROC` (if the computation of integral representations is required).

Then, one simply types COFFEE `<Enter>` in the command line of a terminal, being in the current directory, followed by problem name (without extension) upon prompting by COFFEE.

Post-processing. COFFEE only creates text files (Section C.2.2). A MATLAB function has been created to generate files in the "`.bb`" format allowing visualization of the 3-D results with MEDIT [222]. To generate time-domain results, a script has been created to perform the synthesis of all the frequency-domain results. A MATLAB function has been developed to perform the Fourier synthesis (see Sections 2.6.4 and 3.6). As explained in Section 3.6, the sample frequencies are treated for computational efficiency reasons using a hierarchical sequence of meshes $\mathcal{M}_0, \ldots, \mathcal{M}_n$ (with $\mathcal{M}_n$ the finest mesh). The meshes have been generated using YAMS, starting from the coarsest mesh $\mathcal{M}_0$ and then splitting each triangle into four sub-triangles. Then, an interpolation has been performed from coarse meshes $(\mathcal{M}_0, \ldots, \mathcal{M}_{n-1})$ to the finest mesh $(\mathcal{M}_n)$. Since we know that new vertices are created at each edge mid-point (from mesh $\mathcal{M}_i$ to mesh $\mathcal{M}_{i+1}$), and because the interpolation is linear, it is easy to do this interpolation. The difficulty comes from the need to have all the interpolated solutions defined on the same mesh, with displacement nodal values listed in the same order for all frequencies, to apply the Fourier transform. It is not easy to sort the vertex coordinates since they are real valued. The solution adopted here exploits the fact that when a new vertex is created, it always has at most 2 neighbour points (connected by an edge) in the parent mesh $\mathcal{M}_i$ (Fig. C.8). Moreover, YAMS sorts the vertices in the following way when the embedded mesh $\mathcal{M}_{i+1}$ is created. First, all the vertices of $\mathcal{M}_i$ are copied in the same order and then all the new vertices are appended. As a result, noting N_i the number of nodes in $\mathcal{M}_i$, it is easy to see that the two nodes that define the edge to which a new node belongs are the two only neighbour nodes with a number at most equal to N_i. This observation makes it easy to order all the results on meshes $(\mathcal{M}_0, \ldots, \mathcal{M}_{n-1})$ in the same way as $\mathcal{M}_n$. Again, a stand-alone MATLAB file performs this interpolation procedure. The algorithm used to determine the neighbour points can be found in [85].

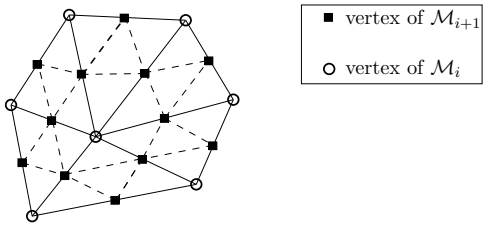

Figure C.8: *A vertex of $\mathcal{M}_i$ has at most two neighbour vertices on $\mathcal{M}_{i+1}$.*

Appendix D

Special functions

Contents

In this work, some special functions have been used. We recall in this Appendix some properties of these functions. The reader can find more details in [1].

D.1 SPHERICAL HANKEL FUNCTION OF THE FIRST KIND

The spherical Hankel functions of the first kind are used in the definition of the transfer function, eq. (2.9). The Hankel functions of the first kind are written:

$$H_\nu^{(1)}(x) = J_\nu(x) + iY_\nu(x)$$

where J_ν (resp. Y_ν) are the standard Bessel functions of the first (resp. second) kind and are real-valued functions when their argument x is real, as is the case in this thesis. The Bessel functions are the solutions of the Bessel equation:

$$x^2\frac{d^2f_\nu}{dx^2} + z\frac{df_\nu}{dx} + (x^2-\nu^2)f_\nu = 0 \quad (f_\nu = J_\nu, Y_\nu, H_\nu)$$

The spherical Bessel functions are related to the standard Bessel functions by the following definitions:

$$j_n(x) = \sqrt{\frac{\pi}{2x}}J_{n+1/2}(x), \quad y_n(x) = \sqrt{\frac{\pi}{2x}}Y_{n+1/2}(x), \quad h_n^{(1)}(x) = \sqrt{\frac{\pi}{2x}}H_{n+1/2}^{(1)}(x)$$

where the index n takes integer values. The first values of the spherical Bessel functions are:

$$\begin{aligned}
j_0(x) &= \frac{\sin(x)}{x}, & y_0(x) &= -\frac{\cos(x)}{x},\\
j_1(x) &= \frac{\sin(x)}{x^2} - \frac{\cos(x)}{x}, & y_1(x) &= -\frac{\cos(x)}{x^2} - \frac{\sin(x)}{x},\\
j_2(x) &= (\frac{3}{x^3} - \frac{1}{x})\sin(x) - \frac{3\cos x}{x^2}, & y_2(x) &= -(\frac{3}{x^3} - \frac{1}{x})\cos(x) - \frac{3\sin x}{x^2}.
\end{aligned}$$

As a result, the first values of the spherical Hankel functions are:

$$h_0^{(1)}(x) = \frac{e^{ix}}{ix}, \quad h_1^{(1)}(x) = -\frac{e^{ix}}{ix}(1+\frac{i}{x}), \quad h_2^{(1)}(x) = \frac{ie^{ix}}{x}(1+\frac{3i}{x}-\frac{3}{x^2}).$$

The spherical Bessel functions satisfy the following reccurence formula:

$$z_{n+1}(x) = \frac{2n+1}{x} z_n(x) - z_{n-1}(x) \quad (z_n = j_n, y_n, h_n) \tag{D.1}$$

For small values of x ($x \ll 1, \ell$), the spherical Bessel functions follow the asymptotic forms:

$$j_\ell(x) = \frac{x^\ell}{(2\ell+1)(2\ell-1)\dots 3.1}(1-\frac{x^2}{2(2\ell+3)}) + o(x^{\ell+4}),$$
$$y_\ell(x) = -\frac{(2\ell-1)(2\ell-3)\dots 3.1}{x^{\ell+1}}(1-\frac{x^2}{2(1-2\ell)}) + o(\frac{1}{x^{\ell-3}}).$$

For large values of x ($x \gg \ell$), their asymptotic behavior is:

$$j_\ell(x) = \frac{1}{x}\sin(x-\frac{\ell\pi}{2}) + o(\frac{1}{x^2}), \quad y_\ell(x) = -\frac{1}{x}\cos(x-\frac{\ell\pi}{2}) + o(\frac{1}{x^2}),$$
$$h_\ell^{(1)}(x) = (-i)^{\ell+1}\frac{e^{ix}}{x} + o(\frac{1}{x^2}).$$

For the numerical computation of y_n, the recursion formula (D.1), with starting values y_0 and y_1 has been implemented. However, forward recursion (D.1) is numerically unstable when applied to j_n. For example, for $x = 0.5$, the relative error between j_ℓ computed using either the recurrence formula (D.1) or the Matlab function `besselj` is seen in Table D.1 to rapidly increase with ℓ.

The solution implemented in the present code is to use an inverse recursion (Algorithm D.1), where n is the largest order of the spherical Bessel function whose computation is required. Using this recursion, the relative error is now very low (Table D.2).

Table D.1: *Numerical error introduced for the computations of j_ℓ, using the recursion formula (D.1).*

ℓ	3	4	5	6	7	8	9	10
error	$3\,10^{-7}$	$8\,10^{-8}$	$3\,10^{-7}$	$2\,10^{-4}$	$2\,10^{-3}$	10^{-1}	10^{2}	$2\,10^{5}$

Table D.2: *Numerical error introduced for the computations of j_ℓ, using the inverse recursion with larger order $n = 10$.*

ℓ	3	4	5	6	7	8	9	10
error	$4\,10^{-16}$	$2\,10^{-15}$	10^{-15}	10^{-16}	10^{-15}	0	$5\,10^{-14}$	$8\,10^{-11}$

D.2 LEGENDRE POLYNOMIALS

The following differential equation, with $\ell \in \mathbb{N}$:

$$\frac{d}{dx}\big[(1-x^2)\frac{d}{dx}P_\ell\big] + \ell(\ell+1)P_\ell = 0,$$

has for solution, an order ℓ polynomial, called Legendre polynomial. The first few Legendre polynomials are:

$$P_0(x) = 1, \quad P_1(x) = x, \quad P_2(x) = \frac{1}{2}(3x^2-1),$$

$j0 = 0$
$j1 = 1$
for $k = int(n + 2x) : -1 : 0$ **do**
  $jk = (2k + 3)\, j1/x - j0$
  if $k \leq n$ **then**
    $j_{val}(k) = jk$
  end if
  $j0 = j1$
  $j1 = jk$
end for
$j0 = \sin x/x$
$a = j0/j_{val}(0)$
$j_{val}(0 : n) = a\, j_{val}(0 : n)$

Algorithm D.1: *Inverse recursion used for the computation of j_ℓ.*

$$P_3(x) = \frac{1}{5}(5x^3 - 3x), \qquad P_4(x) = \frac{1}{8}(35x^4 - 30x^2 + 3).$$

The Rodrigues' formula gives the explicit expression of polynomials P_ℓ as:

$$P_\ell(x) = \frac{1}{2^\ell \ell!}\frac{d^\ell}{dx^\ell}[(x^2 - 1)^\ell].$$

The Legendre polynomials satisfy various recursion relations (the first one being used in Section 2.4.3):

$$\begin{aligned}(\ell + 1)P_{\ell+1} - (2\ell - 1)xP_\ell + \ell P_{\ell-1} &= 0,\\ P'_{\ell+1} - xP'_\ell - (\ell + 1)P_\ell &= 0,\\ (x^2 - 1)P'_\ell - \ell x P_\ell + \ell P_{\ell-1} &= 0,\end{aligned}$$

and also satisfy the identity:

$$P_\ell(-x) = (-1)^\ell P_\ell(x).$$

In [58], the following formula is used to define the optimal quadrature over the unit sphere (Section 2.4.3):

$$P_\ell(\boldsymbol{x}.\boldsymbol{y}) = \frac{4\pi}{2\ell + 1}\sum_{m=-\ell}^{\ell} \bar{Y}_{\ell,m}(\boldsymbol{x})Y_{\ell,m}(\boldsymbol{y}) \quad (||\boldsymbol{x}|| = ||\boldsymbol{y}|| = 1).$$

An important property of the Legendre polynomials, which is used in this work (Section 2.4.4), is that they are orthogonal with respect to the L^2 scalar product on $[-1, 1]$:

$$\int_{-1}^{1} P_m(x)P_n(x)dx = \frac{2}{2n + 1}\delta_{mn}.$$

For the definition of the direct and inverse extrapolation steps (Section 2.4.4), the associated Legendre polynomials were used. They can be expressed in terms of derivatives of the Legendre polynomials, for $\ell \geq m \geq 0$ and $\ell \in \mathbb{N}$:

$$P_\ell^{(m)}(x) = (-1)^m(1 - x^2)^{m/2}\frac{d^m}{dx^m}(P_\ell(x)).$$

The relation linking $P_\ell^{-m}(x)$ for $m \geq 0$ to $P_\ell^m(x)$ is:

$$P_\ell^{-m}(x) = (-1)^m\frac{(\ell - m)!}{(\ell + m)!}P_\ell^m(x).$$

The associated Legendre polynomials are also orthogonal for a given m:

$$\int_{-1}^{1} P_{\ell'}^{m}(x) P_{\ell}^{m}(x) dx = \frac{2}{2\ell+1}\delta_{\ell\ell'}.$$

A useful recursion formula is

$$(\ell-m)P_{\ell}^{(m)}(x) = (2\ell-1)xP_{\ell-1}^{(m)}(x) + (\ell+m-1)P_{\ell-2}^{(m)}(x) \quad (0 \le m \le \ell),$$
$$P_{m}^{(m)}(x) = (-1)^{(m)}(1-x^2)^{m/2}\frac{(2m)!}{2^m m!}, \qquad P_{m+1}^{(m)}(x) = (2m+1)xP_{m}^{(m)}(x). \quad \text{(D.2)}$$

Then, let $Q_{\ell}^{(m)}$ denote a renormalized version of $P_{\ell}^{(m)}$ defined by

$$Q_{\ell}^{(m)} = \sqrt{\frac{2\ell+1}{4\pi}\frac{(\ell-m)!}{(\ell+m)!}}P_{\ell}^{(m)}. \quad \text{(D.3)}$$

This definition and recursion (D.2) imply the following recursion for the $Q_{\ell}^{(m)}$:

$$\sqrt{\ell^2-m^2}Q_{\ell}^{(m)}(x) = \sqrt{4\ell^2-1}xQ_{\ell-1}^{(m)}(x) + \sqrt{(\ell-1)^2-m^2}\sqrt{\frac{2\ell+1}{2\ell-3}}Q_{\ell-2}^{(m)}(x) \quad (0 \le m \le \ell),$$
$$Q_{m}^{(m)}(x) = \frac{(-1)^{(m)}}{\sqrt{4\pi}}\frac{(1-x^2)^{m/2}}{2^m}\frac{\sqrt{(2m+1)!}}{m!}, \qquad Q_{m+1}^{(m)}(x) = \sqrt{2m+3}xQ_{m}^{(m)}(x), \quad \text{(D.4)}$$

which is used in the present implementation to compute $B_{i'i}^{m,\ell}$ in eq. (2.33-2.34).

D.3 SPHERICAL HARMONICS

In spherical coordinates, the Laplace's equation is written:

$$\frac{1}{r^2}\frac{\partial}{\partial r}(r^2\frac{\partial f}{\partial r}) + \frac{1}{r^2}\Big(\frac{1}{\sin^2\theta}\frac{\partial^2 f}{\partial \phi^2} + \frac{1}{\sin\theta}\frac{\partial}{\partial\theta}(\sin\theta\frac{\partial f}{\partial\theta})\Big) = 0. \quad \text{(D.5)}$$

The *spherical harmonics* are the functions appearing in the general solution of (D.5) sought using separation of variables in spherical coordinates, and are given by

$$Y_{\ell,m}(\theta,\phi) = \sqrt{\frac{2\ell+1}{4\pi}\frac{(\ell-m)!}{(\ell+m)!}}P_{\ell}^{(m)}(\cos\theta)e^{im\phi}, \qquad -\ell \le m \le \ell$$

with $\theta \in [0;\pi]$ and $\phi \in [0;2\pi]$. Spherical harmonics $Y_{\ell,m}$ are L^2-othonormal on the unit sphere. A function $g(\theta,\phi)$ in $L^2(S^2)$ can hence be written on a basis of spherical harmonics:

$$g(\theta,\phi) = \sum_{\ell=0}^{+\infty}\sum_{m=-\ell}^{+\ell} A_{\ell m}Y_{\ell,m}(\theta,\phi), \quad \text{(D.6)}$$

where, using the orthonormality of spherical harmonics, we have:

$$A_{\ell m} = \int_{\partial\Omega} \bar{Y}_{\ell,m}(\theta,\phi)g(\theta,\phi)$$

where $\bar{Y}_{\ell,m}$ is the complex conjugate of $Y_{\ell,m}$. These properties are used in Section 2.4.4.

Appendix E

Solution of linear viscoelastic equations in the frequency-domain using real Helmholtz boundary integral equations

Contents

Concurrently with the principal subject of the thesis, some work has been performed with Professor H.B. Bui on boundary integral equation for viscoelasticity. This work has been published in a short Note for C.R. Mecanique [42].

E.1 INTRODUCTION

The main advantage of boundary element method (BEM) is that only the domain boundary is discretized. As a result, the method is well suitable for the study of problems in unbounded domains. So, the boundary integral formulation of linear elasticity is used to study seismic wave propagation [191].

But, the ideal model of a linear elastic soil is not adapted in a lot of cases. It is necessary to take into account the soil damping factor and so to use a formulation for dynamic viscoelasticity.

In time domain, various methods have been proposed for BEM formulation of viscoelasticity [188]. They are sorted into three kinds. The first formulation is developed by applying the elastic-viscoelastic *correspondence principle*. An integral transform (according to time) is performed on the boundary integral equation of elastodynamics. Generally, Laplace transform is considered, for example in the works of Rizzo [172] or Kusama [129]. Then, the viscoelastic fundamental solutions are obtained by applying the elastic-viscoelastic correspondence principle to elastodynamic solutions. Various works deal with the reduction of the last step: the back transform to time domain.

The second class of methods uses the fundamental solutions of elastodynamics in time domain. Once the convolution with time shape functions is integrated analytically, the equation is

transformed in Laplace domain where the correspondence principle is applied. Then, a numerical inverse transformation is required [92] to lead to a time domain boundary element formulation. Various works use the "convolution quadrature method" developed by Lubich [136] to evaluate the convolution [189].

The last class of methods directly requires the knowledge of the viscoelastic fundamental solutions in time domain. Using differential systems of Kelvin and Boltzmann models, Mesquita [149] determines integral formulations adapted to each model. With those methods, only for the simplest viscoelastic models, the fundamental solutions are available analytically and one does not consider works in elastodynamics.

In frequency-domain, the usual method is to replace the Lamé's constants by complex values [67].

In this additional work, a simple method to formulate the boundary integral equations for viscoelasticity, with a Zener model (i.e. standard 3 parameters solid), is presented. This method, based on the introduction of new intermediate variables, reuses the classical formulation of elastodynamics and presents the advantage to keep real valued Lamé's constants. To the authors knowledge, a formulation similar to ours does not exist in the literature.

E.2 RHEOLOGICAL MODEL

Various rheological models exist to model the viscoelastic behavior of a material [79]. The Kelvin-Voigt model is well adapted to model solids. The Maxwell model is in general used to model fluids. The rheological model used herein is a Zener with a dashpot impedance η and elastic constants k_0 and k_1 (Fig E.1). In this model, if $\dot{\epsilon} = 0$, so the dashpot has not effect, it is called a "relaxed modulus". The model is equivalent to two springs connected in series. On the contrary, if $\dot{\epsilon} = \infty$, the dashpot does not have time to react, it is called an "instantaneous modulus".

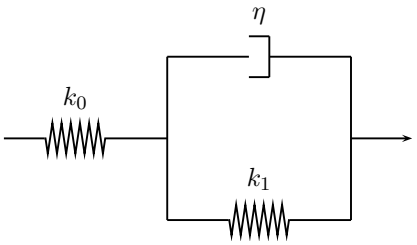

Figure E.1: *Zener model.*

E.3 FORMULATION OF THE PROBLEM

In the following, usual typeface letters denote scalar quantities while boldface letters denote vectors, matrices or tensors. The partial derivate is denoted using a comma ($\frac{\partial f}{\partial x} = f_{,x}$).

The study is made in the frequency-domain. The main idea is to avoid the definition of the displacement in the classical form $\boldsymbol{u}(\boldsymbol{x}, t) = \boldsymbol{u}(\boldsymbol{x})e^{i\omega t}$ (ω denoting the circular frequency) but under the restrictive condition:

$$\boldsymbol{u}(\boldsymbol{x}, t) = \boldsymbol{v}(\boldsymbol{x}) \cos \omega t \tag{E.1}$$

where $\boldsymbol{v}(\boldsymbol{x})$ is a real function. As a result, the variables $\boldsymbol{x}$ and t are uncoupled.

The three-dimensional generalization of the Zener constitutive law has been proposed by I. Goriacheva in [96] and is used in the present Note, denoting $\boldsymbol{\sigma}$ the stress tensor and $\boldsymbol{\epsilon}$ the strain

tensor:

$$\left\{\begin{array}{lcl} \boldsymbol{\sigma}^* & = & \boldsymbol{\sigma} + \beta\frac{\partial \boldsymbol{\sigma}}{\partial t} \\ \boldsymbol{\epsilon}^* & = & \boldsymbol{\epsilon} + \alpha\frac{\partial \boldsymbol{\epsilon}}{\partial t} \\ \boldsymbol{u}^* & = & \boldsymbol{u} + \alpha\frac{\partial \boldsymbol{u}}{\partial t} \end{array}\right. \tag{E.2}$$

The coefficients α and β ($\alpha > \beta$) are determined by:

$$\alpha = \frac{\eta}{k_1}, \quad \beta = \frac{\eta}{k_0 + k_1}.$$

The tensors $\boldsymbol{\sigma}^*$ and $\boldsymbol{\epsilon}^*$ are linked by the constitutive equation of isotropic linear elasticity, with the Lamé's coefficients λ and μ of the relaxed modulus, $\boldsymbol{\sigma}^* = L\boldsymbol{\epsilon}^*$.

With notation (E.1), we note that $\boldsymbol{u}(\boldsymbol{x}, t)$ and $\dot{\boldsymbol{u}}(\boldsymbol{x}, t)$ are phase shift by $\pi/2$. Using notation (E.2), we obtain $\boldsymbol{u}^*(\boldsymbol{x}, t) = \boldsymbol{v}(\boldsymbol{x})[\cos\omega t - \alpha\omega \sin\omega t]$. Noting the angle ψ such that $\tan\psi = \alpha\omega$ ($0 \leq \psi < \pi/2$, i.e. $\cos\psi \neq 0$), it follows:

$$\boldsymbol{u}^*(\boldsymbol{x}, t) = \frac{\boldsymbol{v}(\boldsymbol{x})}{\cos\psi}\cos(\omega t + \psi). \tag{E.3}$$

Clearly, the variables $\boldsymbol{u}^*$ and $\boldsymbol{u}$ are phase shift by ψ but have the same circular frequency ω.

Then, noting $\boldsymbol{\sigma}(\boldsymbol{x}, t) = \boldsymbol{w}(\boldsymbol{x})\cos(\omega t + \theta)$, we obtain $\boldsymbol{\sigma}^*(\boldsymbol{x}, t) = \boldsymbol{w}(\boldsymbol{x})[\cos(\omega t + \theta) - \beta\omega \sin(\omega t + \theta)]$. Defining in the same way that for $\boldsymbol{u}$, the angle ϕ such that $\tan\phi = \beta\omega$ ($0 \leq \phi < \pi/2$, i.e. $\cos\phi \neq 0$), it follows:

$$\boldsymbol{\sigma}^*(\boldsymbol{x}, t) = \frac{\boldsymbol{w}(\boldsymbol{x})}{\cos\phi}\cos(\omega t + \phi + \theta). \tag{E.4}$$

But, the variables $\boldsymbol{\sigma}^*$ and $\boldsymbol{u}^*$ are known to satisfy the linear elasticity equations, as a result they have to be in phase. It follows that $\psi = \phi + \theta$. Finally, $\boldsymbol{\sigma}$ and $\boldsymbol{u}$ have to be phase shift by $\theta = \psi - \phi$.

E.4 BOUNDARY INTEGRAL FORMULATION

The boundary integral equation method for this formulation of viscoelasticity is now defined using the well-known method for elastodynamics. In fact, the main advantage of this formulation is that only a simple change of variables is introduced.

Boundary integral equation. The quantities $\boldsymbol{\sigma}^*$ and $\boldsymbol{u}^*$ which are linked by the elastic law, are now shown to satisfy the dynamic equation. $\boldsymbol{\sigma}$ and $\boldsymbol{u}$ can satisfy the dynamic equation $div\boldsymbol{\sigma} - \rho\ddot{\boldsymbol{u}} \cong 0$ if and only if $\boldsymbol{\sigma}$ and $\boldsymbol{u}$ are almost in phase, that is to say if and only if the angle θ is small. The difference introduced by the dephasing between $\boldsymbol{\sigma}$ and $\boldsymbol{u}$, in the dynamic equation, is proportional to $\rho\omega^2\theta$. It can be easily proved that $\theta \cong |\alpha - \beta|\omega$. As a result, $\rho\omega^2\theta$ is proportional to $\rho\omega^3|\alpha - \beta|$ and we remark that we have $div\boldsymbol{\sigma} - \rho\ddot{\boldsymbol{u}} \cong 0$ to order $O(\omega^3)$. It follows that:

$$div\boldsymbol{\sigma}^* - \rho\ddot{\boldsymbol{u}}^* \equiv (div\boldsymbol{\sigma} - \rho\ddot{\boldsymbol{u}}) + \beta(div\dot{\boldsymbol{\sigma}} - \rho\dddot{\boldsymbol{u}}) + (\beta - \alpha)\rho\dddot{\boldsymbol{u}} \cong (\beta - \alpha)\rho\dddot{\boldsymbol{u}} \tag{E.5}$$

Using the definition of $\boldsymbol{u}$ (E.1), we obtain that $div\boldsymbol{\sigma}^* - \rho\ddot{\boldsymbol{u}}^* \cong 0$ and that the difference introduced in this dynamic equation is equally proportional to $\rho\omega^3|\alpha - \beta|$ if and only if:

$$|\alpha - \beta|\omega \ll 1 \qquad \text{that is to say} \qquad |\theta| \ll 1. \tag{E.6}$$

As a result, if ω is much less than the limit frequency $\omega_1 = 1/|\alpha - \beta|$, the notation (E.1) is compatible with elastodynamics.

Since $|\alpha - \beta|$ is proportional to the viscosity coefficient η (for a given set of elastic constant k_0 and k_1), the lower the coefficient η, the higher the limit frequency ω_1 (in soil mechanics η is small so that ω_1 is very large). Thus the hypothesis of "low" frequency $\omega \ll \omega_1$ (including the quasi-static

case $\omega = 0$), which we suppose in the following, is satisfied in soil mechanics, for a large frequency range. This leads to the boundary integral formulation which is the same as for elastodynamics:

$$div\ \boldsymbol{\sigma}^* + \rho\omega^2 \boldsymbol{u}^* = 0, \quad \boldsymbol{\sigma}^* = L\boldsymbol{\epsilon}^*.$$

This formulation is now recalled [31]. The stress vector $\boldsymbol{T^n u}$ on a plane of normal $\boldsymbol{n}$ is defined by the operator (λ and μ representing the Lamé's constants): $\boldsymbol{T^n} = 2\mu\partial_n + \lambda \boldsymbol{n}.\boldsymbol{div} + \mu \boldsymbol{n} \wedge \boldsymbol{rot}$.

Noting Ω the region of space occupied by an elastic solid with isotropic constitutive properties, the displacement $\boldsymbol{u}$ at an interior point $\boldsymbol{x} \in \Omega$ is given by:

$$u_k(\boldsymbol{x}) = \int_{\partial\Omega} [(\boldsymbol{T^n u(y)})_i U_i^k(\boldsymbol{x}, \boldsymbol{y}; \omega) - u_i(\boldsymbol{y})(\boldsymbol{T^n U^k}(\boldsymbol{x}, \boldsymbol{y}; \omega))_i] dS_y \qquad (\boldsymbol{x} \in \Omega), \qquad \text{(E.7)}$$

where $U_i^k(\boldsymbol{x}, \boldsymbol{y}; \omega)$ denotes the i-th component of the elastodynamic fundamental solution, in the frequency-domain, for an infinite space. When $\boldsymbol{x} \in \partial\Omega$, a singularity occurs in $\boldsymbol{y} = \boldsymbol{x}$. With the help of a well-documented limiting process, equation (E.7) yields the integral equation:

$$c_{ik}(\boldsymbol{x}) u_i(\boldsymbol{x}) = (P.V.) \int_{\partial\Omega} [(\boldsymbol{T^n u(y)})_i U_i^k(\boldsymbol{x}, \boldsymbol{y}; \omega) - u_i(\boldsymbol{y})(\boldsymbol{T^n U^k}(\boldsymbol{x}, \boldsymbol{y}; \omega))_i] dS_y \qquad (\boldsymbol{x} \in \partial\Omega), \quad \text{(E.8)}$$

where $(P.V.) \int$ indicates a Cauchy principal value (CPV) singular integral and the *free term* $c_{ik}(\boldsymbol{x})$ is equal to $0.5\delta_{ik}$ in the usual case where $\partial\Omega$ is smooth at $\boldsymbol{x}$.

Boundary conditions. We consider a domain Ω, of boundary $\partial\Omega$ on which mixed but independent boundary conditions are imposed ($\partial\Omega = \partial\Omega_1 + \partial\Omega_2$ and $\partial\Omega_1 \bigcap \partial\Omega_2 = \emptyset$). On $\partial\Omega_1$, the imposed displacement is noted as in (E.1):

$$\boldsymbol{u}^d(\boldsymbol{x}, t) = \boldsymbol{u}^d(\boldsymbol{x}) \cos \omega t,$$

on $\partial\Omega_2$, the stress vector is written in the same manner:

$$\boldsymbol{t}^d(\boldsymbol{x}, t) = \boldsymbol{w}^d(\boldsymbol{x}) \cos \omega(t + \theta).$$

Let's assume that the data $\boldsymbol{u}^d$ on $\partial\Omega_1$ and $\boldsymbol{\sigma}^d.\boldsymbol{n}$ on $\partial\Omega_2$ are compatible (if $\boldsymbol{u}$ can be defined in form (E.1) so the variables are phase shift by $\theta = \psi - \phi$). For example, the following data are compatible:

1. $\boldsymbol{u}^d \neq 0$ (circular frequency ω) on $\partial\Omega_1$ and $\boldsymbol{\sigma}^d.\boldsymbol{n} = 0$ on $\partial\Omega_2$
2. $\boldsymbol{u}^d = 0$ on $\partial\Omega_1$ and $\boldsymbol{\sigma}^d.\boldsymbol{n} \neq 0$ (circular frequency ω) on $\partial\Omega_2$

As a result, the intermediate variables $\boldsymbol{u}^*$ and $\boldsymbol{\sigma}^*$, are necessarily in phase. The problem in $\boldsymbol{u}^*$ and $\boldsymbol{\sigma}^*$ is solved using the well-known boundary integral formulation of elastodynamics in the frequency-domain. Having the solution $\boldsymbol{u}^*$ (resp. $\boldsymbol{\sigma}^*$), $\boldsymbol{u}$ (resp. $\boldsymbol{\sigma}$) is easily computed. Indeed, the solutions of the elastodynamic problem $\boldsymbol{u}^*$ and $\boldsymbol{\sigma}^*$ have respectively an amplitude equal to $\frac{v(x)}{\cos\psi}$ and $\frac{w(x)}{\cos\phi}$ ((E.3) and (E.4)). So, to compute the amplitude of $\boldsymbol{u}$ (resp.$\boldsymbol{\sigma}$), one only has to multiply the amplitude of $\boldsymbol{u}^*$ (resp.$\boldsymbol{\sigma}^*$) by $\cos\ \psi$ (resp. $\cos\ \phi$) where $\psi = \tan^{-1} \alpha\omega$ and $\phi = \tan^{-1} \beta\omega$.

E.5 CONCLUSION

A new and simple formulation of time harmonic viscoelasticity (including the quasi-static case) have been presented. Hence, it has been shown that this problem reduces to a classical elastic problem by a simple change of variables if the boundary conditions respect a restrictive condition. It makes possible to reuse existing numerical tools of time harmonic elastodynamics. The speed up of the computation can be done using the Fast multipole method [41].

References

[1] M. Abramowitz and I. A. Stegun. *Handbook of mathematical functions, with formulas, graphs, and mathematical tables*. Dover Publications, 1991.

[2] J. D. Achenbach. *Wave propagation in elastic solids*. North Holland, 1984.

[3] S. Ahmad and G. D. Manolis. Dynamic analysis of 3-D structures by a transformed boundary element method. *Computational Mechanics*, 2:185–196, 1987.

[4] K. Aki and K. L. Larner. Surface motion of a layered medium having an irregular interface due to incident plane SH waves. *Journal of Geophysical Research*, 75:933–954, 1970.

[5] K. Aki and P. G. Richards. *Quantitative Seismology*. University Science Books, 2nd edition, 2002.

[6] M. H. Aliabadi. *The boundary element method. Applications in Solids and Structures*, volume 2. Wiley, 2002.

[7] G. Alléon, M. Benzi, and L. Giraud. Sparse approximation inverse preconditioning for dense linear systems arising in computational electromagnetics. *Numerical Algorithms*, 16:1–15, 1997.

[8] F. Alouges, S. Borel, and D. P. Levadoux. A stable well-conditioned integral equation for electromagnetism scattering. *Journal of Computational and Applied Mathematics*, 204:440–451, 2007.

[9] X. Antoine and Y. Boubendir. An integral preconditioner for solving the two-dimensional scattering transmission problem using integral equations. *International Journal of Computer Mathematics*, 85:1473–1490, 2008.

[10] F. C. Araújo, C. J. Martins, and W. J. Mansur. An efficient BE iterative-solver-based substructuring algorithm for 3D time-harmonic problems in elastodynamics. *Engng. Anal. Bound. Elem.*, 25:795–803, 2001.

[11] P. Y. Bard. Diffracted waves and displacement field over two-dimensional elevated topographies. *Geophys. J. Int.*, 71:731–760, 1982.

[12] P. Y. Bard and M. Bouchon. The seismic response of sediment-filled valleys. Part 1: the case of incident SH waves. *Bull. Seism. Soc. Am.*, 70:1263–1286, 1980.

[13] P. Y. Bard and M. Bouchon. The seismic response of sediment-filled valleys. Part 2: the case of P and SV waves. *Bull. Seism. Soc. Am.*, 70:1921–1941, 1980.

[14] P. Y. Bard, E. Chaljub, C. Cornou, F. Cotton, and P. Gueguen, editors. *Third International Symposium on the Effects of Surface Geology on Seismic Motion*, 2006.

[15] U. Basu and A. K. Chopra. Perfectly matched layers for time-harmonic elastodynamics of unbounded domains: theory and finite-element implementation. *Comp. Meth. Appl. Mech. Engng.*, 192:1337–1375, 2003.

[16] U. Basu and A. K. Chopra. Perfectly matched layers for transient elastodynamics of unbounded domains. *Int. J. Numer. Meth. Engng.*, 59:1039–1074, 2004.

[17] K. J. Bathe. *Finite element procedures in engineering analysis*. Prentice-Hall, 1982.

[18] M. Bebendorf. Approximation of boundary element matrices. *Numerische Mathematik*, 86:565–589, 2000.

[19] M. Bebendorf and S. Rjasanow. Adaptive low-rank approximation of collocation matrices. *Computing*, 70:1–24, 2003.

[20] E. Bécache, S. Fauqueux, and P. Joly. Stability of perfectly matched layers, group velocities and anisotropic waves. *J. Comp. Phys.*, 188:399–433, 2003.

[21] M. Benjemaa. *Étude et simulation numérique de la rupture dynamique des séismes par des méthodes d'éléments finis discontinus*. PhD thesis, Université de Nice Sophia-Antipolis, 2007. In French, hal.inria.fr/docs/00/22/28/70/PDF/these.pdf.

[22] J. P. Bérenger. A perfectly matched layer for the absorption of electromagnetic waves. *J. Comp. Phys.*, 114:185–200, 1994.

[23] J. P. Bérenger. Three-dimensional perfectly matched layer for the absorption of electromagnetic waves. *J. Comp. Phys.*, 127:363–379, 1996.

[24] D. E. Beskos. Boundary element methods in dynamic analysis. *Appl. Mech. Rev.*, 40:1–23, 1987.

[25] D. E. Beskos. Boundary element methods in dynamic analysis: Part II. *Appl. Mech. Rev.*, 50:149–197, 1997.

[26] G. Beylkin, R. Coifman, and V. Vokhlin. Fast wavelet transforms and numerical algorithms. *Comm. Pure Appl. Math.*, 44:141–183, 1991.

[27] J. Bielak, O. Ghattas, and E. J. Kim. Parallel octree-based finite element method for large-scale earthquake ground motion simulation. *Computer modeling in engineering and science*, 10:99–112, 2005.

[28] J. Bielak and R. C. Maccamy. Symmetric finite-element and boundary integral coupling methods for fluid-solid interaction. *Quart. Appl. Math.*, 49:107–119, 1991.

[29] J. A. Board, J. W. Causey, J. F. Leathrum, A. Windemuth, and K. Schulten. Accelerated molecular dynamics simulation with the parallel fast multipole algorithm. *Chem. Phys. Lett.*, 198:89–94, 1992.

[30] F. Bonilla. *Computation of linear and nonlinear site response for near field ground motion*. PhD thesis, University of California at Santa Barbara, 2000.

[31] M. Bonnet. *Boundary Integral Equation Method for Solids and Fluids*. Wiley, 1999.

[32] M. Bonnet. Exploiting partial or complete geometrical symmetry in 3D symmetric Galerkin indirect BEM formulations. *Int. J. Numer. Meth. Engng.*, 57:1053–1083, 2003.

[33] M. Bonnet. Topological sensitivity for 3D elastodynamic and acoustic inverse scattering in the time domain. *Comp. Meth. Appl. Mech. Engng.*, 195:5239–5254, 2006.

[34] M. Bonnet, G. Maier, and G. Polizzotto. Symmetric Galerkin boundary element methods. *Appl. Mech. Rev.*, 51:669–704, 1998.

[35] R. Bost. Modélisation de la propagation d'ondes en milieu amortissant par formulation multipôle rapide (équations intégrales de frontière). Master thesis, ENTPE Vaulx en Velin (in French), 2008.

[36] M. Bouchon, M. Campillo, and S. Gaffet. A boundary integral equation-discret wavenumber representation method to study wave propagation in multilayered media having irregular interfaces. *Geophysics*, 54:1134–1140, 1989.

[37] M. Bouchon and F. J. Sánchez-Sesma. Boundary integral equations and boundary elements methods in elastodynamics. *Adv. Geophys.*, 48:157–189, 2007.

[38] H. D. Bui, B. Loret, and M. Bonnet. Régularisation des équations intégrales de l'élastostatique et de l'élastodynamique. *C.R. Acad. Sci. Paris, série 2, Mécanique, Physique, Chimie, Sciences de*

l'univers, Sciences de la Terre, 300:633–636, 1985. In French.

[39] J.M. Carcione, D. Kosloff, and R. Kosloff. Wave propagation simulation in a linear viscoelastic medium. *Geophys. J. Int.*, 95:597–611, 1988.

[40] B. Carpentieri, I. S. Duff, L. Giraud, and G. Sylvand. Combining fast multipole techniques and an approximate inverse preconditioner for large electromagnetism calculations. Technical report, CERFACS TR/PA/03/77, 2003.

[41] S. Chaillat, M. Bonnet, and J. F. Semblat. A fast multipole method formulation for 3D elastodynamics in the frequency domain. *C. R. Mecanique*, 335:714–719, 2007.

[42] S. Chaillat and H. D. Bui. Resolution of linear viscoelastic equations in the frequency domain using real Helmholtz boundary integral equations. *C. R. Mecanique*, 335:746–750, 2007.

[43] E. Chaljub, D. Komatitsch, J. P. Vilotte, Y. Capdeville, B. Valette, and G. Festa. Spectral-element analysis in seismology. *Adv. Geophys.*, 48:365–419, 2007.

[44] Y. H. Chen, W. C. Chew, and S. Zeroug. Fast multipole method as an efficient solver for 2D elastic wave surface integral equations. *Computational Mechanics*, 20:495–506, 1997.

[45] H. Cheng, W. Y. Crutchfield, Z. Gimbutas, L. F. Greengard, J. F. Ethridge, J. Huang, V. Rokhlin, N. Yarvin, and J. Zhao. A wideband fast multipole method for the Helmholtz equation in three dimensions. *J. Comp. Phys.*, 216:300–325, 2006.

[46] R. M. Christensen. *Theory of viscoelasticity*. Courier Dover Publications, 2nd edition, 2003.

[47] S. H. Christiansen and J. C. Nédélec. A preconditioner for the electric field integral equation based on calderón formulas. *SIAM J. Numer. Anal.*, 40:1100–1135, 2002.

[48] R. Clayton and B. Engquist. Absorbing boundary conditions for acoustic and elastic wave equations. *Bull. Seism. Soc. Am.*, 67:1529–1540, 1977.

[49] D. Clouteau. *Propagation d'ondes dans des milieux hétérogènes. Application à la tenue des ouvrages sous séismes*. PhD thesis, École Centrale Paris, 1990. In French.

[50] D. Clouteau, M. L. Elhabre, and D. Aubry. Periodic BEM and FEM-BEM coupling. Application to seismic behaviour of very long structures. *Computational Mechanics*, 25:567–577, 2000.

[51] F. Collino and F. Millot. La méthode multipôle à deux composantes pour l'électromagnétique. CERFACS Rapport Technique TR/EMC/01/22, 2001.

[52] F. Collino and C. Tsogka. Application of the perfectly matched absorbing layer model to the linear elastodynamic problem in anisotropic heterogeneous media. *Geophysics*, 66:294–307, 2001.

[53] T. A. Cruse. A direct formulation and numerical solution of the general transient elastodynamic problem. Part II. *J. Math. Anal. Appl.*, 22:341–355, 1968.

[54] T. A. Cruse. Numerical solutions in three-dimensional elastostatics. *Int. J. Solids Struct.*, 5:1259–1274, 1969.

[55] T. A. Cruse and F. J. Rizzo. A direct formulation and numerical solution of the general transient elastodynamic problem. I. *J. Math. Anal. Appl.*, 22:244–259, 1968.

[56] P. Dangla, J. F. Semblat, H. Xiao, and N. Delépine. A simple and efficient regularization method for 3D BEM : application to frequency-domain elastodynamics. *Bull. seism. Soc. Am.*, 95:1916–1927, 2005.

[57] E. Darve. The fast multipole method I: Error analysis and asymptotic complexity. *SIAM J. Numer. Anal.*, 38:98–128, 2000.

[58] E. Darve. The fast multipole method: Numerical implementation. *J. Comp. Phys.*, 160:195–240, 2000.

[59] E. Darve and W. Fong. A black-box fast multipole method. In 8^{th} *World Congress on Computational Mechanics*, 2008.

[60] E. Darve and P. Havé. Efficient fast multipole method for low-frequency scattering. *J. Comp. Phys.*, 197:341–363, 2004.

[61] E. Darve and P. Havé. A fast multipole method for Maxwell equations stable at all frequencies. *Phil. Trans. Roy. Soc. (London)*, A362:603–628, 2004.

[62] P. J. Davis and P. Rabinowitz. *Methods of numerical integration*. Academic Press, 1975.

[63] E. Delavaud. *Simulation numérique de la propagation d'ondes en milieu géologique complexe: application à l'évaluation de la réponse sismique du bassin de Caracas (Venezuela)*. PhD thesis, Institut de Physique du Globe de Paris, 2007. In French, www.ipgp.jussieu.fr/∼delavaud/ThesisDelavaud.pdf.

[64] N. Delépine. *Modélisation des effets de site sismiques dans les bassins sédimentaires et influence des non-linéarités de comportement des sols.* PhD thesis, ENPC, 2007. In French, http://pastel.paristech.org/3827/01/these_Delepine.pdf.

[65] N. Delépine and J. F. Semblat. Site effects in a deep alpine valley for various seismic sources. In *Third International Symposium on the Effects of Surface Geology on Seismic Motion*, Grenoble, 2006.

[66] C. Di Prisco, M. Stupazzini, and C. Zambelli. Nonlinear SEM numerical analyses of dry dense sand specimens under rapid and dynamic loading. *Int. J. Numer. Anal. Meth. Geomech.*, 31:757–788, 2007.

[67] J. Dominguez. *Boundary Elements in Dynamics*. Elsevier Applied Science Publishers, 1993.

[68] E. Dormy and A. Tarantola. Numerical simulation of elastic wave propagation using a finite volume method. *Journal of Geophysical Research*, 100:2123–2133, 1995.

[69] M. Dumbser and M. Kaser. An arbitrary high-order discontinuous Galerkin method for elastic waves on unstructured meshes-II. The three-dimensional isotropic case. *Geophys. J. Int.*, 167:319–336, 2006.

[70] B. Engquist and L. Ying. Fast directional multilevel algorithms for oscillatory kernels. *SIAM J. Sci. Comput.*, 29:1710–1737, 2007.

[71] M. A. Epton and B. Dembart. Multipole translation theory for the three-dimensional Laplace and Helmholtz equations. *SIAM J. Sci. Comput.*, 16:865–897, 1995.

[72] A. C. Eringen and E. S. Suhubi. *Elastodynamics, Vol. II-Linear Theory.* Academic Press, 1975.

[73] H. Eshraghi and M. Dravinski. Scattering of plane harmonic SH, SV, P and Rayleigh waves by non-axisymmetric three-dimensional canyons: a wave function expansion approach. *Earthquake Engng. Struct. Dyn.*, 18:983–998, 1989.

[74] E. Faccioli, F. Maggio, R. Paolucci, and A. Quarteroni. 2D and 3D elastic wave propagation by a pseudo-spectral domain decomposition method. *J. Seismol.*, 1:237–251, 1997.

[75] G. Festa, E. Delavaud, and J. P. Vilotte. Interaction between surface waves and absorbing boundaries for wave propagation in geological basins: 2D numerical simulations. *Geophys. Res. Lett.*, 32:L20306, 2005.

[76] G. Festa and S. Nielsen. PML absorbing boundaries. *Bull. Seism. Soc. Am.*, 93:891–903, 2003.

[77] G. Festa and J. P. Vilotte. The Newmark scheme as velocity-stress time-straggering: an efficient PML implementation for spectral element simulations of elastodynamics. *Geophys. J. Int.*, 161:789–812, 2005.

[78] M. Fischer and L. Gaul. Application of the fast multipole BEM for structural-acoustic simulations. *J. Comput. Acoust.*, 13:87–98, 2005.

[79] W. Flügge. *Viscoelasticity*. Springer, 1975.

[80] A. Frangi. A fast multipole implementation of the qualocation mixed-velocity-traction approach for

exterior Stokes flows. *Engng. Anal. Bound. Elem.*, 29:1039–1046, 2005.

[81] A. Frangi and A. Di Gioia. Multipole BEM for the evaluation of damping forces on MEMS. *Computational Mechanics*, 37:24–31, 2005.

[82] A. Frankel. Three-Dimensional Simulation of ground motions in the San Bernardino Valley, California, for hypothetical earthquakes on the San Andreas fault. *Bull. Seism. Soc. Am.*, 83:1020–1041, 1993.

[83] A. Frankel and W. Leith. Evaluation of topographic effects on it P and it S waves of explosions at the northern Novaya Zemlya test site using 3-D numerical simulations. *Geophys. Res. Lett.*, 19:1887–1890, 1992.

[84] A. Frankel and J. Vidale. A Three-Dimensional Simulation of Seismic Waves in the Santa Clara Valley, California, from a Loma Prieta Aftershock. *Bull. Seism. Soc. Am.*, 82:2045–2074, 1992.

[85] P. Frey and P. L. George. *Mesh generation. Application to finite elements*. Wiley, 2008.

[86] L. Y. Fu. Seismograph synthesis for piecewise heterogeneous media. *Geophys. J. Int.*, 150:800–808, 2002.

[87] Y. Fu and G. J. Rodin. Fast solution method for three-dimensional Stokesian many-particle problems. *Comm. Numer. Meth. Engng*, 16:145–149, 2000.

[88] Y. H. Fu, K. J. Klimkowski, G. J. Rodin, E. Berger, J.C. Browne, J. K. Singer, R. A. Van de Geijn, and K. S. Vemaganti. A fast solution method for three-dimensional many-particle problems of linear elasticity. *Int. J. Numer. Meth. Engng.*, 42:1215–1229, 1998.

[89] H. Fujiwara. The fast multipole method for the integral equations of seismic scattering problems. *Geophys. J. Int.*, 133:773–782, 1998.

[90] H. Fujiwara. The fast multipole method for solving integral equations of three-dimensional topography and basin problems. *Geophys. J. Int.*, 140:198–210, 2000.

[91] T. Fukui and K. Inoue. Fast multipole boundary element method in 2D elastodynamics. *J. Appl. Mech. JSCE*, 1:373–380, 1998. In Japanese.

[92] L. Gaul and M. Schanz. Dynamics of viscoelastic solids treated by boundary element approaches in time domain. *Eur. J. Mech. A/Solids*, 13:43–59, 1994.

[93] S. Gavoille, C. Mariotti, C. Rey, and A. Delaplace. A coupling discrete/finite element strategy: application to a seismic problem. In 2^{nd} *International Conference on Computational Methods for Coupled problems in Science and Engineering*, 2007.

[94] J. E. Gómez and H. Power. A multipole direct and indirect BEM for 2D cavity flow at low Reynolds number. *Engng. Anal. Bound. Elem.*, 19:17–31, 1997.

[95] J. E. Gómez and H. Power. A parallel multipolar indirect boundary element method for the Neumann interior Stokes flow problem. *Int. J. Numer. Meth. Engng.*, 48:523–543, 2000.

[96] I. G. Goriacheva. Contact problem of rolling of a viscoelastic cylinder on a base of the same material. *J. Appl. Math. Mech.*, 37:877–885, 1973.

[97] K. F. Graff. *Wave motion in elastic solids*. Dover, 1991.

[98] R. W. Graves. Simulating seismic wave propagation in 3D elastic media using staggered-grid finite differences. *Bull. Seism. Soc. Am.*, 86:1091–1106, 1996.

[99] L. Greengard. *The rapid evaluation of potential fields in particle systems.* MIT Press, 1988.

[100] L. Greengard, J. F. Huang, V. Rokhlin, and S. Wandzura. Accelerating fast multipole methods for the Helmholtz equation at low frequencies. *IEEE Computational Science Engng.*, 5(3):32–38, 1998.

[101] L. Greengard, M. C. Kropinski, and A. Mayo. Integral equation methods for Stokes flow and isotropic

elasticity in the plane. *J. Comp. Phys.*, 125:403–414, 1996.

[102] L. Greengard and V. Rokhlin. A fast algorithm for particle simulations. *J. Comp. Phys.*, 73:325–348, 1987.

[103] L. Greengard and V. Rokhlin. A new version of the fast multipole method for the Laplace equation in three dimensions. *Acta Numerica*, 6:229–269, 1997.

[104] M. Guiggiani and A. Gigante. A general algorithm for multidimensional cauchy principal value integrals in the boundary element method. *J. Appl. Mech.*, 57:906–915, 1990.

[105] N. A. Gumerov and R. Duraiswami. *Fast multipole methods for the Helmholtz equation in three dimensions*. Elsevier, 2005.

[106] B. B. Guzina and M. Bonnet. Small-inclusion asymptotic of misfit functionals for inverse problems in acoustics. *Inverse Problems*, 22:1761–1785, 2006.

[107] B. B. Guzina and R. Y. S. Pak. Elastodynamic green's functions for a smoothly heterogeneous half-space. *Int. J. Solids Struct.*, 33:1005–1021, 1996.

[108] B. B. Guzina and R. Y. S. Pak. On the analysis of wave motions in a multi-layered solid. *Quart. J. Mech. Appl. Math.*, 54:13–37, 2001.

[109] W. Hackbusch. A sparse matrix arithmetic based on $\mathcal{H}$-matrix. Part I: Introduction to $\mathcal{H}$-matrices. *Computing*, 62:89–108, 1999.

[110] W. Hackbusch and Z. P. Nowak. On the fast matrix multiplication in the boundary element method by panel clustering. *Numerische Mathematik*, 54:463–491, 1989.

[111] J. G. Harris. *Linear elastic waves*. Cambridge University Press, 2001.

[112] K. Hayami and S. A. Sauter. Application of the panel clustering method to the three-dimensional elastostatic problem. In C. A. Brebbia and M. Marchetti, editors, *Boundary Elements XIX*, pages 625–634. Compututational Mechanics Publublications, 1997.

[113] R.L. Higdon. Absorbing boundary-conditions for elastic-waves. *Geophysics*, 56:231–241, 1991.

[114] T. J. R. Hughes. *The finite element method - linear static and dynamic finite element analysis*. Dover Publications, 2000.

[115] T. J. R. Hughes, A. Reali, and G. Sangalli. Duality and Unified Analysis of Discrete Approximations in Structural Dynamics and Wave Propagation: Comparison of p-method Finite Elements with k-method NURBS. *Comp. Meth. Appl. Mech. Engng.*, 197:4104–4124, 2008.

[116] A. Ibrahimbegovic and A. Delaplace. Microscale and mesoscale discrete models for dynamic frature of structures built of brittle materials. *Comp. Struct.*, 81:1255–1265, 2003.

[117] L. J. Jiang and W. C. Chew. A mixed-form fast multipole algorithm. *IEEE Trans. Antennas Propag.*, 53:4145–4156, 2005.

[118] L. F. Kallivokas, T. Juneja, and J. Bielak. A symmetric galerkin BEM variational framework for multi-domain interface problems. *Comp. Meth. Appl. Mech. Engng.*, 194:3607–3636, 2005.

[119] E. Kausel. *Fundamental solutions in elastodynamics: A compendium.* Cambridge University Press, 2006.

[120] B. L. N. Kennett. *Seismic wave propagation in stratified media*. Cambridge University Press, 1983.

[121] D. Komatitsch, Q.Y. Liu, J. Tromp, P. Süss, C. Stidham, and J. H. Shaw. Simulations of ground motion in the Los Angeles basin based upon the spectral-element method. *Bull. Seism. Soc. Am.*, 94:187–206, 2004.

[122] D. Komatitsch and R. Martin. An unsplit convolutional perfectly matched layer improved at grazing incidence for the seismic wave equation. *Geophysics*, 72:SM155–SM167, 2007.

[123] D. Komatitsch and J. Tromp. A perfectly matched layer (pml) absorbing condition for the second-order elastic wave equation. *Geophys. J. Int.*, 154:146–153, 2003.

[124] D. Komatitsch and J. P. Vilotte. The spectral element method: an efficient tool to simulate the seismic response of 2D and 3D geological structures. *Bull. Seism. Soc. Am.*, 88:368–392, 1998.

[125] D. Kosloff, M. Reshef, and D. Loewenthal. Elastic wave calculations by the Fourier method. *Bull. Seism. Soc. Am.*, 74:875–891, 1984.

[126] G. Krishnasamy, F. J. Rizzo, and T. J. Rudolphi. Hypersingular boundary integral equations: their occurrence, interpretation, regularization and computation. In PK Banerjee and S. Kobayashi, editors, *Developments in Boundary Element Methods*. Elsevier, 1992.

[127] V.D. Kupradze. *Three dimensional problems of the mathematical theory of elasticity and thermoelasticity*. North Holland, 1979.

[128] S. Kurz, O. Rain, and S. Rjasanow. The adaptive cross approximation technique for the 3D boundary element method. *IEEE Transactions on Magnetics*, 38:421–424, 2002.

[129] T. Kusama and Y. Mitsui. Boundary element method applied to linear viscoelastic analysis. *Appl. Math. Modelling*, 6:285–290, 1982.

[130] V. W. Lee. Three-dimensional diffraction of plane P, SV and SH waves by a hemispherical alluvial valley. *Soil Dyn. Earthquake Engng.*, 3:133–144, 1984.

[131] W. I. Liao, T. J. Teng, and C. S. Yeh. A series solution and numerical technique for wave diffraction by a three-dimensional canyon. *Wave Motion*, 39:129–142, 2004.

[132] S. W. Liu, S. K. Datta, M. Bouden, and A. H. Shah. Scattering of obliquely incident seismic waves by a cylindrical valley in a layered half-space. *Earthquake Engng. Struct. Dyn.*, 20:859–870, 1991.

[133] Y. J. Liu, N. Nishimura, Y. Otani, T. Takahashi, X. L. Chen, and H. Munakata. A fast boundary element method for the analysis of fiber-reinforced composites based on a rigid-inclusion model. *J. Appl. Mech.*, 72:115–128, 2005.

[134] C. C Lu and W. C. Chew. Fast algorithm for solving hybrid integral equations. *IEE Proc. H Microwaves, Antennas and Propagation*, 140:455–460, 1993.

[135] C. C Lu and W. C. Chew. A multilevel algorithm for solving a boundary integral equation of wave scattering. *Microwave and Optical Technology Letters*, 7:466–470, 1994.

[136] C. Lubich. Convolution quadrature and discretized operational calculus. I. *Numerische Mathematik*, 52:129–145, 1988.

[137] C. Lubich. Convolution quadrature and discretized operational calculus. II. *Numerische Mathematik*, 52:413–425, 1988.

[138] J. N. Lyness and D. Jespersen. Moderate degree symmetric quadrature rules for the triangle. *Journal of the Institute of Mathematics and its Applications*, 15:19–32, 1975.

[139] J. Lysmer and L. A. Drake. A finite element method for seismology. volume 11, chapter 6, pages 181–216. Academic Press, New York, 1972.

[140] R. Madariaga. Dynamics of an expanding circular fault. *Bull. Seism. Soc. Am.*, 66:639–666, 1976.

[141] A. I. Madyarov and B. B. Guzina. A radiation condition for layered elastic media. *J. Elasticity*, 82:73–98, 2006.

[142] A. A. Mammoli and M. S. Ingber. Stokes flow around cylinders in a bounded two-dimensional domain using multipole-accelerated boundary element methods. *Int. J. Numer. Meth. Engng.*, 44:897–917, 1999.

[143] A. A. Mammoli and M. S. Ingber. Parallel multipole BEM simulation of two-dimensional suspension

flows. *Engng. Anal. Bound. Elem.*, 24:65–73, 2000.

[144] G. D. Manolis and D. E. Beskos. *Boundary element methods in elastodynamics*. Unwin Hyman, 1988.

[145] V. Mantič. A new formula for the C-matrix in the Somigliana identity. *J. Elasticity*, 33:191–201, 1993.

[146] C. Marcinkovich and K. B. Olsen. On the implementation of perfectly matched layers in a three-dimensional fourth-order velocity-stress finite difference scheme. *Journal of Geophysical Research-Solid Earth*, 108:2276, 2003.

[147] K. J. Marfurt. Accuracy of finite-difference and finite-element modeling of the scalar and elastic wave equations. *Geophysics*, 49:533–549, 1984.

[148] M. Margonari and M. Bonnet. Fast multipole method applied to elastostatic BEM-FEM coupling. *Comp. Struct.*, 83:700–717, 2005.

[149] A. D. Mesquita and H. B. Coda. A simple Kelvin and Boltzmann viscoelastic analysis of three-dimensional solids by boundary element method. *Engng. Anal. Bound. Elem.*, 27:885–895, 2003.

[150] M. Messner and M. Schanz. Accelerating an Elastodynamic Boundary Element Formulation by using Adaptive Cross Approximation. In 8^{th} *World Congress on Computational Mechanics*, 2008.

[151] K. C. Meza-Fajardo and A. S. Papageorgiou. A Nonconvolutional, Split-Field, Perfectly Matched Layer for Wave Propagation in Isotropic and Anisotropic Elastic Media: Stability Analysis. *Bull. Seism. Soc. Am.*, 98:1811–1836, 2008.

[152] P. Moczo, J. Kristek, V. Vavrycuk, R. J. Archuleta, and L. Halada. 3D heterogeneous staggered-grid finite-difference modelling of seismic motion with volume harmonic and arithmetic averaging of elastic moduli and densities. *Bull. Seism. Soc. Am.*, 92:3042–3066, 2002.

[153] P. Moczo, J. O. A. Robertsson, and L. Eisner. The finite-difference time-domain method for modeling of seismic wave propagation. *Adv. Geophys.*, 48:421–516, 2007.

[154] H. Mogi and H. Kawakami. Analysis of scattered waves on ground with irregular topography using the direct boundary element method and Neumann series expansion. *Bull. Seism. Soc. Am.*, 97:1144–1157, 2007.

[155] T. K. Mossessian and M. Dravinski. Application of a hybrid method for scattering of P, SV, and Rayleigh waves by near-surface irregularities. *Bull. Seism. Soc. Am.*, 77:1784–1803, 1987.

[156] T. K. Mossessian and M. Dravinski. Amplification of elastic waves by a three dimensional valley. Part 1: Steady state response. *Earthquake Engng. Struct. Dyn.*, 19:667–680, 1990.

[157] T. K. Mossessian and M. Dravinski. Amplification of elastic waves by a three dimensional valley. Part 2: Transient response. *Earthquake Engng. Struct. Dyn.*, 19:681–691, 1990.

[158] N. Nemitz and M. Bonnet. Topological sensitivity and FMM-accelerated BEM applied to 3D acoustic inverse scattering. *Engng. Anal. Bound. Elem.*, 32:957–970, 2008.

[159] N. Nishimura. Fast multipole accelerated boundary integral equation methods. *Appl. Mech. Rev.*, 55:299–324, 2002.

[160] N. Nishimura, K. I. Yoshida, and S. Kobayashi. A fast multipole boundary integral equation method for crack problems in 3D. *Engng. Anal. Bound. Elem.*, 23:97–105, 1999.

[161] Y. Niu and M. Dravinski. Direct 3D BEM for scattering of elastic waves in a homogeneous anisotropic half-space. *Wave Motion*, 38:165–175, 2003.

[162] S. Ohnuki and W. C. Chew. Error minimization of multipole expansion. *SIAM J. Sci. Comput.*, 26:2047–2065, 2005.

[163] K. B. Olsen, R. J. Archuleta, and J. R. Matarese. Magnitude 7.75 earthquake on the San Andreas fault: three-dimensional ground motion in Los Angeles. *Science*, 270:1628–1632, 1995.

[164] Y. Otani and N. Nishimura. A periodic FMM for Maxwell's equations in 3D and its application to problems related to photonic crystals. *J. Comp. Phys.*, 227:4630–4652, 2008.

[165] R. Y. S. Pak and B. B. Guzina. Seismic soil-structure interaction analysis by direct boundary element methods. *Int. J. Solids Struct.*, 36:4743–4766, 1999.

[166] R. Paolucci. Amplification of earthquake ground motion by steep topographic irregularities. *Earthquake Engng. Struct. Dyn.*, 31:1831–1853, 2002.

[167] A. P. Peirce and J. A. L. Napier. A spectral multipole method for efficient solution of large-scale boundary element models in elastostatics. *Int. J. Numer. Meth. Engng.*, 38:4009–4034, 1995.

[168] R. Potthast. A survey on sampling and probe methods for inverse problems. *Inverse Problems*, 22:R2, 2006.

[169] E. Reinoso, L. C. Wrobel, and H. Power. Three-dimensional scattering of seismic waves from topographical structures. *Soil Dyn. Earthquake Engng.*, 16:41–61, 1997.

[170] E. Reinoso, L. C. Wrobel, and H. Power. Two-dimensional scattering of P, SV and Rayleigh waves: preliminary results for the valley of Mexico. *Earthquake Engng. Struct. Dyn.*, 26:595–616, 1997.

[171] F. J. Rizzo. An integral equation approach to boundary value problems of classical elastostatics. *Quart. Appl. Math.*, 25:83–95, 1967.

[172] F. J. Rizzo and D. J. Shippy. An application of the correspondence principle of linear viscoelasticity theory. *SIAM J. Appl. Math.*, 21:321–330, 1971.

[173] V. Rokhlin. Rapid solution of integral equations of classical potential theory. *J. Comp. Phys.*, 60:187–207, 1985.

[174] V. Rokhlin. Rapid solution of integral equations of scattering theory in two dimensions. *J. Comp. Phys.*, 86:414–439, 1990.

[175] V. Rokhlin. Diagonal forms of translation operators for the Helmholtz equation in three dimensions. *Appl. Comp. Harmonic Anal.*, 1:82–93, 1993.

[176] V. Rokhlin. Sparse diagonal forms for translation operators for the Helmholtz equation in two dimensions. *Appl. Comp. Harmonic Anal.*, 5:36–67, 1998.

[177] T. Rüberg. *Non-conforming Coupling of Finite and Boundary Element Methods in Time Domain*. PhD thesis, TU Graz, 2007.

[178] Y. Saad. A flexible inner-outer preconditioned GMRES algorithm. *SIAM J. Sci. Comput.*, 14:461–469, 1993.

[179] Y. Saad. *Iterative methods for sparse linear systems*. SIAM, 2nd edition, 2003.

[180] Y. Saad and M. H. Schultz. GMRES: a Generalized Minimal Residual Algorithm for solving nonsymmetric linear systems. *SIAM J. Sci. Comput.*, 7:856–869, 1986.

[181] E. H. Saenger, N. Gold, and S. A. Shapiro. Modeling the propagation of elastic waves using a modified finite-difference grid. *Wave Motion*, 31:77–92, 2000.

[182] T. Sakuma and Y. Yasuda. Fast multipole boundary element method for large-scale steady-state sound field analysis. Part I: Setup and validation. *Acta Acustica united with Acustica*, 88:513–525, 2002.

[183] F. J. Sánchez-Sesma. Diffraction of elastic waves by three-dimensional surface irregularities. *Bull. Seism. Soc. Am.*, 73:1621–1636, 1983.

[184] F. J. Sánchez-Sesma and M. Campillo. Diffraction of P, SV, and Rayleigh waves by topographic features: a boundary integral formulation. *Bull. Seism. Soc. Am.*, 81:2234–2253, 1991.

[185] S. A. Sauter. Variable order panel clustering. *Computing*, 64:223–261, 2000.

[186] M. Schanz. Multistep time discretization of boundary integral equations in dynamics. In S. N. Atluri and P. E. O'Donoghue, editors, *Modelling and simulation based engineering*, pages 223–228. Tech Science Press, 1998.

[187] M. Schanz. A boundary element formulation in time domain for viscoelastic solids. *Communications in Numerical Methods in Engineering*, 15:799–809, 1999.

[188] M. Schanz. *Wave Propagation in Viscoelastic and Poroelastic Continua. A Boundary Element Approach.* Springer, 2001.

[189] M. Schanz and H. Antes. A new visco- and elastodynamic time domain Boundary Element Formulation. *Computational Mechanics*, 20:452–459, 1997.

[190] J. F. Semblat and J. J. Brioist. Efficiency of higher order finite elements for the analysis of seismic wave propagation. *J. Sound Vib.*, 231:460–467, 2000.

[191] J. F. Semblat, A. M. Duval, and P. Dangla. Seismic site effects in a deep alluvial basin: numerical analysis by the boundary element method. *Computers and geotechnics*, 29:573–585, 2002.

[192] J. F. Semblat, R. Paolucci, and A. M. Duval. Simplified vibratory characterization of alluvial basins. *C. R. Geoscience*, 335:365–370, 2003.

[193] J. F. Semblat and A. Pecker. *Waves and vibrations in soils*. IUSS Press, 2008.

[194] K. Sertel and J. L. Volakis. Incomplete LU preconditioner for FMM implementation. *Microwave and Optical Technology Letters*, 26:265–267, 2000.

[195] R. P. Shaw. Diffraction of acoustic pulses by obstacles of arbitrary shape with a Robin Boundary condition. *J. Acoust. Soc. Am.*, 41:855–859, 1967.

[196] C. Somigliana. *Sopra l'equilibrio di un corpo elastico isotrope*. Il nuovo ciemento, 1886.

[197] J. Song and W. C. Chew. Fast multipole method solution using parametric geometry. *Microwave and Optical Technology Letters*, 7:760–765, 1994.

[198] J. Song, C. C. Lu, and Chew W. C. Multilevel fast multipole algorithm for electromagnetic scattering by large complex objects. *IEEE Trans. Antennas Propag.*, 45:1488–1493, 1997.

[199] A. H. Stroud and D. Secrest. *Gaussian quadrature formulas*. Prentice-Hall, 1966.

[200] G. Sylvand. *La méthode multipôle rapide en électromagnétisme. Performances, parallélisation, applications*. PhD thesis, ENPC, 2002. In French, http://pastel.paristech.org/308/.

[201] T. Takahashi, N. Nishimura, and S. Kobayashi. A fast BIEM for three-dimensional elastodynamics in time domain. *Engng. Anal. Bound. Elem.*, 27:491–506, 2003.

[202] T. Takahashi, N. Nishimura, and S. Kobayashi. A fast BIEM for three-dimensional elastodynamics in time domain. *Engng. Anal. Bound. Elem.*, 28:165–180, 2004.

[203] M. Tanaka, V. Sladek, and J. Sladek. Regularization techniques applied to boundary element methods. *Appl. Mech. Rev.*, 47:457–499, 1994.

[204] J. Tausch. Sparse BEM for potential theory and Stokes flow using variable order wavelets. *Computational Mechanics*, 32:312–318, 2003.

[205] M. D. Trifunac and A. G. Brady. A study on the duration of strong earthquake ground motion. *Bull. Seism. Soc. Am.*, 65:581–626, 1975.

[206] M. Vallon. Estimation de l'épaisseur d'alluvions et sédiments quaternaires dans la région grenobloise par inversion des anomalies gravimétriques. Technical report, LGGE, Université Joseph Fourier, 1999. IPSN/CNRS (in French).

[207] J. Virieux. P-SV wave propagation in heterogeneous media: velocity-stress finite-difference method. *Geophysics*, 51:889–901, 1986.

[208] M. S. Warren and J. K. Salmon. Astrophysical N-body simulations using hierarchical tree data structures. In *Proceedings of the 1992 ACM/IEEE conference on Supercomputing*, pages 570–576, 1992.

[209] L. T. Wheeler and E. Sternberg. Some theorems in classical elastodynamics. *Archive for Rational Mechanics Analysis*, 31:51–90, 1968.

[210] N. Yarvin and V. Rokhlin. Generalized gaussian quadratures and singular value decompositions of integral operators. *SIAM J. Sci. Comput.*, 20:699–718, 1998.

[211] L. Ying, G. Biros, and D. Zorin. A kernel-independent adaptive fast multipole algorithm in two and three dimensions. *J. Comp. Phys.*, 196:591–626, 2004.

[212] T. Yokoi. The high order Born approximation applied to improve the solution of seismic response of a three-dimensional canyon by the Indirect Boundary Method. *Physics of the Earth and Planetary Interiors*, 137:97–106, 2003.

[213] K. I. Yoshida. *Application of fast multipole method to boundary integral equation method*. PhD thesis, Kyoto University, 2001.

[214] K. I. Yoshida, N. Nishimura, and S. Kobayashi. Application of new fast multipole boundary integral equation method to crack problems in 3D. *Engng. Anal. Bound. Elem.*, 25:239–247, 2001.

[215] D. W. Zingg. Comparison of high-accurate finite-difference methods for linear wave propagation. *SIAM J. Sci. Comput.*, 22:476–502, 2000.

[216] D. W. Zingg, H. Lomax, and H. Jurgens. High-accuracy finite-difference schemes for linear wave propagation. *SIAM J. Sci. Comput.*, 17:328–346, 1996.

SOFTWARES AND LIBRARIES

[217] Intel Math Kernel Library for the Linux Operating System, User's guide. 2007.

[218] E. Anderson, Z. Bai, C. Bischof, S. Blackford, J. Demmel, J. Dongarra, J. Du Croz, A. Greenbaum, S. Hammarling, A. McKenney, and D. Sorensen. *Lapack user's guide, third edition*. SIAM, 1999. http://www.netlib.org/lapack/; http://www.netlib.org/blas/.

[219] H. Borouchaki and P. Laug. BL2D-V2: bidimensional mesh generator. Technical description, 2002.

[220] V. Frayssé, L. Giraud, and S. Gratton. A set of Flexible-GMRES routines for real and complex arithmetics. CERFACS Technical Report TR/PA/98/20, public domain software available on www.cerfacs.fr/algor/Softs, 1998.

[221] V. Frayssé, L. Giraud, S. Gratton, and J. Langou. A set of GMRES routines for real and complex arithmetics on high performance computers. CERFACS Technical Report TR/PA/03/3, public domain software available on www.cerfacs.fr/algor/Softs, 2003.

[222] P. Frey. Medit: An interactive mesh visualization software. INRIA Rapport Technique n°0253, 2001.

[223] P. Frey. YAMS: A fully automatic adaptive isotropic surface remeshing procedure. INRIA Rapport Technique n°0252, 2001.

[224] F. Hecht. BAMG: Bidimensional Anisotropic Mesh Generator. http://www.ann.jussieu.fr/∼hecht/ftp/bamg/, 2006.

ABSTRACT

Simulating wave propagation in 3D configurations is becoming a very active area of research. The main advantage of the BEM is that only the domain boundaries are discretized. As a result, this method is well suited to dealing with unbounded domains. However, the standard BEM leads to fully-populated matrices, which results in high computational costs in CPU time and memory requirements. The Fast Multipole Method (FMM) has dramatically improved the capabilities of BEMs for many areas of application. In this thesis, the FMM is extended to 3D frequency-domain elastodynamics in homogeneous and piecewise-homogeneous media (using in the latter case a FMM-based BE-BE coupling). Improvements of the present FM-BEM are also presented: preconditioning, reduction of the number of moments, and formulation of a multipole expansion for the half space fundamental solutions. Seismological applications are given for canonical problems and the Grenoble valley case.

Key words: Fast multipole method; Boundary element method; Wave propagation; Seismic wave amplification; Elastodynamics; Computational mechanics.

RÉSUMÉ

La simulation de la propagation d'ondes pour des configurations 3D est un domaine de recherche très actif. Le principal avantage de la BEM est de ne discrétiser que les frontières du domaine. Elle est ainsi bien adaptée aux domaines infinis. Cependant, la BEM classique conduit à des matrices pleines et donc à des coûts de calcul et mémoire importants. La FMM a permis d'augmenter de manière significative les capacités de la BEM dans beaucoup de domaines d'application. Dans ce travail, la FMM est étendue aux équations de l'élastodynamique 3D dans le domaine fréquentiel, pour des domaines homogènes puis, grâce à une stratégie de couplage BE-BE, aux problèmes multi-domaines. D'autres améliorations de la méthode sont aussi présentées: préconditionnement, réduction du nombre de moments, développement multipôle pour les fonctions de Green du demi-espace. Des applications en sismologie sont présentées pour des modèles canoniques ainsi qu'au modèle de la vallée de Grenoble.

Mots clés: Méthode multipôle rapide; Méthode des éléments de frontière; Propagation d'ondes; Amplification des ondes sismiques; Élastodynamique; Mécanique Numérique.